5-2019

Plasma oxidation of liquid precursors for complex metal oxides.

Babajide Patrick Ajayi
University of Louisville

PLASMA OXIDATION OF LIQUID PRECURSORS FOR COMPLEX METAL OXIDES

By

Babajide Patrick Ajayi

B.Sc., Obafemi Awolowo University, Ile-Ife, Nigeria, 2008

M.S., King Fahd University of Petroleum & Minerals, Saudi Arabia, 2013

A Dissertation

Submitted to the Faculty of the

J.B. Speed School of Engineering of the University of Louisville

in Partial Fulfillment of the Requirements

for the Degree of

Doctor of Philosophy in Chemical Engineering

Department of Chemical Engineering

University of Louisville

Louisville, Kentucky

May 2019

PLASMA OXIDATION OF LIQUID PRECURSORS FOR COMPLEX METAL OXIDES

By

Babajide Patrick Ajayi

B.Sc., Obafemi Awolowo University, Ile-Ife, Nigeria, 2008

M.S., King Fahd University of Petroleum & Minerals, Saudi Arabia, 2013

A Dissertation Approved On

April 15, 2019

By the Following Dissertation Committee:

_____
Dr. Mahendra K. Sunkara (Dissertation Director)

_____
Dr. Gautam Gupta

_____
Dr. Joshua Spurgeon

_____
Dr. Thomas Starr

_____
Dr. Jacek B. Jasinski

_____
Dr. Farshid Ramezanipour

DEDICATION

To the three amazing women in my life: Oreoluwa, Folasade and Olayinka Ajayi

ACKNOWLEDGMENTS

This dissertation is a milestone in more ways than one: on a personal level, this work and the Ph.D. degree that accompanies it is an achievement I will treasure for years, and in the context of pushing the envelope of the materials science related energy research, the broader impact of this work is truly remarkable. Thus, I would like to take a moment to thank everyone who has been a part of this journey with me. Ever since I have stepped foot on United States soil I have been overwhelmed with a deluge of support from within the University of Louisville – Chemical Engineering Department and Conn Center for Renewable Energy Research, and beyond, so; the next few paragraphs shall be dedicated to acknowledging people and institutions who have offered support, funding and resources; shared ideas; advice; or materials, or assisted with experiments or theoretical calculations.

I am profoundly grateful to my advisor, Dr. Mahendra Sunkara, who doubles as the Director of Conn Center for Renewable Energy Research and Professor of Chemical Engineering, University of Louisville. His invaluable support is instrumental towards the successful completion of this dissertation. He not only came up with the research topic, he provided research assistantship funding and guided me over five years of the development of this process. Last but not least, his career advice and moral support are most definitely appreciated and will remain with me forever.

My dissertation committee supported me through all these years, so; I am thanking Dr. Jacek Jasinski, Dr. Joshua Spurgeon, Dr. Thomas Starr, Dr. Gautum Gupta, and Dr.

Farshid Ramezanipour. Specifically, the brilliance and contributions of Drs. Jasinski and Spurgeon are the key factor in the successful execution of many of the projects reported in this dissertation, and for this, I owe them a debt of gratitude.

My sincere thanks goes to the following collaborators and/or members of staff of Conn Center: Ms. Eunice Salazar (Conn Center), Mr. Andrew Marsh (Conn Center), Dr. Gamini Sumanasekera (Conn Center), Dr. William (Hank) Paxton (Conn Center), Dr. Arjun Thapa (Conn Center), Dr. Sudesh Kumari (Conn Center), Dr. Madhu Menon (University of Kentucky), Dr. Dali Qian (University of Kentucky), Dr. Eric Stach (Brookhaven National Lab), Dr. Dmitri Zakharo (Brookhaven National Lab), Dr. Uros Cvelbar (Jozef Stefan Inst., Slovenia), Dr. Antonis Andriotis (Foundation Research and Tech., Greece), Dr. Dominika Ziolkowska (University of Warsaw, Poland), Dr. Sagar E. Shirsath (University of New South Wales, Australia) and Dr. Srinivasan Rasipuram (University of Louisville). The contributions of lab mates are also much appreciated. I am grateful to Daniel F. Jaramillo-Cabanzo, Apolo Nambo, Muhammad Z. Akram, Sonia Calero and Veerendra Atla for an eventful stay at the University of Louisville.

Heartfelt thanks go to my God, my source of eternal inspiration, and to my family: Folasade and Oreoluwa Ajayi for their prayers, patience and support, to my parents: Mr. and Mrs. Joseph Ajayi, for invaluable advice and prayers, and siblings: Tolulola Agboola, Modupe Adebimpe, Mosunmola Adegoke and Josephine Olufunmilayo Omosanwoeni for being there for me, every step of the way.

Finally, my research would have been impossible without the aid and support of University of Louisville PhD Fellowship award, and two National Science Foundation

research grants: NSF EPSCoR under the cooperative agreement No. 1355438 and NSF Solar Project grant No. DMS 1125909.

ABSTRACT

PLASMA OXIDATION OF LIQUID PRECURSORS FOR COMPLEX METAL OXIDES

Babajide Patrick Ajayi

April 15, 2019

Clean energy production and storage are two of the most significant challenges in the 21st century currently limited by the discovery and development of new and advanced materials. Complex oxides and alloys made using earth-abundant elements will play a crucial role in technology development moving forward, however, current preparation techniques are limited by their inability to produce complex oxides and alloys with precise composition control at fast timescales.

A concept was proposed to produce mixed metal oxides with composition control through the oxidation of liquid precursors *via* plasma oxidation. It was hypothesized that the oxidation process can be completed in fast timescales owing to the rapid heating and cooling of the plasma process.

Even though the rapid timescales for oxidation can be understood through fast heating processes during plasma exposure, the mechanisms responsible for composition control are not immediately obvious. So, fundamental experiments were carried out to elucidate the nucleation and growth steps responsible for metastable non-stoichiometric oxide formation. Interrupted oxidation experiments completed within twenty seconds revealed the following steps during plasma exposure of liquid droplets: the nucleation of

monometallic oxide phases from an amorphous nutrient, solid-state reaction into intermediate mixed oxide phase, and formation of metastable phase. Evidence also suggests the fast kinetics of the oxidation process depends on the enormous heat released from the recombinative reactions among plasma species present in the plasma.

The viability of a select set of plasma-synthesized oxides were tested in energy conversion and storage technologies. The technique was successfully used to synthesize $W_{0.99}Ir_{0.01}O_{3-\delta}$ alloy which showed high oxygen evolution reaction (OER) activity and stability in acid with an overvoltage reduction in the excess of 500 mV compared to the same composition prepared *via* standard thermal oxidation route. The structural dilution of iridium with earth-abundant tungsten will enable the efficient use of scarce iridium resources. In alkaline media OER, charge-transfer type double perovskite ($La_{0.9}Ca_{0.1}Co_{0.5}Ni_{0.5}O_{3-\delta}$) prepared *via* the rapid plasma method shows excellent activity rivaling best performing complex oxide electrocatalysts. Most importantly, the obtained experimental data, combined with density functional theory calculations allows for relating the high OER activity to the strong hybridization of the transition metal 3*d* and oxygen 2*p* bands. Again, this technique has been used to fabricate manganese-enriched nickel-manganese-cobalt (NMC) oxides. The resulting NMC materials were tested as cathodes in lithium ion battery and show competitive results compared with NMCs prepared through other routes.

This dissertation presents a concept utilizing plasma oxidation of liquid precursors for composition control of complex oxides and alloys. The presented concept could expedite the accelerated discovery and development of advanced materials for energy conversion and storage. Furthermore, the underlying nucleation and growth mechanistic

aspects for forming non-stoichiometric oxide phases will add scientific knowledge to our understanding of the synthesis of materials far from equilibrium.

TABLE OF CONTENTS

LIST OF TABLES

LIST OF FIGURES

CHAPTER 1

INTRODUCTION

The production and supply of clean energy using highly efficient, durable and low-cost materials is perhaps one of the most prominent challenges facing mankind in the present time. The availability of technologies for clean energy production and storage requires discovery and development of advanced materials made using earth-abundant elements that can facilitate efficient energy conversion and storage[1-2]. In terms of solar technologies, one needs to discover materials made using earth-abundant elements that can absorb visible and infra-red solar radiation and possess high electron mobility[3]. Current set of known materials with such properties are limited. Also, the discovery of inorganic equivalent of halide perovskites with similar light absorption and electronic mobility is highly desired[3]. In electrochemical energy storage, almost all the concepts depend upon discovery new materials with high ionic conductivity and high capacities. In the case of lithium-ion battery technology, cathode material dictates battery performance and is the most expensive of the battery components, accounting for up to 35% of the materials cost[4]. Reducing the cost of the cathode material represents a significant decrease in the cost of the battery. The cost of making a cathode depends mostly on raw material and production costs, where materials cost accounts for up to 60% of the total cost[4]. The incumbent cathode material manufacturing techniques require many processing steps and produce environmentally unfriendly chemical byproducts, adding to cost, and reducing their

commercial appeal. This is especially true for solid-solution such as $LiNi_{1/3}Mn_{1/3}Co_{1/3}O_2$ which are difficult to produce using the traditional approach. Improving energy and power density also require discovery of new materials for anode, cathode and solid electrolyte used in lithium ion, sodium ion and multi-valent ion intercalation technologies.

Another way to store solar energy is to store it within chemical bonds[5]. One of such methods is the use of electricity (from solar energy or other renewable source) to split water into hydrogen and oxygen. Since it is practicable to convert the stored chemical energy in hydrogen into usable electrical energy using the proton exchange membrane fuel cells (PEMFCs), PEMFCs will be a key technology in any visualized model of the so-called *hydrogen economy* moving forward. Water splitting involves two reactions: (1) oxygen evolution reaction (OER); which occurs at the anode (2) hydrogen evolution reaction (HER), which takes place at the cathode. OER is the slower of the two, requiring the transfer of four electrons across electrodes and so; efficient catalysts are needed to drive it to completion at a rapid pace. The state-of-the-art OER electrocatalysts currently in use in water electrolyzers are made from noble metals such as iridium and ruthenium oxide known as platinum group metals (PGM). Iridium is approximately four-orders-of-magnitude less abundant than most regular non-noble metal electrocatalysts such as nickel, cobalt, iron, manganese. The 2020-target set by the U.S. Department of Energy for the maximal catalyst loading value is 0.125 mg of PGM per 1 cm^2 electrode area[6], even so, there remain questions as to whether these noble metals could be scaled-up to meet the world's energy needs. Some earth-abundant and non-noble metal OER catalysts, including nickel-iron oxide, cobalt oxide, manganese oxide, and others, have overpotentials comparable to iridium oxide in alkaline conditions, but they are easily digested in the

strongly acidic electrolyte. Many of these issues can be addressed by designing complex structures involving diverse elements in order to tailor material properties in a way that it overcome these limitations[7]. Complex metal oxides are distinct class of inorganic materials which are essential to many industrial chemical and clean energy applications, providing inexpensive routes to solving the above energy challenges and for efficient production of platform or high-value chemicals[5].

1.1 Need for New Synthesis Methods

The synthesis of complex metal oxides, which is composed of various elements ranging from alkaline-earth, alkali, transition and post-transition metals in multinary systems (with more than one metal cations and one oxygen anion) such as ternary, quaternary, etc., present an enormous challenge in material processing and property screening for efficient end use. For example, there are about 8,000 and 700,000 possible combinations in a ternary and quaternary systems respectively[8], so; the non-triviality of the challenge in finding best possible candidate from the colossal parameter space is immediately apparent, and this challenge becomes even more daunting when one factors in solid-solutions and alloys into the equation.

In the report issued by the Basic Sciences Advisory Committee of the U.S. Department of Energy, one of five challenges for science and imagination, and more specifically, the fifth challenge is[9] "*How do we characterize and control matter away - especially very far away - from equilibrium?"*. This challenge underscores the fact that the preferential disposition of both artificial and natural condensed matter is to exist at equilibrium conditions, the most stable state of matter, following a natural law motivated mostly by the minimization of energy. There is a whole body of knowledge on materials at

equilibrium, but the research depth of non-equilibrium matter is superficial at best, given the synthesis challenge. There is a growing interest in using non-equilibrium materials such as complex metal oxides in solving energy challenges[10], but the incumbent techniques employed in the synthesis of multi-element complex oxides require elevated temperatures which unfortunately favors strongly the phase segregation into stable equilibrium phases. Accordingly, a good number of the solid-solution composition space is not actually synthesized, possibly circumventing, sometimes unwittingly, promising energy-harnessing materials. Also, these conventional techniques lack the ability to control composition of complex oxides directly from the precursor composition, the biggest issue yet in tailoring materials property *via* electronic property modulation, which have implications in catalysis, energy storage, superconductivity, magnetism, thermoelectric effect and solar conversion.[11-15]

The classical route for synthesizing complex oxides is the solid-state chemistry which involves the mechanical milling and/or high temperature heat treatment of oxides, carbonates or nitrates[16]. Solid state route is severely limited by its long treatment time and elevated processing temperature and pressure[17]. Also, wet chemical techniques such as sol-gel[18], co-precipitation[19] solvothermal techniques[20], Pechini[21], are other state-of-the-art methods. Nonetheless, these approaches require extended heat treatments, making them inadequate, owing to equilibrium phases formed at the end of these processes[22]. In addition, they are low-yield methods involving multiple and arduous processing steps. Furthermore, the differences in precipitation rates in the coprecipitation method, and the fact that some metal-organic structure can be transformed into different phases before being frozen-in inside the organometallic framework in the sol-gel and Pechini methods can seriously limit

these syntheses approach in their ability to control final oxide composition from the precursor composition. More so, with these methods, it is quite a challenge to control the size and composition of mixed metal oxide nanoparticles, a key parameter determining the intrinsic properties and performance of these materials.

Therefore, there is a staggering need for synthesis techniques that are free from bottlenecks common with the conventional methods, including but not limited to multiple step processing routes, long synthesis hours, inadequate control of stoichiometry and composition, and so on. Combinatorial chemistry, involving automatic and parallel generation of multi-component solution-based precursors, has been employed to accelerate the process of materials discovery[23], but there are little or no evidence to suggest the thermal oxidation conversion strategy employed is sufficiently suitable to make homogeneous phase oxides with excellent compositional control. As an illustration, if a synthesis technique lacks compositional control so much so that a minuscule 0.1% sub-stoichiometry results from inaccurate control of metal cations ratio, this error is tantamount to about ~10^{19} cm^{-3}.[8]

1.2 Proposed Concept

Here, a concept on oxidation of liquid precursors using atmospheric plasmas is proposed for obtaining complex oxide particles with composition control**.** Our hypothesis is that the use of plasmas with oxygen radicals and rapid heating will yield non-equilibrium synthesis conditions with fast timescales. The promise of the concept is that ultrafast timescales for energy delivery and oxidation would allow for the synthesis of complex oxides far away from equilibrium, with precise composition control.

There have been attempts to utilize plasmas for materials processing with ultra-fast timescales of reaction. Earlier studies using plasma oxidation schemes have shown ultra-fast timescales for both molten metals [24] and metal oxides in the presence of alkali salts. Studies involving inductively coupled plasma for droplet-to-particle concept has been successful but only shown with single component systems [25-26]. Schaefer and co-workers[27] studied the gas phase nucleation and *in vacuo* deposition of iron oxide nanoparticles from ferrocene vapor in a microplasma reactor. The difficulties inherent in vapor phase nucleation are lack of precise compositional control in making multi- metal oxides. There have been attempts on the use of flame pyrolysis for synthesizing metal oxide nanostructures but mostly limited to simple oxides with limited data on composition control. Flame pyrolysis has been commercially used for production of titania and related materials valued at $15b/year [28]. Many of the nanoparticles in the current market are monometallic oxides such as SiO_2, TiO_2, Al_2O_3, but new and emerging markets require complex and functional materials such as doped materials and multi-component solid-solutions used in specialty applications and prepared via methods that support facile stoichiometry control.

While there are few studies on synthesis of mixed metal oxides by plasma oxidation of liquid droplets[29-30], none to the best of our knowledge, has provided insights into the fundamental understanding of plasma-liquid interaction, enough to give a clear pathway for the oxidative process. Also, the design and implementation of the plasma approach in large-scale manufacturing as a cost-effective method remains an ongoing investigation among researchers.

1.3 Objectives of Dissertation

Even though, there are prior attempts at utilizing plasmas and flames for processing metal oxide nanostructures, there is no clear demonstration about composition control for complex oxides with compositions faraway from equilibrium, furthermore, there were no previous work on the fundamental understanding of the process. Thus, there are two broad objectives and three specific objectives listed as follows:

1) Obtain fundamental understanding about how plasma oxidation of solution precursors can produce complex oxides with exceptional stoichiometric control with multi-element composition. The specific objectives under this broad objective are:
    a) Determine the role of recombinative heating of plasma species
    b) Study the mechanistic steps involved in plasma oxidation to obtain non-equilibrium composition
    c) Determine whether these steps are different for equilibrium composition
2) Demonstrate the viability of the plasma-synthesized materials as energy materials in energy storage and conversion technologies. The specific objectives are:
    a) Device a new acid-stable mixed noble/non-noble metal oxide electrocatalysts in OER using the plasma oxidation method
    b) Obtain a rational activity descriptor for basic media OER using catalysts synthesized via plasma method
    c) Obtain data for scalable high-volume manufacturing of complex oxide cathodes used in lithium-ion battery

1.4 Organization of Dissertation

This dissertation contains nine distinct chapters organized in a fashion outlined below:

Chapter one presents the materials synthesis challenges as it relates to prohibitive factors preventing complex oxides from going mainstream in many commercial applications. Also presented here are the energy challenges and why renewables lag behind in many industrial processes. Finally, the hypothesis and the roadmap of the dissertation is presented.

Chapter two presents a brief review of complex metal oxides detailing history, structure-function relationship and thermodynamics. Also, the challenges and opportunities inherent in the state-of-the-art and the plasma-oxidation methods are discussed at length, especially as it relates to seamless control of stoichiometry, the comparison of the ease of preparation of materials, and the energy-focused applications where complex oxides have been deployed in solving energy challenges. Newer concepts in materials design such as high entropy alloys are also discussed.

Chapter three presents an overview of the experimental methods and materials adopted in this dissertation, including specifics of materials development and reactors set-up and design, instruments and data analysis procedures for determination of key surface and textural properties including other physicochemical characteristics of the samples. The main electroanalytical chemistry tools and techniques for assessing the performance of the materials were also discussed.

Chapter four presents an antecedent data of results detailing how the plasma-oxidation methodology display exceptional and firm control of composition of complex metal oxides and solid-solutions.

Chapter five presents a study that elucidates the role played by plasma-liquid interactions in this process, investigate the mechanism of formation of complex oxides, and study the impact of recombinative heating from radicals or other plasma species.

Chapter six presents materials testing example of electrocatalysis of oxygen evolution reaction in acidic media, using solid-solution of two monometallic oxides (tungsten trioxide and iridium oxide).

Chapter seven display a data of results as it relates to the activity prediction of electrocatalysts of the charge-transfer type complex oxide. The DFT predicted activity trend for plasma-synthesized perovskite was compared with the experimental oxygen evolution activity in basic media.

Chapter eight presents another material testing example in energy storage technology. Manganese-rich NMC were synthesized and their performance as cathodes in lithium-ion battery technology were tested and reported.

Chapter nine presents the conclusions and recommendations of study

CHAPTER 2

BACKGROUND

2.1 General Remarks and Scope of Review

This dissertation is centered on the fabrication of complex metal oxides *via* rapid plasma method, and the materials performance data of the plasma-prepared samples in renewable energy processes such as water-splitting oxygen evolution reaction and lithium ion battery technology. This chapter shall thus focus on the background studies on the state-of-the-art and conventional methods of synthesis and the electrochemistry behind the energy conversion and storage processes employed in the characterization of samples. Specifically, this review shall cover history, methods, challenges, and strategies for the preparation of complex or mixed metal oxides, and how their structures affect their properties in chemical/energy transformation and energy storage processes, with a particular focus on mixed metal oxide phase and their solid-solutions, non-stoichiometric mixed oxides and solid solution of monometallic oxide phases. Also reviewed is the state-of-the-art materials in use in several renewable energy technologies.

2.2 Historical Perspective

The earliest record of fired clay was dated back to 22000 B.C. in prehistoric China[31]. Other remarkable prehistoric periods in the evolution of ceramic technology includes: 8000 B.C.; the first fired earthenware vessels was discovered in the Near East, 4000 B.C.; the first recorded Egyptian glazed ceramic wares, 1500 B.C; was traced to the

first glass manufacturing and 700 B.C.; the first record of green, black and red stonewares[32]. The industrial revolution saw a pronounced improvement in the fabrication of soft and hard-paste porcelains, tin-glazed wares, jasperwares and stonewares across Europe and United States[32].

As ceramic technology advanced from ornamental and domestic use to a smarter functionality as we have in sensors and actuators, catalysts, ferromagnets, superconductors, solid-electrolytes, and supercapacitors; synthesis methodology has since evolved from the more traditional ceramic processing route known as the high-temperature solid-state chemistry approach to more rational *soft chemistry* approach[33]. Perhaps the best way to capture the essence of the modern-era synthesis approach is to discuss the *sol-gel* technique. Nanotechnology spawned many new techniques, sol-gel being a prominent one[34]. The need for nanosized materials has opened the door to more systemic approach rather than the pre-modern-era dependence brute force and extreme synthesis conditions. Geffcken and Berger first reported the synthesis of single metal oxide coatings about 80 years ago[35], large scale production of rear-view mirrors, anti-reflective coatings on mirrors and sunlight attenuating windows containing multicomponent metal oxides were completed in 1959, 1964 and 1969 respectively[36].

2.3 Complex Oxides for Energy Conversion and Storage Processes

Various complex oxides containing diverse and multi-component metals including alkali, alkaline, rare-earth, transition, metalloid and noble metals and their applications in many renewable energy processes are reviewed in this section. Complex oxides are at the heart of several technologies in renewable energy which includes, but not limited to solid-electrolytes[37], rechargeable lithium ion battery[38], electrocatalysis[39], photocatalysis[40],

thermoelectricity[41], and heterogeneous catalysis[42]. These materials sometimes contain at least one transition metal whose shifting chemical states are essential to many properties including redox, electronic, and catalytic properties, or their structure may be tailor-made for insertion and deinsertion of charged carriers, or in other cases they may have good photo-absorbing properties or may comprise of layers which serve as either electron transport path or as phonon scattering region. Also, their refractory properties make them interesting choice in high temperature processes such as heterogeneous catalysis, thermoelectricity, ionic conductors, etc.

Table 2.1 gives a summary of the state-of-the-art materials and some selected materials still in development, their performances in several energy technologies and the preparation routes adopted in their synthesis.

2.3.1 Thermoelectric device

Thermoelectricity is a unique way of converting waste heat into electricity, conversely, thermoelectricity works as a heat pump in refrigerators. The conversion efficiency is determined by the figure of merit, ZT, which by definition is[43]:

$$ZT = \frac{\alpha^2 T}{\rho\kappa} = \frac{PF}{\kappa} = \frac{\alpha^2 T}{\rho(\kappa_1+\kappa_2)} \qquad 2.1$$

where α is the Seebeck coefficient, κ is the thermal conductivity (κ_1 and κ_e are the lattice thermal and carrier thermal conductivities respectively), ρ is electrical resistivity. PF is power factor and T is temperature in Kelvin. An efficient thermoelectric material possesses small κ and ρ, but large $|\alpha|$. Even though there is no cap for ZT, a benchmarking protocol has set the ZT of viable thermoelectric (TE) device to 1. Oxides generally have low ZTs compared to state-of-the-art TEs, but their refractory properties induce temperature

gradients which makes them highly efficient TEs. Also, oxides, through composition control can be structurally engineered for optimum conversion efficiencies. Decent ZTs

Table 2.1 Selected complex oxides and their applicability in energy conversion and storage

Energy Applica-tion	Material	Preparation route	Performance	Remarks	Ref
OER anode	$Ba_{0.5}Sr_{0.5}Co_{0.8}Fe_{0.2}O_{3-\delta}$	Combustion	η=145 mV at 50μAcm^{-2}	Basic media OER. The perovskite has e_g close to 1 giving it a high covalency of metal-oxygen bonds. Better intrinsic activity than iridium oxide	39
	$Ni_{0.5}Mn_{0.5}Sb_{1.7}O_y$	Sputter deposition	η=672mV at 10mAcm^{-2}	Acid electrolyte. Catalyst is solid solutions of $NiSb_2O_6$ with $MnSb_2O_6$	7
	$Ni_{0.9}Fe_{0.1}O_x$	Solution cast	η=336mV at 10mAcm^{-2}	Activity attributed to *in situ* formation of layered oxyhydroxide phase ($Ni_{0.9}Fe_{0.1}OOH$). Basic media OER	44
	$SrCoO_{2.7}$	Co-precipitation	η=336mV at 10mAcm^{-2}	Basic media. Lattice oxygen freed-up by O_2 vacancies was attributed to activity	45

ORR cathode	$MnCo_2O_4$/N-rmGO	Hydrothermal	0.70 V *vs*. RHE, at *J*= 151 $mAcm^{-2}$	Outperforms Pt/C. Hybrid of spinel oxide and mildly reduced nitrogen doped graphene oxide. Basic media ORR	[40]
	$Co_xMn_{3-x}O_4$	Reduction of amorphous MnO_2	80mV *vs.* Ag/AgCl at 43.2 mA mg^{-1}	Bifunctional catalyst, i.e., also active for OER. Prepared at room temperature	[46]
CO_2 photo-reduction photo-catalyst	$BaLa_4Ti_4O_{15}$	Polymerizable complex method	Active towards CO and HCOOH	Performs in the presence of Ag cocatalyst (2 wt. %) as a photocatalyst in reduction of CO_2	[47]
	$MnCo_2O_4$	Solvothermal	Active towards syngas	Microsphere morphology	[48]
Li-ion battery electrode	$LiCoO_2$	Solid-state	140 mAh g^{-1} max. 3.8V	Low capacity, low voltage, cobalt is both expensive and toxic. Cathode.	[49]
	$LiNi_{1/3}Mn_{1/3}Co_{1/3}O_2$	Solid-state	200mAh g^{-1} in 3.5-5.0V	High capacity retention at high voltage. Low cobalt cathode material	[50]
	$LiMn_2O_4$	Pechini	135mAh g^{-1}/ 4.5V cut-off	Cathode. Good rate capability, high capacity fading, inexpensive material.	[51]
	$Li_4Ti_5O_{12}$	Controlled hydrolysis	131 mAh g^{-1} at 50 C	Hollow microsphere. High rate capability anode material	[52]
Solid-state electrolyte	$Li_5La_3Nb_2O_{12}$	Sol-gel	$\sigma_{Li}=1\times10^{-5}$ S cm^{-1} at 22°C	Stable against $LiCoO_2$ and $LiMn_2O_4$ cathodes	[53]

	$Li_{0.34}La_{0.56}TiO_3$	Sol-gel	$\sigma_{Li}=7\times10^{-5}$ S cm^{-1}	Reduction around 1.5V *vs* Li/Li^+ not suitable for graphite and lithium anode	[54]
Solar conversion PV/PEC photo-electrode	$BiVO_4$	Electrochemdeposition and solution cast	0.60 V *vs*. RHE, at *J*= 2.73mA cm^{-2}	Photoanode for water splitting. FeOOH/NiOOH layer helps reduce recombination.	[55]
	$CuFeO_2$	Sol-gel	0.35 V *vs*. RHE, at *J*= 1.51mA cm^{-2} (1 sun)	Photocathode for solar water reduction (*p*-type). Low-temp. synthesis	[56]
	$CuCrO_2$	Hydrothermal	OCV; 102 mV, solar efficiency; 0.0194%	Photocathode in dye sensitized solar cells (*p*-type)	[57]
CH_4 reforming catalyst	$La_{1.95}Ca_{0.05}Zr_{2-x}Rh_xO_7$	Pechini	X_{CH4} ~ 95% H_2/CO = 0.91	Dry reforming. *x*=0.055	[58]
	$La_{0.95}Ce_{0.05}NiO_3$	Citrate method	X_{CO2} ~ 62%, X_{CH4} ~ 50%	Dry reforming	[59]
	Ni-Co/ZSM-5	Hydrothermal	X_{CH4} = X_{CO2} = ~ 60%	ZSM-5 prepared via hydrothermal, Ni-Co loaded via wet impregnation. Dry reforming	[60]
Thermo-electric device	$Ca_3Co_4O_9$	Reactive solid-phase epitaxy	*ZT*~ 0.3 at 1000K	Na_xCO_2 was ion exchanged to form oxide (*p*-type).	[61]
	$Zn_{0.96}Al_{0.02}Ga_{0.02}O$	Solid-state	*ZT*~ 0.65 at 1247K	Inert synthesis atmosphere (*n*-type)	[62]

	BiCuSeO	Solid-state and spark plasma sintering	*ZT*~ 0.70 at 773K	*ZT* is close to performance benchmark of 1 (*p*-type).	[11]

have been found in *p*-type bulk oxide semiconductors such as Na_xCoO_2[63], $Ca_3Co_4O_9$[64], and $Bi_2Sr_2Co_2O_9$ [65]and perovskites such as $La_{0.95}Sr_{0.05}CoO_3$[66], and $Bi_{0.78}Sr_{0.4}RhO_{3+\delta}$[67]. Among oxide TEs reported, $Zn_{0.96}Al_{0.02}Ga_{0.02}O$[62] and BiCuSeO[11] are some of the best performing with ZTs of 0.65 (at 1247K) and 0.70 (at 773K) respectively.

2.3.2 Solid-state electrolytes.

While lithium ion battery plays a crucial role in energy storage especially in consumer electronics and electric vehicles, the commercial lithium ion battery contains liquid-phase electrolytes that are environmentally unfriendly which also raises some safety concerns due to their flammability. There are accelerated efforts to replace liquid-phase electrolytes with solid-phase electrolytes that possess high Li conductivity, which are called Li-ion conductors. Li-ion conductors are expected to lead the revolution to "all-solid-state-rechargeable-batteries" and to a large extent solid oxide fuel cell (SOFC) technology. The benchmark for viability of solid electrolytes for their implementation is the ionic conductivity, which should exceed 1×10^{-3} S cm^{-1} at room temperature[54, 68]. To that end, two class of materials are being looked at in the current literature: oxides and sulfides, but to date, the better ionic conductivity achieved with some sulfides ($Li_{10}GeP_2S_{12}$:1×10^{-2} S cm^{-1})[69] have put them ahead of oxides with significantly lower ionic conductivity. However, oxides have commercial appeal due to their low-cost, ease of preparation and facile ability to enhance their performance through structural engineering.

The oxides that are good candidates for solid electrolytes are garnets[70], perovskite[54], and Ruddlesden-Popper phase[71], LISICON (from the acronym: LIthium Super Ionic CONductors)[72]. Table 2.1 displays the highest ionic conductivities (σ_{Li}) recorded till date, garnet and perovskite with conductivities of 1×10^{-5} S cm^{-1} and 7×10^{-5} S cm^{-1} respectively, being the prominent ones. Oxides like LISICON can be structurally enhanced to improve ionic conductivities, for example, $Li_{2+2x}Fe_{1-x}SiO_4$ (with $0 \leq x \leq 0.3$) has a slow kinetics at the stoichiometric composition (x=0), however lithium-rich composition saw an improvement in the Li^+ diffusivity by at least two orders of magnitude[73]. This improvement was attributed to Li^+ occupying the octahedral sites interstitially.

2.3.3 Electrocatalysts in oxygen evolution and oxygen reduction reactions

Water splitting reaction (splitting of water into hydrogen and oxygen) is an important component of a promising energy infrastructure[5]. The incumbent route of producing hydrogen is *via* methane reforming reaction, but this method is energy demanding and lacks carbon neutrality. Electrocatalytic water splitting takes place in a device called electrolyzers, and it offers a clean and efficient means of producing hydrogen, a source of clean fuel. The liberation of oxygen is called oxygen evolution reaction (OER), whereas, the release of hydrogen is known as hydrogen evolution reaction (HER). The reverse process, i.e., oxygen reduction reaction (ORR) and hydrogen oxidation reaction (HOR) takes place in fuel cells and generates electricity. Besides its usefulness in clean energy, the other product of water splitting, oxygen, is generated onboard submarines and space shuttles/stations employing electrolysis taking place within stacks of PEM (Proton Exchange Membrane) cells known as cell stacks. Personnel onboard these submarines and space-shuttles utilizes generated oxygen for respiratory needs. Inside the cell stack is a sub-

component known as the Membrane Electrode Assembly (MEA) and it is within this MEA that electrocatalysts are employed to drive both the oxidation and reduction processes. PGM catalysts are the electrocatalysts in use, but they add a significant cost to the submarine electrolysis cell stack valued at $1 million each[74].

OER is a kinetically sluggish half-reaction of water splitting, requiring the transfer of four electrons across electrodes (as against two electrons for HER), and so; efficient catalysts are needed to drive it completion at a rapid rate. The electrolyte media could be alkaline (or base) or acid. In water electrolyzers, the basic media reactions and the equilibrium potential (E^0) are:

$$4OH^- \rightarrow O_2 + 2H_2O + 4e^- \ (E^0_{anode} = 1.23 \text{ V vs RHE, OER}) \qquad 2.2$$

$$2H_2O + 2e^- \rightarrow H_2 + 2OH^- \ (E^0_{cathode} = 0.0\text{V vs RHE, HER}) \qquad 2.3$$

and in acid, the equations, and the equilibrium potentials are:

$$2H_2O \rightarrow O_2 + 4H^+ + 4e^- \ (E^0_{anode} = 1.23\text{V vs RHE, OER}) \qquad 2.4$$

$$2H^+ + 2e^- \rightarrow H_2 \ (E^0_{cathode} = 0.0\text{V vs RHE, HER}) \qquad 2.5$$

In fuel cells, basic reactions are:

$$O_2 + 2H_2O + 4e^- \rightarrow 4OH^- \ (E^0_{cathode} = -1.23 \text{ V vs RHE, ORR}) \qquad 2.6$$

$$H_2 + 2OH^- \rightarrow 2H_2O + 2e^- \ (E^0_{anode} = 0.0\text{V vs RHE, HOR}) \qquad 2.7$$

In acid:

$$O_2 + 4H^+ + 4e^- \rightarrow 2H_2O \ (E^0_{cathode} = -1.23\text{V vs RHE, ORR}) \qquad 2.8$$

$$H_2 \rightarrow 2H^+ + 2e^- \ (E^0_{anode} = 0.0\text{V vs RHE, HOR}) \qquad 2.9$$

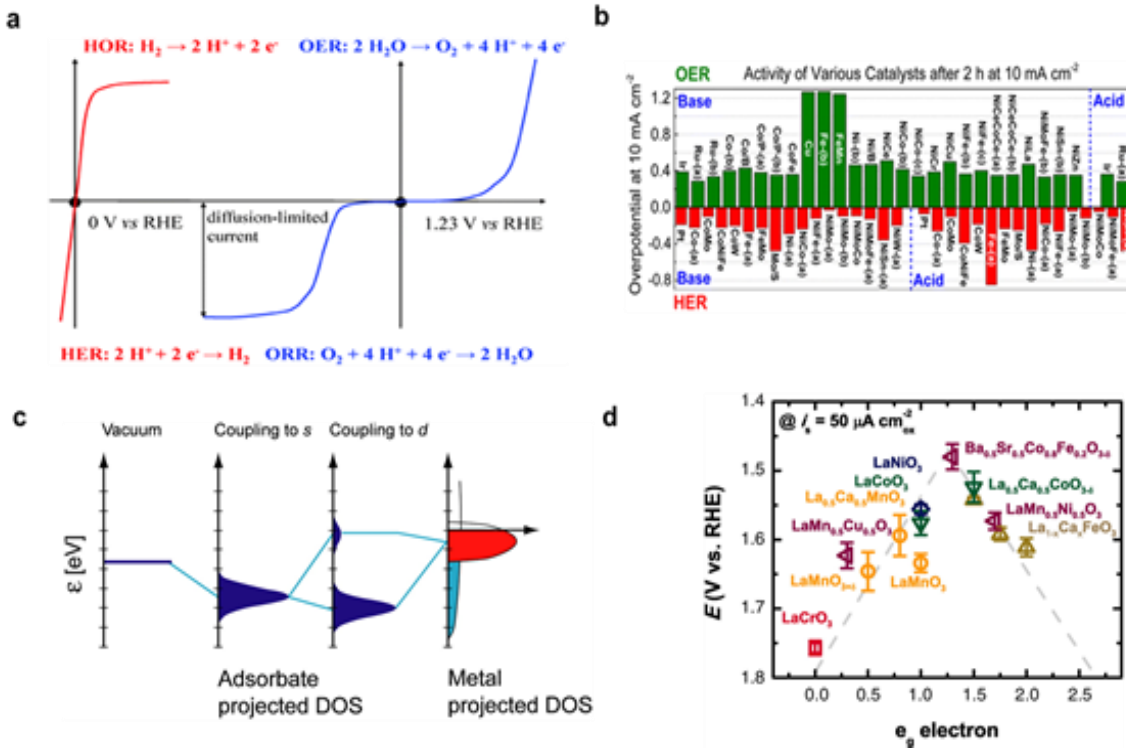

Figure 2-1| (a) Polarization curves of OER, ORR, HER and HOR in acid. Adapted from Ref. 75 (b) Overpotentials of selected catalysts in both acid and basic media OER and HER at 10mA cm^{-2} at 2h stability testing. Adapted from Ref.76 (c) Illustration of the formation of a chemical bond between an adsorbate valence level and the *s* and *d* states of a transition-metal surface. Adapted from Ref. 80 (d) Volcano plot of potentials vs RHE @ 50μA cm^{-2} against the filling of the e_g states. Error bars are according to standard deviation of three data sets. Adapted from Ref. 39

A summary of these acid-based reactions can be found in Figure 2-1(a)[75]. Due to its slow kinetics, the equilibrium potential in OER is 1.23V, however, an excess potential

above this value (called overpotential, η, in Table 2.1) is required to have appreciable current densities. Consequently, the large anodic overpotential required for this process seriously limits the water splitting reaction. Figure 2-1(b)[76] is based on a benchmarking protocol that assumes the overpotential necessary to achieve a current density of 10 mA cm^{-2} after 2h of testing, the estimated current density anticipated for a solar-to-fuels conversion efficiency of 10 % under 1 sun illumination. From the figure, in the basic media OER, there are lots of choice catalysts with η under 400mV, whereas, in the acid media, only two catalysts, all noble metals (iridium and ruthenium oxides) have η under 400mV after 2h of testing. Apart from the noble metals, most metals are digestible in strongly acidic solutions, placing a significant stability roadblock in acid-based OER besides the slow kinetics issue. There have been efforts to apply non-noble metals in acid-based OER, but the overpotentials are significantly high (Table 2.1)[7], other efforts are geared towards mixed oxides containing noble metals and non-noble metals, but noble metal concentrations in these solid-solutions can reach up to 40 mol.% for substantial OER activity[77-78].

Studies on OER electrocatalysis (especially basic media OER) have been focusing on predicting activity trends using either molecular orbital theory[39] or density functional theory (DFT)[45, 79]. Either of these predictive analyses have leveraged on the *d*-band model[80] which describes bond formation at a transition-metal surface, as shown in Figure 2-1(c), and the interaction between adsorbate valence states and the *s* and *d* states of a transition-metal surface. The strength of the interaction is defined by the level to which the antibonding state between the adsorbate state and the surface of the metal *d* states is occupied. The more the *d* states are in energy relative to the Fermi level, the emptier the

antibonding states and the stronger the surface-adsorbate interaction. A *sweet spot* of surface-adsorbate interaction is crucial for high OER activity[39, 79, 81], which is a catalysis concept first explained by the Sabatier principle[82]. Suntivich *et al*[39] found that, for a σ*-orbital (e_g) occupation, an e_g-filling close to 1 could be correlated to the highest activity. These results are summarized in a volcano plot illustrated in Figure 2-1(d). The optimum e_g-filling of ~1 was found for $Ba_{0.5}Sr_{0.5}Co_{0.8}Fe_{0.2}O_{3-\delta,}$ while perovskites such as $LaNiO_3$ and $LaCoO_3$ with e_g filling less than 1 shows some weak activity, whereas; catalysts such as $La_{0.5}Ca_{0.5}CoO_{3-\delta}$ and $LaMn_{0.5}Ni_{0.5}O_3$ with e_g filling above 1 are not sufficiently active towards OER. These poor activities on either side of the volcano summit were attributed to the too strong (for $e_g < 1$) or too weak (for $e_g > 1$) transition metal−oxygen covalent bonding, suggesting that a peak activity is achieved at a balanced (neither too strong nor too weak) bond strength. The tracking of the position of the O-2*p* band relative to the Fermi level using DFT has been reported as the basis of OER activity[79], where high activity and stability was rationalized as having the O-2*p* band center neither in close proximity nor too distant from the Fermi level.

Pt has been the most studied ORR electrode and is still the most active one. In fact, the commercially used electrocatalysts in fuel cells are Pt nanoparticles supported on a conductive carbon black. As is with OER, efforts are ongoing to reduce the dependence on noble metals such as Pt. Aside this, the surface of Pt NPs may become deactivated in the operating conditions of fuel cell[83]. As a result, Pt has been alloyed or being made to form intermetallic compounds with other metals such as Ni[84], Cr[85], and Ag[86]. Non-noble metal containing complex oxides such as spinels and perovskites have garnered traction as of

late[46, 87-88], with many of these catalysts performing with dual functionality in both OER and ORR electrocatalysis (Table 2.1).

2.3.4 Lithium ion battery electrodes

Rechargeable lithium ion battery (LIB) technology has theoretical gravimetric energy density up to 1725 Wh/kg and the practical energy density of a packaged battery system is estimated to about 500 Wh/kg[89] for automotive or power grid applications. Historically, LIB came into the commercial scene through the effort of Sony Corp. in 1991, and it is basically the exchange of Li^+ ion between graphitic anode and $LiCoO_2$ cathode, producing specific energy up to 180 Wh kg^{-1}, and averaging a voltage of 3.8 V [90](Table 2.1). However, further advancements are essential for LIBs to remain competitive for an extended period. To consolidate the gains from LIB research, lower cost, safe operation, and further improvement in energy and power densities[77] are some of the most prominent challenges that need urgent attention. As a result, goals were set in many countries, and most notably, the United States Department of Energy (DOE) initiative[91], which entrusted to a group of researchers clearly defined aims of tripling the specific energy from 180 Wh kg^{-1} to at least 500 Wh kg^{-1} while maintaining 1000 charge-discharge cycles.

$LiMn_2O_4$ spinel are interesting cathode materials owing to its abundance and low-cost, environmental benignancy, and offers even better safety to end-users. The most significant drawbacks are their low theoretical capacity (148 mAh g^{-1})[92], poor specific energy (154.3 Wh kg^{-1}) and relatively inferior capacity retention owing to dissolution of Mn^{2+} ions and Jahn-Teller distortions. The dissolution of Mn^{2+} from the spinel electrodes is made possible via a disproportionation reaction ($2Mn^{3+} \rightarrow Mn^{2+} + Mn^{4+}$) in the presence of acidic impurities in the electrolyte. $LiMn_2O_4$ is spinel phase with a cubic structure which

has a space group $Fd\bar{3}m$ (Figure 2-2(a)) and consists of the LiO_4 tetrahedron and MnO_6 octahedron sublattices. Typically, Li occupies 8a, Mn occupies16d and O occupies the 32e sites of the space group respectively. In a structure with formula $Li_xMn_2O_4$, Li^+ fills the octahedral sites in the composition range $0 \leq x \leq 1$ and the tetrahedral sites in the range $1 \leq x \leq 2$. The $[Mn_2]O_4$ framework that make up the host structure contains a network of channels created *via* the face-shared tetrahedral lithium (8a) sites and empty octahedral 16c sites which allows Li^+ transportation in 3D. Occasionally, the empty octahedral 16c sites and interstitial sites are available to Li ion during excessive lithiation to form $Li_{1+x}Mn_2O_4$, where $0 \leq x \leq 0.1$ is cubic, $0.1 \leq x \leq 0.8$ is a region having mixed cubic-tetragonal phase, and a fully tetragonal phase at $0.8 \leq x \leq 1.25$. [93] An example of such tetragonal phase is $Li_2Mn_2O_4$ shown in Figure 2-2(b), and it comes with an associated unit cell volume expansion of up to 6.5%. This first-order phase transition is made possible by the cooperative Jahn-Teller distortion which may lead to permanent loss in capacity as a result of the strain induced on the structures[93-95]. The degree of distortion is monitored by the ratio of the lattice parameters (tetragonal, c/a >1 and cubic c/a =1). Many have proposed an ordered lithium insertion as the plausible explanation for the two-plateau profile of the charge-discharge curve of $Li_xMn_2O_4$. It is reported that that Li^+ ions are positioned at available 8a sites and are ordered in $Li_{0.5}Mn_2O_4$. The voltage profile consists of two plateaus: upper and lower plateaus, the upper plateau region of discharge represents a two-phase region, an equilibrium between λ-MnO_2 and $Li_{0.5}Mn_2O_4$, and in the second plateau, $Li_{0.5}Mn_2O_4$ and $LiMn_2O_4$ co-exists in equilibrium[12], where λ-MnO_2/$Li_{0.5}Mn_2O_4$ transitions occur at voltage of 4.1 V (vs. Li/Li^+) and $Li_{0.5}Mn_2O_4$ /$LiMn_2O_4$ transition at 3.9 V (vs. Li/Li^+)[96]

Materials with formula $LiMO_2$ (M = transition metals) are called layered oxides and are one of the first materials tested as cathodes. $LiCoO_2$, aside its low specific energy and low voltage, is also toxic, thermally unstable and expensive. Materials designer have tried to replace $LiCoO_2$ with $LiNiO_2$, while $LiNiO_2$ is even more unstable thermally, it is

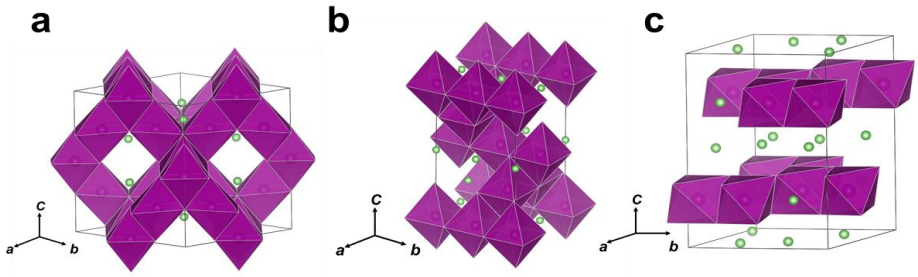

Figure 2-2| (a) Crystal structure of lithium manganese oxide phases where MnO_6 octahedra is represented by the pink octahedron shape and the Li^+ is the green ball for a (a) cubic spinel structure of $LiMn_2O_4$ (space group: $Fd\bar{3}m$) (b) tetragonal spinel structure $Li_2Mn_2O_4$ with space group $I4_1/amd$ and (c) monoclinic structure of Li_2MnO_3 phase with space group C2/m.

inexpensive and has a higher energy density relative to $LiCoO_2$ with a theoretical specific capacity of 275 mAh g^{-1}. Another major disadvantage with $LiNiO_2$ structure is the occupation of Ni^{3+} ion in the Li site obstructing the pathway for Li^+ diffusion. Since Mn is the least expensive, and most stable of Co, Ni and Mn, $LiMnO_2$ seem an interesting alternative. However, the structural changes that occur during cycling when Mn^{3+} forms $Mn_{(aq)}^{2+}$ and Mn^{4+} in a reaction called disproportionation, results in its poor cycling.

$Mn_{(aq)}^{2+}$ dissolves in the electrolyte and this affects the stability of the solid-electrolyte interphase (SEI) layer. Solid-solution such as $LiNi_{0.5}Mn_{0.5}O_2$ while having similar energy density as $LiCoO_2$ and synthesized with a fraction of the cost, the migration of Ni^{3+} to the Li-site has remained a prohibitive issue. Synthesizing a solid-solution involving all three (Ni, Mn, Co, or NMC), $LiNi_xMn_yMn_{1-x-y}O_2$, has proven an excellent way of circumventing most of the problems arising from the standalone lithium-transition-metal layered oxide cathodes. For example, NMC with formula $LiNi_{1/3}Mn_{1/3}Mn_{1/3}O_2$ has higher specific capacity than $LiCoO_2$ while utilizing 67 % less the amount of cobalt. It is already a commercial success, but market competition will require a more cost-effective production route than the present laborious and multistep co-precipitation method used in product manufacturing. Variations of the NMCs are the lithium-rich NMCs, nickel-rich NMCs and manganese-rich NMCs, each with its distinctive features. For example, $xLi_2MnO_3.(1-x)LiNi_{1/3}Mn_{1/3}Mn_{1/3}O_2$ is sometimes called Li_2MnO_3 stabilized $LiNi_{1/3}Mn_{1/3}Mn_{1/3}O_2$, is a formulation that goes under the Li-rich NMC category. There is an ongoing debate whether Li_2MnO_3 and $LiNi_{1/3}Mn_{1/3}Mn_{1/3}O_2$ are solid-solutions or composites[97]. Li_2MnO_3 is monoclinic (Figure 2-2(c)) and has lithium ions occupying part of the transition metal-site to form $LiMn_6$ units, therefore the Li_2MnO_3 phase can be also written as $Li[Li_{1/3}Mn_{2/3}]O_2$, where one-third of the Mn sites are occupied by Li^+. The cathode material, $xLi_2MnO_3.(1-x)LiNi_{1/3}Mn_{1/3}Mn_{1/3}O_2$, can achieve above $200mAhg^{-1}$ at high operational potential due to Li_2MnO_3 being activated above 4.5 V vs Li^+/Li. Nickel-rich lithium metal $Li[Ni_{1-x}M_x]O_2$ (M = transition metal, $x \leq 0.4$) is the most favorable cathode material in rechargeable lithium ion battery because of their low-cost and high capacity delivering up to 200 mAh/g. Contrarily, its inferior thermal stability has limited their commercial usefulness. The

delithiated form of the host material $Li_{1-\delta}[Ni_{1-x}M_x]O_2$ is highly reactive, participating in side reactions such as oxygen evolution reaction where oxygen is released, the gas-phase oxygen combines with electrolyte leading to runaway reactions. Other side reactions include the formation of rock-salt $Li_xNi_{1-x}O$, which have been known to lead to poor cyclability. Several groups have made concerted efforts to ameliorate this safety concern by coating the surface of host structure with Al_2O_3, $AlPO_4$, AlF_3.[98] In most cases, the thickness of the coating material is less than 10 nm, and thus offers less than adequate protective shell around the host structure. In similar vein, core-shell architectures such as $Li[(Ni_{0.8}Co_{0.1}Mn_{0.1})_{0.8}(Ni_{0.5}Mn_{0.5})_{0.2}]\ O_2$ and $Li[(Ni_{0.8}Co_{0.2})_{0.8}(Ni_{0.5}Mn_{0.5})_{0.2}]O_2$, have been developed with the core having great capacity while the shell $Li[Ni_{0.5}Mn_{0.5}]O_2$ offered thermal stability[99]. However, the sharp contrast in composition at the interface could be a barrier to Li^+ diffusion. Concentration-gradient core-shell architectures[100] prepared by co-precipitation have been developed to overcome Li^+ diffusion issues, however; making generic concentration-gradient core shell oxide materials could be a daunting challenge.

2.3.5 Methane reforming catalysts

Dry reforming of methane (DRM) has garnered much awareness because of the increasing concern to utilize two of the most noxious greenhouse gases in making chemical building blocks of hydrogen and carbon monoxide, according to the reaction:

$$CO_2 + CH_4 \rightarrow 2H_2 + 2CO \ (\Delta H_{298K} = +247 \text{ kJ mol}^{-1})$$

Syngas, a mixture of hydrogen and carbon monoxide can be employed to make synthetic fuel *via* the Fischer-Tropsch synthesis or Mobil's methanol-to-gasoline process. It is also a useful intermediate in variety of hydrocarbon compounds synthesis. A major issue with dry reforming of methane is catalyst deactivation which has been attributed to either

sintering of the active metal or coke formation on active sites of the catalyst. Dry reforming reactions usually takes place at elevated temperatures (900-1000˚C), at this temperature, sintering of particles may be favored. The other aspect of catalyst deactivation (coke formation) occurs due to the disproportionation of carbon monoxide to give coke, according to the reversible Boudouard reaction:

$$2CO_{(g)} \leftrightarrow C_{(s)} + CO_{2(g)}$$

or sometimes due to the thermal decomposition of methane:

$$CH_4 \rightarrow C_{(s)} + 2H_{2(g)}$$

The grand challenge in DRM is designing a catalyst that is thermally stable and resistant to coke using less complicated methods. While nickel supported catalysts are favorable because of their efficient activity, low-cost and availability, unfortunately, they are susceptible to coke and hence prone to surface active sites deactivation; whereas, noble metal-based catalyst though expensive are resistant to coke. Complex oxides are generally not active towards DRM, but the structural engineering by way of substituting some of its lattice with an active noble metal and/or aliovalent cation in order to induce crystal point defects such as oxygen vacancies in its structure have been recorded to be the reason behind improved activity towards DRM[58, 101-102]. Oxygen vacancies promotes lattice mobility which can help reduce coking issues[102]. Another advantage of complex oxide is its thermal stability at the DRM reaction temperature (900 – 1000 °C) ensuring catalyst sintering is minimized. Complex oxides that have been used as catalysts in DRM includes perovskites, pyrochlores, fluorites and zeolites[58-60, 101], and some of their performance result can be found in Table 2.1

2.3.6 Photocatalysis and solar energy conversion

Complex oxides are also key materials in photoconversion processes whether in thermochemical splitting of water and carbon dioxide with concentrated solar energy into liquid fuels[103] or the photocatalytic reduction of carbon dioxide into fuel intermediates like syngas[48] or formic acid[47] or photoelectrochemically splitting water into hydrogen[56] or in photovoltaic applications[57]. Some performance data of these oxides can be found in Table 2.1

2.4 Structure and Property Relationship of Complex Metal Oxides

The key to understanding the properties of complex oxides which makes them interesting materials in many energy applications is the knowledge of their crystal chemistry. So, this section shall cover the crystal structures of common mixed oxide phase discussing their innate properties and modification carried out by materials engineer to enhance their properties.

2.4.1 Perovskite

2.4.1.1 Normal perovskite [ABO_3]

Structures of the type ABO_3 called *perovskite*, crystallizes in atmospheric conditions as different structures or may not crystallize at all if certain conditions are not met. Dense structures such as cubic-perovskites are usually precipitated at higher than atmospheric pressures but are stable at atmospheric conditions. Perovskites, with formula ABO_3, are class of complex oxides with relatively larger A-cation ionic radius compared

with B-cation. The most common polymorphs available in these structures are cubic and hexagonal. Stacking configuration of closed-pack AO_3 layer defines the structure-type, where B-cation sits in a space between the layers in the O-ion octahedra. The phase obtained whether cubic or hexagonal is characterized by the type of stacking. BO_6 octahedra share only corners if the stacking is cubic, however, if hexagonal, BO_6 octahedra form unique *c*-axis sequence of face-shared octahedra. Since the size of the A-site tetrahedra is finite, there is a limitation on the size of the A-cation acceptable within the sub-lattice without causing a deformation on the structure. If the A-cation size is out of these acceptable range, the energetics of the entire system will be such that other structures may become more feasible to crystallize. A tolerance limit, *t*, proposed by Goldsmidt[104] defines the limit on the ionic radius of A (r_A) relative to B (r_B) and O (r_O):

$$t = (r_A + r_B)/2^{1/2}(r_B + r_O) \qquad 2.1$$

The idealized scenario is to have a cubic structure with $t = 1$. Under atmospheric conditions, perovskites must have of tolerance in the range $0.75 < t < 1.0$, and since A and B are have twelve-fold and six-fold coordination respectively, more criteria need to be defined. This coordination chemistries put a lower limit of the ionic radii as: $r_A > 0.90$ Å and $r_B > 0.51$Å[105]. For cases where r_A is less than 0.90 Å at atmospheric pressures, other structures like corundum, pyroxene, garnet and ilmenite, may become possible. In many of the applications deploying perovskite-type compounds as catalysts, two things are clear: (1) the distortion of the structures may in some cases, lead to catalyst active sites[106] (2) The A-site, constituted by rare-earth and alkaline-earth metals, is directly passive to catalyst activation[107], but may indirectly instigate activation by the aliovalent substitution of cations to induce oxygen vacancies. The B-site on the other hand, comprising of transition metals,

is the epicenter of catalyst activation sites, this is especially true when the *d*-orbitals of the B-cations overlap with *p*-orbitals of the oxygen anion. This overlap or as is more appropriately termed as hybridization creates a pathway for the mobility of charged carriers and is thus responsible for electronic conductivity. Further properties of the perovskite-type structure can be found in several monographs[105, 108]

2.4.1.2 Double perovskites [$A_2BB'O_6$]

Similar to the perovskite structure but with a mixed transition element in the B-site. There are reports that the B and B´ atoms ordering with the cubic structure are such that nearest neighbors are unidentical atoms, i.e., fully disordered.

2.4.2 Garnet [$A_3B_2(XO_4)_3$]

Garnet structure is the generic form of all complex metal oxides derivable from the ideal garnet structure with the general formula $A_3B_2(XO_4)_3$, a typical example of such is $Sr_3Al_2(TiO_4)_3$ (cubic unit cell and space group $Ia\bar{3}d$, space group number 230). A-sites are 8-fold coordinated (antiprismatic sites), B-sites are 6- fold coordinated (octahedral sites), and X-sites are 4-fold coordinated (tetrahedral sites). Complex oxides such as $Nd_3Te_2(LiO_4)_3$ which is a lithium-constituted garnet structure, where lithium occupies the X-site or tetrahedral sites, have wide use as a solid-electrolyte in all-solid-state lithium ion battery, however, such use is severely limited by low lithium-ion conductivity. A way around this is to have lithium-ion occupying the A- or B-site, as well as the tetrahedral sites in order to have oxides with high concentration of Li-ions to increase Li conductivity[54].

2.4.3 Layered Oxides

2.3.3.1 Ruddlesden-Popper phase [$(AO)_nABO_3$]

If the A/B and A/O ratio changes in a perovskite, a Ruddlesden-Popper structure may result. Excess A-cation in such a structure can lead to, for example, a structure like $Ca_3Ti_2O_7$ (n = 2) comprising of layers of CaO rocksalt sandwiched between n layers of $CaTiO_3$ perovskite. If the rocksalt in the space within the interlayer is made from metal with low Z number, such as lithium, these layered compounds are very important material for several energy storage technologies, and given the large gap between the interlayers, it is reasonable to speculate that the interlayer spaces could be a pathway for ionic transportation. So, we can expect to have a high ionic conductivity due to Li mobility and high diffusion rate from the lattice[71, 109]. This is the main idea behind solid-state lithium-ion conductors popularized in recent years[71, 109-110],and it has been the focus of intensive research on the development of solid electrolytes for lithium ion batteries[110]. Besides energy storage applications, Ruddlesden-Popper phases have found wide applications in CO_2 capture[111], photocatalysis[112] and ion-exchange.[113]

2.4.3.2 Delafossite [ABO_2]

The delafossite group are a class of complex oxides that crystallizes as ABO_2. *A* could be alkaline earth or alkali metals, while *B* are mostly transition metals or group III metals. This group is also a layered oxide and is formed when linearly coordinated A-cation is stacked with the layers of edge-sharing BO_6 octahedra. There are some notable polytypes within this group: hexagonal 2H (space group of $P6_3/mmc$) types occur when two A-layers are stacked with each later rotated half-a-revolution in with respect to each other, however, if the stacking were done in identical direction to each layer we will have a rhombohedral

3R type (space group $R\bar{3}m$)[114]. There are several applications of these complex oxides ranging from transparent conductive oxides[115], to cathode materials for lithium-ion batteries[116] to photocatalysis[117], to photovoltaics[57], to photoelectrochemistry[56].

2.4.4 Spinel [AB_2O_4]

Majority of the spinels have a cubic structure assigned to the $Fd\bar{3}m$ space group where he tetrahedral cation (A) and the octahedral cations (B) occupies a fixed position at points 8a and 16d respectively. This structure usually crystallizes as closed-pack alternating between one tetrahedron and an octahedron in which the lattice is occupied by the tetrahedral and octahedral sites in a 2:1 ratio[118]. There are two distributions between the A- and B-cation: normal and inverse distribution. In the normal distribution, written as $A[B_2]O_4$, where the entity in parenthesis indicate octahedral sites , the A-site is completely located in the tetrahedral position whereas, the B-site is positioned at the octahedral sites. On the other hand, for inverse distribution written as $B[AB]O_4$, the A-cation is completely positioned in the octahedral site, leaving one-half of the B-cation in octahedral site, and the other one-half in the tetrahedral site. Intermediate distribution could also be actualized and is represented as $A_{1-x}B_x[A_xB_{2-x}]O_4$, where x is termed as the degree of inversion.

Several reports have indicated that the inversion phenomenon could be a strategy for activation of spinel oxides in catalysis[119-121]. Specifically, as reported by Wu *et al*[121], an inverse spinel $Co[CoFe]O_4$ produces even a better oxygen reduction reaction activity than the well-known Pt/C catalyst by 42mV. This reason adduced for this unusually good activity performance from a spinel is the *dissimilarity effect* of unidentical Co and Fe occupying the octahedral site conferring interesting qualities to the adsorption energy of oxygen and expanding O-O bond length in relation to the normal spinel. Although Li- and

Mn occupy two different sublattices connected in three-dimensions, the migration of Li+ from vacant tetrahedral sites to the interstitial sites of the octahedra in $LiMn_2O_4$ has been attributed to the high rate capable of the spinel as cathode material in lithium ion batteries[51].

2.4.5 Pyrochlore [$A_2B_2O_6O'$]

The structural formula of pyrochlore oxide is written as $A_2B_2O_6O'$ or more generally as $A_2B_2O_7$. The space group is $Fd\bar{3}m$, with the atoms occupying following Wyckoff positions A: 16*c*, B: 16*d*, O: 48*f* and O´: 8*a*. Pyrochlores can be viewed in many ways, but the distorted fluorite is the most common one. Rather than write the structure as $(A, B)_4X_8$, it is written as $A_2B_2O_7$, with the eight anion missing, modifying the structure considerably. [122]

2.5 Thermodynamic Concepts

2.5.1 Thermodynamics of metastable phases

In the rational design of materials, fundamentals of crystal chemistry, thermodynamics as well as the structure-function relationships, catalytic, optical and electronic properties should be well understood from the conceptual stage of design[17, 123]. They are two steps to achieving this: (1) predicting the crystal phase and chemical composition that will most likely give the expected properties (2) identify the best methods to synthesize such materials [33]. The best performing materials such as low-temperature polymorphs, pillared or layered oxides, alloys, doped materials, solid-solutions and intercalation compounds are all thermodynamically metastable phases[33], and examples of these superior performance can be found in photovoltaics[124], photocatalysis[125] and ionic conductivity[126]. The metastable composition space is usually overlooked during conceptual design of new materials, and if this trend continues, materials engineer face the danger of

overlooking potentially beneficial materials in the search for next-generation energy materials [127]. The traditional synthesis routes require solid-solid reaction at temperatures close to 1000 °C, the problem with this is that at such high temperatures, stable phases are most likely to be formed. From the synthesis standpoint, mild conditions of temperature and pressure are required to make metastable compounds, as a result, a new field of materials synthesis termed soft chemistry or *chimie douce* was birthed between 1950s and 1960s to take up this challenge[17, 33]. Wilhelm Ostwald[128-130] formulated the step rule which states that a phase that is nucleated from a solution or melt need not be the most stable thermodynamically. When there are many thermodynamically allowable phases when crystallizing a solid from a solution, sometimes the phase farthest away from equilibrium may be the most favored kinetically rather than the most stable phase. The process parameters material engineers are looking to optimize to favor metastable crystals are processing time and/or processing conditions such as temperature or pressure. In essence, short times and low-temperature and low-pressure non-equilibrium process conditions may favor metastability if Ostwald's step rule applies. This, along with non-equilibrium thermodynamics is the central philosophy behind the *chimie douce* movement. Perhaps, it is best to clarify the types of metastabilities and describe the focus of this dissertation at this juncture. In general, metastable phases possess a higher free-energy than the corresponding stable phases, but higher free-energy can be achieved in more ways than one, hence, the differences in the type of metastability. Compositionally-metastable compounds derive their metastability from the frozen-in disorder enhancing entropy and free-energy. Doped materials, solid-solutions, alloys, high entropy alloys and metallic glasses are good examples of this [131]. Topologically-metastable compounds on the other

hand derive metastability from a *pot pourri* of structures arising from the flexibility of bonds and bond-angles or high free-energy arising from particle size or shape. Examples are zeolites, porous compounds and nanomaterials. The scope of this dissertation is the compositionally-metastable complex oxides.

2.5.2 Entropy and enthalpy of solid-solutions *vs*. stable phases

The best way to predict the formation of phases is the minimization of Gibbs free energy equation. The integral molar Gibbs energy for phase ϕ is:

$$G_m^{\Phi} = \sum_i x_i\left(G_i^{\Phi}\right) + G_{m(mix)}^{ideal} + G_{m\,(excess)}^{\Phi} \quad 2.2$$

The index *i* represents the elemental constituents, $G_{m(mix)}^{ideal}$ is the ideal molar Gibbs energy of mixing, and $G_{m\,(excess)}^{\Phi}$ is the excess molar Gibbs energy. $G_{m(mix)}^{ideal}$contains molar enthalpy of mixing ($H_{m(mix)}^{ideal}$)and molar configurational entropy of mixing($S_{m(mix)}^{ideal}$), we take $H_{m(mix)}^{ideal} = 0$ and $S_{m(mix)}^{ideal} = -R\sum_i x_i ln(x_i)$, R is the gas constant. Also, $S_m^{\Phi} = S_{m(mix)}^{\Phi} + S_{m(excess)}^{\Phi}$ and $G_{m\,(excess)}^{\Phi} = H_{m\,(excess)}^{\Phi} - T(S_{m\,(excess)}^{\Phi})$, combining all these equations lead to:

$$G_m^{\Phi} = H_m^{\Phi} - T(S_m^{\Phi}) \quad 2.3$$

Phase (ϕ) here signifies liquid, gas or solid, but the phase of interest is the solid-solutions (SS) or stable phases (SP). So, Equation 2.3 is modified to represent Gibb's free energy of SS as:

$$G^{SS} = H^{SS} - T(S^{SS}) \quad 2.4$$

As before, in ideal case, $H^{SS} = 0$ and $S_{ideal}^{SS} = -R\sum_i x_i ln(x_i)$ and in non-ideal sub-regular and regular solution, $H^{SS} \neq 0$. Atomic ordering in ideal case is a perfect randomization scenario and so phase separation is possible when either of $H^{SS} > 0$ or $H^{SS} < 0$ occur. Models have been limited to configurational entropy of ideal solutions only, other entropy contributors such as vibrational, magnetic and electronic influences are ignored.

Stable phases have ordered arrangements of the different atom types on the sub-lattices. The lattice type is different from that of the matrix material(s) of SS - which is more randomized, whereas the stable phases are characterized by long-range order. As before, the Gibb's free-energy of the stable phase is:

$$G^{SP} = H^{SP} - T(S^{SP}) \quad 2.5$$

where H^{SP} and S^{SP} are molar formation enthalpy and entropy of stable phases respectively. Usually, S^{SP} is insignificant enough to be ignored but in cases of complex oxides where more than one atom occupies or share a sub-lattice, S^{SP} can no longer be ignored. The ideal configurational entropy, estimated from sub-lattice model is[132]:

$$S_{ideal}^{SP} = \frac{-R\left\{\sum_{y=1}^{y} a^y \sum_{i=1}^{M} q_i^y ln(q_i^y)\right\}}{\sum_{y=1}^{y} a^y} \quad 2.6$$

where the total number of element species, *i*, is M; a^y is the number of sites on the *y* sub-lattice and q_i^y is the fraction of element species *i* randomly distributed on the *y* sub-lattice. The enthalpies of SS and SP are different due to the dissimilarities in atomic ordering patterns, and central to understanding the determination of H^{SP} is the bond enthalpies

between i and j first-neighbor atoms, ζ_{ij}; and the type of first-neighbor atoms, n_{ij}. The enthalpy of a solid is computed by adding up the products of all the terms as:

$$H = \sum_{ij}\left(n_{ij}\zeta_{ij}\right) \qquad 2.7$$

In this equation, while SP and SS with the same composition may have the same value of ζ_{ij}, the n_{ij} values would be unidentical due to ordering differences. All of these concepts are based on same-size atoms, for different-sized atoms, uncertainties regarding the position or location of the atoms might introduce additional term called excess configurational entropy. Further discussions about the subject can be found in the review article of Ref.[133].

2.6 Challenges and Opportunities in Complex Metal Oxide Synthesis.

The greatest challenge in materials manufacturing is fabricating a homogeneous composition in multicomponent-based materials. This issue is even more important when one considers the fact that only in a homogenous multicomponent material can electronic structure be altered, which can confer interesting properties in many materials employed as a catalyst[134-135], photocatalysts[136], ferromagnets[137], thermoelectric[138] and energy storage materials[139]. Other desirable but elusive attributes material designers are looking to have a firm grip on is the control of grain and/or particle size[32] morphology and microstructures[140]. Besides this challenge, the dream of every materials scientist is to have their lab-synthesized materials put to industry-wide use, but the multiple steps and long processing hours associated with most lab-scale techniques could be a hindrance towards scalability.

In the following sub-sections, an expanded discussion of the challenges and opportunities in complex oxide synthesis shall be itemized.

2.6.1 Scalability

Scalability in general, describes a production unit or system whose capacity can change on demand without necessarily compromising reliability, performance, functionality, and cost efficiency. Specifically, in commercial-scale production, the bottom-line objective would be increased production at minimal cost and at rapid production rates. There are many articles with the word *scalable* in their title and keywords but only a handful of those can indeed satisfy the requirements for scalability. Perhaps it is important to start off by defining the standard dichotomous processes currently employed in product manufacturing: Batch (or discrete) and continuous processing, within the context of scalability in high-volume manufacturing. Batch process is a stage-wise technique used in manufacturing which requires prolonged treatments, and therefore slow and not cost efficient due to high energy consumption. Batch processes are also low-yield methods as they involve multiple steps and laborious processes, each bearing a risk of introducing impurities into the final product, creating batch-wise inconsistencies in the process. Most noteworthy is the fact that the scale-up of these techniques can be difficult due to the long reaction times and multiple steps required. However, low initial cost outlay and low production risk (defective batch can easily be identified and disposed of) are some of the advantages of batch process. The batch processes currently in place for complex oxide preparation are solvothermal [141], sol-gel[142], polyol[143-144], solid-state reaction[145]. In stark contrast, however, starting materials pass through unit operation/unit process in a repeated and uninterrupted manner in continuous processing. This is possible because

usually only one process step is involved, and that single step should be both rapid and facile for continuous processing to be achievable. The initial outlay cost may be huge, but it offers some advantages: not only is it the best approach for large-scale manufacturing, it is also a tractable method that can also handle small volume production without sacrificing product quality, also, it is more cost-effective in the long term, with a high degree of reliability in functionality and performance of products. At the moment, the commercialized complex oxides are produced via batch processes driving up cost and jeopardizing the commercial attractiveness of the technologies they were utilized in. So, there is a lot of interest in devising an alternative production route that will facilitate the continuous processing of complex oxides and alloys.

2.6.2 Composition controllability

The conventional synthesis routes of soft-chemistry and solid-state reaction have recorded a lot of success, but there are certain applications that requires compositional homogeneity of final complex oxide which is a difficult task with these well-known techniques. Liquid-phase nucleation routes such as sol-gel, coprecipitation and Pechini have been developed for multinary metal oxide synthesis with either particulate gels, alkoxide and citrate gels or hydroxides. The methods are based on hydrolyzing metal precursors into metal alkoxide and other salts and thermolyzing these into multicomponent metal oxides. It is generally claimed that the cations are well mixed at the molecular level in a three-dimensionally coordinated network of space, in a way that shortens the diffusion distance during thermolysis and hence ensures a homogenous cationic distribution[146]. In reality, gels do not always precipitate into the intended crystal phase[147-148]. The homogeneity of the solution phase does not necessarily translate to a homogenous solid

phase, because, according to Delattre *et al*[149], the metal-organic structures may have transformed into separate phases before been frozen-in into a solid network. The controllability of the phase, stoichiometry, composition and microstructure of the resulting product in the coprecipitation method is somewhat satisfactory, but the differences in precipitation rates among intermediate precipitates could lead to uneven distribution of ions/atoms in some cases[150]. Solid-state chemistry sometimes require temperatures in the excess of 1000 °C , and such harsh condition can unfortunately create abnormal grain growth and give less than adequate homogeneity[151]. In summary, the conventional methods have some nagging issues as it relates to the control of composition, so the search for a new technique have been largely based on either modifying the existing methods or looking for alternative routes.

2.6.3 High entropy alloys (HEAs)

This is an emerging field in materials science and engineering with the pioneering works published around 15 years ago[152-154]. Conventional alloys consist of one or two prominent metals with a low amount of other metals. In HEAs, however, the alloys consist of at least five metals of equimolar proportions. Additionally, HEAs can be defined according to the value of a solid-solution configurational entropy. As we seen earlier, the configurational entropy is $S_{ideal}^{SS} = -R\sum_i x_i ln(x_i)$, and so by definition HEAs have $S_{ideal}^{SS} > 1.61R$ [133].

This is a revolutionary concept in materials design as the focus would be at the center of a multicomponent phase diagrams. Contrarily, conventional alloys focus on vertices and faces. This will open up a new vista into the previously unexplored parameter space of composition and phase. In varying applications such as construction[155], thermal

insulation/conduction[156], electric conduction[156], thermoelectricity[157], and catalysis [158-159], the unique qualities of HEAs by way of lighter and more resilient alloys enhances resistance to heat and corrosion, it also improves catalyst surface activity and energy conversion efficiencies. The arrangement of atoms in a crystal induces certain structural properties, however, since electronic properties may also be altered doing same, HEAs may possess catalytic or electrochemical properties never seen with regular alloys. In the early years of the development of HEAs, the primary focus was on metal alloys, but in recent years there has been significant growth in other materials group such as ceramics and semiconductors. These multi-metal oxide HEAs can have exceptional catalytic properties especially when deployed in oxidative reactions. As an example, carbothermal shock synthesis was adopted in the synthesis of HEA nanoparticles was found to be useful as ammonia oxidation catalysts with ~100% conversion and >99% nitrogen oxide selectivity over extended runs[159]. The challenge before materials engineer is to extend this HEA fabrication capabilities to more complicated ceramics such as nitrides, chalcogenides, phosphides and oxides.

2.6.4 Synthesis of nanostructural complex oxides

The search for a scalable and unique synthesis technique that simultaneously controls the chemical composition of the metals and one-dimensional (1D) growth remains. For example, research into 1D nanocathodes related to nickel-manganese-cobalt (NMC) and nickel-cobalt-aluminum (NCA) in lithium ion batteries, to the best of our knowledge, are unavailable in current literature, even though they are the most favorable and popular choice for cathode materials owing to their high specific capacity. Therefore, the non-triviality of the challenge in synthesizing $LiMO_2$ (M = transition metals and aluminum)

may have undermined the progress of research into 1D nanostructural cathodes. This goes without saying that a lot of opportunities are abound in this field of research and other related fields where 1D growth of complex oxides are critical to their operation.

2.7 Routes to Complex Metal Oxide Synthesis

The methods available for synthesizing complex oxides can be categorized based on whether the reactants are solid, liquid or in gas phase. Figure 2-3 shows the summary of the methods. It is worth noting that solid-state reaction has been in use since prehistoric times, whereas; liquid-phase nucleation has been around for more than 40 years since the first gas-phase nucleation method was reported. So, both the solid-state and liquid-phase nucleation routes are regarded as the conventional methods in this study.

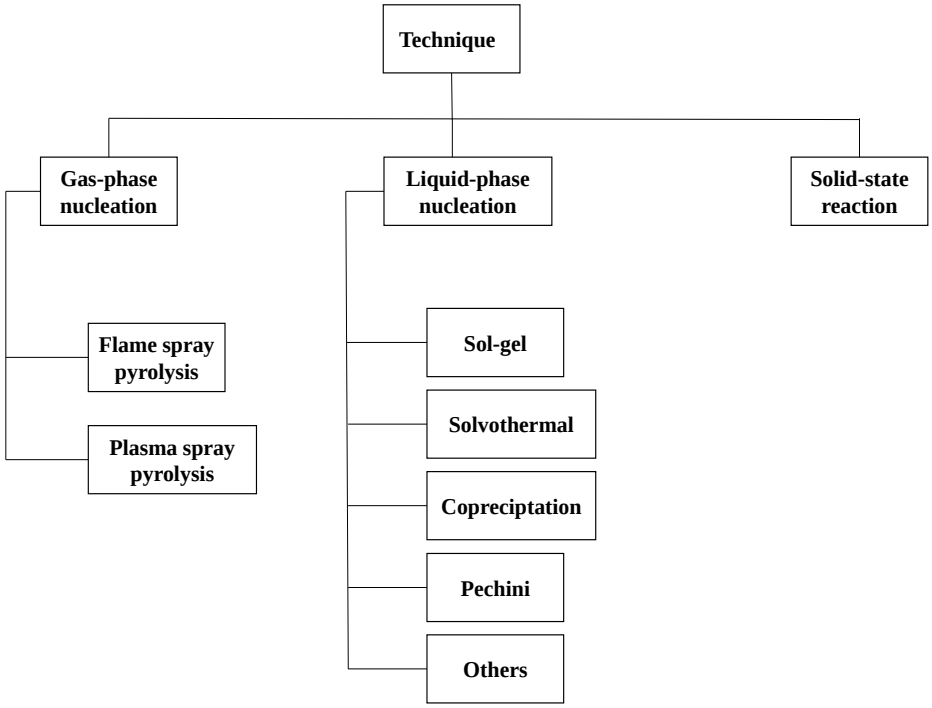

Figure 2-3| Summary of the techniques available for synthesis complex oxides.

2.7.1 Solid-state reaction

In general, solid-state reaction involves synthesis technique with at least one

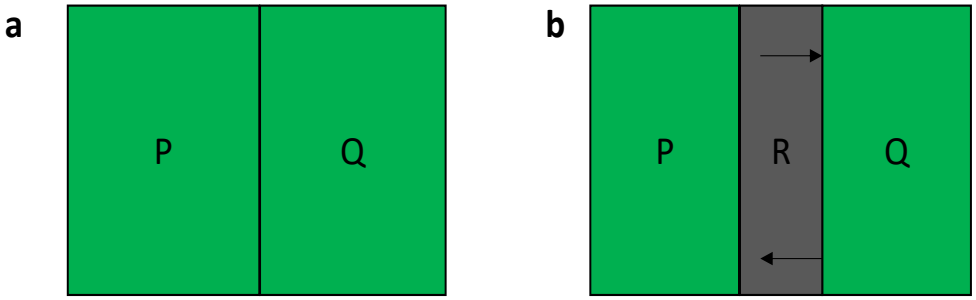

Figure 2-4| Solid/solid reaction showing reaction progression at (a) time, *t = 0* (b) *t = t*

reactant in the solid-phase. So; solid/solid, solid/liquid and solid/gas are grouped under this category. Solid/gas system does not necessarily mean a gaseous reactant but could also involve a gaseous product, in fact, a gaseous product are the most common types in this system. Also, in many situations, "solid/solid" systems do in fact mean solid/liquid as the high temperature required to initiate the reaction will turn at least of the reactants into a melt phase. Figure 2.4 displays the progression of two solids P and Q. Two solids hardly react at room temperature due to low entropy (or high Gibb's free energy), but when a suitable temperature is attained, there is diffusion of ions P and Q in the opposite directions into a product phase R, which is formed following its nucleation. The most common reaction temperature is two-thirds of the melting temperature of one of the reactants. The product layer becomes thicker as time, t increases. At long times, diffusion length becomes

longer and product phase acts as a barrier slowing the reaction rate. The rate law is parabolic operating between 1200 – 1500 °C, when the reaction rate is diffusion limiting, and is represented by the rate equation[160]:

$$x^2 = c.t \qquad 2.8$$

where c is the rate constant, x is the thickness of the product layer. Owing to this slow reaction rates, additional ions being introduced into the system may not enjoy unfettered migration, which may hinder the facile distribution of cations in the product layer. This slow processing time often lead to stable phases as against the metastable ones due to ions having enough time to attain equilibrium conditions.

2.7.2 Liquid-phase nucleation

It is also called the wet-chemical methods. Liquid phase nucleation method is different from solid-state reaction in the sense that diffusional limitations is eliminated owing to reactants being dispersed in a solvent. Also, it is a self-assembly method where a molecular reactant is stacked on one at a time leaving the general bonding structures of most atoms intact[17]. In this method, materials precipitate out of solution as either hydroxides, oxalates, sulfates and so on. The advantage with this method is that particle size and microstructure can be controlled but these powders needed to be filtered out from a solvent or more appropriately, supernatant and calcined afterwards to remove the organics and water vapor in order to generate the desired oxide phase. Calcination step can promote aggregation destroying the microstructure, also; the high temperature and long calcination time can lead to stable phases. This process route depends on nucleation and growth of sample from a solution that is under supersaturated condition. Nucleation can occur either heterogeneously or homogenously depending on whether a solid substrate is

involved in this process. In heterogeneous nucleation, a solid interphase provides *seed* to initiate nucleation, whereas, homogenous nucleation takes place without an intervening phase. The various methods of liquid-phase nucleation techniques are discussed below.

2.7.2.1 Sol-gel method

It is a unique method for the synthesis of metal oxide and mixed metal oxide nanoparticles. The method is advantageous because of its firm control on resulting microstructures of oxide particles. The outline of steps in this process is presented in Figure

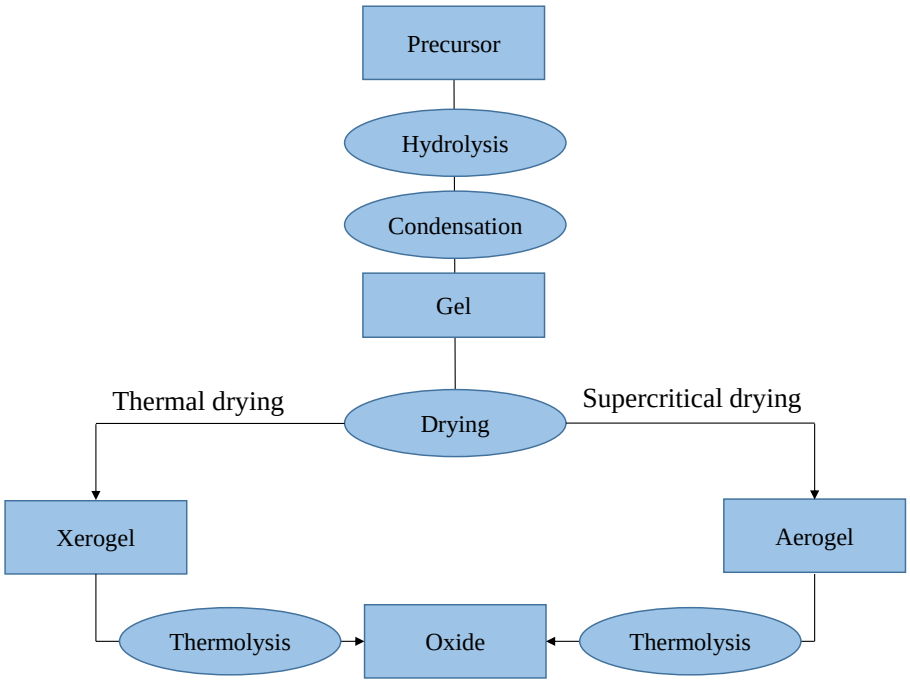

Figure 2-5| Flow diagram showing the various steps of sol-gel technique. Rectangular shapes represent *materials* and oval represents *steps*

2-5. The steps are (1) hydrolysis (2) condensation (4) drying (5) thermolysis [161].

The precursor is hydrolyzed into metal hydroxide called *sol*, which is quickly followed by condensation to three-dimensional *gel*. The drying route used determines the next material formed, supercritical drying forms aerogel and regular thermal drying leads to xerogel. The final step is the calcination (or thermolysis) at moderately elevated temperature to get rid of the organic and/or water molecule and crystallize the desired oxide phase.

2.7.2.2 Pechini method

The method is named after its inventor [21] who consolidated the sol-gel process, giving it more control of microstructure and composition. The most significant advantages of the Pechini method is the capability to form a precursor of polymer network where two or more metals embedded homogeneously throughout the network [162]. As seen in Figure

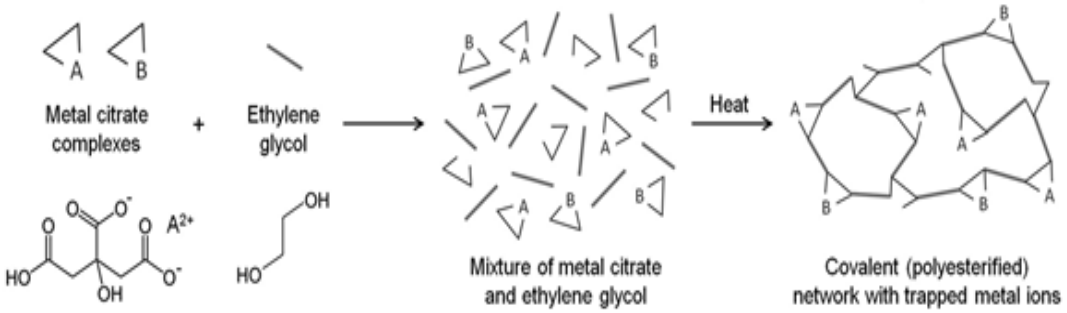

Figure 2-6| Pechini process involving two metal cations A and B, adapted from Ref. 162

2-6, metal citrate complexes formed from a solution two-component metal precursors (containing cations A and B) and citric acid is combined with ethylene glycol, the mixture is mildly heated and stirred a polymeric network of material. This is a transesterification reaction between metal citrate complex and ethylene glycol to form a covalent polymer matrix containing metal cations distributed evenly. This rigid (covalent) framework

ensures the cationic distribution remains the same during and after calcination to the desired ceramic material.

2.7.2.3 Coprecipitation method

The technique ranks as one of the oldest routes to making multicomponent metal oxide. This method involves the preparation of aqueous solution constituted by the desired multicomponent cations and mixing with another solution which contains the precipitating agent. The precipitate is separated from the supernatant by filtration, dried and calcined to crystalize the intended complex metal oxide phase. Conditions such as rate of mixing precursors and precipitating agent, temperature, pH, and concentration have to be optimized to produce acceptable final oxide products[150]. The controllability of the phase, stoichiometry, composition and microstructure of the resulting product are somewhat satisfactory, but the dissimilar precipitation rates among intermediate compounds could lead to compositional inhomogeneity in some cases[150]. The process is time-consuming, and also, aggregate formation and phase separation could result during calcination at elevated temperatures.

2.7.2.4 Solvothermal technique

This is the enclosure of a mixture of solvent (hence *solvo*), reactants and other agents (mineralizers, templating agents, etc.) in a sealed reactor called *autoclave.* The sealed reactor is heated to temperatures just above the boiling point of the solvent for a long time in a process termed *ageing*. Specifically, in an aqueous solvent, the reactor is heated above 100 °C and the process is termed *hydrothermal* synthesis. Under this condition of sealed vessel and temperature, an autogenous pressure is built up, which assists in the supersaturation of the nutrients. Also, the viscosity of water, as well as its

dielectric constant are significantly reduced under the hydrothermal conditions, the solubility of the reactants can also be impacted by this[163]. This method is good for preparing single crystals, and well-ordered polycrystalline materials. The method was first popularized for growing large single crystal quartz[164], as well as zeolites[165-166], but a lot of researchers are using this techniques to grow mixed oxides such as pervoskites[167], pryrochlores[167], garnet[168] and Ruddlesden-Popper phase[169].

2.7.2.5 Other methods

The soft chemistry routes consist of some other less known techniques such as freeze-drying[170], flux method[171], and room-temperature reduction-recrystallization (RTRR) method[46]. In the RTRR method, a reductant ($NaBH_4$) was used to reduce mixed precursors of $CoCl_2.6H_2O$ and MnO_2 into a precipitate of non-stoichiometric metastable $Co_xMn_{3-x}O_4$ spinel at room temperature. Also, key in this approach is the ability to switch between tetragonal or cubic spinel depending on the phase of the starting MnO_2. What's more, the obtained spinel phase possesses exceptional bifunctional ability when deployed as electrocatalysts for both OER and ORR (oxygen reduction reaction).

Flux methods use molten salts to synthesize complex oxides at temperatures ranging from 200 - 500 °C. It consists of reacting molten multicomponent alkali hydroxide melts, which can have eutectic temperatures as low as 175 °C. The acid-base equilibria:

$$2OH^- \leftrightarrow H_2O + O^{2-}$$

suggests the solubility of wet acidic fluxes (right-hand side of equilibria) and their recrystallization as dry basic fluxes (left-hand side of equilibria)[33].

2.7.3 Gas-phase nucleation

The liquid-phase approach leverages on mild reaction conditions such as temperature and pressure to make metastable phases, whereas in gas phase nucleation methods, these reaction conditions may be extreme, but the reaction times are rapid. In the justification of Ostwald's step rule[130], either of mild reaction condition or rapid processing time are necessary to make metastable phases. This makes a lot of sense because the molecular reactants are *frozen-in* in their metastable states without having ample time to reach equilibrium state. Another way gas-phase nucleation method differ from the liquid-phase nucleation methods is that there are no solvent wastes to contend with, as the complex oxide particles nucleates directly from aerosol (liquid precursor dispersed in gas) to particles in what is called gas-to-particle conversion. Besides, the unit operation normally used to separate oxide particles from solvent/supernatant will be eliminated for the same reason[172]. Other attractive feature of this method is the report that particle size can be controlled from droplet size of liquid in aerosol, also, the composition of the liquid droplet completely mirrors the composition of the precipitated oxide phase giving it exceptional control of composition. Absent agglomeration, particles generated have narrow particle size distribution, however, particles can sometimes agglomerate and coagulation/sintering are the two competing processes which are responsible for agglomeration [173].

The gas-phase nucleation method can be categorized according to the media used in the gas-to-particle conversion. In general, there are two main media (1) flame (2) plasma, as represented in Figure 2-3, and each process is discussed in more details below.

2.7.3.1 Flame spray pyrolysis

Flame aerosol technology is already commercialized for the synthesis of carbon black, titania, silica, zirconia and alumina nanoparticles, with that market already valued at $15b per annum[28], however, complex oxides are not. As we seen many times in this review, most of the energy applications of interest require materials with increasing level of complexities. The method consists of high energy flame with combustion temperature averaging between 1500 – 2757°C[174-177] – and powered from a mixture of fuel and oxygen, a combustible solvent, a combustible or sometimes a non-combustible liquid precursor, an atomizer or aerosol generating system, a particle collection system and a combustion chamber. The spray head or nozzle is the inlet of the combustion chamber where the liquid

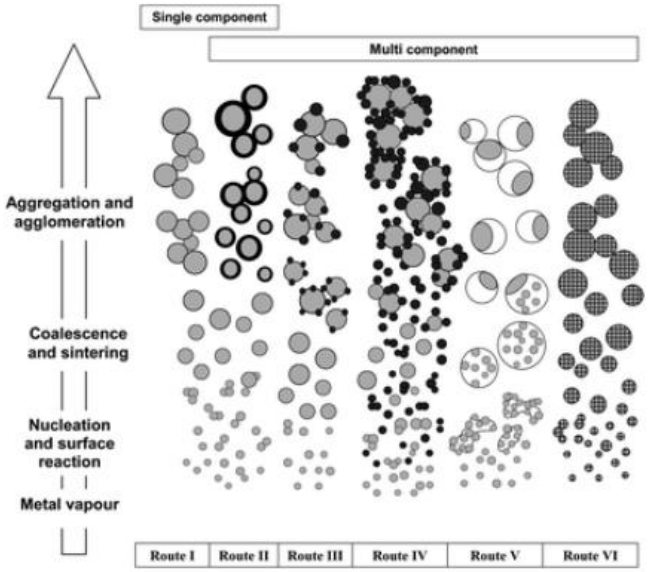

Figure 2-7| Gas-to-particle transition for single and multicomponent systems. Adapted from Ref. 178

precursor and oxygen are fed in to generate an aerosol of atomized precursor dispersed in

oxygen. The aerosol travels through the flame and undergoes some physicochemical transformations from evaporation to nucleation. After this, particles grow by condensation, coagulation coalescence and sintering. There can be variation in these steps depending on whether the precursors are single or multicomponent[178] (see Figure 2-7). Punginsang[174] *et al* suggested the reaction steps in the formation of binary oxide Bi_2WO_6 proceed *via* the reaction of monometallic oxides Bi_2O_3 and WO_3 even though the starting materials are nitrate and hexaethanolate respectively. The maximum temperature of the flame (~2757 °C) is about 1000 °C higher than the boiling points of Bi_2O_3 and WO_3, giving it sufficient energy to gasify the monometallic oxide intermediates. Because the boiling points of Bi_2O_3 and WO_3 are somewhat different, their evaporation and condensation rates are expected to be different. This could unfortunately lead to poor control of the composition final mixed oxide phase.

2.7.3.2 Plasma spray pyrolysis

This method is similar to FSP in all regards, except that the flame media is substituted with plasma. Several technologies, especially in the semiconductor industry have used plasma-assisted technologies in many ways including etching[179], plasma enhanced chemical vapor deposition[180], plasma-assisted chemical vapor deposition[181], ion implantation[182], sputtering[183], and so on. Plasma chemistry and plasma-induced reactions can occur at relatively low temperatures, or under non-equilibrium conditions, and many of these plasma-induced reactions are spontaneous processes making it perfect media to fabricate metastable phases. These plasma reactions result in the high heating rate, making the reactions rapid, also materials experience accelerated cooling as they exit plasma,

making the plasma a perfect media to freeze-in atoms before they attain equilibrium position.

In general, plasmas are defined as quasineutral gas of charged and neutral particles that exhibit collective behavior[184]. A gas is defined by Brownian motion as conceptualized in the kinetic theory of gases, whereas, with plasmas, apart from the local inter-particle collisions between nearest neighbor particles, a particle far away can also affect the collisional pattern due to the influence of electric field, this phenomenon is called a collective behavior. A plasma is created when a sufficient energy is supplied to gas, enough to cause electric breakdown or allow the gas to conduct electricity in a process called ionization. In ionization, for example, a gas particle, *A*, loses an electron from its valence shell to create a positive ion ($A \rightarrow A^+ + e-$), an exact inverse process called recombination could take place simultaneously where the positive ion an electron recombines to form A ($A^+ + e- \rightarrow A$). Recombination could also result from combination of neutrals, a positive and negative ion, leaving behind a large heat (exothermic reaction). A plasma is usually initiated and sustained by supplying electromagnetic energy to a gas, and these energies come in several forms including direct current, radio frequency, and microwave energy[185]. These electromagnetic energy forms are called plasma source. The choice of plasma source depends on the expected plasma density (electron/ion density) and/or plasma temperature. The plasma temperature can be looked at in a way that the plasma has two sub-systems: electrons and heavy particles or gas (heavy particle comprises of gas and charged particles, where gas temperature is approximately equal to the ion temperature), with each system having its own distinct temperature: T_e for electron temperature and T_g for heavy particle temperature. In local thermodynamic equilibrium (LTE) plasma these two subsystems are

not differentiable, whereas for non-LTEs local gradients are large, hence the two subsystems are delineable.

Table 2.2 Example of various atmospheric pressure plasma systems

Source	Excitation frequency	Species temperature and density	Ref.
DC arc	Low frequency	T_e=T_g~8,000-14,000K $n_e = 10^{21} – 10^{26}$ m^{-3}	[186]
Pulsed DC (Dielectric barrier discharge)	Low frequency	T_e= 10,000-100,000K T_g<700K $n_e = 10^{18} – 10^{21}$ m^{-3}	[187]
Inductively coupled plasma	Radio frequency	T_e=T_g = 6,000-11,000K $n_e = 10^{21} – 10^{26}$ m^{-3}	[186]
Microwave	High frequency	T_g < 4,000K $n_e = 3x10^{20}$ m^{-3}	[188]

Table 2.2 gives an example of plasma source, their excitation frequencies and the properties including temperatures and densities of plasma species. The DC arc and

inductively coupled plasma are mostly LTEs, the pulsed DC arc is non-LTE while the microwave plasma is partial LTE. Coupled with the fact the that the microwave plasma is electrodeless (advantageous owing to the absence of contamination problems arising from

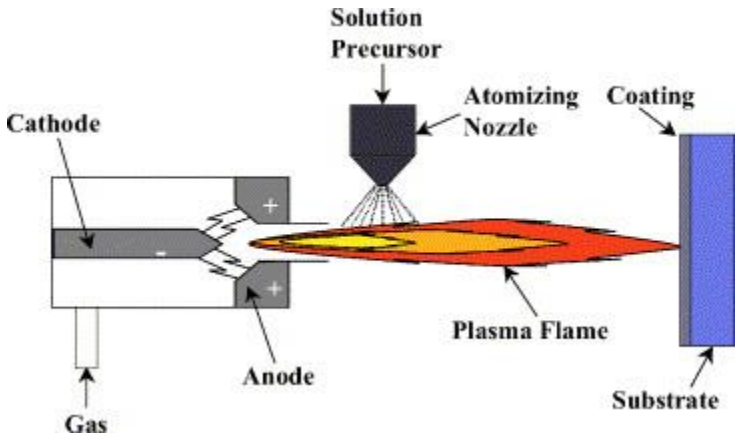

Figure 2-8| DC arc plasma spray set-up for thermal barrier coatings. Adapted from Ref.192

complex oxide deposition on electrodes), the partial LTE makes it an interesting choice due to the non-equilibrium conditions necessary to make metastable phases. Most of the applications of plasma spray pyrolysis are applied in thermal barrier coatings (TBCs)[189-191]. Figure 2-8 shows a typical DC arc plasma spray coating set-up for TBCs, solution precursor or suspensions sprayed perpendicular to the direction of the plasma jet, the momentum of the plasma carries the spray particles onto a substrate material to be coated[192]. The plasma spray pyrolysis has not been successful beyond coating applications, but it will be interesting to test these plasma-synthesized materials in a more functional role as energy-harnessing materials.

2.8 Chapter Summary

This chapter has covered history, energy-focused applications, structure and property relationships, challenges, thermodynamics and the several routes available for the synthesis of complex oxides. It is quite evident from current literature that the slow processing times and extreme temperatures required for either treatment (solid-state) or post-treatment (liquid-phase nucleation) makes the synthesis of complex oxides far from equilibrium untenable. So, many of the important processes in energy conversion where these materials have been utilized may be underperforming probably owing to the fact that metastable phases may have been bypassed sometimes unwittingly by the material designer because not many compositions have been actually realized. Literature also suggests that the ability to have firm control on materials composition is lacking in many of these incumbent methods, additionally, the several process steps inherent in these classical methods may hinder their large-scale manufacturing, and it comes as no surprise that many of these materials from literature are not fully commercialized. Other than thermal barrier coating, the plasma is seldom used in the preparation of complex oxides needed to address the multifaceted energy and materials challenges. This in spite of the fact that it has many attributes tailor-made for the synthesis of oxides of multicomponent type, this dissertation is about addressing this gap. Also, no work has been done to date to offer insights into fundamental understanding of the mechanism in which plasma or even flame pyrolysis process complex oxide synthesis.

CHAPTER 3

EXPERIMENTAL AND ANALYTICAL METHODS

3.1 Introduction

In this chapter, the procedure in the experimental study of the synthesis of polycrystalline complex oxides from solution-phase precursors in the atmospheric plasma is presented here, and this includes, the design and construction of the reactor systems and key components, variation of process parameters to optimize reactor conditions, etc. The characterization and analytical steps employed in both qualitative and quantitative analyses of the surface, morphology, composition and textures are also presented here. An assortment of techniques such as scanning electron microscopy (SEM), energy dispersive spectroscopy (EDS), X-ray diffractometer (XRD), Rietveld analysis, Brunauer-Emmett-Teller (BET) surface area analysis, X-ray photoelectron spectroscopy (XPS), transmission electron microscopy (TEM), inductively coupled plasma mass spectrometer (ICP-MS), and thermogravimetric analysis (TGA) shall be discussed in this chapter, including the detailed measurement conditions and analytical settings. Electroanalytical techniques such as cyclic voltammetry, galvanostatic charge/discharge measurement, chronopotentiometry, including the electrode fabrication methods shall be covered in this chapter. Finally, the computational procedures using the first principle DFT, in the analysis of the electronic band structure of complex oxides shall be presented here.

3.2 Batch Operation

3.2.1 Reactor system

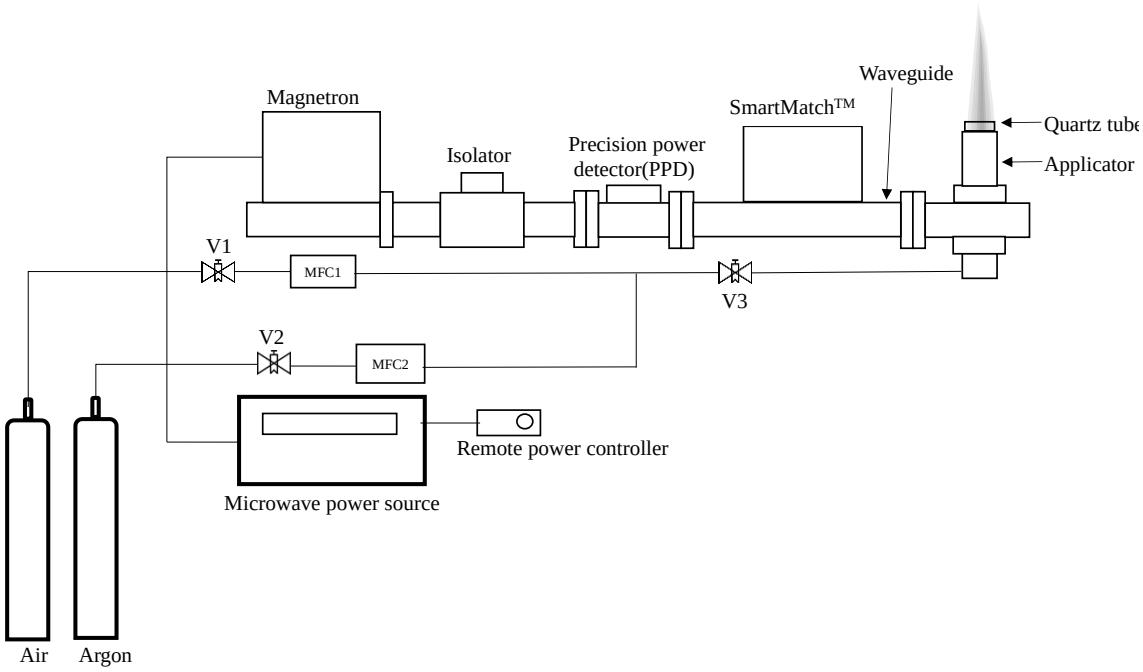

Figure 3-1| Atmospheric microwave plasma batch reactor system for thin film complex oxide synthesis

The schematic of the batch-operated reactor system for the synthesis of thin-film based complex oxides is shown in Figure 3.1. In this setup, an electrode-less atmospheric microwave plasma jet system was assembled with a commercially available units comprising of a microwave power generator (AX2530, SmartPower^{TM}) which converts AC power to DC, a magnetron head (ASteX FI20162-2, 2.45 GHz) with a maximum stationary power of 3 kW, which coverts DC power to microwave energy, an isolator that absorbs reflected microwave power from the applicator and a precision power detector (PPD) that

monitors power propagated in the waveguide for feedback optimization. The SmartMatch^{TM} optimizes the coupling of power to the plasma for reproducible impedance matching. At the far end of the waveguide was attached to an applicator consisting of a quartz tube of about 1 in. in diameter and 3 ft. long, and a cooling water line with maximum flow of 3 slpm (standard liters per minute) which supplies cooling to the SmartPower^{TM}, magnetron head, isolator, PPD, SmartPower^{TM} and the waveguide. The microwave plasma was ignited in the applicator by inserting a copper wire into the resonant cavity from the top of the reactor, moving it around the walls of the resonant cavity until a plasma jet was generated. The flow rates of gases were controlled with mass flow controllers (MFC1 and MFC2) connected to the top and side of the quartz tube, and gases are flowed at an angle of 60°, to create a spiral flow path in order to avoid the quartz tube from melting due to overheating. Initially, an easily ionizable gas such as Ar with low dielectric breakdown constant was introduced into the reactor to ignite the plasma, when the plasma is stable, an appropriate processing gas (air, oxygen, nitrogen, etc) was admitted to the reactor and the flow Ar was turned off.

This custom-built reactor comprises of a magnetron that generates microwaves of 2.45 GHz frequency, also called as the S-band. The microwaves from the magnetron are transmitted by a rectangular waveguide (WR-284) which allows the propagation of microwaves in the TE_{10} mode. A cavity magnetron consists of a resistively heated cathode (usually barium oxide) emits electrons into interaction space between the cathode and the anode comprising of several cylindrical cavities. A permanent magnet is positioned on the magnetron in such a way that the direction of magnetic field is parallel to the axis of the cathode, resulting in a deflection the electron in the path perpendicular to the magnetic

field lines. Electron reaching one end of the cavity induce a positive charge while the other end of the cavity is at negative charge. The oscillation of electrons in the anode cavities results in the loss of some its kinetic energy, alongside the generation of microwave energy. A coupling loop connecting the magnetron with the waveguide transmits this microwave into the waveguide. The isolator allows microwave propagation in one direction and is used to prevent the reflected microwaves from entering the magnetron, while the power detector module measures forward and reflected power. SmartMatch^{TM} is a complex microwave matching unit which uses phase-magnitude detection tool and a sophisticated predictive matching algorithm to provide rapid and reproducible matching of source (microwave) and load (plasma). SmartMatch^{TM} uses the measurement of power detector module to estimate the phase and magnitude of the reflections. The controller in the SmartMatch^{TM}, through a complex algorithm, moves three tuning stubs into the ideal position matching the load impedance and maximizing microwave power coupling into the plasma.

3.2.2 Sample preparation

The steps in the preparation of thin film on fluorinated tin oxide (FTO)-coated glass or any other suitable substrate is illustrated by Figure 3-2(a). Prior to oxide deposition, the substrates were cleaned by ultrasonication in an alkaline aqueous washing solution, deionized water, ethanol, and then deionized water again for 10 min per step. For FTO–glass electrodes, the metal precursor solution was directly cast on the substrate and exposed to the plasma jet to form a thin film of the mixed-metal oxide. A laser pyrometer was used

to monitor the temperature of the substrate, and in general, operating plasma power of 500-600 W guarantees substrate temperatures do not exceed 500 °C, the limit of thermal stability of FTO-coated glass. This technique is rapid, with the oxide film formed in most cases within 14s. Figure 3-2(b) shows a device constructed to extract reactive heat from

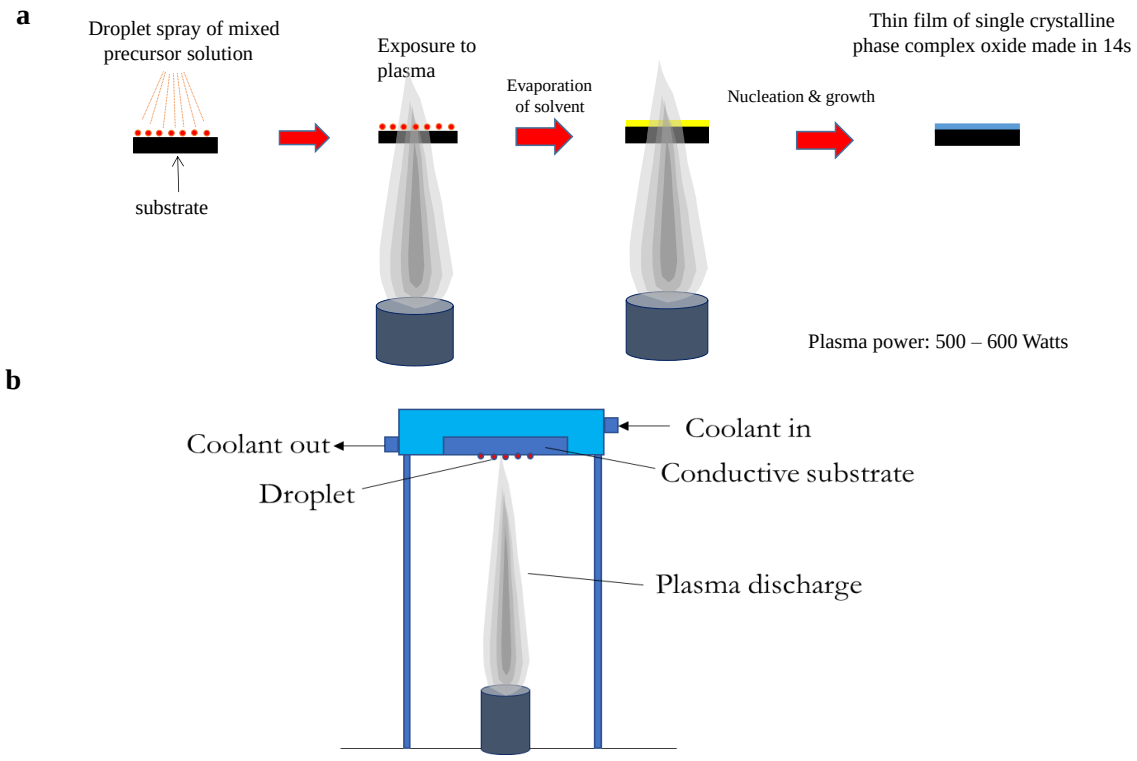

Figure 3-2| (a) Different stages of solution to complex oxide conversion in the batch process (b) substrate cooling device to extract recombinative heat from sample during plasma exposure

the substrate as part of the experiment investigating the overall influence of the

recombinative heating in the formation of complex oxides. Results from this experiment can be found in chapter 5 of this dissertation.

3.3 Continuous Operation

This section shall cover tasks related to design of continuous plasma processing reactors wherein the precursors are airborne with the final oxide products made from gas-phase nucleation of aerosol precursors. This operation is convenient for oxide nanopowders

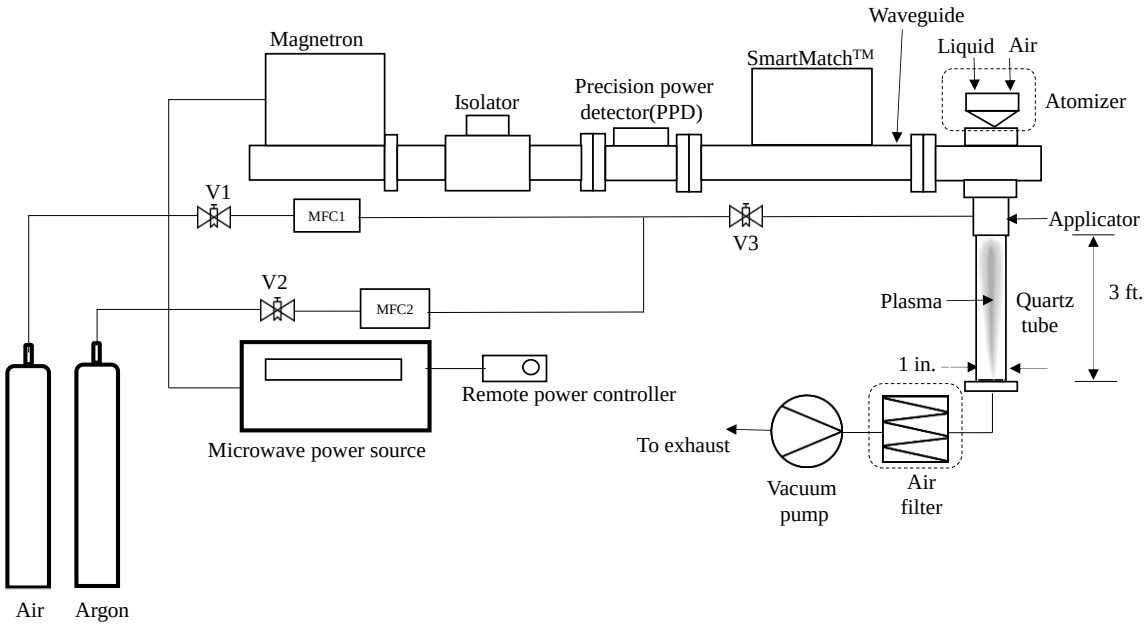

Figure 3-3| Atmospheric microwave plasma continuous reactor system for nanopowder complex oxide synthesis

production.

3.3.1 Reactor system and sample preparation

The reactor set-up is shown in Figure 3-3, the set-up is similar to batch operated system in section 3.2.1 with a few modifications. A 3 ft. quartz tube is used with most of the 3 ft length below the waveguide. Compressed air and precursor liquid are forced

through the nozzle of an atomizer which creates an aerosol of liquid precursor droplets dispersed in air. The vacuum pump help directs the nanopowders into the air filter where the particles are collected.

3.4 Materials Characterization

3.4.1 X-ray diffraction

An X-ray diffractometer is used to determine the crystallography of a crystalline oxide. X-rays are generated using an X-ray tube comprising of heated tungsten filament contained in a low-pressure chamber. A cathode (tungsten metal) emits electrons when heated up thermionically[193]. A high voltage (typically 40kV) is applied across electrodes so that the emitted electrons are accelerated towards an anode (copper, molybdenum, etc) called targets so that on reaching the target, electrons lose energy *via* two mechanisms: firstly, the electrons can decelerate as they approach the nucleus of the atoms in the anode due to opposing electric field from the nucleus towards the electrons. This slowing down of electrons produce Bremsstrahlung or white X-rays[194]. Secondly, the electrons can knock out the electrons in the inner shells of the copper atoms. Electrons in the valence shells relax to the inner shells and the difference in energy is emitted in the form of continuous X-rays. The continuous copper X-rays are not pure, they contain Cu-Kα_1, Cu-Kα_2 and Cu-Kβ X-rays, but needing just Cu-Kα_1 for analysis, an array of mirrors called primary monochromators, coupled with Ni filter are placed in the path of these impure X-rays allowing only Cu-Kα_1 through the sample. Diffracted X-rays are passed through anti-scatter and soller slits into a scintillation counter detector.

A Bruker D8 powder X-ray diffraction (XRD) system was used for crystal structure and phase analysis using non-monochromated Cu-Kα radiation produced by an

X-ray tube operated at 40 kV and 40 mA. The sample XRD patterns were scanned between 20–80° at a scan speed of 4 seconds per step with a step size of 0.02°. XRD detector is LYNXEYE detector operated in 0D mode and uses a scintillation counter. Bruker EVA software and powder diffraction file (PDF 3) were used for phase identification.

3.4.2 Rietveld refinement analysis and crystal structure depiction

This is an advanced XRD analysis tool that refines several crystallographic parameters including peak shape, preferred orientation (or texture), lattice parameters in order to establish a calculated diffraction patterns[195]. The matching of the calculated pattern with experimentally obtained data (observed) could help to determine quantitative results such as grain size, occupancy or even phase composition in multiphase samples. The Rietveld method optimizes the calculated pattern to minimize the weighted sum of squared differences between the observed and calculated intensity values, i.e., it minimizes[196]:

$$\sum_i w_i\left(y_{c,i} - y_{o,i}\right)^2 \qquad 3.1$$

where the weight, $w_i = \frac{1}{\sigma^2}\left[y_{o,i}\right]$, y_c and y_o represents intensity values of the calculated and observed data. There are many discrepancy indices used to test the accuracy of data. Weighted profile R-factor, R_{wp}, is the most common and is defined as:

$$R_{wp} = \sqrt{\frac{\sum_i w_i\left(y_{c,i} - y_{o,i}\right)^2}{\sum_i w_i\left(y_{c,i}\right)^2}} \qquad 3.2$$

The expected R-factor, R_{exp}, is the best possible R_{wp}, defined as:

$$R_{exp} = \sqrt{\frac{\nu}{\sum_i w_i\left(y_{o,i}\right)^2}} \qquad 3.3$$

where ν is the degree of freedom. Another discrepancy index is chi-square (χ^2), and is defined as:

$$\chi^2 = \left(\frac{R_{wp}}{R_{exp}}\right)^2 \qquad 3.4$$

At the start of refinement, χ^2 is initially large if model is poor and gets better as the model improves, ideally χ^2 have a value equal to one for good models but should not be less than one. $\chi^2 < 1$ implies overestimation of uncertainties. Crystallographic data analysis software GSAS-EXPGUI[197] and FullPROF[198] were employed to analyze and/or quantify the phases of materials in the Rietveld method for structure refinement. Atomic positions, cell parameters, background, scale-factors, and profile parameters were all refined. Additionally, a March–Dollase[199] algorithm was employed for the correction of preferential orientation. The crystallographic information files (CIF) were exported from GSAS-EXPGUI into VESTA[200] in order to draw the crystal structures of the samples, while images were rendered using Tachyon ambient occlusion lighting implemented in Visual Molecular Dynamics **(**VMD).[201]

3.4.3 BET surface area analysis

To quantify the surface area of the mixed-metal oxide, Brunauer–Emmett–Teller (BET) analysis was performed with a Micromeritics TriStar 3000 porosimeter. Samples were carefully weighed and degassed before performing the measurements to remove any adsorbed contaminants from the surface and pores of the sample. Calculations for the BET surface area were done using the TriStar 3000 analysis program.

3.4.4 Scanning electron microscopy and EDS measurement

A scanning electron microscope comprises of two main components- (i) electron gun column and (ii) detector. The electron gun column generates electron, by thermionic emission, and focuses the electrons on the sample[202]. In field emission (FE-SEM) mode, a high voltage is applied to material with a very sharp tip, the potential at the tip of the material is deformed creating a pathway for the escape of electrons by tunneling effect. FE-SEM is the mode of choice in high resolution scan. Electromagnetic lenses (condenser and objective) are used to further focus the electron beam, these comprise of wound coils enclosed in cast iron yolks with a small narrow opening. When a current pass through the coils, it produces a magnetic field around that axis of the coils that deflects and focuses the electron beam. The strength of the magnetic field can be varied by changing the current passing through the coils. The condenser lens is used to reduce the diameter of the electron beam that has been accelerated towards the anode and the objective lens is used to focus the electron beam on the sample. The focused electron beam from the objective lens can be rastered along the sample using scanning coils that deflect the position of the electron beam by applying a small voltage between the coils. The secondary electrons emanating from the sample are finally detected using an Everhart-Thornley detector (ETD). The SEM is coupled with an energy dispersive spectroscopy (EDS) which determines the elemental composition and mapping of sample. When the electron beam hits a sample, some inner shell electrons are displaced, exciting these atoms to higher energy state. Relaxation of these atoms from their excited state allows X-rays to be are emitted from the material. The resulting X-rays have wavelengths/energies related to difference in energy levels between

which the relaxation occurs. And because these shell transition energies are characteristic of particular elements, the X-ray spectrum provides a *fingerprint* of the sample[203].

Electron micrographs of the morphology and EDS measurements of the complex oxides were performed with a FEI Nova 600 and a TESCAN VEGA3 SB-EasyProbe scanning electron microscopes (SEM) at accelerating voltages of 10–15 kV and 20 kV, respectively.

3.4.5 Inductively coupled plasma mass spectrometer

An inductively coupled plasma mass spectroscopy (Thermo Scientific XSERIES 2 ICP-MS) method was used to determine the elemental composition in the mixed metal oxide. Prior to ICP-MS analysis, the oxide was digested in trace metal grade HNO_3 (BDH), filtered and dissolved in a matrix of 2% w/v HNO_3 solution to make an analyte of known concentration, analytes are then atomized and carried into the plasma torch by a carrier gas (Ar). The ions generated in the energetic plasma are introduced into the mass spectrometer, where analytes are identified according to their mass-to-charge (m/z) ratios and are quantified by a detector. Detector signals are compared with pulses from those of a multi-element ICP-MS standard (Inorganic Ventures) which make up a linear calibration curve.

3.4.6 X-ray photoelectron spectroscopy

The surface of the sample was analyzed using two X-ray photoelectron spectroscopy (XPS) instruments: Thermo Scientific MultiLab 2000 and TFA XPS Physical Electronics. The MultiLab 2000 instrument is coupled with a highly efficient Alpha110 hemispherical electron energy analyzer. The energy analyzer integrated with twin anode X-ray source, produces both high quality and small area XPS down to 100 µm. To line up the sample analysis position more precisely, a high-quality microscope and CCD camera

is provided in the MultiLab 2000 system. The optional twin-crystal X-ray monochromator provides high resolution XPS and the benefits of source-defined XPS in small area analysis. The base pressures in the XPS analysis chambers were approximately 6.1–8.0 Pa. The samples were excited with X-rays over a 400 µm spot area with monochromatic Al-$K\alpha_{1,2}$ radiation at 1486.6 eV. The photoelectrons were detected with a hemispherical analyzer positioned at an angle of 45° with respect to the normal to the sample surface. The energy resolution was about 0.5 eV. Survey-scan spectra were made at a pass energy of 187.85 eV and a 0.4 eV energy step, while for C-1s, O-1s, Ni-2p, Mn-2p, Co-2p, W-4f and Ir-4f, individual high-resolution spectra were taken at a pass energy of 29.35 eV and a 0.125 eV energy step. All the spectra were calibrated with C-1s spectra. The spectra were fitted using XPSPEAK 4.1 software, and a Shirley-type background subtraction was used.

3.4.7 Raman spectroscopy

The measurement is performed by focusing a laser beam onto the sample. Raman signal gives the information on molecular vibrational and rotational motions of a material. Raman scattering occurs because a molecular vibration can change the polarizability of a material. When photons hit the sample at a certain frequency the molecules excite from ground state to virtual states and fall back to the ground state or lower level states emitting a photon. If the frequency of the emitted photon is same as the incident photon, this phenomenon is called Rayleigh or elastic scattering and does not give any information in identifying the sample. In contrast, when the frequency of the emitted photon is different, the change in the frequency is identified as Raman shift and is characteristic for a given sample.

In this study, room temperature Raman measurements were performed in a backscatter configuration using an inVia Renishaw micro-Raman spectrometer, equipped with a 50x objective lens, visible light optics, an 1800 mm^{-1} diffraction grating, and a HeNe laser producing 633 nm excitation wavelength. The silicon peak at 520 cm^{-1}, measured from a standard silicon wafer, was used for the system calibration. The spectra were analyzed using a peak fitting algorithm implemented in Origin Pro 8.5.

3.4.8 Transmission electron microscopy

TEM detects the elastically scattered electrons that are transmitted through a sample. If the sample is crystalline, diffraction of electrons through the plane of the crystals results in diffraction patterns. Images in the TEM can be obtained either in the bright field (BF) mode or dark field mode. In dark field (DF) image the direct beam is blocked by an aperture in the back focal plane and the diffracted beam of electrons that have strongly interacted with the sample are used for image formation. Hence, the DF images give information about the defects in the sample. In the bright field mode, an aperture is placed in the back focal plane and only the direct beam of electrons that have interacted with the sample are used for image formation and the diffracted electron beam are blocked. As a result of this, the electrons interacting with atoms of higher atomic mass and thicker regions produced a darker contrast which means the BF images give information of the thickness of the sample. High Resolution TEM (HRTEM) mode in the TEM is used for high resolution imaging of crystalline material and can provide resolution up to 0.25nm point to point, with a line resolution of 0.12nm possible. In this technique several diffracted beams are used to form the image. Selected area diffraction (SAED) analysis has been performed on oxide sample to understand the crystallinity of the sample. This can selectively perform

analysis on very small parts of the sample independently under the electron beam by using an aperture which sends only small part of the beam. Crystal quality can be determined from the obtained diffraction pattern. For example, if the sample is polycrystalline it gives rise to a series of ring patterns whereas single crystalline sample gives discrete spot patterns. If the crystalline oxide sample is few nm in size, the HRTEM may not be able to capture images in TEM mode, due to strong diffraction contrast. In such situations, high-angle annular dark field scanning transmission electron microscopy (HAADF-STEM) is a perfect mode to image sub-nm sized particles and single atoms - with high contrast by forming the image with electrons that are scattered incoherently into high angles. The diffraction and phase contrast are disabled in this TEM mode, counts depend on atomic number Z. STEM resolution is 0.18nm on the HAADF detector. TEM is fitted with an electron spectrometer to measure the electron energy loss spectroscope (EELS). EELS is techniques that measure the variation in the loss of kinetic energy of electrons after they interact with a sample. This data is used to determine the atomic structure, chemical state, quantity and the interaction between an atom and its nearest neighbors.

HR-TEM, SAED, nanoprobe-based energy dispersive X-ray spectroscopy (EDS), and STEM were conducted using two instruments FEI Tecnai F20 transmission electron microscope and JEOL 2010F transmission electron microscope, with an accelerating voltage of 200 kV.

3.4.9 Thermogravimetric analysis

Thermogravimetric analyses were performed in a differential thermogravimetric analyzer, (model SDT Q600 from TA Instruments, precision of temperature measurement ±2 °C, microbalance sensitivity <5 μg), with which the precursor weight loss and rate of

weight loss as functions of time or temperature were recorded continuously, under dynamic conditions, in the range 20–1000 °C. The experiments were carried out at atmospheric pressure, under nitrogen atmosphere, with a flow rate of 40 ml/min, at ramp rate of 10 °C min^{-1}. A precursor weight of 20 mg was placed in the crucible. The experiments were replicated at least twice.

3.5 Electrochemical Characterization

All measurements were performed for the electroanalytical studies for OER electrocatalysis in a three-electrode setup using a Biologic SP-200 potentiostat. A Pt gauze counter electrode was separated from the main cell compartment with a glass frit and a saturated calomel electrode (SCE) served as the reference electrode. All potentials were converted and referred to the reversible hydrogen electrode (RHE) using the Nernst equation[204]:

$$E_{RHE} = E_{SCE} + 0.241 + 0.059\text{pH} \qquad 3.5$$

All electrochemical measurements were performed in aqueous 1.0 M H_2SO_4 at a scan rate of 20 mV s^{-1} with continuous stirring of the electrolyte during cyclic voltammetry (CV) and chronopotentiometry (CP) measurements. Catalysts current density vs potential was measured in each case for samples that were plasma-oxidized directly on FTO-coated glass substrates, and electrodes prepared via plasma oxidized powders prepared into catalysts ink and drop-casted on glassy carbon (GC). Potentiostatic electrochemical impedance spectroscopy (EIS) measurements were performed before every experiment to determine the uncompensated solution resistance, R_u, and the potentiostat subsequently compensated for 85% of R_u during electrolysis. The typical electrochemical cell in these experiments had a resistance, R_u ~10–20Ω in 1 M H_2SO_4. The current densities were determined relative

to the geometric projected electrode area throughout this study. In basic electrolyte experiments, the procedure is similar as with acidic electrolyte, 1.0 M solution NaOH was used and R_u was around 20-25Ω. The methodology for determining upper and lower bounds on the turnover frequency (TOF) are described in the Appendix 3.

In the electroanalytical analysis of lithium-ion battery cathodes, the galvanostatic charge-discharge measurements were carried out using Arbin instrument. Charge and discharge measurement were carried out at the voltage range of 4.7 – 2.0V with different current densities of 10, 50, and 100 mA/g. The cyclic voltammetry measurement was carried out at the voltage range of 4.7– 2.0V with scan speed of 1mV/s using eDAQ e-corder potentiostat.

3.6 Electrode Fabrication

3.6.1 Anodes for OER electrocatalysis

In the case of the acidic media OER, catalysts current density *vs* potential was measured in each case for samples that were plasma-oxidized directly on FTO-coated glass (Hartford Glass, Hartford, CT) substrates as thin films, and electrodes prepared *via* plasma oxidized powders prepared into catalysts ink and drop-casted on glassy carbon. The Ir-rich compositions on FTO/glass displayed highly stable behavior. However, plasma oxidation with the tungsten precursor led to delamination issues under extended operation, so films were instead ballmilled to microparticles and bound to a GC disk for extended galvanostatic measurements[205]. The ball-milled samples were made into a catalyst ink and electrochemically characterized for stability with a similar setup and experimental conditions using a rotating disk electrode (RDE) with the GC disk as the working electrode rotated at 1600 rpm and by monitoring the potential of the working electrode at a constant

current density of 10 mA cm^{-2}. Catalyst inks were prepared by horn sonication of oxides and 40µl 5% of Nafion 117 solution (Sigma Aldrich), 3.8 mL DI water, 1.0 mL 2-propanol yielding inks with final concentrations of 80 mg of oxide per ink. 10µ L of catalyst ink was drop-casted onto a GC electrode 0.196 cm^2 area, (Pine, NC) polished to a mirror finish with alumina slurry. The particle binding method had limitations, however, and the Nafion binder film was observed to partially delaminate after extended testing. The unsteady performance of the WO_3 (x = 0), which is known to be stable at pH 0.0 under anodic potentials [206-207], was attributed to this issue.

All the electrodes in basic media electrocatalysis were synthesized directly from the plasma in the methods discussed in section 3.2.2 of this dissertation.

3.6.2 Cathodes for lithium ion battery

The electrode materials for $LiNi_{0.2}Mn_{0.6}Co_{0.2}O_2$ was prepared using 80 wt.% of active material with 10 % of acetylene black binder and 10 % of PVDF (polyvinyledine fluoride) in N-methylpyrolidone (NMP). The well-mixed slurry was coated onto Al sheet using doctor blade. The coated active material on Al sheet was dried at 120 °C for 1h to remove the NMP solution. The electrode was cut into a size of 2.0 cm^2. The loading of active $LiNi_{0.2}Mn_{0.6}Co_{0.2}O_2$ cathode electrode was 1.3-1.4 mg/cm^2. The electrode was vacuumed at 160°C for 5 h in a vacuum oven. The cell assembling was carried out in an argon filled dry glove box. The $LiNi_{0.2}Mn_{0.6}Co_{0.2}O_2$ was used as a working electrode and Li foil as an anode separated by 2 piece of glass fiber filter (ADVANTEC, GB-100R, Japan) using 2032 coin-type cell. The electrolyte used was 1.0M $LiPF_6$-EC (ethylene carbonate): DMC (dimethyl carbonate) (1:2 by volume).

3.7 Computational Procedure

In this section, a procedure for the density functional theory (DFT) calculations of $La_{1-x}Ca_xNi_{0.5}Co_{0.5}O_{3-\delta}$ structure discussed in chapter 7 is presented here. For the theoretical study, we used first-principles (DFT) in the generalized gradient approximation (GGA) and the Perdew-Burke-Ernzerhof (PBE) [208] augmented by including the Hubbard-U corrections (GGA+U formalism) [209] based on Dudarev's approach[210] as implemented in the Vienna Ab-initio Simulation Package (VASP) [211]. We used a unit cell of $Ca_nLa_{24-n}(CoNi)_{12}O_{72-\delta}$ consisting of 120 atoms (δ=0) in the perovskite structure and in various atomic configurations specified by the atomic concentrations x and y. Oxygen vacancies were simulated by letting the concentration δ to be different than zero. All our initial structures were obtained by substitutional replacements. U values were used only for the transition metals. In particular, we used $U_{d,Co} = U_{d,Ni} = 4.0$ eV. The projected augmented wave (PAW) potential [210] is used to describe the core electrons. After testing for convergence, we settled for a 2x2x1 Γ-centered pack for *k*-vectors sampling. A kinetic energy cutoff of 520.0 eV was found to be sufficient to achieve a total energy convergence of the energies of the systems to within 10^{-5} eV. Gaussian smearing of 0.05 eV was chosen to accelerate the electronic convergence. The optimization of atomic positions (including full cell optimization) could proceed without any symmetry constraints until the force on each atom is less than 5 $meVA^{-1}$.

The reaction calculator in Materials Project[212] was used to calculate the formation energy per atom in La/Mn oxide system in chapter 5. This software allows users to estimate tens of thousands solid-state reaction enthalpies from a database of density functional theory calculations. Also, this calculator does the computation with experimental

enthalpies (at 298K and 1atm) where available. The reaction calculator's energies are generally a good estimate of room temperature formation enthalpies, although all calculations were performed at 0K and 0atm.

3.8 Chapter Summary

The methods and procedures for the analysis of samples, theoretical calculations and design and construction of reactor systems have been highlighted in this chapter.

CHAPTER 4

A RAPID AND SCALABLE METHOD FOR MAKING MIXED METAL OXIDE SOLID SOLUTION FOR ENABLING ACCELERATED MATERIALS DISCOVERY[1]

4.1 Introduction

Many grand challenges in energy conversion and storage need discovery of new materials[40]. However, there are not too many reported synthesis approaches that could easily be implemented for the rapid screening and rational understanding of structure-property relationships. Specifically, the challenges include semiconductors for photoelectrochemical water splitting[5], stable electrocatalysts for oxygen evolution and reduction[46] and nitrogen reduction[213] and for many heterogeneous gas-solid reactions including carbon dioxide reduction[5]. Many of the above challenges require synthesis of multi-element solid solutions with stoichiometry over a wide-range of compositions regardless of phases present.

[1] The texts in this chapter were reproduced with the permission (see Appendix 12) of Cambridge University Press. Original article was published as "B. P Ajayi, S. Kumari, D. Jaramillo-Cabanzo, J. M. Spurgeon, J.B. Jasinski, M. K. Sunkara, (2016), A rapid and scalable method for making mixed metal oxide alloys for enabling accelerated materials discovery. J Mater Res, 31, 1596-1607, https://doi.org/10.1557/jmr.2016.92". Formatting styles were changed to adapt original article to the style of this dissertation, and some data from the supporting information in the original article are included in this chapter.

The conventional synthesis method is a solid state route that involves the mechanical milling of oxides, carbonates or nitrates[16]. Solid state route is highly unfavorable because it requires long processing time and elevated temperature and pressure[17]. Consequently, wet chemical methodologies such as sol-gel[18], co-precipitation[19] solvothermal techniques[20], pyrolysis in air[23] have all been proposed to deal with this problem. However, these methods require prolonged heat treatments and therefore are primarily restricted to equilibrium phases[22]. Besides, they are also low yield methods and involve multi-step and laborious processes, each bearing a risk of introducing impurities to the final product. More so, with these methods, it is quite a challenge to control the size and composition of mixed metal oxide nanoparticles, a key parameter determining the intrinsic properties and performance of these materials.

So, there have been concerted efforts to make mixed metal oxide in a single step from inexpensive materials with high scalability and control over size and final product stoichiometry, by using the flame spray pyrolysis (FSP) methods such as vapor-fed flame spray pyrolysis [214], liquid-fed flame spray pyrolysis[215-216] and liquid-fed flame assisted spray pyrolysis[217]. Unfortunately, metal oxides produced through vapor-fed spray pyrolysis are limited to few oxides such as zirconium, aluminum, titanium, and silicon based oxides[214]. In addition, the starting materials of this synthesis route are basically volatile chlorides that release by-products such as hydrogen chloride gas which are not benign from the environmental standpoint. Vapor-fed FSP has been improved upon by the incorporation of a liquid feed system [214], making the process cleaner and has been shown with many metal oxides. Both liquid-fed flame assisted and flame spray pyrolysis use either the enthalpy of combustion of precursors or external high enthalpy value flame for

providing temperatures up to 2800 K.[218] Earlier works on combinatorial synthesis have used pyrolysis in air to convert precursor to mixed metal oxides, but have failed to show strong evidence that solid solutions are really formed[14, 23]. Many of these techniques have only demonstrated to produce certain stable phases of mixed metal oxide. However, it is crucial to be able to synthesize mixed metal oxide solid solutions over complete range of compositions for discovering new materials and for addressing grand challenges in energy conversion and storage.

Specifically, in this chapter, the synthesis of mixed transition metal oxide comprising of binary metal oxides (nickel manganese oxide, nickel iron oxide) and ternary mixed metal oxides (involving nickel, manganese and iron) have been demonstrated with exceptional control over composition and phases. In order to understand the functional behavior of these synthesized materials, we tested the activity of the above nanoparticles as an electrocatalyst for oxygen evolution reaction (OER). The OER, $2H_2O \rightarrow 4H^+ + O_2 + 4e^-$ (acidic solution) or $4OH^- \rightarrow 2H_2O + O_2 + 4e^-$ (basic solution) is heavily reliant on efficient electrocatalysts because it is kinetically sluggish and thus constitutes an outlet for efficiency loss and places a significant overpotential requirement in water splitting reactions[39, 219]. Cogent understanding of the structural morphology and composition of catalysts at a molecular level has been instrumental in the rational design of robust electrocatalysts with high activities. The state-of-the-art OER electrocatalysts like RuO_x, IrO_x and Pt are quite expensive; hence it is important to find low-cost and readily available alternatives. High-throughput materials synthesis and screening have recently been employed to find these alternatives, and the oxides of first row transition metals like nickel, iron and cobalt have been reported to be good candidates[220-221].

4.2 Complex Oxide Thin Film Synthesis and Characterization

The reactor set-up in section 3.2.1 was used for most of the synthesis. The precursor solutions were prepared using mixtures of nickel, iron and manganese nitrates in desired proportion. Chemically pure grade of nickel (II) nitrate hexahydrate, manganese (II) nitrate hydrate, and iron (II) nitrate non-hydrate (research grade, Sigma Aldrich) were used as starting materials without further purification. Appropriate amounts of the precursors were weighed out and dissolved in deionized water to make up 1.0 M solution. About ~0.1ml of prepared metal precursor solution was sprayed onto 2 cm^2 fluorine-doped tin-oxide (FTO) coated glass substrates (Sigma Aldrich) which were exposed to a plasma jet with an input power of 500W and a volumetric flow of 2 slpm (standard liters per minute) Ar, 11 slpm air, for 30 s. The argon gas is only necessary for plasma ignition and is turned off after obtaining a stable plasma. The substrate temperature is measured using a pyrometer and is determined to be anywhere between 500-550°C. The catalyst adhered very well to the surface of the substrate forestalling any use of a surfactant. The plasma power was set in such a way that the temperature of the substrate did not exceed 550 ˚C. The maximum temperature of 550 ˚C is set by the thermal stability of FTO-coated glass substrates, and the choice of FTO-coated glass substrates is based on its poor electrocatalytic properties. Substrates were cleaned prior to deposition by ultrasonication in an alkaline aqueous solution, deionized water, ethanol, and deionized water for 10 minutes per step.

A Bruker D8 powder X-ray diffraction (XRD) system was used for crystal phase analysis. The data were processed to analyze sample $NiMn_{0.2}Fe_{1.8}O_4$ using FullProf.2k[198] (Version 4.30—Apr, 2008-ILL JRC) in the Rietveld method for structure refinement. Program refinement of the first samples was started with the space group Fd3m, origin at

−3 m, O in 32e−, A site in 8f, and B site in 16c. In the first step the global parameters, such as 2θ-zero and background, were refined. In the next step, the structural parameters, such as lattice parameter, atomic coordinates, and site occupancy, were refined.

4.3 Results and Discussion

Experiments were conducted using several binary and ternary systems and the results are analyzed with various techniques to confirm that the composition of resulting solid solutions can be tuned over entire ranges. In fact, the data shows complete tunability with respect to compositional control using precursor composition in liquid droplets. Specifically, the results with nickel and manganese oxides for binary systems and nickel, manganese and iron oxide solid solutions for ternary systems are illustrated. In addition, the resulting ternary solid solutions are investigated for their performance as electrocatalysts for oxygen evolution reaction.

4.3.1 Nickel-manganese oxide ($Ni_xMn_{1-x}O_y$)

The mixed metal oxides are in general represented by $Ni_xMn_{1-x}O_y$ where $0.0 \leq x \leq 1.0$ and y is dependent on the type of phase present. Throughout the full range of composition, $0.0 \leq x \leq 1.0$, as shown in Figure 4-1(a), the phase(s) present depends mainly on the *x* composition in the sample. Two clear phase regimes can be identified from XRD: (i) solid solution of $Ni_kMn_{1-k}O$ ($0.9 < x \leq 1$) (ii) a solid solution of $Ni_mMn_{3-m}O_4$ ($0.05 < x \leq 0.9$), where the indices *k* and *m* define the rock-salt and spinel solid solution series, respectively. In the entire range, there is no segregation of NiO and MnO_x phases as evidenced by the absence of a clear α-Mn_2O_3 (221) peaks and the shrinking of NiO (222) peak from $x = 1.0$ until it disappears at $x = 0.4$.

4.3.1.1 Solid solution of $Ni_kMn_{1-k}O$ ($0.9 \leq x \leq 1$)

In the compositional range of $0.9 < x \leq 1$, a solid solution is formed whose composition can be tuned. The resulting solid solution has the rock-salt phase (space group: *Fm-3m*). The XRD data in Figure 4-1(a) show pure phases for NiO and α-Mn_2O_3 cubic phases and Figure 4-1(b) show the (200) peak of the rock-salt phase (at 43.3°) for $Ni_kMn_{1-k}O$ solid solutions. The 43.3° peak position shifts monotonically to lower angles with the increase of manganese concentration. Figure 4-1(c) shows the plot of the variation of lattice parameter with Mn mol. % doping in Ni lattice. Clearly, the lattice parameter increases non-linearly until it reaches the solubility limit which is about 10 mol% Mn composition or $x = 0.90$. is noteworthy that at compositions above the solubility limit of Mn in Ni lattice, the speciation of the spinel phase is more evident. The crystal structure for sample with $x = 0.90$ was examined with HRTEM and the SAED, and the result are in agreement with the XRD results (Figure 4-2).

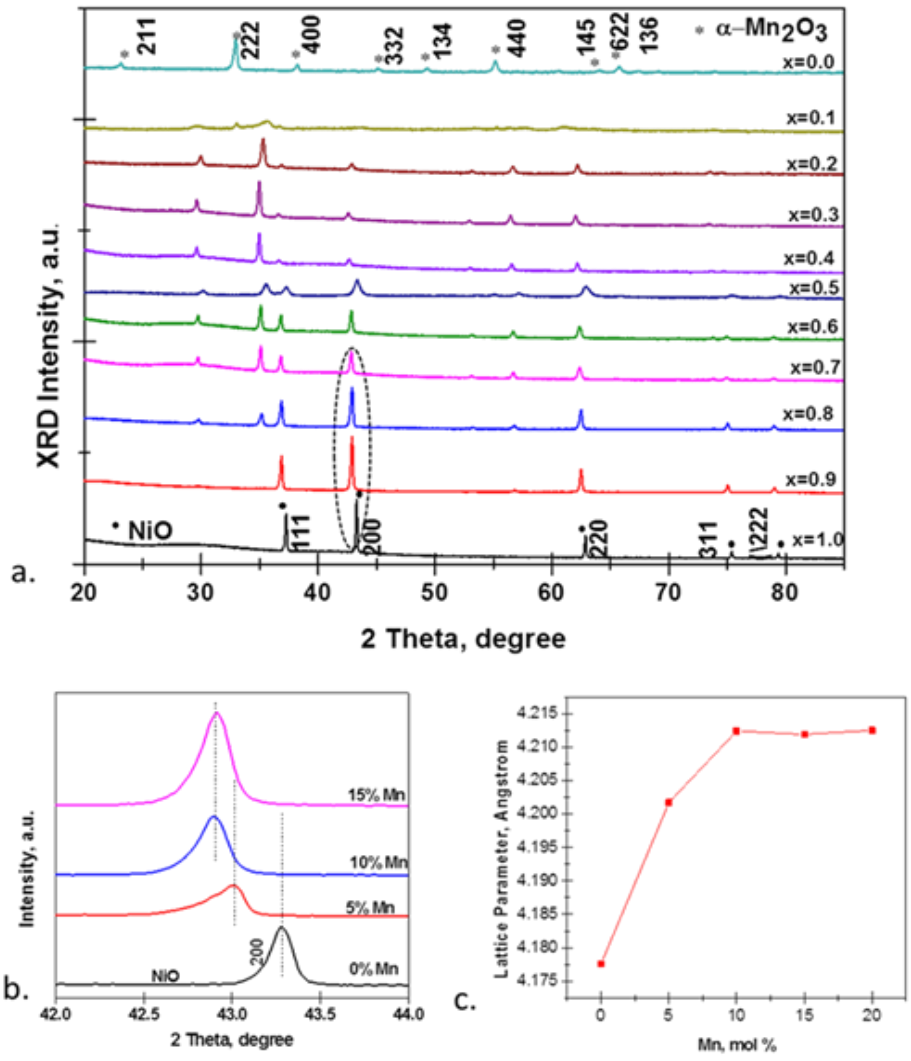

Figure 4-1| (a) X-ray diffraction of $Ni_xMn_{1-x}O_y$ ($0.0 \leq x \leq 1.0$) showing the phases present as *x* is varied, the encircled (200) peak is expanded in Figure 1b for clarity (b)X-ray diffraction showing the (200) plane of NiO lattice shifting to a lower angle with Mn doping (c) Variation of the NiO lattice parameter with Mn doping concentration.

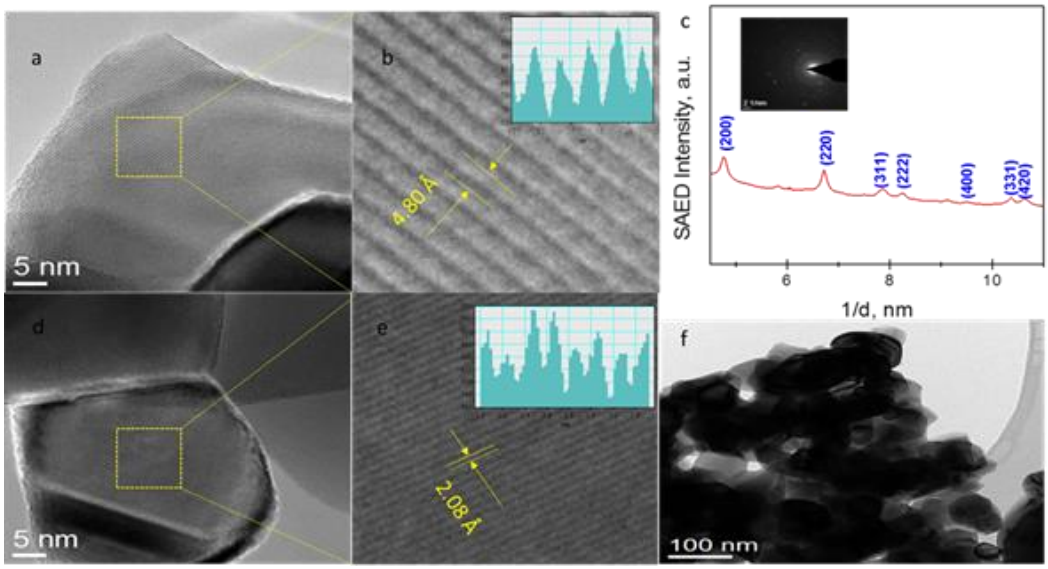

Figure 4-2| (a) High resolution TEM (HR-TEM) of sample *x*=0.9, showing grains with a single lattice fringes having d-spacing indexed to (101) of the tetragonal spinel lattice(b) a close-up view of the lattice fringes showing d_{101} to be 4.80Å (c) Selected area electron diffraction (SAED) of sample x=0.9 (inset) showing the diffraction rings. The intensity line profiles measured from these patterns are as shown, assigned to the rocksalt phase with some spinel peaks, which is in agreement with XRD data (d) High resolution TEM (HR-TEM) of sample *x*=0.9, showing grains with a single lattice fringes having d-spacing indexed to (200) of the rocksalt lattice (e) a close-up view of the lattice fringes showing d_{200} to be 2.08Å (f) Bright field TEM of composition *x*=0.9

4.3.1.2 Solid solution of $Ni_mMn_{3-m}O_4$ spinel ($0.05 \leq x < 0.9$)

In this compositional range ($0.05 < x \leq 0.9$), the XRD data for samples were indexed to spinel solid solutions ($Ni_mMn_{3-m}O_4$). The sample with composition $x = 0.30$ showed well resolved diffraction lines corresponding to a tetragonal spinel phase (ICDD PDF-01-070-9039) with space group number $I4_1/a\ m\ d$ (141). XRD data for samples with the following x composition and the corresponding m values in bracket: 0.50 (1.50), 0.40(1.20), 0.30(0.90), 0.25(0.75), 0.20(0.60), shows that phase pure $Ni_mMn_{3-m}O_4$ bimetal spinel solid solutions exist in the composition range $0.20 < x \leq 0.50$ (or $0.60 < m \leq 1.50$).

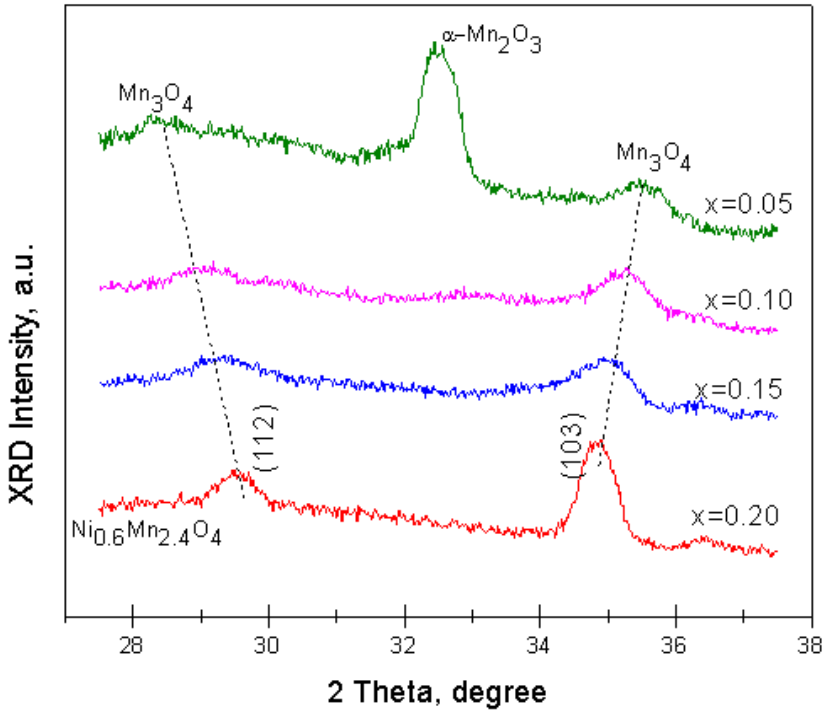

Figure 4-3| XRD reflections of $Ni_mMn_{3-m}O_4$ capturing the speciation from binary metal spinel phase to the mono-metal spinel phase

The series of oxides with composition $0.05 < x \leq 0.20$ shows peak deviation from nickel manganite peaks, and peaks at (112) and (103) were highlighted in Figure 4-3 for emphasis.

There is a widening of the gap between the centerlines of these two peaks coupled with peak broadening until manganese oxide (Mn_3O_4 and α-Mn_2O_3) peaks are evolved at x=0.05. Peak broadening can be ascribed to the non-uniform strain on the spinel lattice and/or decreasing grain size. It is interesting to note that at nickel composition $x \leq 0.05$, there is not enough Ni (II) to diffuse into the solid lattice of Mn_3O_4 to occupy the manganese vacancies or partially replace manganese ions in the tetrahedral or octahedral holes[222]. In the compositional range $0.5 < x \leq 0.9$, there is a co-existence of spinel solid solutions and rock-salt ($Ni_{0.9}Mn_{0.1}O$), however; at $x > 0.5$ only phase pure $Ni_mMn_{3-m}O_4$ can be seen.

The spinel manganates are known to exhibit large tetragonal distortions[223-224]. The tetragonal distortion is a consequence of Jahn–Teller effect of the cubic spinel associated with a high density of Mn^{3+} cations[225]. Large amounts of Mn^{3+} are found in Mn-rich nickel manganese spinels due to the reduced amount of Ni^{2+} on the octahedral sites of the spinel lattice[226] . The Mn valence states is strongly dependent on Ni occupancy in the octahedral sub-lattice, which is a measure of inversion parameter of the spinel lattice. Ni cations moving to the octahedral sub-lattice is balanced by the Mn going in the opposite way (tetrahedral sites). The tetrahedral Mn has a valence state of +2 since Mn^{3+} is a less suitable state in a four-fold coordination. To attain charge neutrality, an equal amount of Mn^{4+} is formed in the octahedral sites to compensate for the Mn^{2+} on the tetrahedral sites resulting into internal disproportionation[227].

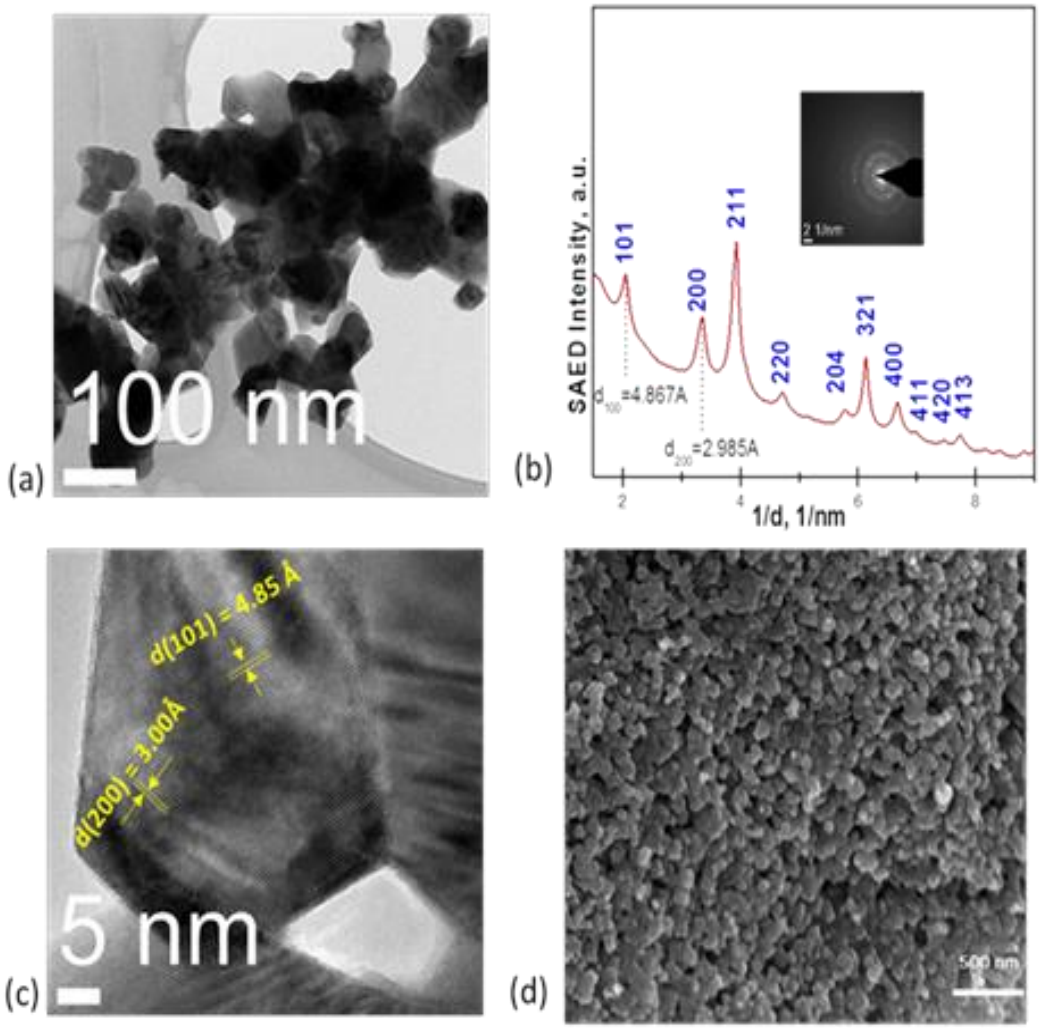

Figure 4-4| (a) Bright field TEM of composition x=0.2 with crystallite size of 50-80nm, (b) Selected area electron diffraction (SAED) of sample x=0.2 (inset) showing ten diffraction rings. The intensity line profiles measured from these patterns are as shown, assigned to the tetragonal spinel, which is in agreement with XRD data (c) High resolution TEM (HR-TEM) showing grains with two lattice fringes having d-spacing indexed to (101) and (200) planes of the tetragonal spinel crystals (d) SEM micrograph of samples x=0.2 showing its morphology

The XRD data is further corroborated with diffraction and EDS analysis in TEM. A representative sample x=0.2 is used as an example to confirm the morphology and crystal structure. Figure 4-4(a) shows the bright field TEM image for the solid solution with composition x=0.2 where a rapidly changing strong diffraction contrast can be noticed, an indication of randomly oriented grains and polycrystallinity of sample. The SAED patterns obtained for sample x=0.2 is shown in the inset of Figure 4-4(b). The intensity line profiles measured from these patterns are shown in Figure 4-4(b). About ten diffraction rings are visible which corresponds to the family of planes of the tetragonal spinel nickel manganite; the other rings were not clearly detectable due to their low intensity. Formation of tetragonal spinel phase is further confirmed from the sample with composition x=0.2 by the HRTEM analysis. We identified two of lattice fringes, one with the d-spacing of 4.85 Å and the other one with the d-spacing of 3.00 Å, which are consistently observed in HRTEM images of the nanoparticles (Figure 4-4(c)). Knowing that the typical accuracy of HRTEM analysis is usually not better than a few percent, the observed lattice fringes can be assigned to the (101) and (200) planes of tetragonal spinel $Ni_{0.6}Mn_{2.4}O_4$. As expected, the HRTEM data did not show any presence of α-Mn_2O_3 and NiO phases in this sample composition. SEM image (Figure 4-4(d)) of the solid solution with sample composition x=0.2 has a morphology resembling cubes interconnected by a channel. Figure 4 shows TEM-EDS compositions of four randomly selected grains of samples with precursor compositions x=0.1 to x=0.9, showing strong agreement with the precursor composition.

4.3.2 Nickel iron oxide $Ni_aFe_{1-a}O_b$ ($0.0 \leq a \leq 1.0$)

Similar bimetallic oxide system was reproduced for nickel ferrite, illustrated in Figure 4.5. Identical to the Ni-Mn-O system, the two clear solid-solutions that are evident are the rocksalt ($Ni_{1-p}Fe_pO$) and the cubic spinel solid-solution phase ($Ni_qFe_{3-q}O_4$). To estimate the degree of solid solution of $Ni_{1-p}Fe_pO$ samples with composition p = 0.0, 0.05, 0.10, 0.20, 0.30 were investigated. XRD reflections show that the samples were single phase up until p = 0.05, beyond this value (i.e. p > 0.05) the evolution of the spinel phase is clearly evident as shown by Figure 4.5(b). This result is to be expected because on saturation of the NiO lattice, the excess Fe ions precipitate out as another phase. The sample with composition p = 0.05 is isostructural with the NiO rocksalt structure (sp. gr. F*m*-3*m*). The solid solubility limit lies in the range 0.05 < p < 0.10 in agreement with earlier report[228]. Increasing the Fe doping beyond 40 mol. % causes the XRD reflections shifting in the reverse direction, which may be ascribed to the onset of solid solution of the $Ni_qFe_{3-q}O_4$ spinel phase (Figure 4.5(d)). Samples with Fe composition from 40 to 70 mol. %, trends in the same direction and corresponds to 0.9 < q < 1.8, beyond 70 % atom Fe, solid solution limit is reached as evidenced by the evolution of the α-Fe_2O_3 phase (Figure 4.5(c)). The Fe rich end of spinel solid solution ranges from only q = 0.9 and q = 1.0, however the Ni rich end has a wide solid solution range, from q = 1.0 to q = 1.8.

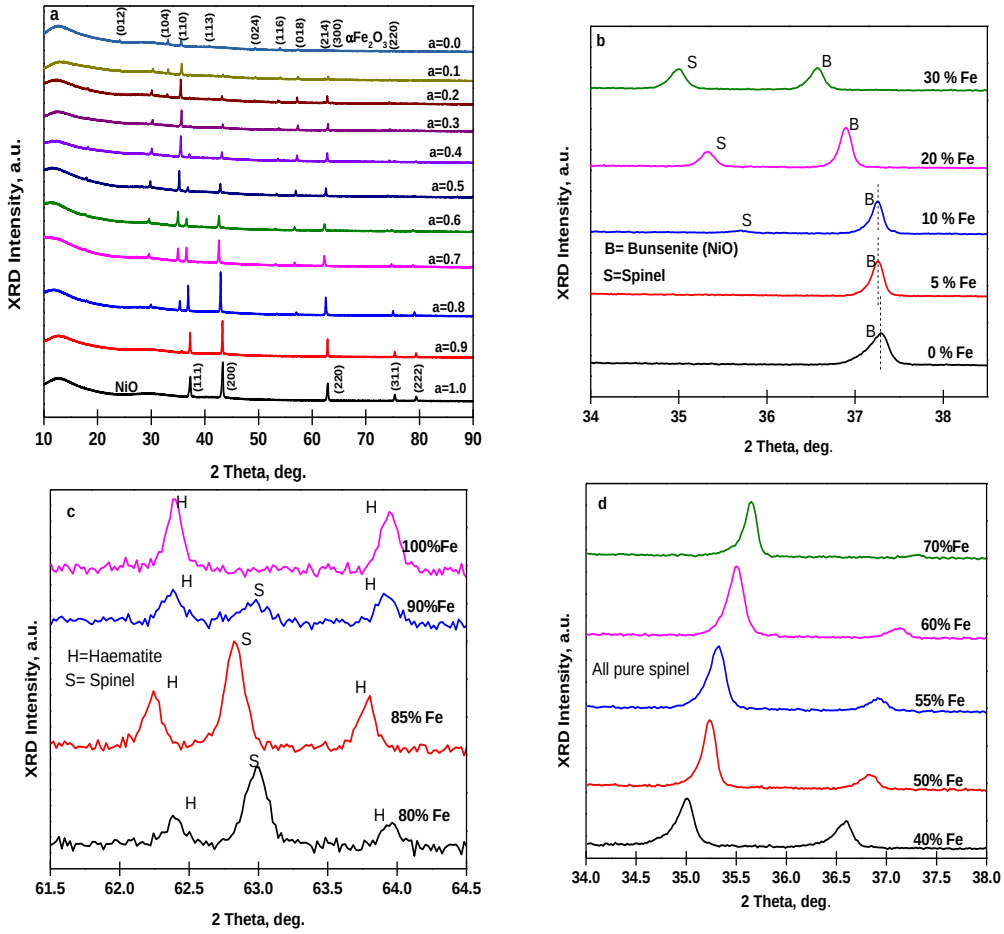

Figure 4-5| (a) X-ray diffraction of $Ni_aFe_{1-a}O_b$ ($0.0 \leq a \leq 1.0$) showing the phases present as a is varied (b) X-ray diffraction of NiO (111) plane showing the precipitation of a new spinel phase after the solid solubility limit has been reached, where S is spinel and B is bunsenite phase . (c) Fe rich $Ni_aFe_{1-a}O_b$ showing the evolution of hematite peaks (H) in relation to spinel (S) with increasing Fe concentration (d) X-ray diffraction showing the spinel solid solution.

4.3.3 Comparison between plasma and thermal oxidation

In order to understand whether one can obtain similar results with thermal oxidation, a sample with composition x=0.2 is investigated using thermal oxidation route. The phases obtained from XRD data were the ilmenite ($NiMnO_3$), bixbyite (α-Mn_2O_3) and the bunsenite (NiO) phases (refer to Figure 4-6(a)), which is identical to the thermodynamically predicted phases that can be found from the phase diagram obtained from Materials Project[212], and illustrated in Figure 4-6b)). However, these results are completely different from the result obtained with plasma oxidation. The difference in the phases can be ascribed to the dissimilar mechanistic steps obtainable in the two oxidation processes, given that the reaction temperature and pressure are same. As can be seen from the results, plasma oxidation better reflects the reaction off-stoichiometry, producing solid

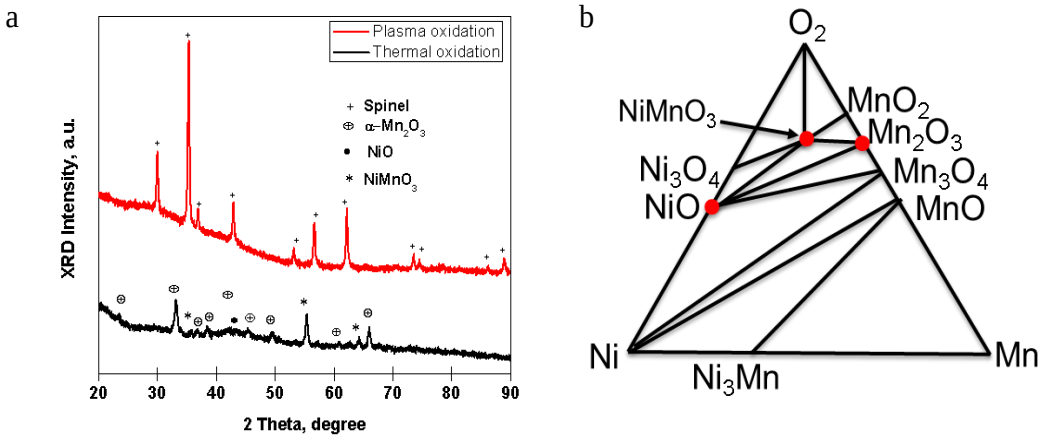

Figure 4-6| (a) X-ray diffraction of the sample with nominal composition of x=0.2 prepared via plasma and thermal oxidation (b) Phase diagram of the Ni/Mn/O system

solution of nickel manganite spinel. However, the thermally oxidized sample are segregated into thermodynamically stable monometal oxide (bunsenite and bixbyite) and mixed metal oxide (ilmenite) phases in agreement with Xiao-Xia and co-workers [229].

In order to explain the differences between thermal and plasma oxidation, a proposed mechanism as elucidated by the schematic presented in Figure 4-7, and it is used to illustrate various stages of oxidation process. The following are the stages of oxidation: first, upon either plasma exposure or thermal heating, the liquid droplet will lose solvent by evaporation until a densified amorphous phase is formed. In the case of thermal oxidation, heating and cooling rate is slow and so atoms have enough time to diffuse,

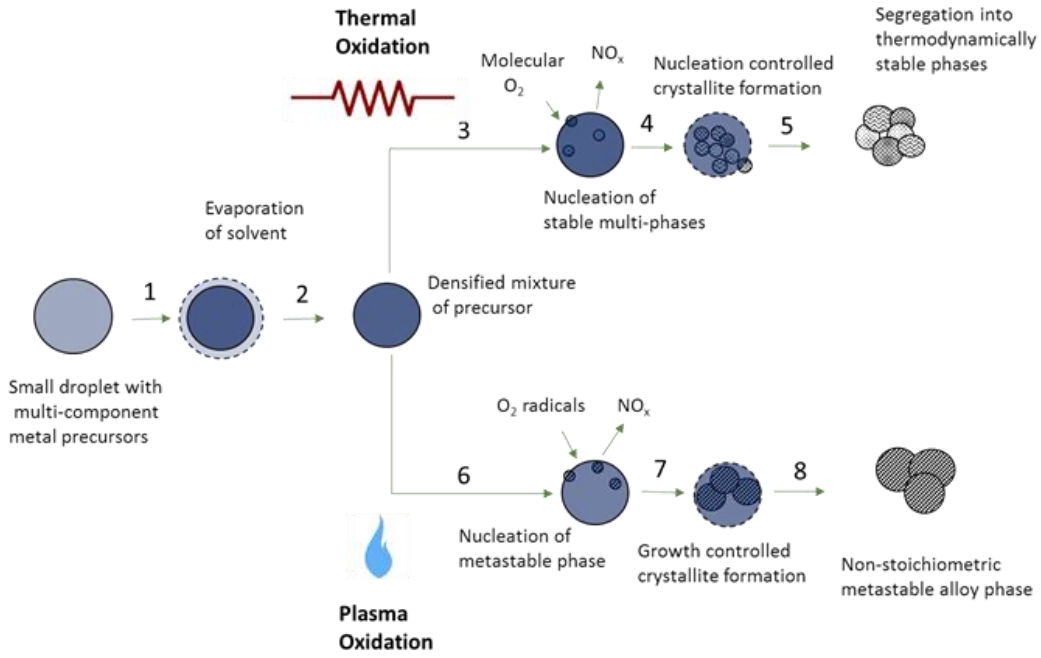

Figure 4-7| Proposed mechanism for the formation of nanoparticles of thermally oxidized and plasma oxidized precursor solutions.

inducing a phase transformation towards thermodynamically stable phases. So, irrespective of precursor composition inside liquid droplets, the resulting materials would consist of thermodynamically stable phases. The oxidation proceeds with diffusion of molecular oxygen into the amorphous mass containing nitrates and the thermal decomposition of the amorphous mass to release NO_x. After an induction period, nuclei are formed. In the case

of plasma oxidation, several processes take place in a very short period of time of a few seconds and they include the following: oxygen radicals can diffuse into the core of the densified amorphous mass of precursor; faster reaction kinetics with oxidation of nitrates with oxygen radicals; and fast heating and cooling rate of the core for nucleation and transport limited ordering of atoms makes for the speciation of metastable phase nuclei. As the growth proceeds with transport limited region, the composition of resulting solid solutions depends directly on the composition of elements in the surrounding environment. The composition of the surrounding nutrients is as homogenous and similar to the supersaturation, thus; the growing crystals reflects this compositional homogeneity and on rapid cooling the diffusion of atoms is suppressed, which leads to a non-equilibrium solid solution phase growth. Average size of crystallites obtained in plasma oxidation is about twice that of thermal oxidation indicating fast growth kinetics compared to thermal oxidation. This mechanism was mainly determined *via* speculation and physical observation only and hence hypothetical in nature, so, further experiments (presented in chapter 5) are necessary to either prove or refute this mechanism.

4.3.4 Ternary solid solutions of $NiMn_zFe_{2-z}O_4$ ($0 \leq z \leq 1$)

Ternary spinel oxides comprising manganese substituted nickel ferrite, with nominal series formula $NiMn_zFe_{2-z}O_4$ (where z=0.0, 0.20, 0.40, 0.60, 0.80 and 1.0) have been successfully synthesized by the plasma spray method. The XRD reflections (Figure 4-8(a)) show highly crystalline nanoparticles with exceptional phase purity. Figure 4-8(b) shows an expanded view of (311) peak position. As can be seen, there is a monotonic shift of the 311-peak position to the left with increasing manganese doping, an indication of the formation of a spinel solid solution. The same family of peaks indexed to cubic spinel phase

(sp. gr. *Fd-3m*) appears in all six samples and no foreign peak was observed, an indication that no other phase co-existed with sample phase. The domain size of microstrain were estimated from Williamson-Hill (W-H) plots (Figure A1, Appendix 1) and tabulated as shown in Table 4.1. After a linear fit to the W-H plot, the micro-strain and domain size were extracted from the slope and vertical axis intercept respectively. Results reveal that the strain portion of the W-H plot has no contribution to the line broadening (Figure A1, Appendix 1) except for the sample z=1.0 with negligible microstrain (0.01%) as shown by Table 4.1. The lattice parameters and unit cell volume expand isotropically as the density of the manganese dopant increases, and the crystal size is in the range 500-590 Å. For uniform strain, the unit cell dimensions change in isotropic fashion which leads to changes in the lattice parameters and a shift of the peaks with no accompanying broadening of the XRD reflections. The shape of peaks is unchanged from z =0.0 to z =1.0 which confirms the absence of anisotropic microstrain. Figure 4-8(c) shows a typical EDS spectrum obtained at 0−20 kV, along with peak assignments for Mn, Ni and Fe elements for various compositions ($0 \leq z \leq 1$). The peak areas fairly match the precursor compositions, confirming the formation of ternary solid solutions (Figure 4-8(d)). After integrating the peak areas of Mn-K_α, Ni-K_α, Fe-K_α and Fe-K_β we converted the X-ray counts into the elemental weight percentages using quantification software. The elemental analysis of the nanoparticles confirms that the proportion of the elements is consistent with the precursor composition (Table 4.2). Figure 4-9 shows the XRD patterns and corresponding Rietveld analysis of as-prepared sample $NiMn_{0.2}Fe_{1.8}O_4$, confirming the formation of spinel phases. Rietveld refinement and Bertaut method[230] are used to determine the cation distribution

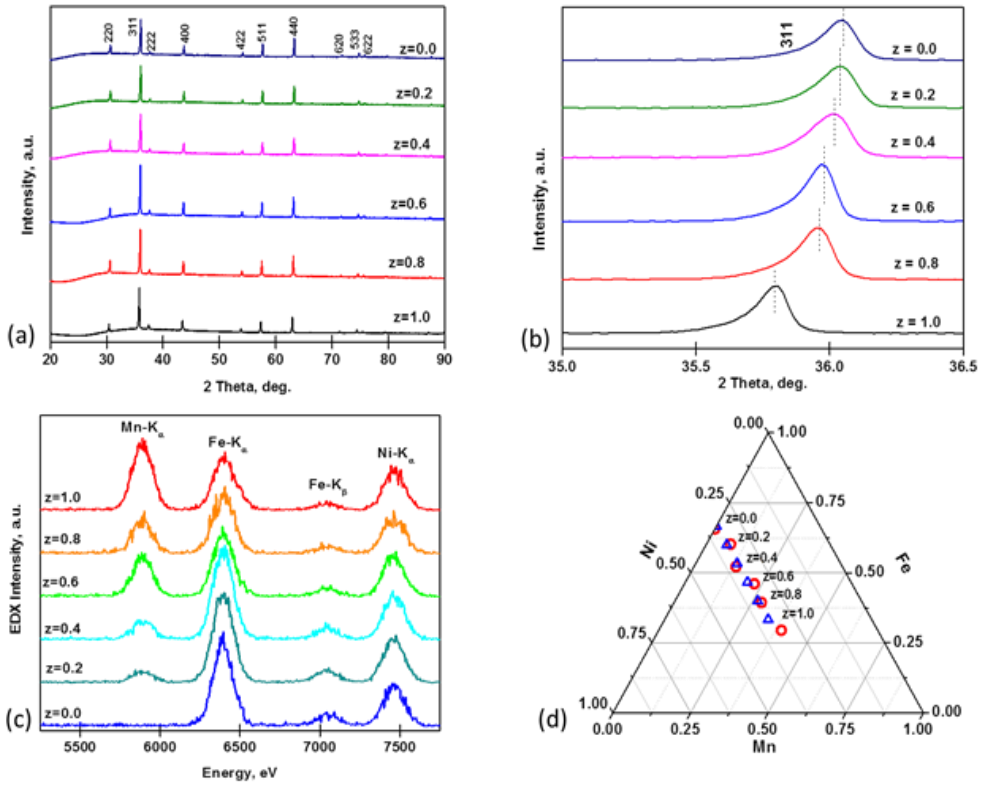

Figure 4-8| (a) X-ray diffraction reflections of ternary spinel oxides comprising manganese substituted nickel ferrite $NiMn_zFe_{2-z}O_4$ ($0 \leq z \leq 1$) showing a single cubic spinel phase (b) Zoom-in of (311) peak position showing a monotonic shift to a lower angle with increasing Mn doping concentration (c) TEM-EDS spectra obtained at 0−20 kV, along with peak assignments for Mn, Ni and Fe elements for various compositions ($0 \leq z \leq 1$). (d) Ternary plot of $NiMn_zFe_{2-z}O_4$ ($0 \leq z \leq 1$) showing an excellent match between the nominal precursor composition (Δ) and the TEM-EDS measured alloy composition (○), in normalized atomic percent.

(Table A2, Appendix 2). Combining the refined results and TEM elemental analysis, the structural formula of $NiMn_{0.2}Fe_{1.8}O_4$ was determined to be $(Ni_{0.1}Mn_{0.15}Fe_{0.75})_{8a}[Ni_{0.9}Mn_{0.05}Fe_{1.05}]_{16d}O_4$, revealing a high degree of inversion in agreement with other results for ferrite spinel[231], where the parenthesis refers to the tetragonal sites while octahedral sites are represented by square brackets. For an AB_2O_4 type spinel, the extent to which sub-lattices are disordered is determined by the inversion parameter *i* which is the fraction of B^{3+} occupying the tetragonal sites, as such *i* can vary from 0, which corresponds to normal spinel and 1, which refers to a structure where all the tetragonal sites are occupied by B^{3+}.

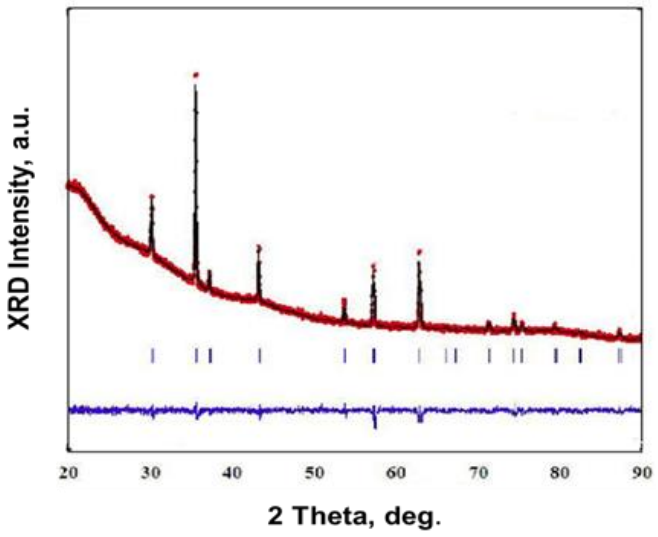

Figure 4-9| Structural analysis of the synthesized nanocrystalline spinels $NiMn_{0.2}Fe_{1.8}O_4$ showing Rietveld refined XRD patterns with experimental data (black line), calculated profiles (red dots), allowed Bragg diffraction positions (vertical bars) and difference curve (blue line).

Table 4.1 Structural parameters of $NiMn_zFe_{2-z}O_4$ ($0.0 \leq z \leq 1.0$) showing how lattice parameter, unit cell volume and anisotropic strain vary υ composition

z	Lattice Parameter (Å)	Cell Volume ($Å^3$)	Domain Size (Å)	Strain %
0.0	8.3347	579.0	590.5	-
0.2	8.3369	579.4	505.6	-
0.4	8.3415	580.4	500.7	-
0.6	8.3528	582.8	587.1	-
0.8	8.3573	583.7	521.5	-
1.0	8.3938	591.4	574.4	0.01

Table 4.2 TEM-EDS analyzed composition of $NiMn_zFe_{2-z}O_4$ ($0.0 \leq \upsilon \leq 1.0$)

	TEM-EDS Analyzed Composition, at. %			
z	O	Mn	Fe	Ni
0.0	61.9 ± 0.7	-	25.1 ± 0.6	13.1 ± 0.5
0.2	61.8 ± 0.4	3.1 ± 0.1	23.6 ± 0.4	12.5 ± 0.3
0.4	61.0 ± 0.4	5.3 ± 0.2	20.4 ± 0.3	13.4 ± 0.3
0.6	58.2 ± 0.5	9.4 ± 0.3	19.3 ± 0.4	13.1 ± 0.4
0.8	57.4 ± 0.4	12.0 ± 0.3	16.8 ± 0.3	13.8 ± 0.3
1.0	55.5 ± 0.5	17.6 ± 0.4	13.1 ± 0.3	13.8 ± 0.3

4.3.5 OER kinetics

A series of $NiMn_zFe_{2-z}O_4$ (z = 0, 0.20, 0.40, 0.60, 0.80 and 1.0) mixed metal oxide films were tested for OER catalysis by studying the cyclic voltammetry at 20 mV/sec scan rate. Two parameters were selected to understand the catalyst performance: (i) overpotential (η) required to reach a current density of 10 $mAcm^{-2}$; (ii) steady state Tafel slope (mV/dec). The data in Figure 4-10(a) shows a decrease in η for OER catalysts with increase in Mn content in the binary metal oxide nickel ferrite. Pure nickel ferrite shows higher overpotential of 0.46 V compared to the ternary metal oxides. Among all the six compositions, z = 0.20 demonstrates the lowest η at 0.39 V. There still remains the challenge of impartially comparing the efficiencies of electrocatalysts, due largely to complications arising from both inadequate standardizations and deviations in average particle size and/or surface areas. It is also notable that the manganese doped ternary metal

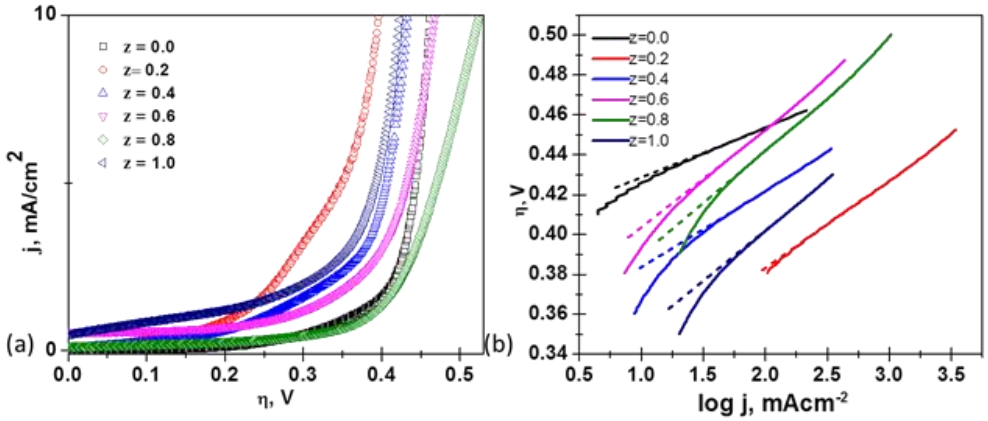

Figure 4-10| (a) Cyclic voltammetry of the conditioned $NiMn_zFe_{2-z}O_4$ ($0 \leq z \leq 1$) films collected in 1 M NaOH solution at a scan rate of 20 mV s^{-1} (b) Steady state Tafel plot for the linear region from 0.35 – 0.50 V.

oxides are more active catalysts than stand-alone NiO_x, FeO_x or MnO_x catalysts. The NiO_x-type catalyst has been previously reported to give 10 mA cm^{-2} at overpotential value of ~ 0.42V [232-233], and the reported overpotential value at current density of 1.0 $mAcm^{-2}$ for FeO_x and MnO_x based catalyst are 0.41 V and 0.51 V respectively[44], which are expected to be at a higher overpotential value when adjusted to the benchmarking current density of 10 $mAcm^{-2}$. Substitution of cations into complex metal oxide crystal lattice has been known to induce oxygen vacancies, and according to Bao et al [234], there is a positive correlation between oxygen vacancy and electrocatalytic activity in OER of nickel-cobalt oxide based catalysts, of which they adduced low H_2O adsorption energy at the defect site to this outcome.

The linear part of the Tafel plots is shown in Figure 4-10(b) obtained for all the six compositions in the overpotential window of η = 0.35 - 0.50 V. The electrodes with lower z value show smaller Tafel slopes less than 45 mV/dec compared to the electrodes with higher content of Mn doping indicating an improvement in the electrocatalytic activity of the catalyst. The data presented in Table 4.3 shows the variation of the overpotential and linear portion of the Tafel slope with composition. The values of the Tafel slope found onthe manganese substituted nickel ferrite solid solutions are comparable to those found elsewhere: $MnFe_{2-x}Cr_xO_4$ (~40mv/dec)[235] and $NiFe_{2-x}Cr_xO_4$ (~40mv/dec)[235]. Strasser and co-workers [236] found through experimental and first principle studies that compressive strain in Pt-Cu solid solution have a strong correlation with its electroactivity in oxygen reduction reaction. Also, the improved activity of the alloy may have been due to the favorable adjustment of the electronic properties of the alloy as a direct effect of the

combination of the completely filled d orbitals (Ni) with semi-filled orbitals (Mn and Fe) according to the Brewer-Engel theory[237].

Besides high catalytic activity, an optimal catalyst material should be stable for their implementation in any operating system. The stability of these catalysts under catalytic conditions was determined using controlled-current electrolysis. The catalyst material was held at a constant current density of 10 mA/cm^2 per geometric area for 2 hours, while the operating potential was measured as a function of time. Figure 4-11 shows the results of the controlled current electrolysis measurements of these catalysts. Clearly,

Table 4.3 Electrode kinetic parameters for the OER of $NiMn_zFe_{2-z}O_4$ ($0.0 \leq z \leq 1.0$) in 1 M NaOH at 298 K

z	η, V @ 10mAcm^{-2}	Tafel slope(0.35-0.50V) mV/dec
0.0	0.46	44.9
0.2	0.39	42.7
0.4	0.43	38.8
0.6	0.46	61.2
0.8	0.45	76.6
1.0	0.42	60.2

η (t=0) and η (t=2h) are similar, an indication that the catalyst is stable under the operating conditions for at least a 2 hours period. The concept of plasma oxidation of precursor solution mentioned here offers excellent metastable phase formation possibilities due to its

fast reaction kinetics and cooling rates. In general, short reaction times allow for the formation of either transient phases in the case of monometal oxides or solid solutions in

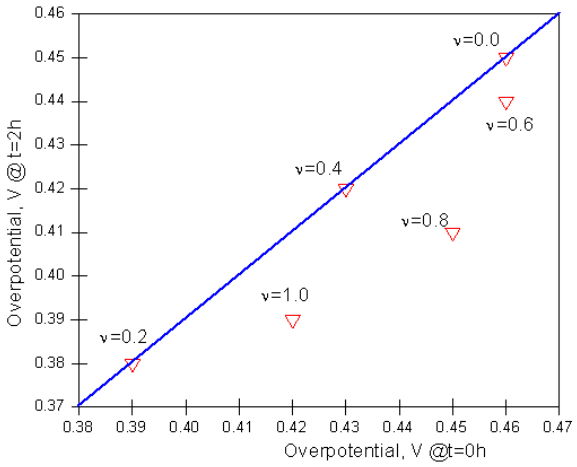

Figure 4-11|Comparison of overpotential values of $NiMn_{\upsilon}Fe_{2-\upsilon}O_4$ ternary alloys before and after 2h stability test.

the case of mixed metal oxides.[238] The process is highly adaptable to any precursor chemical (inorganic and organic, etc.) and any solvent (aqueous, polar, non-polar, organic, etc.) which can be easily incorporated into the spray feedstock. Precursor solution mixtures can be used to produce multi-component systems such as bimetallic and ternary oxides and their solid solutions. Since each droplet contains precursor chemicals in the same stoichiometric composition as desired in the produced particle, the synthesized particles will have exceptional compositional uniformity.

4.4 Chapter Summary

The synthesis technique that can be used to accelerate the discovery of materials for various energy conversion and storage applications is presented. Specifically, this

technique allows a rapid and controlled synthesis of mixed metal oxide particles using plasma oxidation of liquid droplets containing mixed metal precursors. The conventional wet chemical methods for synthesis of multi-metal oxide solid solutions often require time-consuming high pressure and temperature processes, and so the challenge is to develop rapid and scalable techniques with precise compositional control. The concept is demonstrated by synthesizing binary and ternary transition metal oxide solid solutions with control over entire composition range using metal precursor solution droplets oxidized using atmospheric oxygen plasma. The results show the selective formation of metastable spinel and the rocksalt solid solution phases with compositions over the entire range by tuning the metal precursor composition. The synthesized manganese doped nickel ferrite nanoparticles, $NiMn_zFe_{2-z}O_4$ ($0 \leq z \leq 1$), exhibits considerable electrocatalytic activity towards oxygen evolution reaction (OER), achieving an overpotential of 0.39V at a benchmarking current density of 10 $mAcm^{-2}$ for a low manganese content of z = 0.20.

CHAPTER 5

NUCLEATION AND GROWTH OF COMPLEX OXIDES WITH NON-STOICHIOMETRIC COMPOSITIONS DURING PLASMA OXIDATION OF LIQUID PRECURSORS

5.1 Introduction

As detailed in chapter 4, the concept of plasma oxidation of liquid precursors has been demonstrated with composition control of resulting complex oxides. However, the fundamental understanding of the mechanism guiding this process has remained elusive. The ability to control composition in complex oxides cannot be overemphasized as cation ratio is a critical parameter in the performance of these materials in many applications especially solid oxide fuel cells(SOFC)[239-240], catalysis[88, 241], supercapacitance[242-243], and thermoelectricity [244-245]. For example, for La/Mn less than one, the electrical conductivity of $LaMnO_3$ is increased[240, 246] when deployed as SOFC electrodes. It is reported that by inducing about 5% cationic vacancy in $La_{0.95}FeO_{3-\delta}$, an exceptional catalytic bifunctionality was recorded when the material was tested as electrocatalysts in both oxygen evolution reaction (OER) and oxygen reduction reaction (ORR)[88]. Ahuja *et al* concluded that the ratio of Ni/Mn in $Ni_yMn_{1-y}O_x$ affects the supercapacitor electrode performance, with a Ni/Mn ratio of 0.25 giving the optimal performance, with a specific capacitance of ~380 F g^{-1}.

Here, a concept on the use of plasma oxidation involving admixture of aqueous metal precursors will be investigated in this project. The liquid droplets were sprayed into high energy air plasma where they react to form an oxidized solid powder. Earlier studies using plasma oxidation schemes have shown ultra-fast timescales for both molten metals [24] and metal oxides in the presence of alkali salts. Studies involving inductively coupled plasma for droplet-to-particle concept has been successful but only shown with single component systems [25-26].

The main goal of this chapter is to understand the *whys* and the *hows* regarding the plasma rapid action in the conversion of mixed liquid precursors into metastable and solid-solution phases through time-controlled experiments devised to study the evolution of the compositions and phases, and to understand the mechanism of the transfer of heat from plasma to liquid droplets, and how these processes affect materials synthesis from nucleation of the first phase through the evolution of the phases until the ultimate product is formed. It was hypothesized in chapter 4 that reaction kinetics is faster than atomic transportation, and that the transport limited ordering of atoms makes for the evolution of metastable phase nuclei. Then, as the growth proceeds within the transport limited region, the composition of resulting solid solutions depends directly on the composition of elements in the surrounding environment. The composition of the surrounding nutrients is as homogenous and identical to the supersaturation, thus; the growing crystals reflects this compositional homogeneity, and on rapid cooling the diffusion of atoms is suppressed, which leads to a non-equilibrium solid solution phase growth.

5.2 Experimental Procedures

A more detailed report of the plasma synthesis technique is available in in chapter 3. Plasma treatment of the liquid precursors was performed using a homemade atmospheric microwave plasma reactor operated in the batch mode (chapter 3). Chemically pure grades of nickel nitrate hexahydrate (Alfa Aesar) and manganese nitrate tetrahydrate (Alfa Aesar) and lanthanum nitrate hydrate (Alfa Aesar) were used as starting materials without further purification. In another experiment, halides of nickel (nickel chloride hexahydrate, Alfa Aesar) and manganese (manganese chloride hexahydrate, Alfa Aesar) were used instead. Precursors were dissolved in 18 MΩ-cm DI water to a concentration of 0.1 M, and these solutions were mixed as needed to get the desired metal cation stoichiometry. Subsequently, 0.1 mL of the mixed precursor solution was drop-cast and spread onto 2 cm^2 of a quartz substrate (AdValue Technology) which was then exposed to the plasma jet with an input power of 800 W and a volumetric flow of 2 standard liters per minute (slpm) Ar, 11 slpm air, for varying amount of time to obtain a film of material on quartz.

XRD measurement was completed using a Bruker D8 system with a non-monochromated Cu-Kα radiation produced by an X-ray tube operated at 40 kV and 40 mA. The sample XRD patterns were scanned between 20-80° at a scan speed of 4 seconds per step with a step size of 0.02°. Bruker EVA software and powder diffraction file (PDF) were used for phase identification. Surface elemental analysis was performed using XPS with a VG Scientific Multilab 3000 custom-built ultra-high vacuum system with Al-Kα radiation. XPSPEAK 4.1 software was used for peak deconvolution and the XPS data analysis. Room temperature Raman measurements were performed in a backscatter configuration using an

inVia Renishaw microRaman spectrometer, equipped with a 50x objective lens, visible light optics, an 1800 mm^{-1} diffraction grating, and a HeNe laser producing 633 nm excitation wavelength. The silicon peak at 520 cm^{-1}, measured from a standard silicon wafer, was used for the system calibration. (TGA (model SDT Q600 from TA Instruments) was utilized to perform TGA tests on the starting materials. For testing, the materials were placed in the alumina sample pan in the TGA and heat-treated dynamically from room temperature to 1000 °C with a ramp rate of 10 °C/min with an input gas (air) of flowing at 40 mL/min.

5.3 Results and Discussion

The synthesis of two compounds were selected to probe the mechanistic steps involved in the plasma oxidation process. The compounds are off-stoichiometric spinel (nickel manganate) and cation deficient perovskite (lanthanum manganate). These compounds were selected for their wide applications in several processes. In general, nitrate precursors were utilized in study, but to study the effect change in precursor type, more volatile precursors such as halides were also used in the experiments.

5.3.1 Temporal studies on the composition evolution of $Ni_{0.6}Mn_{2.4}O_{4+\delta}$ with plasma oxidation of Ni- and Mn-containing precursors.

The evolution of the phases of the mixed solution precursors containing nickel (II) nitrate hydrate and manganese (II) nitrate hydrate (in molar proportion of Ni/Mn = 1/4) after the exposure to air plasma (plasma power = 800 W) are illustrated in Figure 5-1(a). Evaporation of aqueous solvent was complete in about 4s, yielding an amorphous nutrient of mixed precursor which nourishes the growth of the resulting nuclei. Two seconds later, MnO_2 phase was formed; resulting from the thermal decomposition of manganese(II)

Table 5.1 Evolution of the energy dispersive X-ray spectroscopy (EDS) elemental analysis and phase identification of plasma-processed Ni-Mn nitrate precursor, where L=Liquid, A=Amorphous

Time/s	Elemental Analysis/at. %				Phase			Domain size/Å
	N	O	Mn	Ni	$Ni_{0.6}Mn_{2.4}O_{4+\delta}$	MnO_2	$NiMnO_3$	$Ni_{0.6}Mn_{2.4}O_{4+\delta}$ (311)
2	-	-	-		L	L	L	-
4	12.2	51.5	28.3	8.0	A	A	A	-
6	10.8	53.7	29.4	6.1	no	yes	no	-
8	6.6	52.6	33.4	7.5	no	yes	no	-
10	0	56.6	34.7	8.7	yes	no	yes	159.9
12	0	47.2	42.0	10.8	yes	no	yes	150.1
14	0	33.9	50.8	15.3	yes	no	no	277.9
16	0	55.5	34.3	10.1	yes	no	no	221.4
18	0	48.8	39.8	11.4	yes	no	no	213.4
20	0	50.5	39.3	10.2	yes	no	no	242.7

nitrate hydrate, according to the reaction: $Mn(NO_3)_2 \rightarrow MnO_2 + 2NO_2$, in agreement with the TGA data obtained in Figure 5-1(d) and elsewhere[247-248]. The extended thermogravimetric runs do allow the opportunity of elucidating the thermal process steps

and intermediate product(s) before the final oxide residue is obtained. In similar vein, NiO was formed by the decomposition of nickel nitrate hydrate, though the XRD data did not explicitly indicate the presence of NiO phase. The most probable rationalization of the inability of XRD to detect this phase shall be explained later in this study. Figure 5-1(a) and (c) shows the spinel phase began to evolve in the first 10s and becomes fully developed in 14s, with maximum grain size of the 311 plane obtained in this timeframe (Table 5.1). Despite the large variety of manganese-oxide-based compounds, the Raman spectral features in the high-frequency region of internal vibrations (Figure 5-1(c)) are always assigned to symmetric stretching vibrations of the MnO_6 octahedra (present in both MnO_2 and manganite spinel) with the A_g phonon species for the band above 600 cm^{-1} [249], which appears in the first 6s. Whereas, a second peak centered around 500 cm^{-1} is attributable to the T_{2g} mode related to the Ni-O motion[249], *i.e.* the NiO_4 tetrahedral cation movements in a spinel lattice, which became quite obvious in the first 10s. However, the E_g mode; which is the symmetric bending motion of the oxygen atoms inside the NiO_4 tetrahedron, may have been too weak to be detected in the spectra. This study also reveals the changes in composition as the reaction progresses with the complete elimination of nitrogen after 10s, as illustrated in Table 5.1. The non-isothermal temperatures in TGA allow us to track the changes in the oxidation state of Mn during the thermal process.

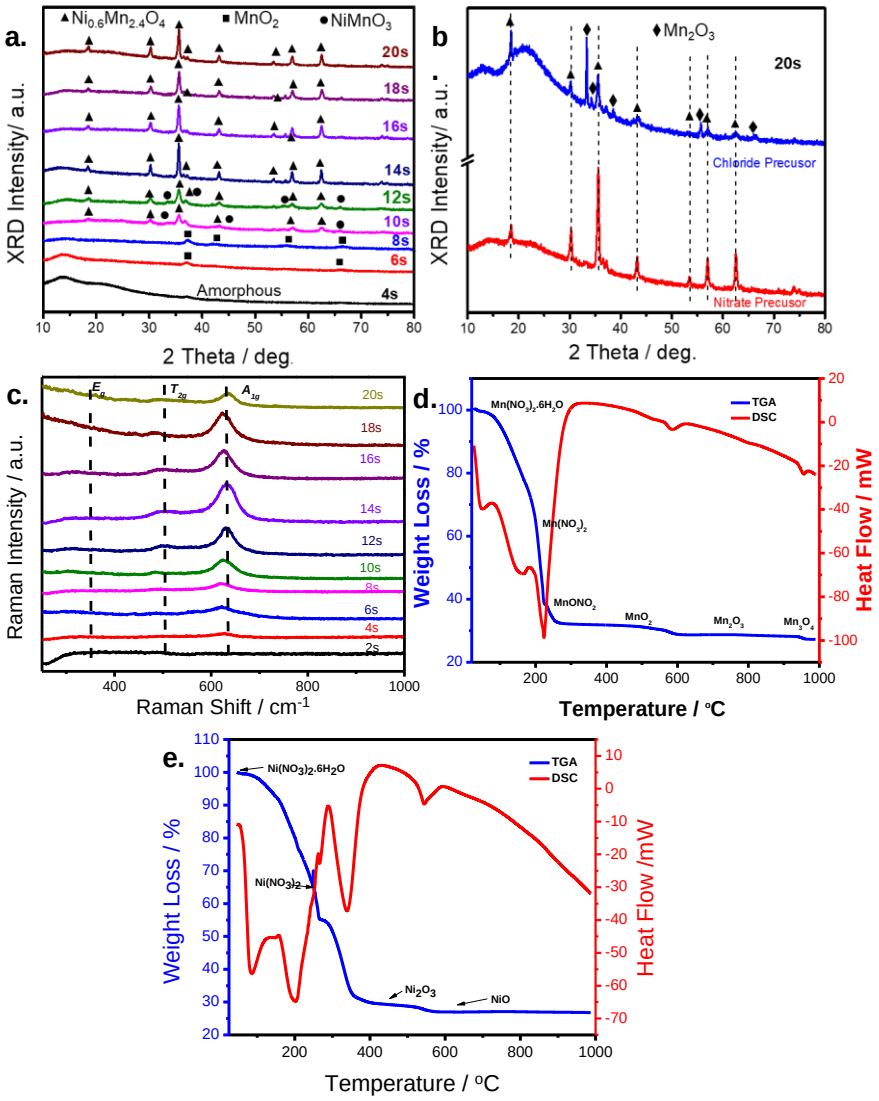

Figure 5-1| (a) XRD showing temporal phase evolution of Ni-Mn nitrate precursor in plasma (b) XRD of Ni-Mn chloride precursor in plasma after 20s (c) Raman spectra showing temporal phase evolution of Ni-Mn nitrate precursor in plasma (d) TGA/DSC of $Mn(NO_3)_2.6H_2O$ at 20°C/min (e) TGA/DSC of $Ni(NO_3)_2.6H_2O$ at 20°C/min

For example, Figure 5-1(d) indicates that Mn transforms from +2 in $Mn(NO_3)_2.6H_2O$ (at 25°C) to +3 in $MnONO_2$ (at 225°C) to +4 in MnO_2 (at 275°C) and back to +3 in Mn_2O_3 (600°C) and ultimately a mixture of +2/+3 in Mn_3O_4(960°C). Similarly, $Ni(NO_3)_2.6H_2O$ changes from +2 to +3 oxidation state of Ni_2O_3 residue at around 400°C, until NiO, with a +2-oxidation number is attained around 600°C (Figure 5-1(e)). It is clear from these steps that the two monometallic oxide residues; NiO and Mn_2O_3 whose solid solutions are responsible for the spinel phase, according to: $NiO + Mn_2O_3 \rightarrow NiMn_2O_4$, are formed around 705°C[250]. Since there are strong evidentiary values from the plasma temporal studies regarding the presence of intermediates such as $NiMnO_3$ and MnO_2, we can speculate that the initial processes in the plasma is similar to the thermal

Table 5.2 Temperature-dependent vapor pressures of Ni and Mn chlorides

Halide	Temperature-dependent vapor pressures of metal halides						
	1 Pa	10 Pa	1 00Pa	1 kPa	10 kPa	100 kPa	Ref.
$MnCl_2$	461°C*	537°C*	633°C*	760°C	933°C	1184°C	Stull [245]
$NiCl_2$	534°C	592°C	662°C	747°C	852°C	985°C	Stull [245]

Values with asterisk (*) were extrapolated using Antoine's equation: $\log_{10}P = A - B/(C+T)$. A, B, C are component specific parameters. P and T are vapor pressure and temperature respectively.

decomposition steps obtained in the TGA. The absence of NiO in XRD may be have been due to either NiO concentration beneath the limit of instrument detection, or the NiO phase evolving faster than it could be tracked within the experimental timeframe. Recall that NiO

is crystallized around 600 °C, and the spinel phase formation was estimated to occur at similar temperature (705 °C), therefore, NiO must have been consumed as soon as they were crystallized.

Despite the non-stoichiometric starting proportions of Ni and Mn, we obtained a single-phase spinel with composition identical to the metal cation composition in the nitrate precursor mixture. However, using chlorides of Ni and Mn as starting materials in the cation ratio of Ni/Mn = 1:4, we obtained a different outcome. According to the XRD data in Figure 5-1(b), it appears stoichiometric spinel ($NiMn_2O_4$) phase was obtained along with segregated Mn_2O_3 phase. It can be suggested from the temperature-dependent vapor pressure data (Table 5.2, Ref.[251]) of these halide precursors that the high volatility and/or the differences in the degree of volatility may play a huge role in the inability to control the stoichiometry of the mixed oxide.

The evolution of surface composition in relation to the bulk is presented in Figure 5.2 (a). There was a substantial deviation from the bulk composition after 6s, with about 6 at. % increase in Mn surface concentration over the bulk composition in 8s. This increase continues until 12s where it reaches a maximum of 8.7 at. % Mn concentration over the bulk level and thereafter drops to 6.8 at. % in 14s. The exact surface conditioning that led to this phenomenon is somewhat unclear, but there is one report suggesting that the migration of Mn^{4+} to the surface may be linked to the high binding energy of Mn^{4+} with oxygen species present in a strongly oxidative environment [252] (plasma in this case). The charge-to-ionic radius ratio of Mn^{4+} is 10.256, which is about twice that of Mn^{3+} (charge-to-ionic radius of 5.172) which comes in second place among Mn^{4+}, Mn^{3+}, Mn^{2+}, Ni^{3+} and Ni^{2+}. Thus, Mn^{4+} produces the most stable monometallic oxide favoring the relaxation to

the minimum total energy of the surface. Noteworthy is the observation that this pronounced deviation from bulk-like constitution of the surface coincides with the exposure time of 8s where considerable polycrystallinity of the sample was first observed in the XRD data of Figure 5-1, showing low-intensity broad diffractograms. The polycrystalline grains formed can become a source or sink for vacancies and other defect chemistries with inherent free energy of formation different than the grains, then the condition of charge neutrality in the bulk may produce a space charge region in the boundaries and surface[253].

There have been several reports on the determination of the chemical state of manganese ions using the Mn2$p_{3/2}$ and Mn2$p_{1/2}$ spectra. For simplicity and clarity, the Mn2$p_{3/2}$ spectra will be the focus of analysis (ignoring Mn2$p_{1/2}$). Figure 5.3 and Table 5.3 shows the evolution of Mn2$p_{3/2}$ XPS spectra of the mixed precursors exposed to air plasma in 6, 8, 10, 12, and 14s. Three distinct deconvoluted spectra (Mn^{2+}: navy blue, Mn^{3+}: magenta and Mn^{4+}: olivine, Figure 5-3) with broad emission lines having a maximum near 643.5 eV, and a minimum close to 639.7 eV were observed for four of them (6, 8, 10 and 12s), whereas; the last sample (14s) had only two fitted peaks at 641.9 and 643.7eV. In general, there was a dramatic shift to lower binding energy, of the sum of the fitted peaks moving from 6 to 8s, and thereafter, a gradual increase in the binding energy from 8 to 14s. This may be rationalized in terms of the decomposition of the metal nitrates into loosely-held intermediates, which give way to nucleation and growth of the spinel compound.

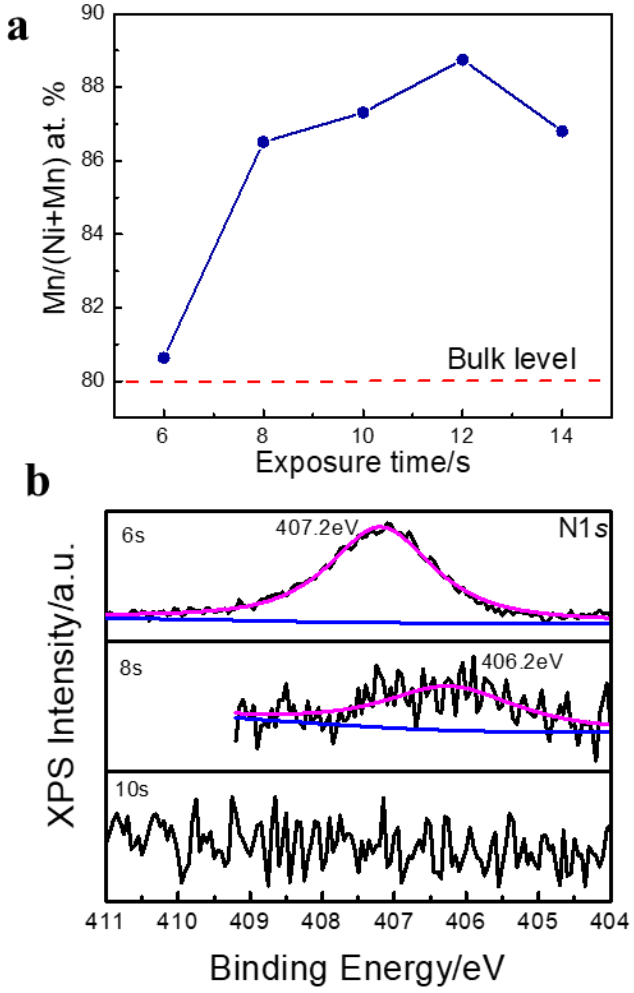

Figure 5-2| (a)Evolution of the XPS spectra of Ni/Mn precursor exposed to air plasma for N1s spectra showing the disappearance of nitrogen in 10s (b) Time-dependent surface concentration of Ni/Mn precursor in relation with the bulk.

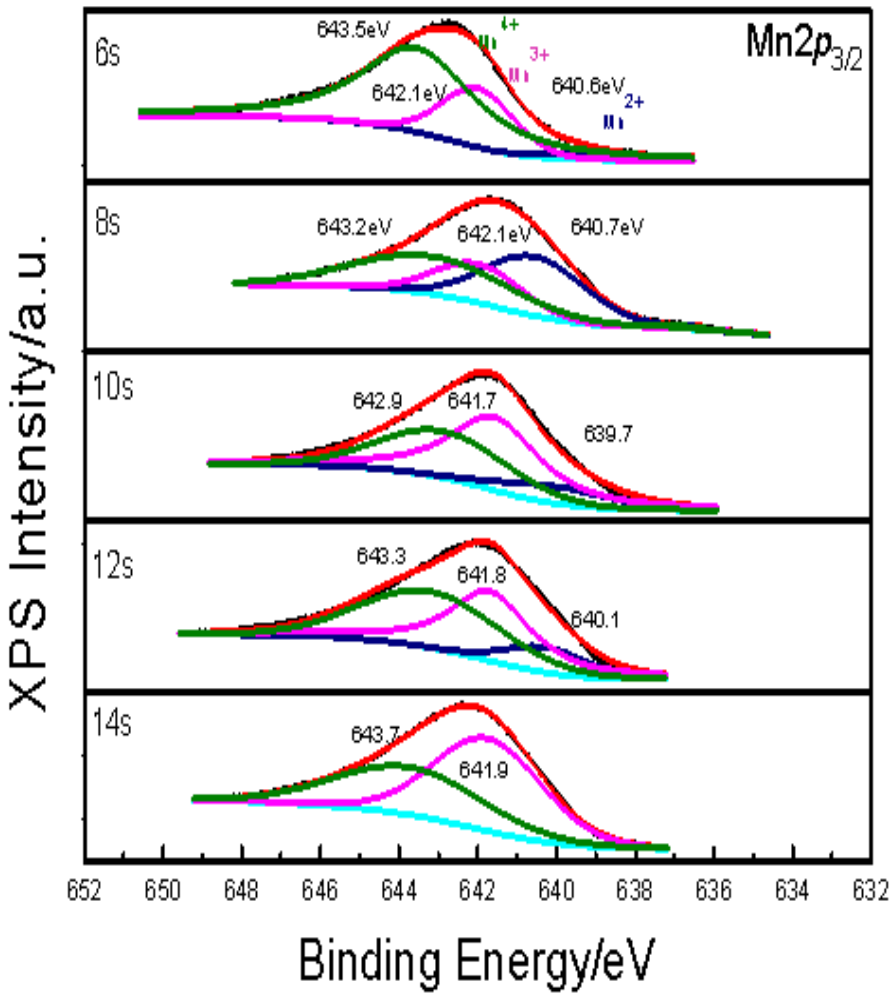

Figure 5-3| Evolution of the Mn2$p_{3/2}$ core-level spectra of Ni/Mn precursor exposed to air plasma.

Many have reported that the Mn2$p_{3/2}$ binding energy of Mn^{2+}, Mn^{3+} and Mn^{4+} ions are in the range 640.2 – 641.6 eV, 641.2 – 642.6eV and 642.3 – 643.8 eV, respectively.[254-255] Peak assignments are tabulated in Table 5.3. One striking feature in these spectra is the emergence of a large Mn^{2+} spectrum in the sample with 8s exposure time, which later reduces in intensity for the samples exposed for 10 and 12s, and the ultimately disappears in 14s. It is not inconceivable to speculate that the Mn^{2+} species formed an intermediate alongside the nitrite or peroxynitrite species characterized earlier in the foregoing paragraph. According to Table 5.3, with an initial high concentration (74%), the concentration of Mn^{4+} was stabilized to 35-41% after 6s, whereas Mn^{2+} showed no time

Table 5.3 XPS data of Mn2$p_{3/2}$ region showing the evolution of the Ni/Mn precursor exposed to air plasma

Exposure Time/s	Binding Energy(FWHM)[a]/eV			Peak Intensity[b]/%		
	Mn^{4+}	Mn^{3+}	Mn^{2+}	I(Mn^{4+})	I(Mn^{3+})	I(Mn^{2+})
6	643.5(3.4)	642.1(2.1)	640.6(3.5)	74.3	22.5	3.1
8	643.2(4.1)	642.1(4.0)	640.7(3.0)	40.4	18.2	41.3
10	642.9(3.8)	641.7(2.7)	639.7(3.3)	34.8	54.2	10.9
12	643.3(4.2)	641.8(2.4)	640.1(2.5)	36.5	48.1	15.4
14	643.7(4.9)	641.9(3.3)	-	40.9	59.1	0

[a] Data in parenthesis represents full width half maximum in eV

[b] Peak intensity refer to the Mn chemical state in percentage of the total peak area

dependence and ultimately vanishes in 14s. Noteworthy is increment in Mn^{3+} concentration with exposure time. Similar binding energy trend was observed for the Ni2$p_{3/2}$ core-level spectra as with Mn2$p_{3/2}$ for the samples exposed to the plasma for 6, 8, 10, 12, and 14s. Initially, there was a high binding energy for sum of the fitted peaks in 6s which swiftly moved dramatically to lower binding energy in the next 2s. Subsequently, a gradual and consistent increase in binding energy was observed until 14s. The final binding energy of the sum of the fitted peaks at 14s was similar to the initial value at 6s. The dramatic shift by about 1.5eV to a lower binding energy might be indicative of perhaps the formation of a metastable or unstable intermediate. As with Mn2$p_{3/2}$, only Ni2$p_{3/2}$ were deconvoluted, as well as the shake-up satellite peaks separated by binding energies ranging from 6.0 – 6.9eV. Two peaks are present in the range 854.4 – 857.6eV (magenta and navy blue, Figure 5-4) and their properties are presented in Table 5.4. The first peak (magenta) which could be found in the range 854.4 – 855.8eV can be assigned to Ni^{2+} while the second peak (navy blue) located between 854.4 – 855.8eV can be assigned to Ni^{3+}. The O1s spectra is shown in Figure 5.5. The first deconvoluted peak (529.4 – 530.8eV, magenta profile, Figure 5-5) can be ascribed to lattice oxygen, the second feature peak (530.8 – 531.9eV, olivine profile, Figure 5-5) is attributable to the adsorbed or trapped oxygen molecule and/or compounds with hydroxyl functional group. The third dominant deconvoluted peak (binding energy of 532.8eV, cyan profile, Figure 5-5), present only in the sample exposed within 6s is due

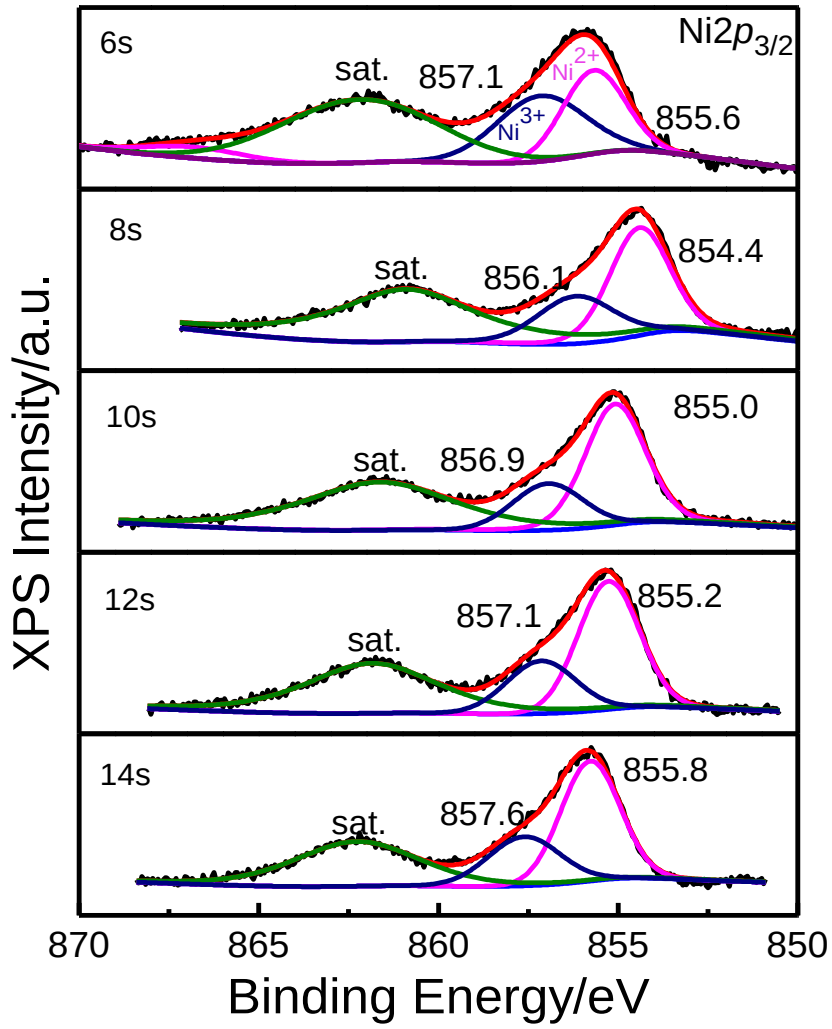

Figure 5-4| Evolution of the Ni2$p_{3/2}$ core-level spectra of Ni/Mn precursor exposed to air plasma.

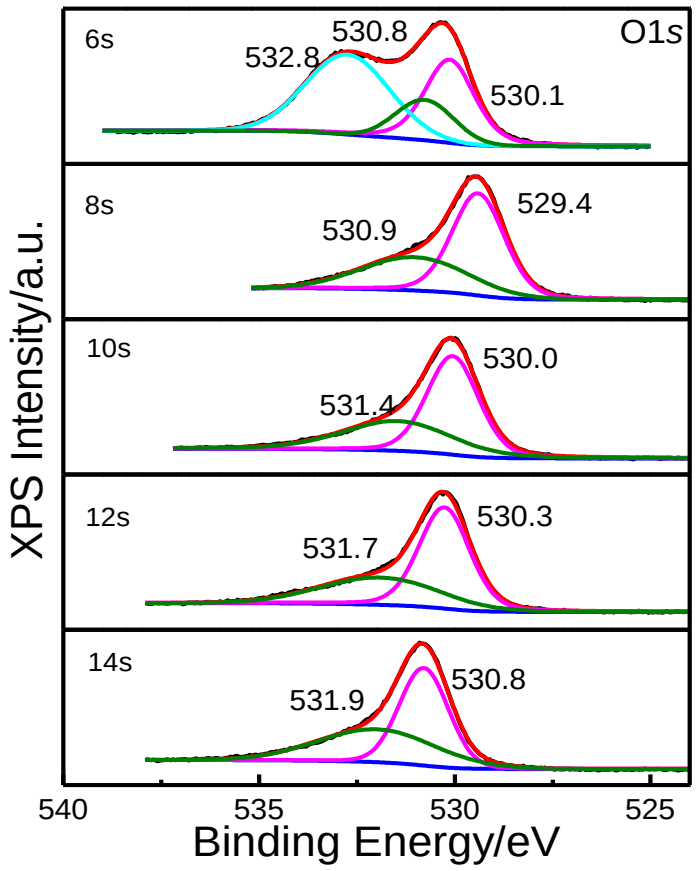

Figure 5-5| Evolution of the O1*s* core-level spectra of Ni/Mn precursor exposed to air plasma.

to O1*s* spectra in nitrate containing salts. This is a clear confirmation that thermal decomposition was incomplete in 6s. Also, the trend reported for both Ni2$p_{3/2}$ and Mn2$p_{3/2}$ continues with O1*s*, with a shift from high to low binding energy going from 6 to 8s, and a consistent shift from low to high binding energy until 14s.

The N1*s* XPS spectra was collected for the samples exposed to the plasma for 6s, 8s and 10s; and the results are shown in Figure 5.2(b). Only three spectra were recorded because the N1*s* spectrum disappears after 10s of exposure in support of the EDS elemental analysis in Table 5.1. The sample exposed in the plasma environment for 6s displayed a high intensity spectrum with a full width half maximum (FWHM) of 1.73eV and a binding energy 407.2eV, 8s of exposure however saw a shift of 1eV to a lower binding energy(406.2eV) with a broader spectrum having FWHM of 2.23eV. The binding energy of 407.2eV matches well with N1s in metal nitrates[256-257] having binding energies ranging from 407.0eV to 407.3eV, however, the binding energy of 406.2eV obtained for the sample with an exposure time of 8s may very well suggest decomposition of the anhydrous nitrate salt may have occurred *via* an intermediate nitrite or peroxynitrite species[258]. The ease with which Mn and Ni nitrates thermally decompose was ascribed to the moderate to high charge densities of Ni^{2+} and Mn^{2+} ions respectively[259]. The high or moderate charge density of the cations pulls toward itself the electronic charge distribution on the nitrate ion, or some of the electronic charge on the nitrate ion are donated to the empty 3*d* orbital of the cation to pave the way for the polarization of the nitrate ion, which in effect weakens the

N-O bond. In the plasma environment, this bond weakening becomes even more severe with the oscillating electric field and the local charge states of the plasma, eliminating any traces of nitrogen-containing species in 10s.

5.3.2 Understanding the role of reactive heating of the plasma species

There are several thermal processes that take place during plasma oxidation. So, it is important to understand the heat transfer processes across the plasma-liquid interphase and their role in the mixed oxide formation. There are many interactions between plasma and liquid droplets, and they include; free electrons, solvated electrons, positive ions and electric field in a plasma system. This section aims to predict the most dominant heat sources among convective, reactive (or recombinative), radiative and electron collisional heating and perform experiments to gauge their influence in the processing of solution precursors into oxides.

The net heat rate required to vaporize a droplet, Q:

$$Q = mc_{pl}(T_0-T_b) - mL_v \qquad 5.1$$

The estimated value of Q is 1.7 x 10^{-4}mJ/s, based on 5μm droplet containing 0.05M of nickel nitrate and manganese nitrate aqueous solution, T_0 is the initial temperature of droplet, L_v is the latent heat of vaporization of droplet, T_b is the boiling point of droplet, c_{pl} is the specific heat capacity of liquid droplet, and m is the mass of droplet. Rate of heat source Q_s is given by:

$$Q_s = a_p h(T_\infty-T_d) + a_p \epsilon\sigma (T_\infty^4 - T_d^4) + \varepsilon + Q_r \qquad 5.2$$

where a_p is the surface area of droplet, T_∞ is the temperature of plasma, T_d is the temperature at the surface of the droplet, ϵ is the emissivity and σ is the Stefan's constant,

5.670×10^{-8} W/m^{2}K^4. The first term on the right-hand side represents convective heating, whereas, the second term represents the heat due to radiative heating from the plasma medium to the surface of the droplet. Heat transfer coefficient (h) is obtained from Nusselt number (Nu) which is given by correlation from Ranz and Marshall[260]:

$$Nu = hD/k = 2 + 0.6Re^{1/2} Pr^{1/3} \qquad 5.3$$

where Re is Reynolds number, Pr is Prandtl number, k is thermal conductivity and D is the diameter of droplet. For the limiting case of creeping flow, where both the droplet and plasma velocity are same, and thus Nu ~2. The electronic collision heating term ε, the third term in Eq. 5.2 is given as a function:

$$f(\varepsilon) = F(\varepsilon)\, \varepsilon^{-1/2} \propto d^2I_p/dV^2 \qquad 5.4$$

Eq. 5.4 is the Druyvestein formula, where f(ε) and F(ε) are the electron energy probability function (EEPF) and electron energy distribution function (EEDF) respectively. The integrated area of the EEDF is used to estimate an average value of ε called $<\varepsilon>$. Electron collisional heating, which scales with $\nu/(\nu^2 + \omega^2)$, is ineffective in microwave plasma because the collision to wave frequency ratio $\nu / \omega << 1$. Here, ν is the electron-neutral collision frequency and ω is the angular frequency (2.45 GHz) of the electromagnetic field. For an electron to collide with a positively charged metal ion, the time it takes to reach the surface ($1/\nu$) should be smaller than the time the surface takes to become negatively charged and repulse the electron ($1/\omega$), due to changing polarity of microwave induced electric field. Using order of magnitude analysis, a 5μm droplet, with $T_\infty = 10^4$K, $T_d = 10^3$K, and ϵ=0.9, the radiative heating is of the order 10^{-2} mJ/s, therefore negligible. Assuming k

= 0.07 J/m-Ks (air), the convective heating becomes 17 mJ/s**.** The last term in Eq. 5.2, Q_r, is the heat release due to these recombination reactions:

$$OH + OH \rightarrow H_2O_2 \quad \Delta H_r(298.15\ K) = -214.6\ kJ/mol$$

$$O + O \rightarrow O_2 \quad \Delta H_r(298.15\ K) = -505.3\ kJ/mol$$

$$H + H \rightarrow H_2 \quad \Delta H_r(298.15\ K) = -444.0\ kJ/mol$$

$$N + N \rightarrow N_2 \quad \Delta H_r(298.15\ K) = -944.9\ kJ/mol$$

Assuming 20 % of the plasma flux are radicals/neutrals, with air flow rate of 10 slpm, for an ideal gas, the molar flow rate is 7.45×10^{-3} mol/s. Also, if the average reactive heat is 1000 kJ/mol, the total reactive heat is then estimated as 1.50×10^{3} mJ/s. These estimated calculations show that the convective and reactive heating are more than sufficient to vaporize the solution until precipitation of oxide. Reactive heating is significantly higher than convective heating, and may play an important role in plasma oxidation, so, experiments were performed to eliminate or perhaps attenuate its contribution using a substrate cooling device illustrated in Figure 5-6(a). The precursor-sprayed substrate is fixed inside a water-cooled device consisting of copper tubes, with the droplet sprayed portion of substrate exposed to the plasma for a period of 14s while flowing cold water through the cooling device in order to extract the recombinative heat released *in situ*. The XRD data shown in Figure 5-6(b) is indicative of an amorphous phase and possible incomplete thermal decomposition of precursor, which is a crucial step in the formation of the spinel oxide. The XPS spectra of N1*s*, O1*s*, Ni2$p_{3/2}$ and Mn2$p_{3/2}$ are shown by Figure 5-6(c-f) for the sample cooled during plasma exposure time of 14s. In general, the spectra

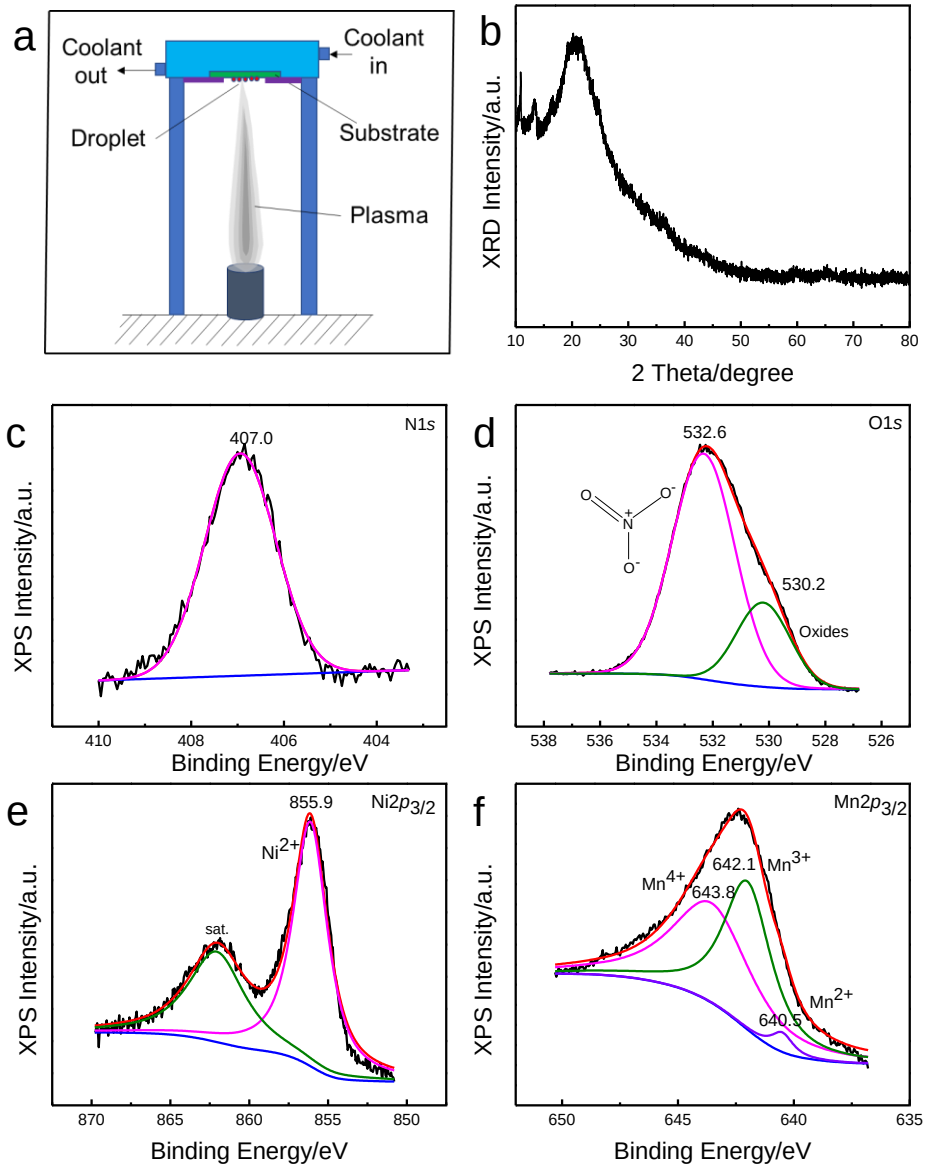

Figure 5-6| (a) Set-up for the in-situ cooling of Ni/Mn precursor during exposure to plasma (b) XRD of the cooled sample with 14s exposure. XPS core-level spectra of water-cooled Ni/Mn precursor with 14s exposure time: (c) N1s (d) O1s (e) $Ni2p_{3/2}$ (f) $Mn2p_{3/2}$

are similar to the spectra of the uncooled samples which were exposed to the plasma for a total of 6s as illustrated by Figure 5-2(a), 8.3, 8.4, and 5.5, with a few exceptions, however. The binding energies of N1*s*, O1*s*, Ni2$p_{3/2}$ (Ni^{2+}) and Mn2$p_{3/2}$ (Mn^{2+}) for the cooled samples are 407.0, 530.2, 855.9 and 640.5eV respectively, while the binding energies of the uncooled samples exposed to the plasma for a total of 6s are 407.2, 530.1, 855.6 and 640.6eV respectively. The major differences between both results are the absence of the adsorbed species from the O1*s* spectra of the cooled sample, also, the peak fitting of the spectra of the cooled sample indicate that Ni^{3+} oxidation state is absent. The presence of N1*s* spectra positioned at a binding energy of 407.0eV confirms our suspicion from earlier that the thermal decomposition of the nitrate was incomplete. The O1*s* spectra clearly indicate that there are two chemical states of oxygen: (1) lattice oxygen from oxides (2) lattice oxygen from NO^{3-}, with the latter making up about 76 at. % of the total oxygen species.

5.3.3 Evolution of non-stoichiometric $La_{0.8}MnO_3$ perovskite

Studies were performed to understand the evolution of non-stoichiometric mixed oxide (perovskite) system with plasma oxidation of liquid precursors. This study was done

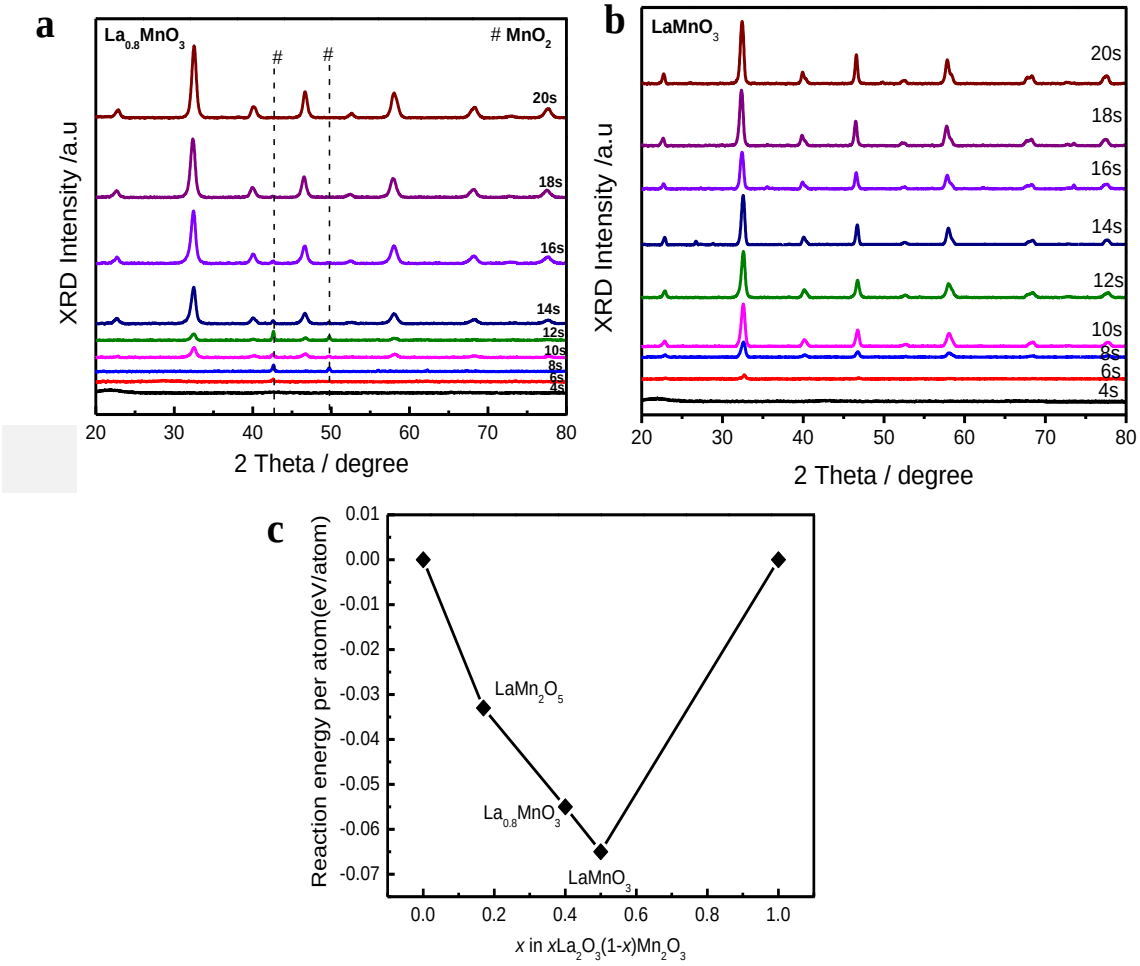

Figure 5-7| XRD showing phase evolution in plasma of (a) La/Mn nitrate precursor in proportion 0.8:1 and (b) La/Mn nitrate precursor in proportion 1:1(c) Reaction formation energy of La_2O_3/Mn_2O_3 alloy system

to understand whether perovskites oxides evolve differently than spinel compounds. Cation-deficient $La_{0.8}MnO_3$ perovskite was prepared *via* similar plasma-based and time-controlled method by varying the plasma exposure times. The XRD patterns (Figure 5-7 (a)) were used to monitor the transitions in the phases per exposure times. As before, an amorphous phase results when the droplets were exposed for 4s. The first detected phase is the ε-MnO_2 (PDF-01-089-5171, hexagonal, space group: $P6_3/mmc$), which appears in the first 6s, and continues to appear until the 12th second. The first detection of the perovskite phase (PDF-01-074-7372, rhombohedral, space group: *R-3c*) occurs after 10s of exposure, with accompanying *ε*-MnO_2 phase. These phase dynamics were identical to the Ni/Mn system in which the spinel phase was nucleated in 10s. While profile of the perovskite peaks is very broad placing the nucleation of perovskite in that timeframe, the manganese (IV) oxide peaks were narrow suggesting fully developed, relatively larger crystals. The MnO_2 peaks disappear after 14s without a trace, also, the increasing narrowness of the 110/104 peaks from 10 – 20s indicated growth of crystal grains. As is the explanation for the inability to detect NiO phase in the XRD data of Ni/Mn system, the absence La_2O_3 phase from the XRD of Figure 5.7(a) may have been due to lanthanum nitrate hexahydrate thermally decomposing to La_2O_3 at around 700°C[261], a higher crystallization temperature than MnO_2 (275°C). So, the crystallization temperature of La_2O_3 is probably close to the solid-state reaction temperature of La_2O_3/Mn_2O_3, consuming La_2O_3 as soon as they were generated.

Surprisingly, when the La/Mn starting proportion was 1:1 or stable/stoichiometric composition, the phase evolution was completely different. The stated hypothesis about the composition of the first nucleated phase mimicking the composition of the surrounding

nutrient seem to be accurate here, as illustrated in the phase dynamics of the XRD data of Figure 5.7 (b). The XRD reflections of the first phase nucleated in 6s was assigned to a perovskite phase (PDF-01-074-7372, rhombohedral, space group: *R-3c*), this very phase was found in the remaining samples with exposure times ranging from 8 – 20s. The data also show increasing crystallite size from 6 – 20s. This is a clear indication of the differences in the nucleation and growth mechanistic steps between the stable and metastable compositions. The reason(s) for these differences is(are) somewhat unclear, but it is suspected that the low-energy available at short times (6 - 12s) before the sample attains steady state temperature in the plasma might just be favorable to nucleate stable phases which require much less energy than the metastable phases, refer to Figure 5.7(c) (computed from Materials Project[212]). So, the mechanism here would not follow solid-state reaction requiring a high-temperature condition to initiate.

5.4 Proposed Nucleation and Growth Mechanism for Complex Oxides and Non-Stoichiometric Compositions

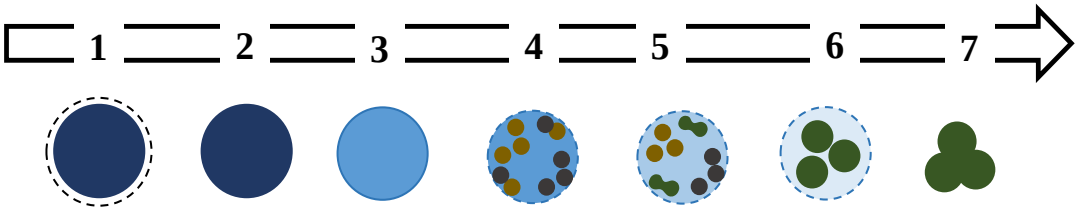

Figure 5-8| Proposed mechanism of plasma-processed nitrate-based precursors. The steps are (1) evaporation precursor solvent (2) amorphous nitrate/nitrite/peroxynitrite phase formation (3) amorphous oxide phase formation (4) nucleation of monometallic oxides (5) alloying of oxides into intermediate compositions (6) growth of alloyed species (7) final non-stoichiometric oxide

The plasma oxidation of precursors is instantaneous due to the fast kinetics resulting from rapid reactive heating of the plasma species. Evidence from experimental study suggests that the synergy from reactive heat and plasma species in (partial) thermal plasmas are necessary for the formation of non-stoichiometric mixed metal oxides. So, a mechanism of plasma-based processing of mixed metal precursors gleaned from the foregoing data is illustrated in Figure 5.8. The plausible steps involve: (1) evaporation of water from droplets containing mixed metal precursors(2) formation of amorphous nitrate/nitrite/peroxynitrite phase (3) formation of amorphous oxide phase (4) nucleation of monometallic oxides through thermal decomposition of part of amorphous oxide phase,

with the heat coming from plasma recombinative heating (5) alloying of nuclei close to each other into stable intermediate compositions (6) growth of alloyed species, so that over time, composition of grains resembles the concentration of the nutrient, and (7) final non-stoichiometric oxide phase. Densification and partial decomposition of the solution precursor will lead to amorphous phase of nitrate, nitrite or peroxynitrite in step 2. It is important to state that these steps may overlap, evidenced by the detection of nitrogen-containing phase in 8s, which is well into step 4 (Figure 5.2(a) and Table 5.1). Nitrogen-containing amorphous species is metamorphosed into a rigid solid constituted by an amorphous metal–oxygen network or amorphous oxide. Evidence for the amorphous oxide phase in step 3 can be found in Figure 5.6(a) showing a partial amorphous oxide phase in O1s spectra of the substrate-cooled oxide film. The slow kinetics in the substrate-cooled sample allow for the resolution of the oxide phase which was undetected in the uncooled sample due to their super-fast kinetics. Although lattice oxygen ascribed to oxides is found in the O1s of the uncooled sample (Figure 5.5) exposed to the plasma for 6s, we cannot say to a high degree of certainty that the portion of those which are amorphous oxide due to the nucleation of nanocrystalline MnO_2 phase in that timeframe.

Plasma could serve as *flux* to enable the crystallization of high temperature phases by improved diffusion of metal elements to help order the randomized metal-oxygen network. Also, the ultraviolet component in the plasma could facilitate photoexcitation, in addition to this, amorphous oxide has a modest absorbance in the ultraviolet range. Photons from plasma could help with bond cleavage, generate active plasma oxidation species like O neutral or ozone or create a conducive milieu to nucleate polycrystalline oxides[262]. Though it was initially hypothesized that the first nuclei would have compositions that is

reflective of the composition of the surrounding nutrient, but counterintuitively, the nucleation of monometallic oxide phase was first noticed, followed by alloying of these phases into more stable bimetallic intermediate phase ($NiMnO_3$) as observed in the Ni/Mn system (step 4). Step 4 is not observable in the La/Mn system probably due to the proximity of the La/Mn starting composition (La/Mn = 0.8:1) to the stable composition (La/Mn = 1:1). This alloying is as a result of the crystals being of very small size, and very close to each other. The nucleation of MnO_2 at short times is supported by the decomposition profile of the TGA data which indicated that the crystallization of MnO_2 is favored at low-temperature (275 °C). By observation and measurement, the steady state temperature of the samples exposed to the plasma is not reached until 15s (red-hot appearance and temperature measurement *via* laser pyrometer), and so, it is expected that at short times, MnO_2 will be crystallized before Mn_2O_3 and Mn_3O_4 in the plasma, which were crystallized in the furnace at 600 °C and 960 °C respectively. Although NiO may have been too small to be detected by XRD or perhaps the lack of detection may have been due to higher crystallization temperature of NiO (600 °C) compared to MnO_2, the detection of the first alloyed phase ($NiMnO_3$) is suggestive of the reaction:

$$Ni^{II}O + Mn^{IV}O_2 \rightarrow NiMnO_3 \; \Delta G(1000\ K) = -9.16 \times 10^5 \text{ kcal mol}^{-1}$$

offering support for the presence of NiO. The computed high negative Gibbs free-energy value shows this reaction is feasible at the suspected reaction temperature. The ramp rate in the plasma is about 3200 °C min^{-1}, reaching steady state temperature of about 800°C in 15s. This is the reference temperature for the low-temperature processing of oxide films by wet-chemical methods[262], but is sufficient for the solid-state reaction herein observed in step 5 as a result of reactants being nanosized and/or the influence super-high plasma ramp

rate and plasma effect mentioned at the beginning of paragraph. Compared to thermal heating coils in conventional furnaces, the heating rates are from 5 – 10 °C min^{-1}, which can go up to 20 °C min^{-1}, and for this reason, the plasma offers much faster kinetics evidenced by the finalization of the non-stoichiometric phase in 14s. The recombinative exothermic heat released from plasma particles is responsible for the exceedingly large heat ramp rate, and the experiment conducted to extract of this heat in order to slow down the kinetics led to the conclusion of a positive effect of this heat in the process. Also, the local bonding environment as indicated by the XPS data shows an increase in Mn^{3+}/Mn^{4+} ratio as the reaction progresses, which were also supported by the TGA data, confirming the chemical state of the spinel manganate. This mechanism is only valid for metastable compositions such as solid solutions or non-stoichiometric compositions.

5.5 Chapter Summary

Series of interrupted experiments were carried out to probe the mechanistic steps involved in the nucleation and growth of non-stoichiometric complex oxides prepared in the plasma. Two non-stoichiometric systems of Ni/Mn and La/Mn were selected, where starting precursors of both systems were dissolved in separate aqueous solution and drops of these solutions were sprayed on an inert substrate and exposed to air plasma for a controlled duration, completed in 20s, using an interrupted interval of 2s. In general, the non-stoichiometric phases were formed in 14s, showing great control of final oxide composition from the precursor composition. However, when the precursor was changed to more volatile compound, this compositional control seems lacking. Back of the envelop estimation suggests convective and reactive heating are the most important sources of heat supply to the precursor, and of these two, reactive heating is the most dominant.

Experiments to isolate reactive heating from the plasma process led to a conclusion that it is vital to the fast kinetics of the plasma oxidation. Evidence suggests initial nuclei is different in composition than the surrounding amorphous oxide nutrient contradicting earlier hypothesis suggesting identical composition. Rather, intermediate monometallic oxide crystalline phases were found, followed by the solid-state alloying of the initially nucleated monometallic oxide phases. Evidence also suggests this mechanism is inoperative for stable compositions. To conclude, the results from this chapter will push forward our understanding of the oxidation mechanisms of solution precursor exposed to partially thermal atmospheric plasmas.

CHAPTER 6

LOW-NOBLE-METAL $W_{1-x}Ir_xO_{3-\delta}$ WATER OXIDATION ELECTROCATALYST *VIA* RAPID PLASMA SYNTHESIS[2]

6.1 Introduction

Renewably-driven water electrolysis may be the most promising pathway for carbon-neutral, sustainable H_2 production.[263-265] The high operating voltage of commercial electrolyzers and corresponding energy loss are largely associated with the sluggish kinetics of water oxidation at the anode.[266-267]The oxygen evolution reaction (OER) (i.e., $2H_2O \rightarrow O_2 + 4H^+ + 4e^-$, in acid) is a kinetically demanding four-electron redox process with even the best catalysts having an overpotential of ~300 mV at 10 mA cm^{-2}, a benchmark current density for use in solar water-splitting.[76]Proton exchange membrane (PEM) electrolyzers, which operate in strong acid, offer a promising way to produce hydrogen of high-grade purity.[268] [269]The advantages of PEM electrolyzers relative to alkaline-based electrolyzers include greater power density, higher efficiency at lower

[2] The texts in this chapter were reproduced with the permission (see appendix 12) of Royal Society of Chemistry. Original article was published as "S. Kumari[§], B. P Ajayi[§], B. Kumar, J. B. Jasinski, M. K. Sunkara, J. M. Spurgeon (2017), A low-noble-metal $W_{1-x}Ir_xO_{3-\delta}$ water oxidation electrocatalyst for acidic media *via* rapid plasma synthesis, Energy & Env. Sci, 10, 2432-2440, https://doi.org/10.1039/C7EE02626A (*[§]Authors contribute equally to this work*)". Formatting styles were amended to adapt original article to the style of this dissertation, and some data from the supporting information in the original article were included in this chapter.

temperatures, and the availability of well-developed membranes with better ionic conductivity, durability, and tolerance to pressure differences.[270] Unfortunately, the high operating potential in a strong acid creates a corrosive environment in which only precious metal oxides have exhibited simultaneously high catalytic activity and stability.

Currently, mixed-metal $IrRuO_x$ nanoparticles are the main OER catalysts used in PEM electrolyzers.[271] Other acid-stable catalyst combinations of platinum group metals have been reported, but these metals are exceedingly rare.[23] Ir is ~10,000 times less abundant than Ni, Co, or W.[272] Even with affordable minimal catalyst loadings, it is unclear if production of these noble metals could be scaled up to meet global energy needs.

A number of effective earth-abundant OER catalysts, including $NiFeO_x$, Co_3O_4, MnO_2, and others,[76, 273-274] have overpotentials comparable to IrO_2 in alkaline conditions, but none are stable in strongly acidic electrolyte.[76, 275] Among other stable oxides for acidic OER, PbO_x has been studied extensively but to date only moderate to high overpotentials have been reported.[276-280] Recently, a F-doped $Cu_{1.5}Mn_{1.5}O_4$ has also shown promise as a water oxidation catalyst in acid.[281] Prior catalysis research has also tried to exploit multimetallic oxides with synergistic properties of the component elements, like the modest-overpotential acid-stable $(Mn\text{-}Co\text{-}Ta\text{-}Sb)O_x$.[282] Some efforts have focused on mixed noble and non-noble metal compositions to achieve acid-stable high activity with minimal noble metal content. Ir has been alloyed with numerous metals to make active acid-stable catalysts, but each of these studies required at least 40 mol. % Ir to be effective.[77, 283-286]

Testing theoretical predictions of new alloys for OER catalysis requires production of a phase-pure composition, which has often been limited by experimental synthesis

techniques. Conventional wet chemical methods such as solution-cast,[287] solvothermal,[288] or sol-gel[289] techniques rely on subsequent heating in air to thermally oxidize the material. The prolonged high-temperature oxidation leads to thermodynamic equilibrium, which can cause phase segregation into species other than the originally targeted composition.[290] In contrast, oxidation in an oxygen plasma is a rapid (~ 1 min) and scalable technique which has been demonstrated to lead to non-equilibrium solid solution phase growth capable of producing homogenous metastable phases.[290] Herein we report plasma-oxidized mixed Ir- and W-metal oxide compositions for OER catalysis. W is an earth-abundant metal with an acid-stable oxide (WO_3)[291] but poor activity for oxygen evolution. Yet with minimal Ir content, plasma-oxidized $W_{1-x}Ir_xO_{3-\delta}$ was acid-stable with promising OER activity.

6.2 Catalyst Synthesis and Electrode Preparation

Plasma oxidation of the liquid precursors was performed using a homemade batch-operated atmospheric microwave plasma flame reactor as described in greater detail in chapter 3. Chemically pure grades of ammonium paratungstate, $(NH_4)_6W_{12}O_{39}\bullet xH_2O$ (Alfa Aesar, 99.9%) and iridium acetate, $Ir(CH_3COO)_n$ (Alfa Aesar, Ir 48-54 wt. %), were used as starting materials without further purification. Precursors were dissolved in 18 MΩ-cm DI water to a concentration of 0.1 M, and these solutions were mixed as needed to get the desired metal cation stoichiometry in mixed-metal oxide compositions. Subsequently, 0.1 mL of the mixed-metal precursor solution was drop-cast and spread onto 2 cm^2 of a fluorine-doped tin-oxide (FTO) coated glass substrate (Hartford Glass, Hartford, CT) which was then exposed to the upstream plasma jet with an input power of 500 W and a volumetric flow of 2 standard liters per minute (slpm) Ar, 11 slpm air, for 90 s to obtain a thin film of catalyst on FTO. FTO-glass and glassy carbon (GC) disks were used as

working electrode substrates for the electrochemical measurements due to their high conductivity and poor electrocatalytic activity for OER. Prior to catalyst deposition, the FTO-glass substrates were cleaned by ultrasonication in an alkaline aqueous washing solution, DI water, ethanol, and then DI water again for 10 min/step. For FTO-glass electrodes, the metal precursor solution was directly cast on the substrate and exposed to the plasma jet to form a thin film of the mixed-metal oxide. For rotating disk electrode (RDE, Pine Instruments) measurements, 5 mm diameter GC disks were sonicated sequentially in pure DI water, acetone, 2-propanol, and then DI water again for 10 min/step. However, because glassy carbon substrates experienced significant degradation if exposed to the plasma jet, direct plasma oxidation of the catalysts on GC disks was not performed. Instead, an established drop-casting protocol for benchmarking nanoparticulate catalysts was used[205] , and well detailed in chapter 3 of this study. Also, an alternative synthesis route was employed to prepare catalyst materials via thermal furnace in order to compare activity performance. TGA experiment described in Appendix 11 was carried out in order to explain the thermal processes of the liquid-gas interfacial reactions and/or thermal decomposition of catalyst sample precursors and to determine the furnace temperature at which crystallization of the respective oxides will occur. A temperature of 500 °C was adopted in synthesis following the TGA results. Materials and electrochemical characterizations details are also already explained in chapter 3 of this dissertation.

6.3 Morphology and Phase Homogeneity

Plasma synthesis can produce variations in structure due to the rapid crystallization and non-equilibrium mixed phase formation, which could have potential consequences for the electrocatalytic behavior of the materials. Electron microscopy showed that there was

Table 6.1 OER catalyst surface area and mass activity data

Catalyst [a]	S_{BET} ($m^2\ g^{-1}$) [b]	Mass activity ($A\ g^{-1}$) @η = 0.3 V [c]
WO_3(P)	3.27	0.0036
IrO_2(P)	5.89	17.4
$W_{0.57}Ir_{0.43}O_{3-\delta}$(P)	6.57	1.46
$W_{0.92}Ir_{0.08}O_{3-\delta}$(P)	11.37	0.077
$W_{0.99}Ir_{0.01}O_{3-\delta}$(P)	3.68	0.220
$W_{0.99}Ir_{0.01}O_{3-\delta}$(T)	8.66	0.014

[a] (P) Plasma oxidized, (T) Thermally oxidized. [b] BET-measured specific surface area per mass of catalyst. [c] Current per total mass of catalyst on the electrode determined at 0.3 V of overpotential, from as-deposited catalyst without optimization for deposition method or mass loading.

strong structural variation in the morphology with the $W_{1-x}Ir_xO_{3-\delta}$ stoichiometry, from a sponge-like microporous structure at x = 0.43 to a smoother layer at x = 0.01 (Figure 6.1) The BET-measured specific surface area per catalyst mass (Table 6.1) consequently did not display a clear trend with Ir content either. Energy dispersive X-ray spectroscopy(EDS) elemental mapping for mixed-metal oxide catalysts showed that W and Ir were uniformly distributed throughout the majority of the sample. Figure 6.2 shows the EDS map for $W_{0.99}Ir_{0.01}O_{3-\delta}$, in which the Ir appears to be evenly distributed with no segregation into concentrated regions. Uniformity of the metal distribution was mostly maintained throughout the phase for compositions with higher percentages of Ir as well, though EDS maps for 8% and 43% Ir samples displayed isolated regions of concentrated W or Ir (Figure 6-3). For the samples investigated, the phase homogeneity depended strongly on the fraction of Ir in the composition. The X-ray diffraction (XRD) data for the plasma-oxidized $W_{1-x}Ir_xO_{3-\delta}$ catalysts indicated that the mixed-metal oxides primarily maintained the triclinic structure of the WO_3, with characteristic peaks for IrO_2 observed at 28º, 35º, and 54º for the x = 0.43 material (Figure 6.4 (a)). This finding was supported for x = 0.43 by Raman spectra showing a faint peak at ~560 cm^{-1} attributed to IrO_2 (Appendix 4, Figure A4) as well as the O1s XPS spectra showing a shoulder with a binding energy at 532.8 eV corresponding to IrO_2 (Appendix 5, Figure A5 (a)). Strong XRD peaks corresponding to metallic Ir were also present for x = 0.43 at 41º, 48º, and 69º (Figure 6-4(a)). However, in decreasing the Ir content to x = 0.08, there was no longer observable IrO_2 in the XRD or

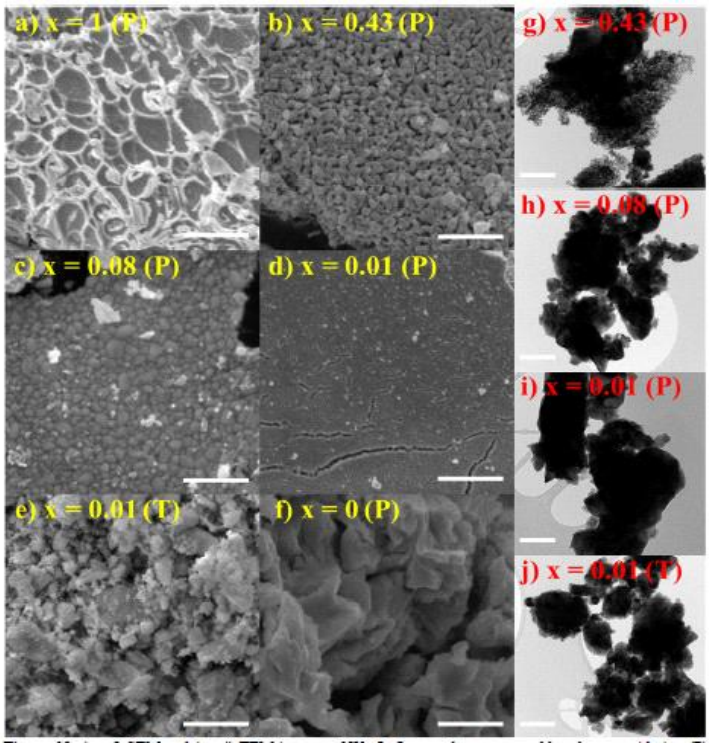

Figure 6-1 | (a – f) SEM and (g – j) TEM images of $W_{1-x}Ir_xO_{3-\delta}$ catalysts prepared by plasma oxidation (P) or by thermal oxidation (T). The scale bar is 5 μm for (a – f) and 100 nm for (g – j).

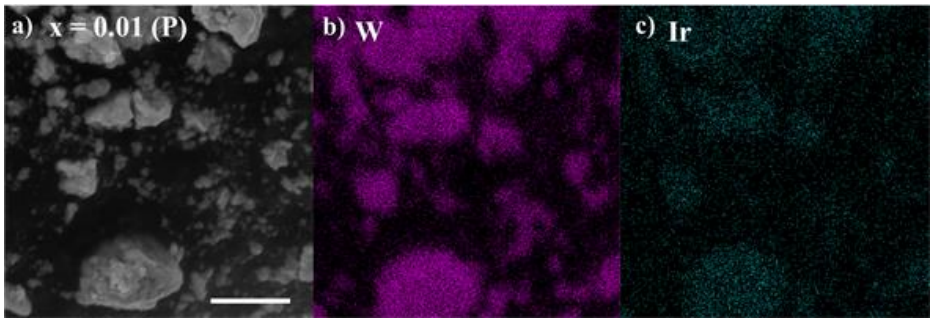

Figure 6-2 | (a) SEM image of the morphology and EDS elemental mapping of (b) W and (c) Ir for ball-milled, plasma-oxidized $W_{0.99}Ir_{0.01}O_{3-\delta}$. The scale bar in (a) is 5 μm

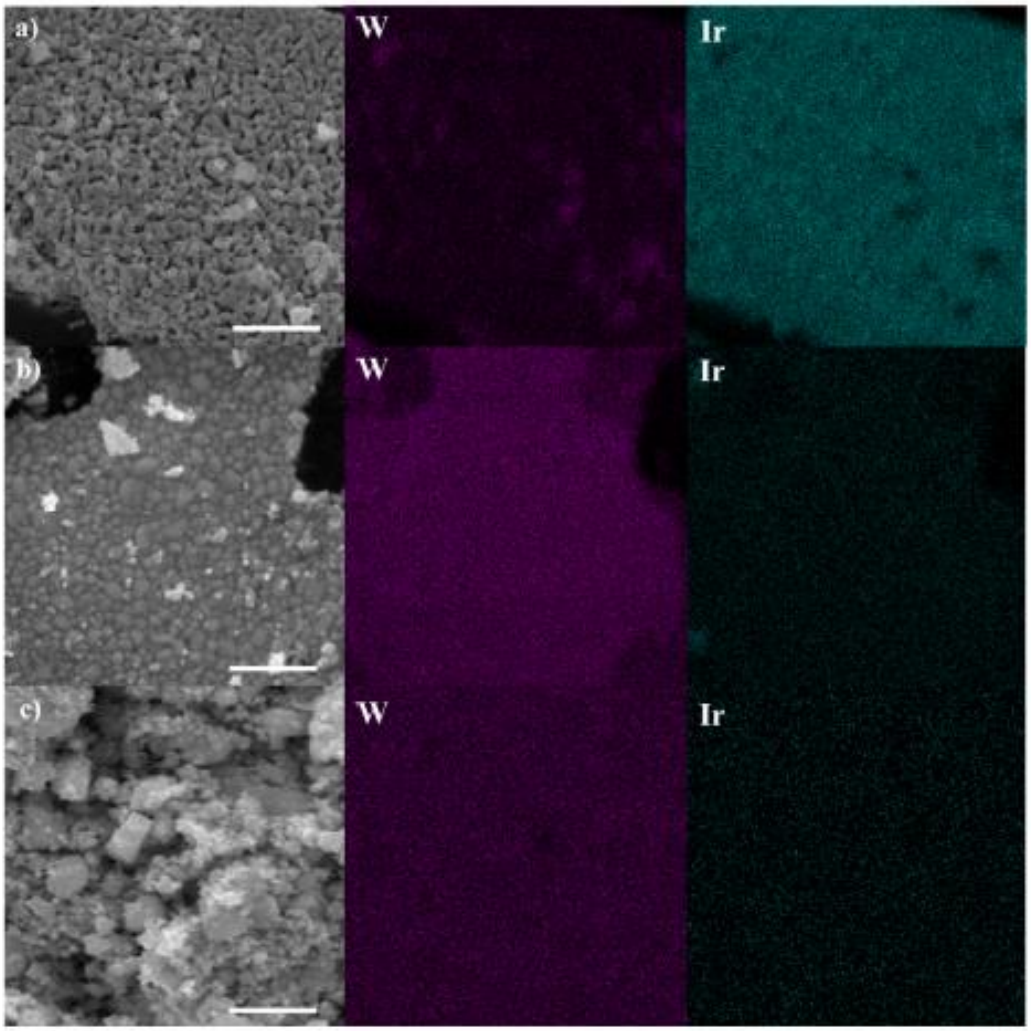

Figure 6-3| (a - c) SEM images of the morphology and EDS elemental mapping of W and Ir for plasma-oxidized samples of (a) $W_{0.57}Ir_{0.43}O_{3-\delta}$ and (b) $W_{0.92}Ir_{0.08}O_{3-\delta}$ and (c) thermally oxidized $W_{0.99}Ir_{0.01}O_{3-\delta}$. The scale bar in (a - c) is 5 μm.

O1s XPS spectra (Appendix, Figure A5 (d)), with only a smaller XRD peak for metallic Ir discernible at 41º. No diffraction peaks for IrO_2 or metallic Ir were observed for x = 0.01,although such peaks may have been below the instrument detection limit. At this low Ir concentration, dispersion of Ir atom in WO_3 lattice is the most efficient, perhaps even create single atom Ir-sites. Single-atom-site catalysis is an increasingly important topic in catalysis[292], and the schematic in Figure 6-4(b) illustrates OER electrolysis based on single

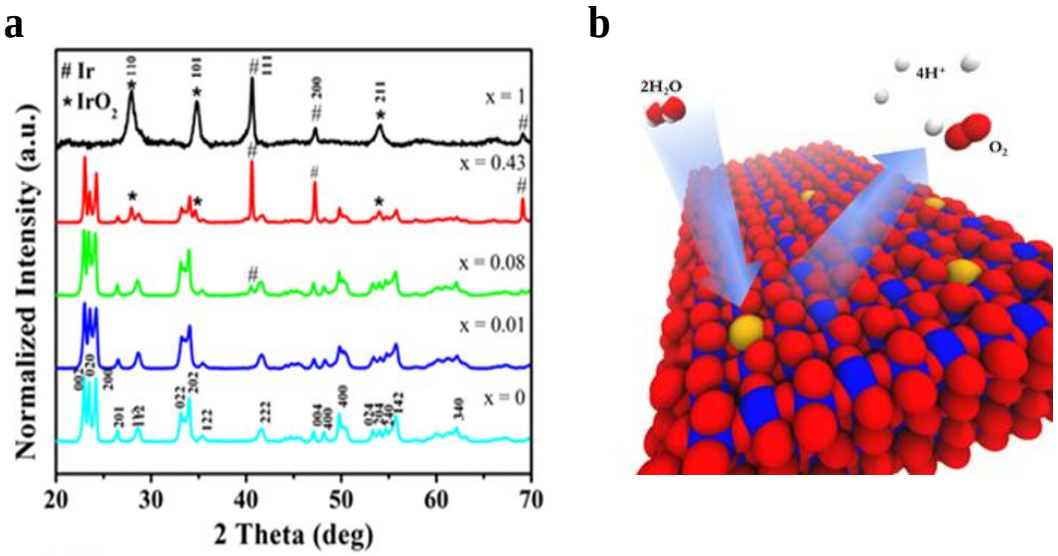

Figure 6-4 | **(a)** XRD data for each type of plasma-synthesized (b) Space-filling model of triclinic structure of $W_{1-x}Ir_xO_{3-\delta}$ in a 3x3x3 supercell, showing OER Ir-active sites, where blue; W atoms, red; O atoms; yellow; Ir and white; protons or H atoms.

atom Ir-site. An XRD Rietveld analysis was employed for phase quantification to estimate the concentration of IrO_2 and metallic Ir observed in nominal compositions with 8% Ir and above (Figure 6-5, and Appendix 6 (Table A6)). Figure 6.5 shows the corresponding Rietveld analysis of the iridium tungsten oxide samples prepared *via* plasma or thermal processes, which confirmed the formation of a triclinic phase. All the reflections in both samples were indexed based on space group $\bar{P}_1$ (no. 2) and coincided with the standard values of triclinic WO_3 [International Center for Diffraction Data (ICDD) PDF card no. 00-020-1323]. The low reliability factor; R_{wp} ($W_{0.99}Ir_{0.01}O_{3-\delta}$-T) = 6.2 %, R_{wp} ($W_{0.99}Ir_{0.01}O_{3-\delta}$-P) = 7.3 %, indicated that the Rietveld refined XRD pattern fit quite well with the experimental data points in spite of the complexities and low symmetry of the triclinic structure, giving calculated cell parameters of $W_{0.99}Ir_{0.01}O_{3-\delta}$ (T) as a = 7.390(2) Å, b = 7.537(1) Å, and c = 7.703(1) Å, while the cell parameters for $W_{0.99}Ir_{0.01}O_{3-\delta}$ (P) were a = 7.329(1) Å, b = 7.518(1) Å, and c = 7.698(1) Å. The a and b lattice parameters were noticeably smaller in $W_{0.99}Ir_{0.01}O_{3-\delta}$ (P), giving it a slightly higher calculated density value of 7.259 g cm^{-3} than the 7.180 g cm^{-3} value for $W_{0.99}Ir_{0.01}O_{3-\delta}$ (T). The rest of the refined parameters are available in Table A6 of Appendix 6.

Figure 6-6 shows high-resolution transmission electron microscope (HR-TEM) images of the $W_{1-x}Ir_xO_{3-\delta}$ catalysts and is consistent with the XRD findings indicating some Ir metal phase segregation. The Ir-rich regions are observable as dark patches in the TEM, which generally correlated with areas of locally enhanced polycrystallinity. This effect was

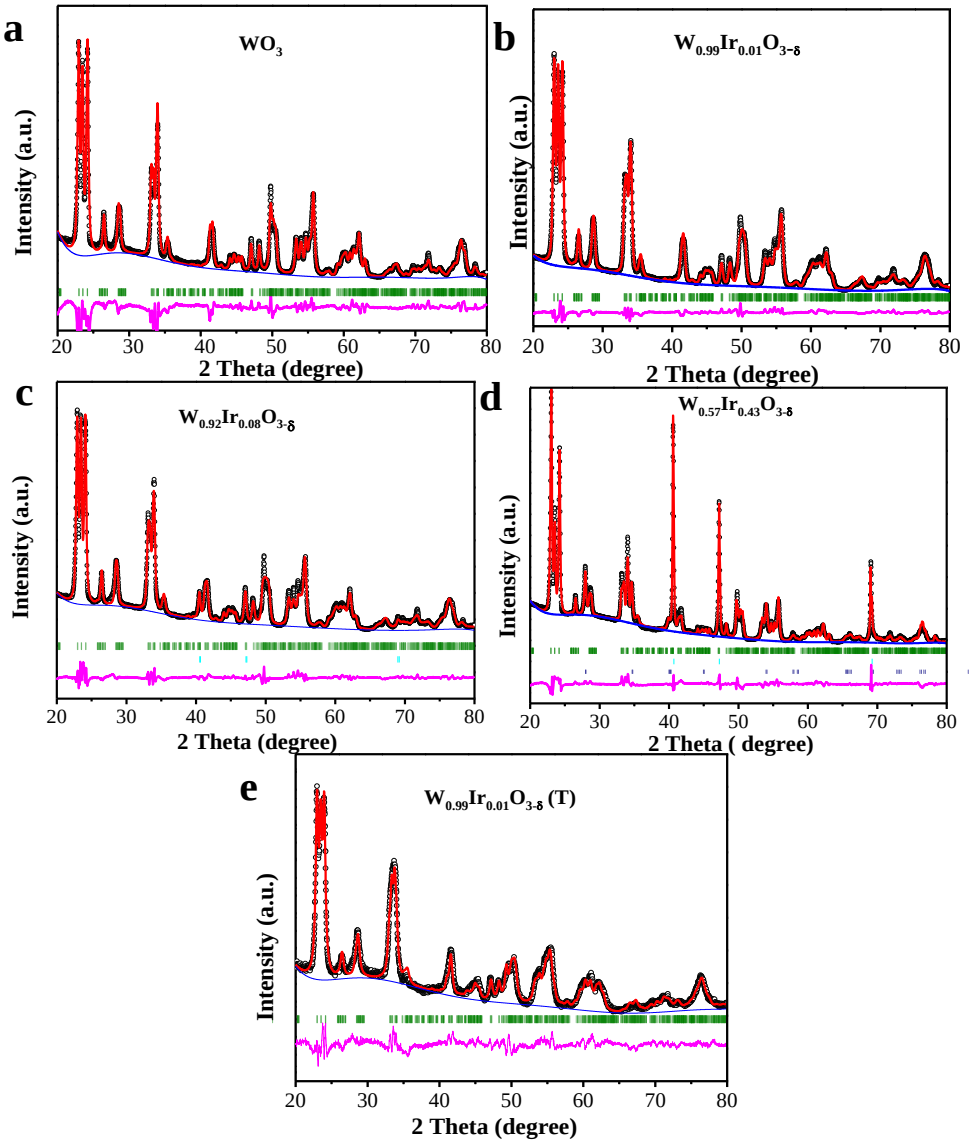

Figure 6-5| XRD Rietveld analysis for plasma-oxidized (P) (a) WO_3, (b) $W_{0.99}Ir_{0.01}O_{3-\delta}$, (c) $W_{0.92}Ir_{0.08}O_{3-\delta}$, and (d) $W_{0.57}Ir_{0.43}O_{3-\delta}$ and thermally oxidized (T) (e) $W_{0.99}Ir_{0.01}O_{3-\delta}$. Black circles mark the observed XRD intensity, the red line is the calculated intensity, the blue line is the background baseline curve, the pink line is the difference between the observed and calculated intensity, and the Bragg lines for the phases are represented by green bars for the single $W_{1-x}Ir_xO_{3-\delta}$ phase, cyan bars for Ir, and purple bars. for IrO_2.

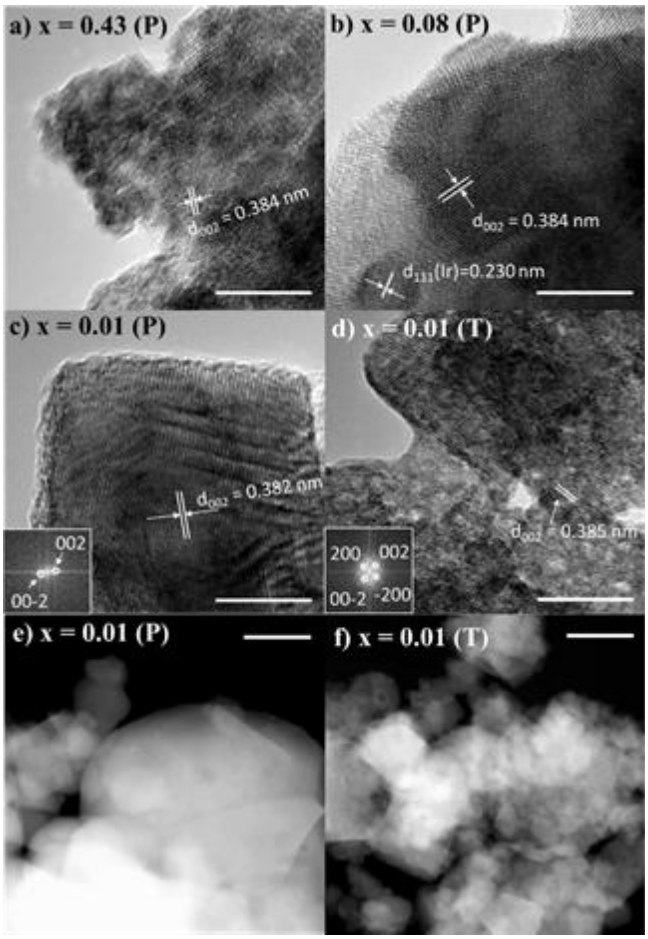

Figure 6-6| (a-d) High-resolution TEM images for the $W_{1-x}Ir_xO_{3-\delta}$ catalyst particles prepared by plasma oxidation (P) or by thermal oxidation (T). The scale bar for (a-d) is 10 nm. Insets show the FFT pattern. (e-f) STEM images for (e) x = 0.01 (P) and (f) x = 0.01 (T). The scale bar for (e-f) is 50 nm

most clearly displayed for $W_{0.57}Ir_{0.43}O_{3-\delta}$, with multiple dark patches and misaligned lattice fringes, whereas the plasma-oxidized $W_{0.99}Ir_{0.01}O_{3-\delta}$ particle was mostly uniform with highly parallel lattice fringes. As shown in Figure 6-6 for each $W_{1-x}Ir_xO_{3-\delta}$ catalyst, the lattice spacing for most of the bulk phase corresponded to a d-spacing of ~3.84 Å, consistent with the (002) planes for a WO_3 crystal. The TEM for the x = 0.08 composition in Figure 6-6(b), however, shows a dark patch with a lattice *d*-spacing of 2.3 Å, which was indexed to Ir (111) and confirmed the presence of Ir metal inclusions. The plasma-oxidized $W_{1-x}Ir_xO_{3-\delta}$ structure thus generally consisted of evenly dispersed Ir throughout the WO_3 phase interspersed with small pockets of Ir-rich metal, as seen further in Figure 6-7 in which additional TEM and EDS mapping specifically targeted regions with Ir-rich clusters. In these maps, the regions with high counts for Ir corresponded to areas with low counts for O, consistent with the presence of metallic Ir inclusions. This data suggests the bulk of each mixed-metal precursor is a phase homogeneous solid solution of $W_{1-x}Ir_xO_{3-\delta}$. However, there is a limit to how much Ir can be favorably incorporated into the WO_3 lattice, and for increasing amounts of Ir beyond 1%, much of it is segregated to Ir and IrO_2 nanoclusters.

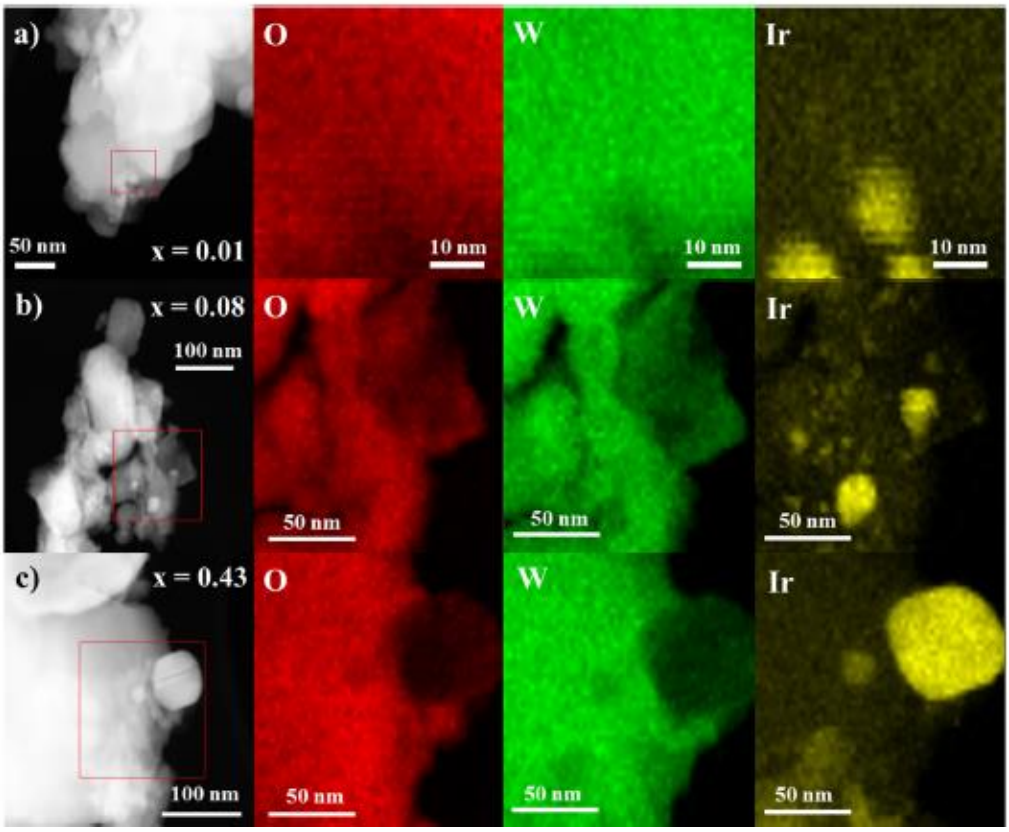

Figure 6-7| TEM images and EDS elemental mapping for O, W and Ir for particles of (a) $W_{0.99}Ir_{0.01}O_{3-\delta}$, (b) $W_{0.92}Ir_{0.08}O_{3-\delta}$, and (c) $W_{0.57}Ir_{0.43}O_{3-\delta}$.

6.4 Electrochemical Performance of Plasma-Oxidized $W_{1-x}Ir_xO_{3-\delta}$

The plasma-oxidized $W_{1-x}Ir_xO_{3-\delta}$ catalyst compositions were made into electrodes and measured as anodes for electrochemical water oxidation in pH 0 aqueous electrolyte (see chapter 3 and section 6.2). Figure 6-8(a) shows the OER current density versus overpotential (*J*-*η*) behavior, with the catalyst activity parameters reported in Table 6.2. The overpotential at 10 mA cm^{-2} projected electrode area was reported in accordance with benchmarking protocol for electrocatalysts for a solar fuels application.[76]

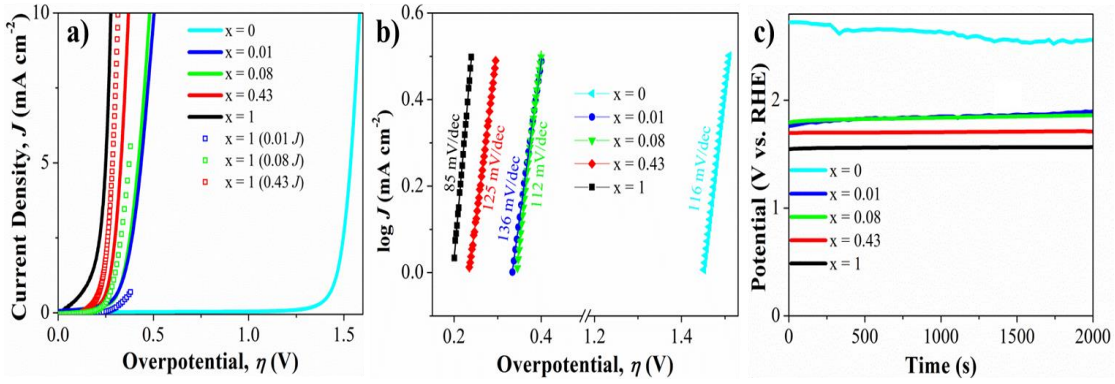

Figure 6-8| The electrochemical characterization for the plasma-synthesized $W_{1-x}Ir_xO_{3-\delta}$ catalysts in 1 M H_2SO_4. (a) OER catalyst current density vs. overpotential (J-η) behavior, with solid lines for performance of catalysts by Ir content x, and data point squares for the current density of IrO_2 (x = 1) scaled relative to the Ir content of the mixed-metal compositions. Overpotential was determined relative to 1.23 V vs. RHE. (b) Tafel plot of the OER catalyst data. (c) Catalyst electrochemical stability for a constant current density of 10 mA cm^{-2}.

The plasma-oxidized IrO_2 (x = 1) had an overpotential of 0.28 V, which puts it on par with literature values for state-of-the-art thermally oxidized IrO_2.[76, 287] On the other

Table 6.2 Comparison of OER catalyst activity.

Catalyst [a]	η @ 10 mA cm^{-2} (V) [b]	Tafel Slope (mV dec^{-1})	TOF_{LB} (s^{-1}) [c] @ η = 0.3 V	TOF_{UB} (s^{-1}) [d] @ η = 0.3 V	$TOF_{LB,Ir}$ (s^{-1}) [e] @ η = 0.3 V	$TOF_{UB,Ir}$ (s^{-1}) [f] @ η = 0.3 V
WO_3 (P)	1.58 ± 0.012	116	$2.2x10^{-6}$	$2.5x10^{-4}$	N/A	N/A
IrO_2 (P)	0.28 ± 0.004	85	$1.0x10^{-2}$	$4.7x10^{-1}$	$1.0x10^{-2}$	$4.7x10^{-1}$
$W_{0.57}Ir_{0.43}O_{3-\delta}$ (P)	0.37 ± 0.002	125	$8.7x10^{-4}$	$4.2x10^{-2}$	$2.0x10^{-3}$	$9.7x10^{-2}$
$W_{0.92}Ir_{0.08}O_{3-\delta}$ (P)	0.48 ± 0.021	112	$4.6x10^{-5}$	$1.5x10^{-3}$	$5.8x10^{-4}$	$1.8x10^{-2}$
$W_{0.99}Ir_{0.01}O_{3-\delta}$ (P)	0.50 ± 0.026	136	$1.3x10^{-4}$	$1.3x10^{-2}$	$1.3x10^{-2}$	$1.3x10^{0}$
$W_{0.99}Ir_{0.01}O_{3-\delta}$(T)	1.07 ± 0.016	301	$8.2x10^{-6}$	$3.5x10^{-4}$	$8.2x10^{-4}$	$3.5x10^{-2}$

[a] (P) Plasma oxidized, (T) Thermally oxidized. [b] Error determined by the standard deviation in measuring three different samples of each type. [c] TOF based on all metal atoms of the catalyst. [d] TOF based on metal atoms at the catalyst surface. [e] TOF based on all Ir atoms of the catalyst. [f] TOF based on Ir atoms at the catalyst surface.

hand, WO_3 (x = 0), devoid of active noble metals, had an overpotential of 1.58 V. Unsurprisingly therefore, higher Ir content mixed-metal catalyst compositions had better overall electrocatalytic performance (Figure 6-8(a)) with lower overpotential (Table 6.2). Nevertheless, with only 1 at.% of the W replaced with Ir atoms during plasma oxidation,

the x = 0.01 composition decreased the overpotential of WO_3 by more than 1 V to η = 0.5 V. In fact, if the current density of the pure IrO_2 (x = 1) electrocatalyst is multiplied by the corresponding x value of the other compositions, the resulting *J*-η behavior outperformed the respective $W_{1-x}Ir_xO_{3-\delta}$ catalyst for x = 0.43 and 0.08 but underperformed for x = 0.01 (Figure 6-8(a)), perhaps indicating greater activity per Ir content for x = 0.01.

Another relevant metric of catalyst activity is the turnover frequency (TOF, defined for OER as the molecules of O_2 generated per metal atom per second), which is included in Table 6.2 for a characteristic overpotential of η = 0.3 V. The method used for calculating TOF is described in Appendix 3. With the uncertainty in the number of metal sites contributing to the reaction, both a lower and an upper bound TOF were calculated. The lower bound turnover frequency (TOF_{LB}) assumed all metal sites contribute to the reaction.[287] The upper bound turnover frequency (TOF_{UB}), in contrast, was approximated assuming that only metal cations at the surface were active reaction sites. The resulting TOF_{LB} for IrO_2 of 0.010 s^{-1} matched well with a similarly calculated TOF for solution-cast thin films of IrO_x,[287] with the calculated TOF_{UB} of IrO_2 increasing to 0.47 s^{-1}. As expected from Figure 6-8(a), the mixed-metal $W_{1-x}Ir_xO_{3-\delta}$ catalysts displayed lower TOF values on a per metal atom basis. However, if the activity is assumed to occur only at the Ir sites and the TOF values are corrected for the reduced Ir content in the mixed-metal oxides, the x = 0.01 composition actually displayed greater lower and upper TOF values than pure IrO_2 (Table 6.2). Figure 6-8(b) shows the Tafel slopes, with the slope for plasma-synthesized IrO_2 (x = 1) of 85 mV dec^{-1} comparable but a bit higher than similar literature values. The plasma-synthesized $W_{1-x}Ir_xO_{3-\delta}$ compositions displayed a distinct increase in the Tafel slope from IrO_2, with values comparable to the slope observed for WO_3 (Table 6.2). This

increased Tafel slope may indicate a shift in reaction mechanism as the lattice becomes dominated by the WO_3 crystal structure and the minimized presence of IrO_2.

The calculated TOF values based on Ir content indicated that only the x = 0.01 composition had higher activity per Ir site than the pure IrO_2 (Table 6.2). From the materials characterization data discussed above, we thus speculate that the phase pure homogeneous $W_{1-x}Ir_xO_{3-\delta}$ solid solution surface had more active OER kinetics per Ir atom while segregation to Ir^0 and IrO_2 phases, particularly as clusters within the catalyst bulk where access to the electrolyte would be hindered, led to a reduced performance on an Ir atom basis. It is also possible that the oxygen deficiency created by balancing charge with Ir^{4+} in the $W_{1-x}Ir_xO_{3-\delta}$ phase leads to oxygen vacancies near the Ir site, with such vacancies reported to contribute to OER activity in metal oxides.[45] Future density functional theory (DFT) modeling of $W_{1-x}Ir_xO_{3-\delta}$ crystal structure and bonding as a function of Ir content on the binding energy with OER intermediates could provide additional insight.

Furthermore, the promising activity with only 1% of the metal sites consisting of Ir was achieved without sacrificing the stability of the material under acidic oxidizing conditions, due to the use of W with its corrosion resistant oxide as the structural support material. The $W_{1-x}Ir_xO_{3-\delta}$ catalyst compositions were evaluated for durability by monitoring the potential during a galvanostatic measurement at 10 mA cm^{-2}, ensuring an equal charge passed per time for each material (Figure 6-8(c)).[76] Using this method, all $W_{1-x}Ir_xO_{3-\delta}$ compositions were measured to be quite stable.

6.5 Plasma vs. Thermally Oxidized $W_{0.99}Ir_{0.01}O_{3-\delta}$

To test if the preparation of the $W_{1-x}Ir_xO_{3-\delta}$ *via* plasma oxidation (P) had a significant effect on the catalyst behavior, the x = 0.01 composition was compared to a material of equivalent stoichiometry prepared with the same precursors via thermal oxidation (T). In the thermal synthesis, furnace temperature was set to 500°C according to the results obtained from the TGA in Appendix 11. Compared to plasma-oxidized material, the thermally oxidized 1 % Ir catalyst showed a rougher microparticulate structure (Figure 6.1 and 6.6). HR-TEM analysis showed larger grain size and higher crystallinity for the plasma-oxidized material (Figure 6-6(c)) compared to the thermally oxidized sample, which exhibited strong contrast variations due to nanoscale polycrystallinity and voids (Figure 6-6(d)). This structural difference is most clearly displayed in the STEM images, in which x = 0.01 (P) particulates showed crystal grains of > 150 nm while x = 0.01 (T) particulates had grains < 50 nm and displayed nanoscopic roughness and porosity (Figure 6-6(e-f)). Figure 6-9 shows the electrochemical and materials characterization comparison between $W_{0.99}Ir_{0.01}O_{3-\delta}$ fabricated by plasma vs. thermal oxidation. Most notably, the same nominal $W_{0.99}Ir_{0.01}O_{3-\delta}$ composition displayed strikingly different electrocatalytic behavior depending on the oxidation method. Thermally oxidized material led to an overpotential of 1.07 V with a high Tafel slope of 301 mV dec^{-1}, compared to 0.50 V and a Tafel slope of 136 mV dec^{-1} when plasma oxidized. The exact structural and chemical differences which lead to strongly enhanced OER activity in plasma relative to thermally oxidized material is somewhat unclear. XRD characterization of the x = 0.01 (T) composition was comparable to the x = 0.01 (P), with all the peaks indexed to the WO_3 phase without any resolvable IrO_2 or Ir peaks within the detection limit (Figure 6-9(c)).

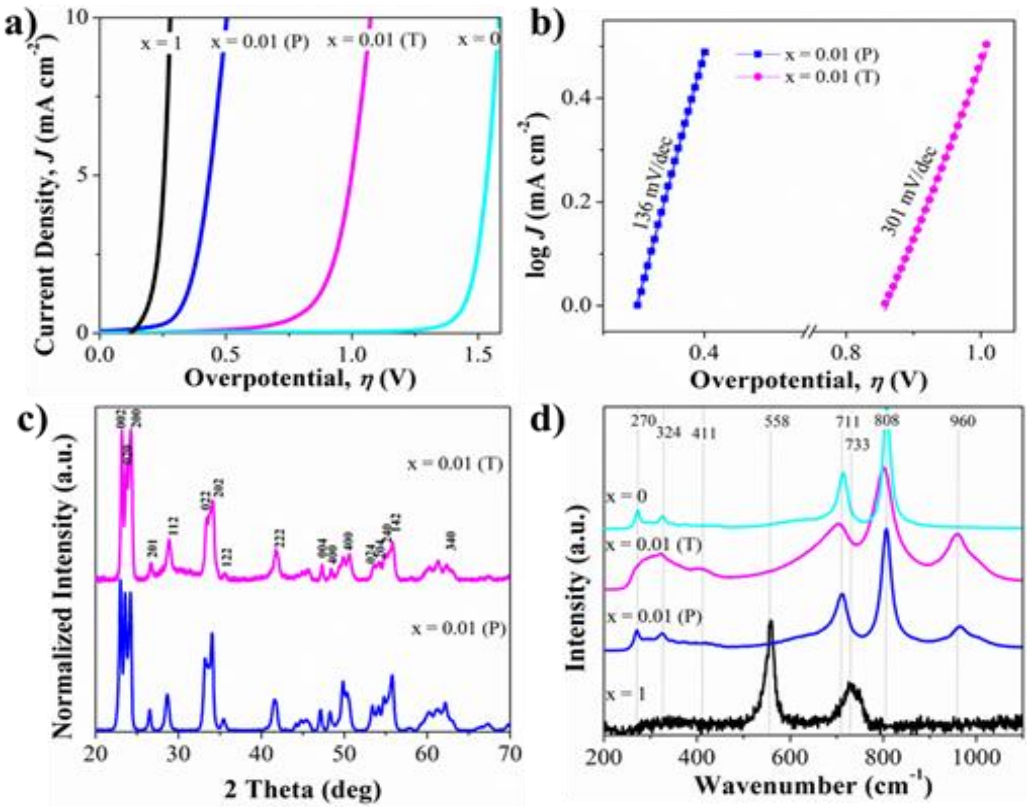

Figure 6-9| Plasma (P) vs. thermally (T) oxidized $W_{0.99}Ir_{0.01}O_{3-\delta}$. (a) OER catalyst current density vs. overpotential (J-η) behavior. Overpotential was determined relative to 1.23 V vs. RHE. (b) Tafel plot of the OER catalyst data. (c) XRD data comparing crystal structure and (d) Raman spectra.

Similarly, Raman spectra for both materials displayed the characteristic WO_3 peaks without the corresponding IrO_2 peaks (Figure 6-9(d)). However, for both x = 0.01 samples there was an additional Raman band peaking at ~960 cm^{-1} not present in either WO_3 or IrO_2, which the literature generally attributes to the ν_s (W=O terminal) symmetric stretching mode.[293-294] This band was present for all the mixed-metal $W_{1-x}Ir_xO_{3-\delta}$ materials (Figure A4, Appendix 4), and similar Raman features have been reported for numerous metal heteropolyoxo tungstate species.[294] This Raman band at ~960 cm^{-1} thus reflects distortion among the tungsten oxide framework and further supports the presence of an iridium polytungstate phase. Also, the noticeable broadening of the Raman bands of the thermal sample relative to the plasma sample has been correlated to greater nanocrystallinity,[295] consistent with the observable nanocrystal domains in the HR-TEM for the x = 0.01 (T) (Figure 6-6).

X-ray photoelectron spectroscopy (XPS) was used to probe the catalyst surface chemical bonding environment, and Figure 6-10 shows the key data with normalized intensity for the ease of peak position comparison. Detailed XPS fitting for the various catalyst types are presented in Appendices 5, 7 and 8. For the O1s orbital, the main peaks at 530 eV and 532.8 eV were attributed to O^{2-} in the WO_3 lattice and IrO_2 lattice, respectively. At a high concentration of Ir (x = 0.43), a distinct shoulder was present at ~533 eV, consistent with the presence of IrO_2 as confirmed by XRD. Although this shoulder was greatly reduced for plasma-oxidized compositions of x = 0.08 and 0.01, it was clearly present for the thermally oxidized x = 0.01 sample. Because no IrO_2 peaks were discernible in the XRD for the x = 0.01 (T) catalyst (Figure 6-9(c)), this phase was either below the XRD detectable limit or restricted to the surface region probed by the XPS.

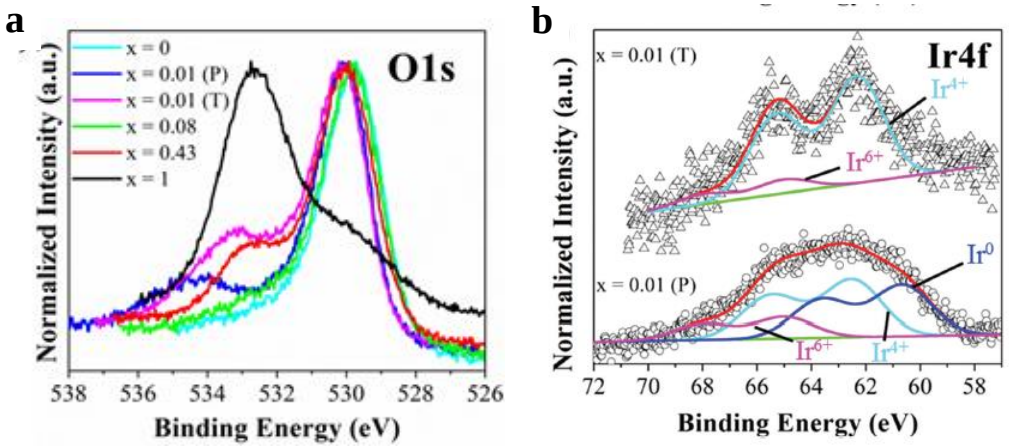

Figure 6-10| XPS spectra of the catalysts for the (a) O1s, and (b) Ir4f peaks for plasma (P) and thermally (T) oxidized $W_{0.99}Ir_{0.01}O_{3-\delta}$.

However, no equivalent IrO_2 O1s peak was present for the x = 0.01 (P), indicating that surface primarily maintained the metastable $W_{1-x}Ir_xO_{3-\delta}$ phase. Spectra for the W4f doublet peaks were comparable for all the catalysts with the W4f7/2 peak at ~35.3 eV, close to literature values for W^{6+} in WO_3 (Figure A7 (Appendix)).[296 297] The Ir4f peaks, in contrast, displayed noticeably different XPS spectra between plasma and thermally oxidized $W_{0.99}Ir_{0.01}O_{3-\delta}$ (Figure 6-10(b)). The Ir4f doublet peak for the x = 0.01 (T) material was well-fit primarily by a single Ir^{4+} peak, while the x = 0.01 (P) Ir4f signal required both Ir^{4+} and a lower binding energy peak to properly fit. The identity of this additional peak is uncertain and could possibly be attributed to either Ir in the mixed-metal polytungstate phase or to trace metallic Ir segregated to the particle surface.

Although it remains uncertain how the exact nature of the structure-function relationship permits dramatic enhancement in the OER catalysis of the plasma-synthesized

compound relative to the thermally synthesized compound, the materials characterization data highlights the physical differences between these forms of $W_{0.99}Ir_{0.01}O_{3-\delta}$ which are likely responsible. Morphologically, the Raman and electron microscopy data indicated that the thermal material consisted of rougher particles with nanocrystalline grains and porosity, in comparison to the smoother plasma material with larger crystal grains. Chemically, although both materials displayed a mixed iridium polytungstate phase of similar crystal structure to WO_3, XPS data indicated that the thermally oxidized catalyst had more segregated IrO_2 domains. Taken together, these observations suggest that the smooth crystalline faces of the metastable $W_{0.99}Ir_{0.01}O_{3-\delta}$ had greater kinetic activity for water oxidation in acid. A more well-developed study focused on theoretically modeling OER at the $W_{1-x}Ir_xO_{3-\delta}$ surface, with crystal models informed by the data reported here, would provide greater insight into how the plasma-synthesized material alters the water oxidation mechanism.

The observed 570 mV difference in the benchmarked overpotential between a plasma vs. thermally oxidized catalyst of the same composition clearly displays the effect that the non-equilibrium reaction and crystallization process can have on a mixed-metal oxide material. Several ambitious research efforts have used combinatorial synthesis and characterization methods to explore the elemental parameter space in search of novel active materials for OER catalysis, with most relying on thermal oxidation to convert the precursors to mixed-metal oxides.[23, 298-299] The plasma vs. thermal oxidation catalyst results herein indicate that such combinatorial efforts could be in danger of bypassing promising materials which may require a metastable phase for high activity.

6.6 Chapter Summary

Acid-based electrolysis has many advantages, but to achieve simultaneous activity and stability, commercial water oxidation catalysts rely on noble metal oxides that are expensive and too rare for the global scale. Here, earth-abundant tungsten was used as a structural metal to dilute the noble metal iridium content while maintaining high activity and stability in acid. Mixed-metal oxide catalysts were synthesized using rapid plasma oxidation in which the non-equilibrium reaction environment permitted better formation of a homogenous $W_{1-x}Ir_xO_{3-\delta}$ phase. With an Ir metal content as low as 1%, a competitive acid-stable overpotential for oxygen evolution was achieved. Relative to high Ir content, low Ir compositions consisted of a more highly crystalline, phase-pure iridium polytungstate which was more catalytically active per Ir content. Moreover, the plasma-synthesized material had a sharp electrocatalytic improvement over an equivalent composition synthesized via standard thermal oxidation, demonstrating the value of non-equilibrium synthesis to find new catalysts.

CHAPTER 7

RELATION OF THE OXYGEN EVOLUTION ACTIVITY WITH OXYGEN *2p* BAND CENTER IN $La_{1-x}Ca_xCo_{0.5}Ni_{0.5}O_{3-\delta}$

7.1 Introduction

Rational design of catalysts through experiment, computation or molecular orbital theory are increasingly becoming more popular than the reliance on intuition and serendipity, as is the traditional practice. Specifically, the OER, $2H_2O \rightarrow 4H^+ + O_2 + 4e^-$ (acidic solution) or $4OH^- \rightarrow 2H_2O + O_2 + 4e^-$ (basic solution) is heavily reliant on efficient electrocatalysts because it is kinetically sluggish and thus constitutes an outlet for efficiency loss and places a significant overpotential requirement in water splitting reactions [39]. Using the plasma oxidation experiments developed in chapter 4 of this dissertation, several compositions of mixed metal oxides can be prepared to understand the correlation of d-band and p-band structure with OER activity. It will allow us to understand and/or verify models for OER activity.

$AA'BB'O_3$ perovskite-type oxides, with transition metal (TM) ions at the BB′-site and rare earth and/or alkaline earth metal occupying the AA′-site, have been studied to understand the interactions of *d*-electrons in the BO_6 octahedra network connected by the apical oxygen atoms with approximately 180° B-O-B bond angle. Specifically, these class of oxides are generating much attention because the degree of freedom to occupy one of the twofold-degenerate e_g orbitals is linked with some interesting physical attributes, such

as the Jahn-Teller effect, orbital ordering, metallicity, ferromagnetism and electrocatalysis [39, 300]. Bockris and Otagawa proposed that the mechanistic model of the catalyst assisted OER in alkaline media, consists of a sequence of reaction intermediates: $S+OH^- \rightarrow S\text{-}OH \rightarrow S\text{-}H_2O_2 \rightarrow S\text{-}O_2H^- \rightarrow O_2$ [13], where the surface active site is denoted by S. As with many other catalytic reactions, the OER can be described qualitatively using the Sabatier principle, also known as a volcano plot, which relates the catalytic activity to the binding energy (BE) of the adsorbed species at the catalyst surface. Since measuring of BE of intermediates is difficult, efforts have intensified to identify other universal OER activity descriptors. Prior studies have suggested several structures and electronic structure-related OER descriptors. For example, the position of the TM *d*-band affects the strength of the TM-oxygen bond on the surface seems to correlate with the OER activity. Similarly, near surface oxygen ions are also important due to the strong hybridization of the O-*2p* and TM-*3d* states and high bond covalency. Both the catalytic activity and stability seems to depend on the bond covalency and on the location of the hybridized states. In the case of perovskite oxides, TM-*3d* states undergo splitting in the crystal field and hybridize with the O-*2p* states, which give rise to e_g (σ-bonded) and t_{2g} (π -bonded) states. Both the position of these hybridized states and their relative occupancy affect the electronic structure and indirectly the catalytic activity. Fundamental properties of the TM ions, such as the number of *d*-electrons, electronegativity, and ionic number, are also potential descriptors. In fact, the OER activity has been correlated with the number of *3d*-electrons for some perovskite oxides[13]. In this work, the BB′-site *d*-band electron occupation was correlated with OER activity for the perovskite molecules with Ni, Co, Fe, Mn, Cr, and V as BB′-site cations. The OER current density at a given overpotential was found to increase with the number

of *d*-electrons, in the following order V < Cr < Mn < Fe < Co < Ni. This linear dependency of the *d*-electron filling is substantially related to the bonding strength of the intermediate with the active B-site. Conversely, Dowden et al [301] published a paper that accounts for the filling of the degenerate e_g and t_{2g} orbitals with increasing *d*-electrons, which gives a non-linear, or more specifically M shaped dependency of the bonding strength of the intermediate to the number of *d*-electrons. Strong bonding exists at d^3 and d^8, whereas, the weak bonding at d^0, d^5 and d^{10} form the minimums. The crystal field stabilization energy which has been well linked to the e_g/t_{2g} occupation[301] has been one of the most important descriptors for the activation barriers in catalytic reactions to date. In furtherance of this concept, Suntivich et al[39] found that, for the σ*-orbital (e_g) occupation, an e_g-filling close to 1 could be correlated to maximal activity. The optimum e_g-filling of ~1 was found for $Ba_{0.5}Sr_{0.5}Co_{0.8}Fe_{0.2}O_{3-\delta,}$ while perovskites such as $LaNiO_3$ and $LaCoO_3$ with e_g filling less than 1 shows some weak activity performance, also; electrocatalysts such as $La_{0.5}Ca_{0.5}CoO_{3-\delta}$ and $LaMn_{0.5}Ni_{0.5}O_3$ with e_g filling above 1 are not sufficiently active towards OER. This poor performance was attributed to the too strong ($e_g < 1$) and too weak ($e_g > 1$) TM−oxygen covalent bonding, suggesting that a peak activity is achieved at a balanced (neither too strong nor too weak) bond strength. Unfortunately, the different spin states of TM ions have made the estimation of the e_g filling of complex oxides to be extremely difficult, even with the spectroscopy and computational techniques [79], as such; extrapolations and conjectures based on oxides with well-known e_g states have been employed to give estimates in some cases[39], [39]. So, researchers are actively working on alternative descriptors which will allow for an uncomplicated design and prediction of active oxygen evolution electrocatalysts.

Some theoretical studies have also suggested the importance of the TM valency[302] and position of the O-*2p* center [209]. This latter parameter seems also to affect the catalyst stability: The calculations indicate that moving the O-*2p* center closer to the Fermi level increases OER activity but having it too close decreases oxide stability due to decrease of the oxygen vacancy formation energy. The oxide energy band gap and location of the Fermi level may also affect the stability. For oxides with large band gaps, the inherent OER related formation of oxygen vacancies, which are double electron donors, may be suppressed and corrosive decompositions may occur. These investigations were done with Mott-Hubbard insulator type oxides where the 3*d*-bands are split by Coulombic force into upper and lower Hubbard bands which results into the insulating character of most oxides. Charge transfer insulators, on the other hand, have received little to no attention as per the correlation of its catalytic character with either molecular orbital theory or the DFT computations. In charge transfer insulators, splitting of 3*d*-band into the upper and lower Hubbard bands is sufficiently great, in fact, large enough to have the O-*2p* band center positioned between them. It is imperative to note at this juncture that the term "insulators" herein refer to either a good or a bad conductor at a given temperature, because; at a finite temperature (T > 0 kelvin), say the room temperature, both metals and insulators exhibit finite DC conductivity.[303]

Here, we present with DFT computations and experimental validation, the successful correlation of the position of the center of mass of the O-*2p* band in the total density of states and the catalyst performance for the charge transfer type complex oxides for the first time. Experimental samples comprise of lanthanum based double perovskites, $La_{1-x}Ca_xCo_{0.5}Ni_{0.5}O_{3-\delta}$ ($0.0 \leq x \leq 0.3$) prepared by the atmospheric microwave plasma

oxidation of liquid droplets of metal precursors, which has shown to be an efficient electrocatalyst in OER. The concept of plasma oxidation of precursor solution mentioned here offers excellent metastable phase formation possibilities due to its fast reaction kinetics and cooling rates[290]. In general, short reaction times allow for the formation of either transient phases in the case of monometallic oxides or solid solutions in the case of mixed metal oxides[238]. The process is highly adaptable to any precursor chemical (inorganic and organic, etc.) and any solvent (aqueous, polar, non-polar, organic, etc.) which can be easily incorporated into the spray feedstock. Precursor solution mixtures can be used to produce multi-component systems such as bimetallic and ternary oxides and their solid solutions in ultra-fast timescales (14 s to 1 minute). Since each droplet contains precursor chemicals in the same stoichiometric composition as desired in the produced particle, the synthesized particles will have exceptional compositional uniformity.

7.2 Synthesis, Electrode Preparation, Electroanalytical and Materials Characterizations and Computational Procedures.

A well detailed description of the custom-made atmospheric microwave plasma set-up used in this synthesis is available in chapter 3. The electrodes were prepared by depositing thin film of perovskite oxide directly on it by using the atmospheric plasma jet (batch operation). The precursor solutions were prepared using mixtures of lanthanum, calcium, nickel and cobalt nitrates in desired proportion. Chemically pure grade of calcium nitrate tetrahydrate, nickel (II) nitrate hexahydrate, lanthanum (III) nitrate hexahydrate, and cobalt (III) nitrate hexahydrate (>99%, Sigma Aldrich) were used as starting materials without further purification. Appropriate amount of the precursors was weighed out and dissolved in deionized water to make up 1.0 M solution. About ~0.1ml of prepared metal

precursor solution was sprayed onto 2 cm^2 fluorine-doped tin-oxide (FTO) coated glass substrates (Sigma Aldrich) which were exposed to the upstream plasma jet with an input power of 500 W and a volumetric flow of 2 slpm (standard liters per minute) Ar, 11 slpm air, for 30. The electrochemical and materials characterization were performed according to the procedures in chapter 3. DFT calculations were completed based on the computational procedures from chapter 3.

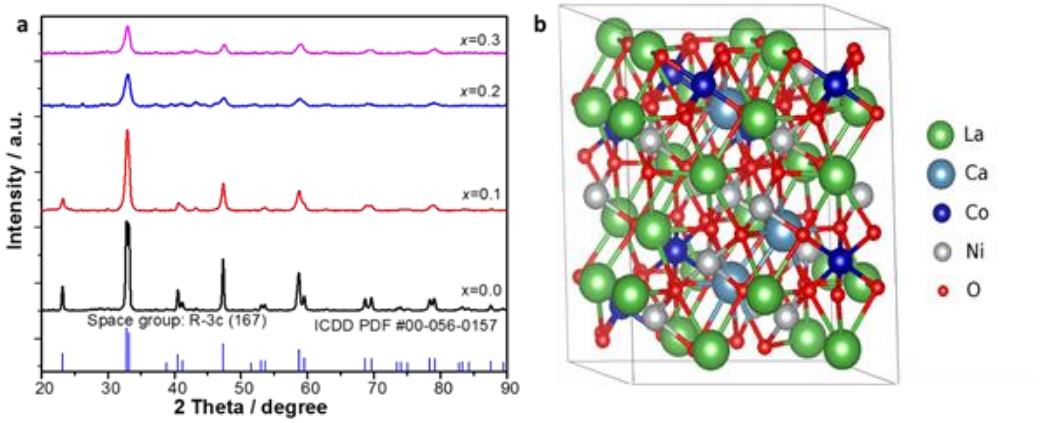

Figure 7-1| (a) X-ray diffraction of $La_{1-x}Ca_xCo_{0.5}Ni_{0.5}O_{3-\delta}$ for x=0.0, 0.1, 0.2 and 0.3, indexed to rhombohedral phase with space group $R\bar{3}c$(ICDD PDF #00-056-0157) (b) Ball and stick model of the $La_{1-x}Ca_xCo_{0.5}Ni_{0.5}O_{3-\delta}$ 120 atom supercell with x = 2/24, optimized using DFT simulations, La atom is green, Ca is light blue, Ni is grey, Co – dark blue while oxygen atom is red.

7.3 Results

7.3.1 Crystal phase analysis

Powder XRD measurements (Figure 7-1(a)) using CuKα radiation shows that the samples are single phase with a rhombohedral unit cell, and all the detected diffraction peaks were consistent with the space group $R\bar{3}c$, No. 167 (ICDD PDF # 00-056-0157).

Figure 7-2 shows the XRD patterns and corresponding Rietveld analysis of as-prepared samples confirming the formation of rhombohedral phases. The table showing

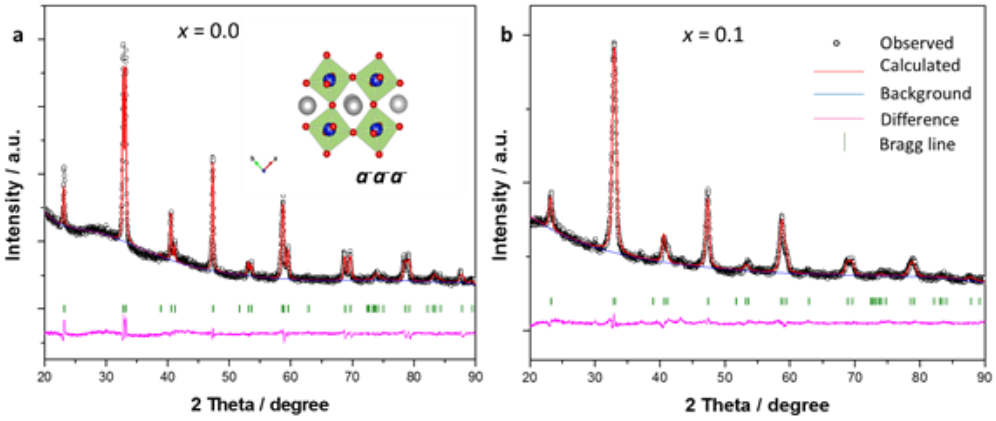

Figure 7-2| Rietveld plots for $La_{1-x}Ca_xCo_{0.5}Ni_{0.5}O_{3-\delta}$ (a) x = 0.0 and (b) x = 0.1. The calculated pattern is shown by a red solid curve; black open circles show the observed intensities. The difference between the observed and calculated intensities is presented by a pink curve. The short vertical bars indicate the position of Bragg lines. The inset of (a) shows a polyhedral structure of $La_{1-x}Ca_xCo_{0.5}Ni_{0.5}O_{3-\delta}$ viewed from the c-direction with the $a^-a^-a^-$ tilt system, where blue : Co, Ni atoms, grey : La, Ca atoms and red : O atoms.

the calculated parameters and the fitting quality is displayed in Table 7.1. The low reliability factor indicated that the Rietveld refined XRD pattern fitted quite well with the experimental data points, giving calculated cell parameters for composition $x = 0.0$ to be $a = b = 5.4677(3)$ Å and $c = 13.1722(9)$ Å. Lattice parameters for the composition $x = 0.1$ were found to be: a = b = 5 .4619(3) Å and $c = 13.2059(4)$ Å. To further evaluate the perovskite structure we used the computer program SPuDS (Structure Prediction Diagnostic Software), developed to study the stability of a wide-ranging tilt patterns in perovskites[304]. Utilizing a rocksalt-type Co-Ni cation ordering and $a^- a^- a^-$ Glazier tilt system (inset of Figure 7-2(a)), a tilt angle of 10.2050°, Goldschmidt tolerance factor of 0.9736 and a global instability index of 0.000264 was obtained. The rhombohedral structure is highly symmetric with a tolerance factor close to unity, despite the $a^- a^- a^-$ tilting of the octahedral sub-lattice[305], and so we can hypothetically utilize the idealized 6-coordinated B-cations with oxygen in the octahedral sub-lattice and 12-coordinated A-cations with oxygen. Though the ionic radius of $Ca^{(II)}$ is slightly larger than $La^{(III)}$ in the 12-fold coordinate symmetry, $r_{Ca(II)}$ is 1.40 Å and $r_{La(III)}$ is 1.36 Å [306], there was no discernible shift in 2 theta as the Ca doping level is increased from 10 at. % to 30 at. % in the A-site. However, the intensity and sharpness of the peaks were reduced in the same trend. This may be attributable to a defective crystal structure resulting from an oxygen vacancy ordering mediated through charge neutrality originating from Ca (II) replacing La (III) in the lattice. The $La_{1-x}Ca_xCo_{0.5}Ni_{0.5}O_{3-\delta}$ 120 atom supercell with x = 2/24, optimized using DFT simulations is shown in Figure 7.1 (b). La atom is green, Ca is light blue, Ni is grey, Co – dark blue while oxygen atom is red. Despite the presence of some defects, the clear fringes observed in HRTEM images and the corresponding fast Fourier transform

Table 7.1 Refined cell parameters (*a, b, c*), atomic positions (*x, y, z*), isotropic thermal factor (U_{iso}), Cagliotti parameters (*GU, GV, GW*), Lorentzian broadening due to domain size (*LX*) and strain (*LY*), and fitting factors (R_{wp}, R_p, and reduced χ^2)

	$La_{1-x}Ca_xCo_{0.5}Ni_{0.5}O_3$	
	$x = 0.0$	$x = 0.1$
a(Å)	5.5677(3)	5.4619(3)
b(Å)	5.5677(3)	5.4619(3)
c(Å)	13.1722(9)	13.2059(14)
U_{iso}(La/Ca) (Å ^{2})	0.027(1)	0.064(2)
U_{iso} (Co/Ni) (Å ^{2})	0.163(9)	0.051(2)
U_{iso} (O) (Å ^{2})	0.010(3)	0.069
x(O)	0.4387	0.4693
y(O)	0.0000	0.0000
z(O)	0.2500	0.2500
GU	150	3043
GV	-39.3	-2324
GW	19.1	533
LX	9.9	31.7
LY	3.4	14
R_{wp} (%)	3.7	3.3
R_p (%)	2.9	2.5
Reduced χ^2	3.172	2.579

(FFT) diffraction pattern of the highlighted rectangular area (Figure 7.3 (a, b)) indicate the crystallinity of the synthesized nanoparticles.

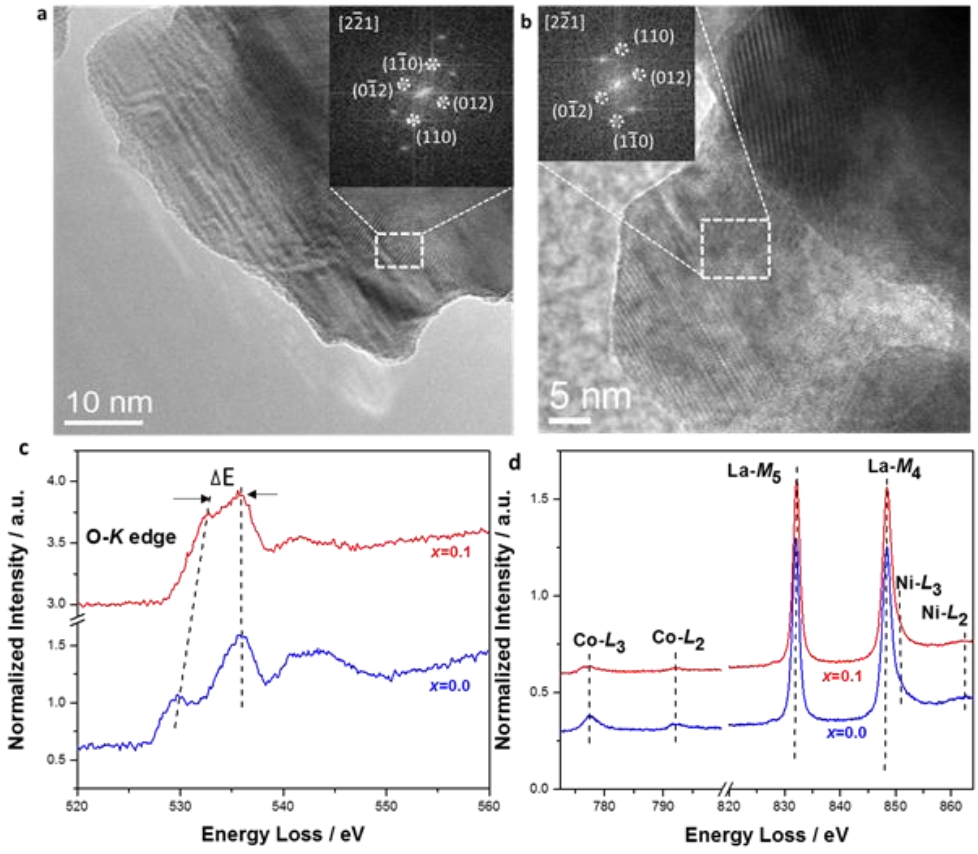

Figure 7-3| High resolution TEM images and fast Fourier transforms(FFTs) of $La_{1-x}Ca_xCo_{0.5}Ni_{0.5}O_{3-\delta}$ (a) x = 0.0, scale bar 10 nm and (b) x = 0.1, scale bar 5 nm, FFTs were indexed using space group $R\bar{3}c$ and lattice parameters a_p x a_p x a_p. Normalized EELS spectra at x = 0.0 and 0.1 in the vicinity of (c) O-K edge and (d) Co-$L_{2,3}$, Ni-$L_{2,3}$ and La-$M_{4,5}$ edges.

The measured d-spacings in $La_{1-x}Ca_xCo_{0.5}Ni_{0.5}O_{3-\delta}$ (x = 0.0, 0.1) were consistent with the spacing between the (110) and the d-spacing between the (012) planes of the single

rhombohedral phase, in the direction of $[2\bar{2}1]$ zone axis, consistent with the XRD analysis. The well-defined points in the FFT pattern agree with the allowed Bragg diffraction of rhombohedral phase.

7.3.2 TEM-EELS

Metal-oxygen atomic bond is one of the greatest considerations when probing the electronic properties complex metal oxides. The proximity of the partially filled TM-3*d* bands and the O-2*p* bands to the Fermi level has been instrumental to probing the electronic properties through the investigation of fine structures of the TM-*L* edge and O-*K* edge in most perovskites. From the dipole selection rules, the O *K* pre-edge structure found near 530 eV is as a result of the excitations of O 1*s* electrons to the 2*p* bands, while TM-*L* edges result from the excitation of 2*p* electrons into empty bound states [307]. Seeing that in perovskites TM-oxygen bands are close enough to be hybridized with each other, interesting variations are expected in both edges when the occupation of the 3*d* bands are altered by way of TM valence states. In perovskites, this can be easily achieved by replacing the trivalent A-cation with divalent one, or by the having partial substitution of trivalent with divalent cation. This may result into a mixed-valence state of the B cation which leads to a complex electronic structure. Contrary to the conclusion in Ref. [107], we found that the A-site substitution plays a vital role in adjusting the O-*K* near-edge structure. For example, in Figure 7-3(c), for composition x = 0.0, we found the pre-edge peak at 529.6 eV, which is attributed to the hybridization of the O 2*p* with Co-Ni 3*d* states, and two more peaks near 535 and 542 eV that are related to the bonding of the O-2*p* with the La 5*d* and Co-Ni 4*sp* bands, respectively; consistent with Refs. [308], [309]. However, substitution with 10

at. % of Ca saw an increase in the pre-peak intensity and a shift of the pre-peak position to 532.7eV from 529.6 eV, shrinking the peak separation energy (ΔE) between the pre-peak and the adjacent peak. Assuming spin transition is negligible, the changes occurring in the O *K* edge fine structure with increasing Ca content may be ascribed to changes in electronic structure. The higher intensity pre-peak may be linked to stronger hybridization between Co-Ni 3*d* band and O-2*p* band, the energy loss peak shift and consequent contraction of ΔE, on the other hand, can be interpreted based on the O *K* edge fine structures of $La_{1-x}Sr_xCoO_3$ discussed elsewhere. According to Ref. [310], increasing Sr content from x = 0 to x = 0.15 in $La_{1-x}Sr_xCoO_3$ saw an expansion in ΔE. Because the host $LaCoO_3$ is a Mott-Hubbard type oxide[55], the O 2*p* band would move up some energy level on doping with Sr to hybridize with the Co 3*d* band following the O 1*s* excitation into the empty or partially filled O 2*p* band. Contrarily, to promote strong *p-d* hybridization in $LaCo_{0.5}Ni_{0.5}O_{3-\delta}$, the O 2*p* band would have to move down some energy levels on doping with 10 at. % of Ca. Evidence from the DFT calculations in this work show that the O-2*p* and TM-3*d* bands in $LaNi_{0.5}Co_{0.5}O_{3-\delta}$ are set-up like a charge transfer type oxide. In summary, the O-2*p* band position of the host oxide provides a clue as to whether the ΔE of the O *K* edge would expand or shrink when the electronic character is altered in favor of *p-d* hybridization. In Figure 7-3(d), the fine structures of Co-$L_{2,3}$, Ni-$L_{2,3}$ and La-$M_{4,5}$ edges are displayed and their intensity ratios before and after doping were compared and tabulated (Table 7.2). In line with expectations, the intensity ratios of the Co-$L_{2,3}$ edge increases from 0.884 (x = 0.0) to 0.971 (x = 0.1) while the opposite is true for La-$M_{4,5}$ (1.011 to 0.981 respectively). The increase in Co-$L_{2,3}$ intensity ratio has been correlated with increase in valence states of Co^{3+} [310], while a reduction in the intensity ratios of La-$M_{4,5}$ has been linked with the valence

Table 7.2 Computation of the Intensities and intensity ratios of Co-$L_{2,3}$ and La-$M_{4,5}$ edges

x	Intensities of Co-$L_{2,3}$ and La-$M_{4,5}$				Intensity ratios of Co-$L_{2,3}$ and La-$M_{4,5}$	
	I(Co-L_3)	I(Co-L_2)	I(La-M_5)	I(La-M_4)	I(Co-L_2)/I(Co-L_3)	I(La-M_4)/I(La-M_5)
0	0.3808	0.3365	1.242	1.255	0.884	1.011
0.1	0.638	0.6208	1.594	1.564	0.971	0.981

state reduction in La^{3+}. The La-$M_{4,5}$ edge probes the unoccupied density of La 4*f* states and can provide a clue as to the valency of La. It is clear from the asymmetry in Figure 7-3(d) that the La-M_4 and Ni-L_3 edges coincides with each other due to the very small energy separation between La 3*d* and Ni 2*p* core levels, invariably obfuscating the accurate estimation of Ni-$L_{2,3}$ intensity ratios.

7.3.3 OER kinetics and electrocatalyst stability

An array of $La_{1-x}Ca_xCo_{0.5}Ni_{0.5}O_{3-\delta}$ (x = 0.0, 0.1, 0.20, 0.30) mixed metal oxide films were tested for OER catalysis by studying the CV at 20 mVs^{-1} scan rate. Two parameters

were selected to understand the catalyst performance: (i) overpotential (η) required to reach a current density of 10 $mAcm^{-2}$ (ii) galvanostatic conditioning at current density of 10 $mAcm^{-2}$ for 2h**.** Figure 7.4 (a) shows the CV curves, obtained by taking average of the forward and backward scans. Secondary *x*-axis indicates the overpotential values also tabulated in Table 7.3. The onset potential of samples x = 0.1 and 0.2 is 1.12 V vs RHE while the onset potentials for samples x=0.3 and x=0.0 are 1.17 and 1.30 V vs RHE respectively. The overpotentials ranges from 330 to 463 mV with sample x=0.1 outperforming the sample set with an overpotential of 330 mV.

Table 7.3 Overpotentials of the double perovskites (x = 0.0, 0.1, 0.2, 0.3) and the corresponding O 2*p* band relative to Fermi level computed by DFT.

Electrocatalysts $La_{1-x}Ca_xCo_{0.5}Ni_{0.5}O_{3-\delta}$	η /mV	O-*2p* band center relative to E_F / eV
x=0.0	463	-2.429
x=0.1	330	-2.669
x=0.2	423	-2.433
x=0.3	400	-

Aside from high activity performance which all good catalysts are expected to have, optimal catalyst material should be stable for their implementation in extreme pH conditions. The stability of these catalysts under catalytic conditions was determined using controlled-current electrolysis. The catalyst material was held at a constant current density of 10 $mAcm^{-2}$ per geometric area for 2 h, while the operating potential was measured as a function of time.

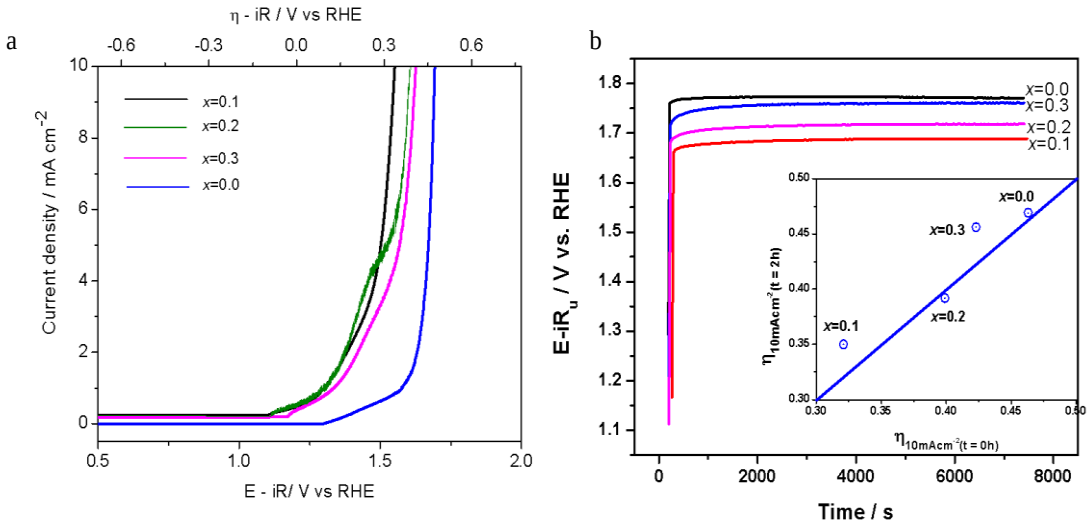

Figure 7-4| (a) Cyclic voltammetry of the conditioned $La_{1-x}Ca_xCo_{0.5}Ni_{0.5}O_{3-\delta}$ ($0.0 \leq x \leq 0.3$) films collected in 1 M NaOH solution at a scan rate of 20 mV s^{-1}(b) Galvanostatic controlled current electrolysis measurement of $La_{1-x}Ca_xCo_{0.5}Ni_{0.5}O_{3-\delta}$, where x = 0.0, 0.1, 0.2, and 0.3, where current is fixed at 10 $mAcm^{-2}$, measured for 2h. Inset: Parity plot of the overpotential at 10 $mAcm^{-2}$ before galvanostatic measurement (horizontal axis) and after 2h of measurement (vertical axis).

Figure 7.4 (b) shows the results of the controlled current electrolysis measurements of these catalysts. The inset of Figure 7.4 (b) shows that, η (t = 0h) and η (t = 2h) are alike to a moderate extent, an indication that the catalyst is stable under the operating conditions for at least a 2 h period. The small deviation of the overpotentials of samples x = 0.1 and x = 0.3 from the 45˚ parity line may have been due to O_2 bubbles that collect around the surface of the electrocatalysts over the 2 h stability test period creating an O_2 mass transport limiting situation.

7.3.4 Relationship between O 2p band center and OER activity

The very influential work of the Zaanen-Sawatzky-Allen[311] was formulated to categorize the oxides of TM compounds, which have been extended to the study of sulfides, iodides and fluorides of TM compounds. This concept is a revolutionary, describing the *d*-*d* Coulombic interaction of the TM 3*d* electrons (U_{dd}) and the charge-transfer (*C*-*T*) energy between TM-3*d* and anion-*p* states (Δ_{CT}) are key features for controlling the underlying physics of the electronic structure of TM compounds. In this theory, both the fundamental structure scheme of C-T insulators does not consider the Coulomb splitting of the TM-3*d* bands into upper and lower Hubbard bands (Mott gap), which causes the insulating behavior of TM oxides. In the first-row TM, the Coulombic splitting increases from left to right, and consequently, the O-2*p* bands could be positioned in such a way that it could become energetically sandwiched between the two Hubbard bands, an outcome not incorporated into standard band structure models. In this case, the energy for a charge excitation is no longer determined by the Hubbard U_{dd} but instead by the charge-transfer energy Δ_{CT}. The Hubbard energy (*U*) responsible for transporting an electron from TM d band to another TM atom is given by[311]:

$$U = E(d^{n+1}) + E(d^{n-1}) - 2E(d^n) \qquad 7.1$$

accordingly, we have to furnish the charge-transfer energy:

$$\Delta = E(d^{n-1}) - E(d^n) + E(p^{m+1}) - E(p^m) \qquad 7.2$$

to shift an electron to an oxygen p level. If $U_{dd} > \Delta_{CT}$ holds, the insulator should no longer be denoted a (multi-band) Mott–Hubbard insulator, but rather a charge-transfer insulator since the energy gap for charge excitations is now determined by the charge-transfer energy Δ_{CT} and no longer by the on-site interaction U_{dd}.

Although the *n* values in $Ca_nLa_{24-n}(CoNi)_{12}O_{72-\delta}$ unit cell consisting of 120 atoms utilized in computation corresponds to non-integer number of atoms in $La_{1-x}Ca_xCo_{0.5}Ni_{0.5}O_{3-\delta}$ for $x = 0.1$, 0.2 and 0.3 and so, approximations such as $x = 2/24 \sim 0.1$, for $n = 2$ are used, and such approximations in no way compromise the qualitative and quantitative trends we can obtain from computational data. From the DFT studies, the valence band in $Ca_nLa_{24-n}(CoNi)_{12}O_{72-\delta}$ is the O 2*p* band which fluctuates across the energy levels on changing the *n* values. As shown in Figure 7-6(a) increasing *n* from 0 to 1 saw a shifting away of the O 2*p* center from the Fermi level, while $n = 2$ corresponds to the furthest away from the Fermi level beyond which there was a reversal in trend. With the exception of $n = 0$, the center of mass of the total density of states of the 3*d* band experienced relatively fewer fluctuations across the energy axis. It interesting to note that, at $n = 2$, we have the strongest hybridization (Figure 7-6(b)) of the O 2*p* and TM 3*d* bands which incidentally corresponds to the highest activity recorded for all catalysts under study.

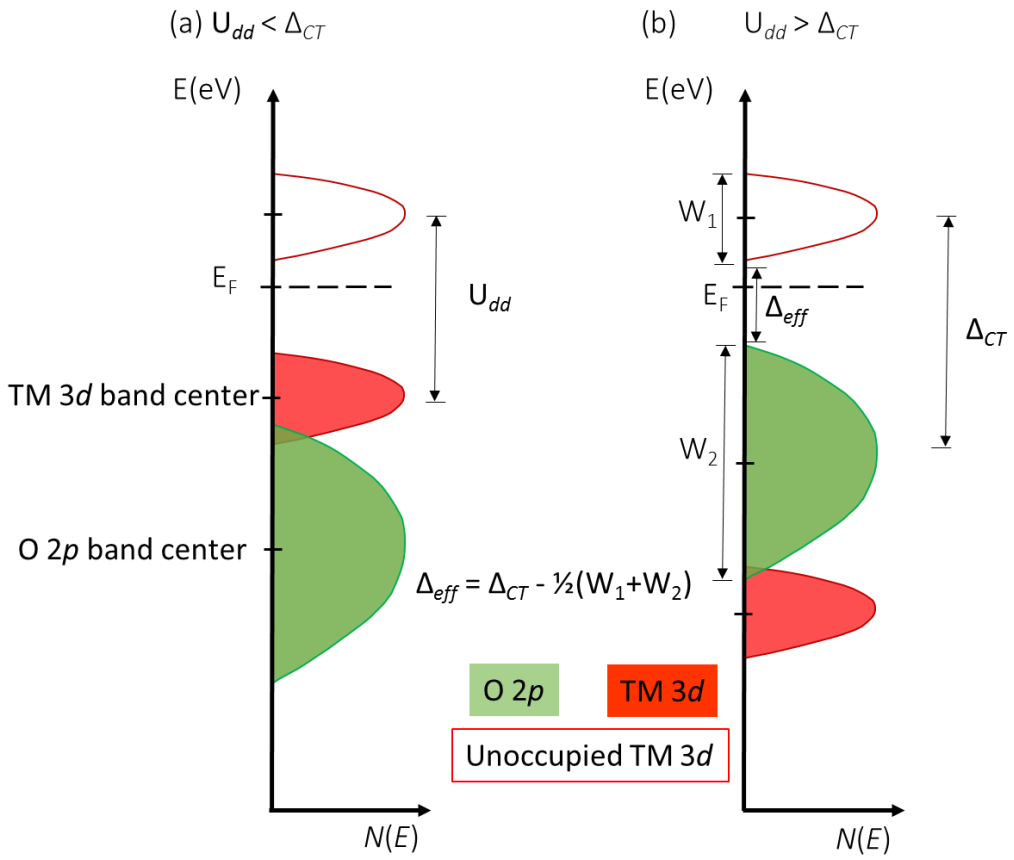

Figure 7-5| Schematic representation of important features used to describe charge dynamics in transition metal oxide (TMO) compounds. Charge-transfer energy Δ_{CT}: energy needed for transferring charge carriers from the *O 2p* band to the *TM 3d* band (with respect to the band center of mass); *Hubbard* energy, U_{dd}: energy needed to remove an electron from the occupied 3*d* band and to add it to the unoccupied 3*d* band; effective charge-transfer energy Δ_{eff}: defined by equation $\Delta_{eff} = \Delta_{CT} - ½ (W_1 + W_2)$. *Where, (a)* $U_{dd} < \Delta_{CT}$, *Mott-Hubbard* insulator results, and *(b)* $U_{dd} < \Delta_{CT}$, charge transfer insulator results.

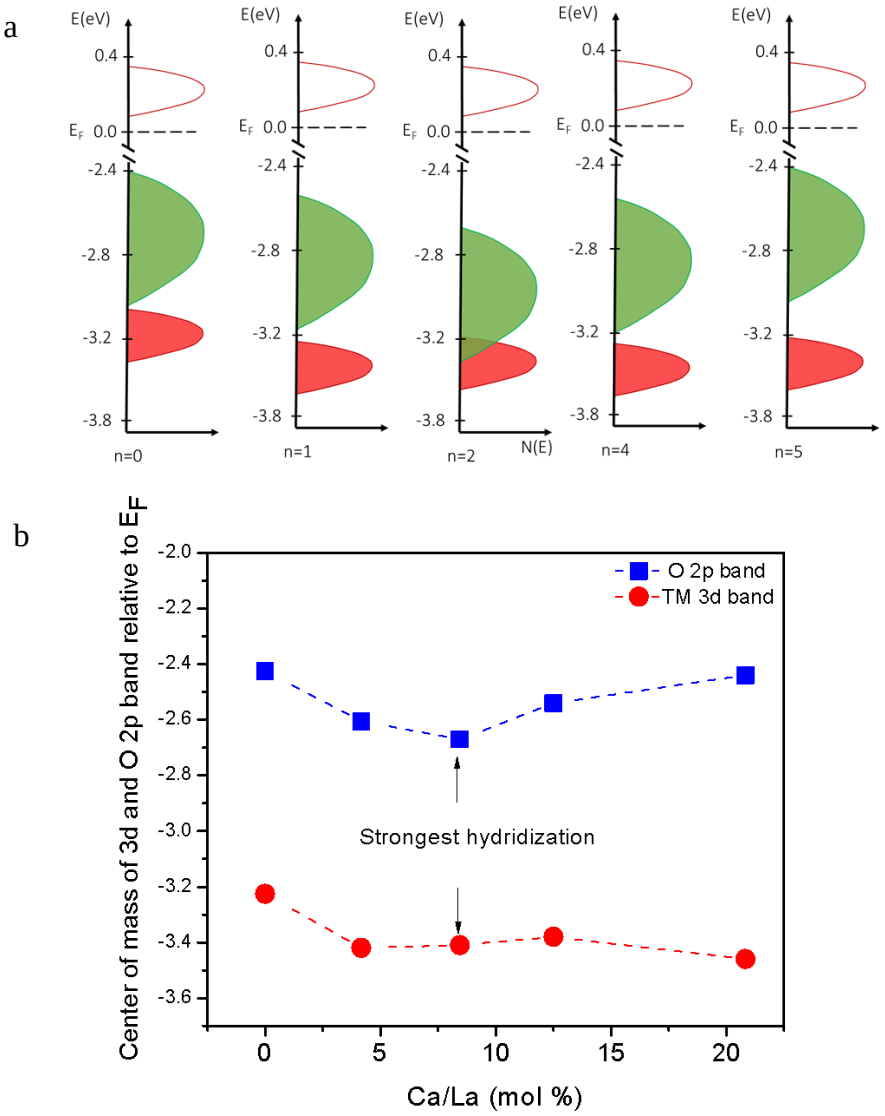

Figure 7-6| (a) The sketch of variations of n in $Ca_nLa_{24-n}(CoNi)_{12}O_{72-\delta}$ for the 120-atom supercell as computed by DFT for (a) n = 0 (b) n = 1; (c) n = 2; (d) n = 4 and (e) n = 5 (b)DFT computation of the center of mass of TM 3*d* and O 2*p* band relative to the Fermi level plotted against the ratio of Ca/La in the 120-atom supercell. Strongest hybridization corresponds to Ca/La ~ 10 mol. %.

Distortions from cubic perovskites are mostly due to the A-cation size and/or doping, therefore, this distortion may extend to the BO_6 octahedra giving it a hybrid character consisting of ionic-covalent blend. Because of this hybrid character, the TM 3*d* orbitals and O 2*p* orbitals may overlap to produce steady bands. Also, the covalent mixing from the *p-d* electron overlap provides an access for electrons to move between the B-site cation and O anion, which is the underlying reason for material conductivity especially in oxides[312]. From Table 7.3, the overpotentials at a current density of 10 $mAcm^{-2}$ of catalyst samples with Ca contents $0 \leq x \leq 0.3$ are as displayed, where for sample $x = 0.1$ (approx. $n = 2$), the overpotential of 330 mV was obtained, which is a competitive value when compared with the best perovskite oxides and noble metal oxides reported till date.

7.4 Discussion

Among all catalysts, the sample with no Ca content ($x = 0.0$) exhibits the poorest activity and from DFT results, its O 2*p* band center is the closest to the Fermi level of all catalysts studied. Contrarily, it was reported that moving the O 2*p* band center closer to Fermi level is the basis of a strategy to create catalysts with high intrinsic OER activities[79]. Perhaps that conclusion is true for Mott-Hubbard oxides where *p-d* hybridization is highly favored by O 2*p* band center moving closer to the Fermi level. As we have seen for charge transfer oxides, moving the O 2*p* band center away from the Fermi level creates the same effect, and so we conclude that band structures play a vital role in determining the activity trend by moving the O 2*p* band center towards or away from the Fermi level. The high activity in $x = 0.1$ sample can be rationalized in terms of the covalent mixing from the *p-d* hybridization which creates electron pathways between the B-site cation and O anion, and the small charge transfer gap in the bands. This small charge transfer gap becomes even

more important when Ca is doped on the A-site. The Co^{3+}/Ni^{3+} ions in the immediate vicinity of doping becomes tetravalent and creating additional holes in the e_g orbital[299], charge carriers may now hop between neighboring Co^{3+}/Ni^{3+} and Co^{4+}/Ni^{4+} ions through the O^{2-} ion links, closing up the charge transfer gap.

7.5 Chapter Summary

The discovery of active and stable oxygen electrocatalysts can be accelerated by exploiting the adjustable electronic character of transition metal *d* bands and oxygen *p* bands which, in effect, plays a crucial role in the catalysis of electrochemical conversion processes such as the oxygen evolution reactions. In this report, experimental and computational studies of charge transfer type complex double perovskites $La_{1-x}Ca_xCo_{0.5}Ni_{0.5}O_{3-\delta}$ ($0.0 \leq x \leq 0.3$) were employed to find the correlation between computed oxygen *p* band and oxygen evolution activity. The catalyst with calcium content of $x = 0.1$ shows overpotential comparable with the best OER perovskite based electrocatalysts reported, with overpotential as low as 330 mV at current density of 10 $mAcm^{-2}$ in alkaline media and controlled current chronoamperometry displayed a 2h stable potential-time profile for all electrocatalysts under study. The high activity and stability of the low-calcium content perovskite is ascribed to the small charge transfer gap resulting into stronger transition metal 3*d* – O 2*p* hybridization.

CHAPTER 8

ATMOSPHERIC PLASMA SPRAY PYROLYSIS OF LITHIATED NICKEL-MANGANESE-COBALT OXIDES FOR CATHODES IN LITHIUM ION BATTERIES[3]

8.1 Introduction

The first commercial lithium ion battery with non-aqueous electrolyte adopted $LiCoO_2$ as the positive electrode. However, due to safety and cost concerns, efforts were made to develop new compounds by reducing the use of Co with Mn and Ni[313]. $LiMnO_2$ exhibited severe capacity fading during electrochemical cycling with phase transition. On the other hand, $LiNiO_2$ suffered from difficulty in their synthesis due to cation mixing and structural degradation caused by irreversible phase transition during electrochemical cycling.[314] Kang *et al.* [224] investigated $LiNi_{0.5}Mn_{0.5}O_2$ by both experimental and *ab initio* studies and concluded that Li/Ni disorder is responsible for the poor rate performance. Moreover, Co was found to improve the conductivity of the lithium layered NMC cathode material [315]. The most successful transition metal (M) layer formulation up to date is

[3] The texts in this chapter was originally published as "B. P Ajayi, A. K. Thapa; U. Cvelbar, J. B. Jasinski, M.K. Sunkara, (2017), Atmospheric plasma spray pyrolysis of lithiated nickel-manganese-cobalt oxides for cathodes in lithium ion batteries, Chem Eng. Sci, 174, 302-310". Formatting styles were amended to adapt original article to the style of this dissertation, and some data from the supporting information in the original article are included in this chapter. No permission required to reuse article per publisher's guidelines in Appendix 12.

inclusive of all three metals - nickel, manganese and cobalt [316-318], hereafter referred to as NMC.

The conventional synthesis method of NMC is a solid state route that involves the mechanical milling of oxides, carbonates or nitrates [16]. Consequently, the wet chemical methodologies such as sol-gel[319], co-precipitation[19] solvothermal techniques[320] were all given some considerations. However, these methods require prolonged heat treatments, and therefore are primarily restricted to equilibrium phases[321]. All the above methods result in low yields as they involve multiple steps and laborious processes, each bearing a risk of introducing impurities into the final product, creating batch-wise inconsistencies in the process. The scale-up of these techniques can be difficult due to the long reaction times (12 – 24 h) required. Moreover, it is quite a challenge to control the size and composition of mixed metal oxide nanoparticles, a key parameter for the properties and performance of these materials. So, it is immediately apparent that a synthesis technique that allows ultrafast timescale of processing, controllable size, composition and crystallinity will facilitate the advancement of large-scale manufacturing of these materials[290].

Beside the material composition, contribution of surface morphology via particle size and packing density of materials which rely on the method of preparation, is an important consideration in materials design. Nano sized cathode materials are effective because they impart larger electroactive surface for rapid lithium diffusion and a higher packing density for enhanced energy storage capabilities[219]. In nanoparticles, the distances over which Li must diffuse are significantly shortened; the nanoparticles can quickly absorb and store large amount of lithium ions without disintegration of the electrode and nanoparticles have large surface areas, short diffusion lengths, and fast diffusion rates

along their many grain boundaries[322]. Spray pyrolysis was found to be an effective production technique leading to an ultra-fast production time, uniform particle composition, particle size control, and is a single-step method.[178] However, the application of this method to cathode materials in the lithium ion batteries was limited to electric furnace spray pyrolysis ($LiM_{1/6}Mn_{11/6}O_4$, M = Mn, Co, Al and Ni)[323], ($Li_{1.2}Mn_{0.54}Ni_{0.13}Co_{0.13}O_2$)[22] and flame spray pyrolysis (LiV_3O_8)[324], ($LiMn_2O_4$, $Li_4Ti_5O_{12}$, $LiFe_5O_8$) [325]. The electrochemical performance data of the spray pyrolyzed material showed that excess lithium containing layered material, $Li_{1.2}Mn_{0.54}Ni_{0.13}Co_{0.13}O_2$ (annealed at 900 °C over 2 h duration) displayed superior electrochemical performance with excellent capacity retention, revealing a reversible capacity of 236 $mAhg^{-1}$ after 100 cycles, when cycled between 2.0–4.8 V at C/10 rate, where 1C = 280 mA g^{-1} [22]. In many of these flame/electric furnace pyrolysis techniques, crystalline materials are not made in a single step. Therefore, additional post-treatment annealing step is imperative before these materials can be deployed as battery electrodes.

Here, we report the advanced synthesis of crystalline NMC materials using an atmospheric spray plasma oxidation, and consequently their electrochemical performance as cathodes in lithium ion batteries. Primarily, studies were performed to understand whether one can make compositionally-controlled NMC materials. Specifically, Mn-rich NMC oxide $LiNi_{0.2}Mn_{0.6}Co_{0.2}O_2$ was prepared and the material was tested for its electrochemical performance.

8.2 Materials Synthesis and Characterization and Electrode Fabrication /Testing.

Chemically pure grade of nickel (II) nitrate hexahydrate, manganese (II) nitrate hydrate, and cobalt (II) nitrate non-hydrate (research grade, Alfa Aesar) were used as

starting materials without further purification. In a typical experiment, continuously operated plasma reactor (chapter 3) input plasma power was set to 1.20 kW using flow of 2 slpm Ar and 11 slpm air, Ar flow was turned off after igniting the plasma (Ar is basically necessary for igniting the plasma). In these experiments, precursor solutions containing appropriate amounts of nitrates of nickel, manganese and cobalt were dissolved deionized water to make 0.50 M solution (with composition of Ni/Mn/Co in 1/3/1 ratio) and was made into aerosols of small droplets and delivered onto air plasma. NMC nanopowders were collected in a high efficiency particulate filter (HEPA) with the action of a vacuum pump. Consequently, the obtained NMC oxide was crushed and well mixed in the solid state with appropriate amount of Li_2CO_3 in such a way that the stoichiometric ratio of lithium to NMC was 1:1, a 5 wt. % excess of Li_2CO_3 was added to compensate for the volatilization of lithium in the high temperature reaction. The mixture was calcined in the furnace at 900˚C (5˚C min^{-1}) for 5h. The as-prepared sample is herein referred to as $LiNi_{0.2}Mn_{0.6}Co_{0.2}O_2$. Electrode fabrication procedures and electrochemical characterizations details are fully explained in chapter 3 of this dissertation. Materials characterization procedures are also available in chapter.

8.3 Results and Discussion

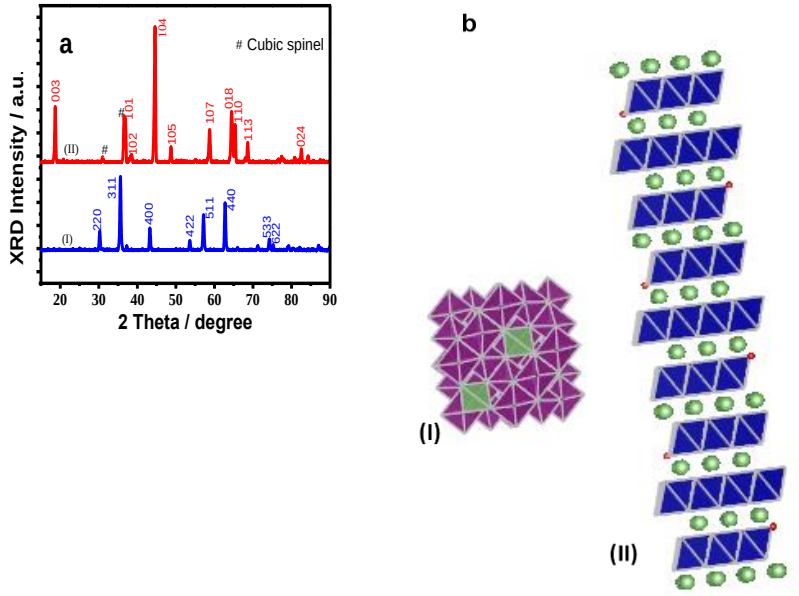

Figure 8-1| (a-I) X-ray diffraction patterns of NMC as-prepared sample from atmospheric microwave plasma (a-II) X-ray diffraction reflections after solid state lithiation of NMC, major phase found is the rhombohedral, α-$NaFeO_2$ type phase, with a minor cubic spinel phase (in red) and (b) General view of the crystal structure viewed along *b* axis for (I) spinel unit cell (green: Li-O tetrahedron, purple: Mn-O octahedron (II) rhombohedral 3×3×3 supercell (green atom: Li, dark blue: TM octahedron)

The X-ray diffraction (XRD) measurements were carried on sample before and after lithiation of NMC oxide material. Figure 8-1(a-I) indicates the XRD reflection of the manganese rich $Ni_{0.2}Mn_{0.6}Co_{0.2}O_x$ oxide before the lithiation step. The well resolved

patterns show good crystallinity, which is indexed to a cubic spinel phase with space group of $Fd\bar{3}m$ (PDF card no. 00-001-0111). The well-defined and sharp peaks in the powder diffraction patterns depicted in Figure 8-1(a-II) exhibit also a good crystallinity of the manganese rich lithium NMC sample obtained after the lithiation step. The two separate crystallographic phases are found to be present in the sample. First, the dominant lithiated phase can be indexed to the hexagonal α-$NaFeO_2$ type crystal structure with a space group of $R\bar{3}m$ (PDF card no. 01-074-4671). The clear distinctions of the hexagonal doublets (018)/(110) located around 65˚ is an indication of the layer character of the sample[326]. The intensity ratio of the (003) to (104) peak is about 0.85, indicating a slight cation mixing with some Ni ion occupying the lithium sites. The second minor phase is indexed to a cubic spinel phase with space group of $Fd\bar{3}m$, with the XRD parameters matching the lithium-deficient spinel $Li_{0.1}Mn_{2.05}O_4$ according to PDF card no. 01-073-5020. Xiao and co-workers concluded that the limit of a layered phase is Mn content of 0.5 beyond which results in the speciation of spinel impurity phase[327]. They also established that the '*a*' lattice parameter found for spinel phase in $LiNi_{0.3}Mn_{0.6}Co_{0.1}O_2$ is 0.8577 nm, which is far more than the *a* lattice parameter of the stoichiometric $LiMn_2O_4$ (0.8235 nm). This indicates a lithium deficient and non-stoichiometric $Li_{0.1}Mn_{2.03}O_4$ spinel phase, consistent with our data. The ratio of the metal ion content in $LiNi_{0.2}Mn_{0.6}Co_{0.2}O_2$ measured by ICP-MS experiment is Li/[Ni,Co,Mn] = 1.015 and Ni/Mn/Co = 1.000/2.952/1.057. The raw data and measurement error estimation is presented in Tables A9 (a) and (b) of Appendix 9. This composition was also confirmed by the transmission electron microscopy energy-dispersive X-ray (TEM-EDS) analysis as displayed in Appendix 10, Figures A10 (a-b) and Tables A9(a) and 9(c). The observed values are in good agreement with the starting

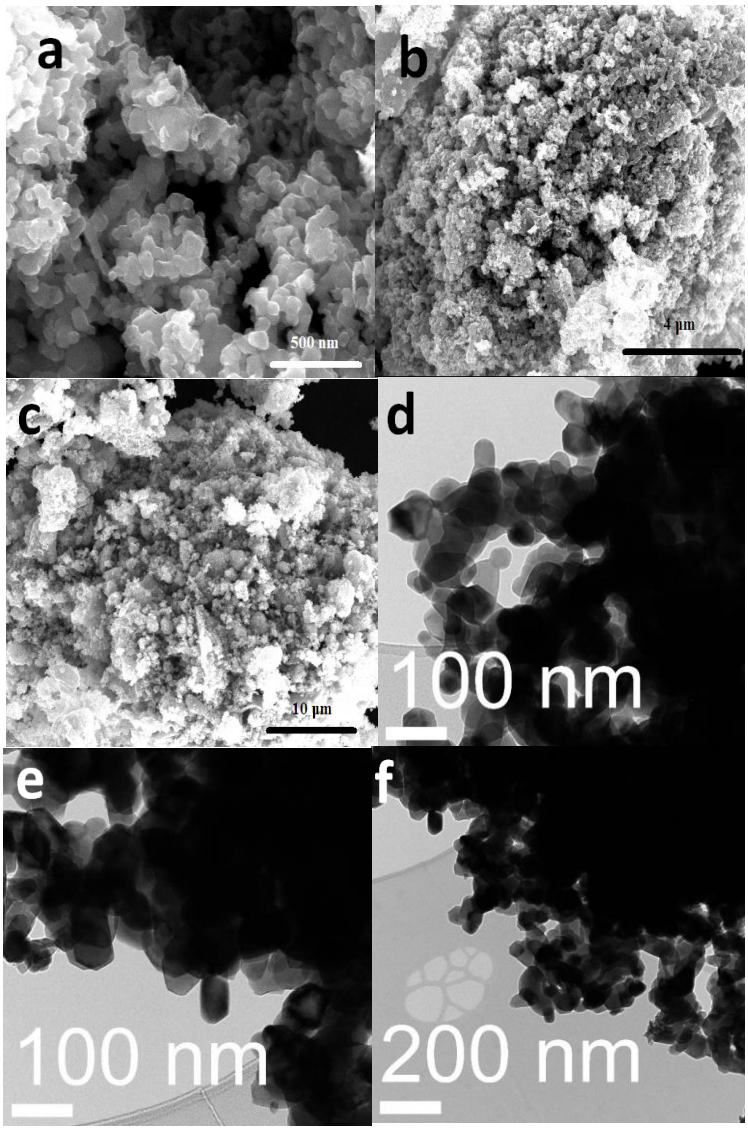

Figure 8-2 | (a)-(c) SEM micrograph showing the surface morphologies of the as prepared NMC oxide nanoparticles of different magnifications (d)-(f) Bright field TEM image of a few particles at two different magnifications.

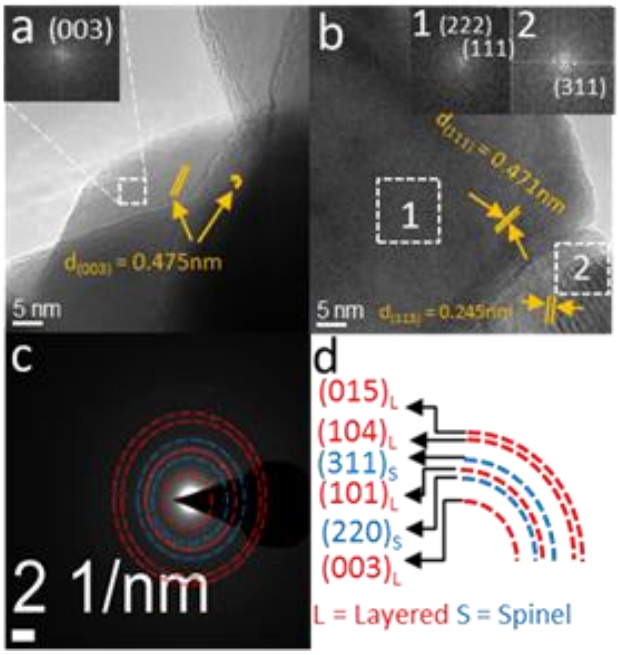

Figure 8-3| High resolution TEM (HR-TEM) of sample $LiNi_{0.2}Mn_{0.6}Co_{0.2}O_2$ (a) presenting grains with a single lattice fringes having d-spacing indexed to (003) of the rhombohedral phase ($R\bar{3}m$) and equal to 0.475 nm. Inset: Fast Fourier Transforms (FFT) of the area marked by the dashed square (b) showing grains with two lattice fringes with one having d-spacing indexed to (111) and the other to (311) plane where $d_{(111)}$ = 0.471 nm and $d_{(311)}$ = 0.245 nm respectively, which is indexed to the cubic spinel phase ($Fd\bar{3}m$) .Inset: Fast Fourier transforms (FFT) of the area marked by the dashed square, where (1) corresponds to (111) plane and (2) corresponds to (311) plane, respectively (c) Selected area electron diffraction (SAED) patterns of the $LiNi_{0.2}Mn_{0.6}Co_{0.2}O_2$ sample displaying ring patterns indexed to the rhombohedral phase ($R\bar{3}m$) (in red) and cubic spinel phase ($Fd\bar{3}m$) (in blue). (d) Assignment of ring patterns to corresponding planes (layered in red, and spinel in blue).

material composition. The surface morphologies of the as-prepared $LiNi_{0.2}Mn_{0.6}Co_{0.2}O_2$ samples are presented in Figure 8-2(a)-(c) with both low and high magnification. The samples reveal irregularly-shaped nanoparticles, with particle size in the range between 50 samples reveal irregularly-shaped nanoparticles, with particle size in the range between 50 nm and 100 nm.

Transmission electron microscopy (TEM) analysis was performed to provide data of the morphology, size and crystal structural phase of the synthesized $LiNi_{0.2}Mn_{0.6}Co_{0.2}O_2$ in pristine condition and is outlined in Figure 8-3. The TEM studies performed include a high resolution TEM (HRTEM), bright field (BF) imaging techniques, fast Fourier transform (FFT) patterns and energy-dispersive X-ray spectroscopy (EDS). The structural information obtained by TEM is in good agreement with the one obtained using XRD, demonstrating that the structure of the pristine sample is explained as a two-phase system including the cubic spinel and rhombohedral layered phase. Figure 8-2(d)-(f) show a BF image of a few typical particles at two different magnifications. The particles appear to be irregularly-shaped nanoparticles as in the case of SEM analysis. The HRTEM image of Figure 8-3(a) belongs to the rhombohedral phase ($R\bar{3}m$), with lattice fringes corresponding to (003) plane and d-spacing, $d_{(003)}$ = 0.475 nm. The inset of Figure 8-3(a) is the FFT of the area marked by the dashed white square indexed to the (003) plane. Figure 8-3(b) contains two distinct lattice fringes corresponding to the (111) and (311) planes with d-spacing values of 0.471 nm and 0.245 nm, respectively. The insets of Figure 8-3(b) are the FFTs of the areas marked by the numbered dashed white squares, where (1) belongs to (111) plane and (2) belongs to (113). Both areas are indexed to the cubic spinel phase

($Fd\bar{3}m$). Furthermore, Figure 8-3(c) indicates the selected area electron diffraction (SAED) of the $LiNi_{0.2}Mn_{0.6}Co_{0.2}O_2$ sample where patterns are indexed to the rhombohedral phase and cubic spinel phase as confirmed by XRD. This is more carefully outlined in Figure 8-3(d), where the assignment of ring patterns is connected to corresponding planes (layered in red, and spinel in blue). At the same time, it is important to point out that the d-spacing of the (111) plane of the spinel phase (0.471 nm) is similar to the d-spacing of the (003) plane of the layered phase (0.475 nm). However, the instrument's sensitivity is not sufficient to delineate between these two, and for this reason, the first ring pattern is assigned to the most dominant layered phase.

To unravel the differences further, the Raman spectra was recorded for the materials in the pristine and spent state (after 50 cycles) and results are seen in Figure 8.4(a) and (b), respectively. The deconvoluted spectra of the pristine $LiNi_{0.2}Mn_{0.6}Co_{0.2}O_2$ (Figure 8.4(a)) clearly exhibits two bands at 500 and 560 cm^{-1}. These two bands are assigned to E_g and A_{1g} Raman-active modes for the transition metal-oxygen arrangements in the layered lithium metal oxide with rhombohedral $R\bar{3}m$ symmetry[328]. The presence of the signature peak of the cubic spinel phase at 630 cm^{-1} indicates that the prepared materials are mixed phase layered-spinel oxide materials [329-330]. Thus, the Raman spectra data clearly supports the XRD evidence. The spinel structure comprises of MnO_6 octahedra and LiO_4 tetrahedra. The Raman band located near 630 cm^{-1} is attributable to the symmetric Mn–O stretching vibration of MnO_6 octahedra[331]. This band is assigned to the A_{1g} symmetry in the O_h^7 spectroscopic space group. The broadening of this signature band in Figure 8-4 (b) could

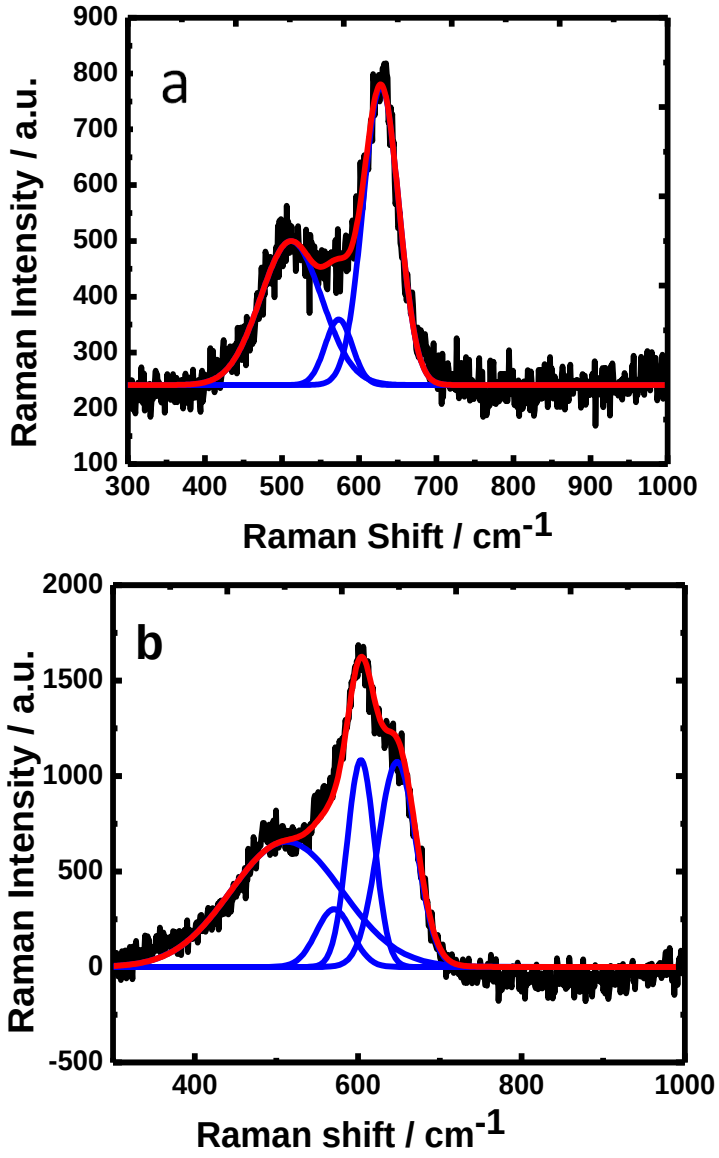

Figure 8-4| (a) Raman spectra of pristine $LiNi_{0.2}Mn_{0.6}Co_{0.2}O_2$ powder and (b) spent $LiNi_{0.2}Mn_{0.6}Co_{0.2}O_2$ cathode material after 50 cycles of testing with deconvoluted peaks.

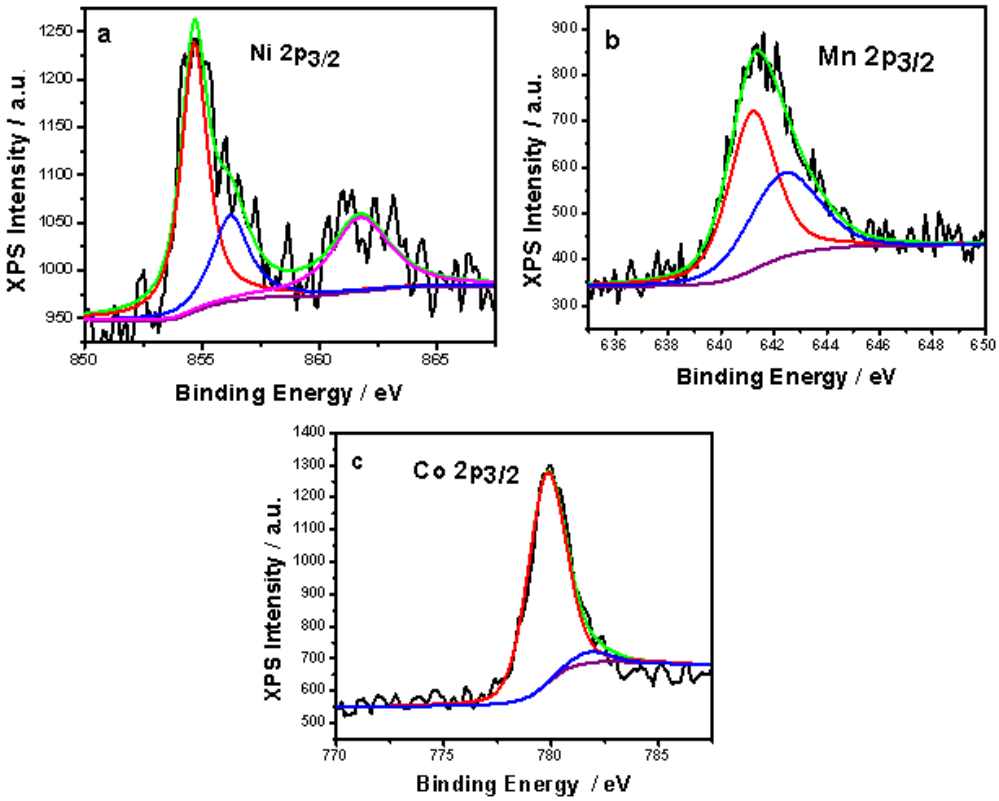

Figure 8-5| XPS high-resolution peaks of pristine $LiNi_{0.2}Mn_{0.6}Co_{0.2}O_2$ screening (a) Ni $2p_{3/2}$ (b) Mn $2p_{3/2}$ and (c) Co $2p_{3/2}$.

be related to the cation–anion bond lengths and polyhedral distortion occurring in $Li_xMn_2O_4$ [329]. Previously, similar case was already reported that the Raman scattering spectra of the $Li_{1+\delta}Mn_{2-\delta}O_4$ spinel, where dominant band centered at 630–650 cm^{-1} corresponded to the Mn–O stretching vibrations[330]. The fitted peaks are presenting two components at 647 and 604 cm^{-1} for the spent sample. It is possible to have Li ions in the 16d octahedral sites in $Li_{1+\delta}Mn_{2-\delta}O_4$, and therefore a distortion of the cubic lattice into tetragonal lattice is not an unexpected phenomenon. These leads into the breakdown of the translation symmetry because of the non-systematic location of the metal ions on the

octahedral sites; imposing some extra bands in addition to the Raman-active mode vibrations predicted by the space group theory for an ideal spinel structure[330]. Moreover, the two bands at 500 and 560 cm^{-1} in Figure 8-4(b) are assigned to E_g and A_{1g} Raman-active modes caused by the transition metal-oxygen arrangements in the layered lithium metal oxide with rhombohedral ($R\bar{3}m$) symmetry. However, these peaks remained unchanged even after cycling.

To determine the surface states of elements in the lithium NMC oxide, the X-ray photoelectron spectroscopy (XPS) was performed and typical results are presented in Figure 8-5(a) – (c). The best fitted peaks for the Ni $2p_{3/2}$ spectrum correspond to binding energy values. The main peak with a binding energy of 854.0 eV corresponds to the Ni^{2+} and the less prominent one at 856.3 eV corresponds to Ni^{3+} [332]. The deconvolution of the Mn $2p_{3/2}$ reveals binding energy values centered at 641.7 eV and 642.1 eV; the major one being the binding energy centered at 642.1 eV, ascribed to the manganese IV oxidation state, which is in agreement with the report by Shaju *et al.* [332]. The Mn^{3+} state is represented by the binding energy at 641.7 eV. Further analysis revealed the Co $2p_{3/2}$ peak located at 779.8 eV., which is assigned to Co^{3+} in Co_2O_3, re-confirming the +3 oxidation state of Co in the samples [333]. The surface elemental analysis is shown in Table A9(a) of Appendix 9, showing a deviation from the nominal values, this is not a surprising outcome because XPS elemental analysis can only provide a semi-quantitative surface composition up to about 10 nm depth into the surface of sample, and especially since $LiNi_{0.2}Mn_{0.6}Co_{0.2}O_2$ is a two-phase system, XPS data precludes the accurate determination of the bulk composition.

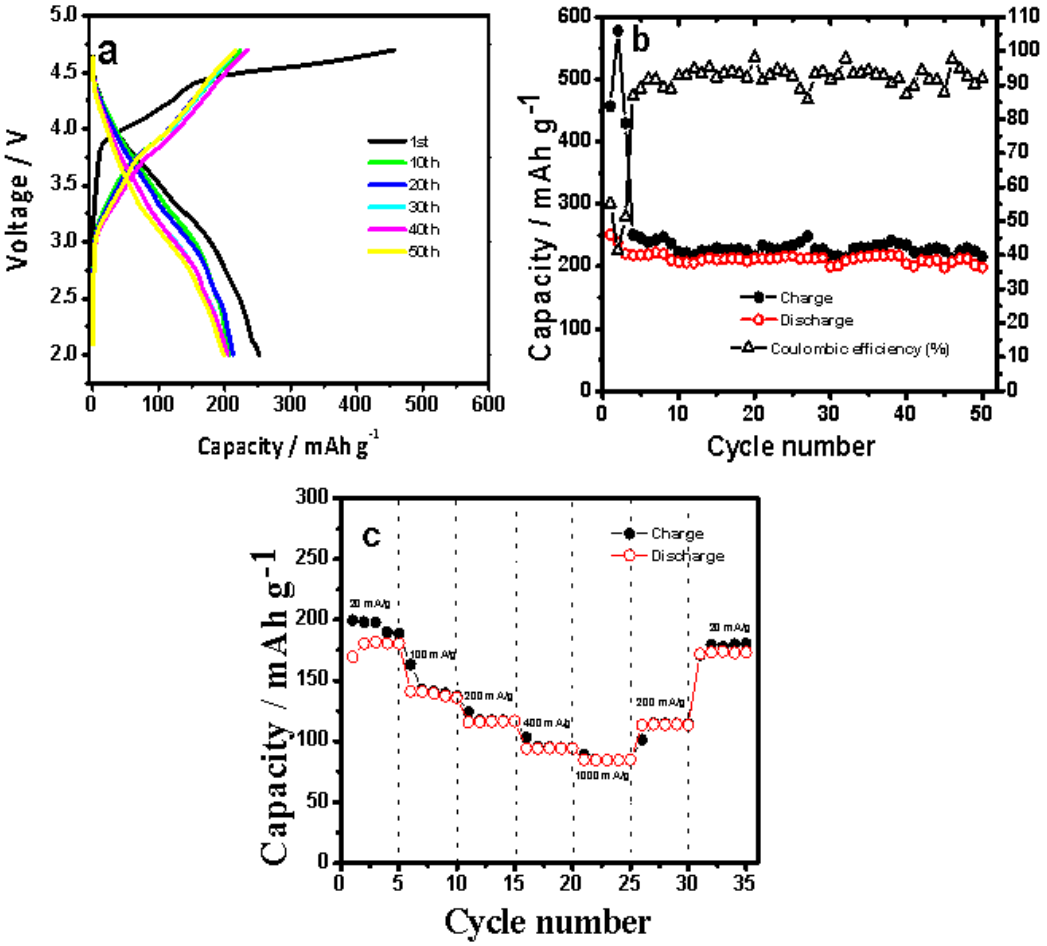

Figure 8-6| (a) Charge-discharge curves of $LiMn_{0.6}Ni_{0.2}Co_{0.2}O_2$ cathode electrode at a current of 10 mAg^{-1} (b) Capacities versus cycle number of $LiMn_{0.6}Ni_{0.2}Co_{0.2}O_2$ cathode electrode at a current of 10 mAg^{-1} over 50 charge-discharge cycles. The secondary axis shows the Coulombic efficiency over 50 cycles (c) C-rate tests of $LiNi_{0.2}Mn_{0.6}Co_{0.2}O_2$ cathode electrode for Li-ion battery at different current densities between 2.0 V to 4.7 V.

The electrochemical lithiation behavior is shown in Figure 8-6(a) which depicts the voltage profile of the $LiNi_{0.2}Mn_{0.6}Co_{0.2}O_2$ electrode during the galvanostatic charge–discharge cycles. Two regions are quite conspicuous in the first charge, and to some extent in the second charge cycle. The first sloping region from 3.9 V to 4.4 V could be assigned to the oxidation of transition metal ions to the +4 oxidation state, [334] while the second sloping region from 4.4 V to 4.7 V is consistent with the oxidation of O^{2-} ions to molecular oxygen, and the attendant extraction of lithium ions from the lattice in the form Li_2O [335]. The initial charge profile is accompanied with an irreversible voltage plateau at 4.4 V to 4.7 V, and can be ascribed to oxidation of Ni^{2+} to Ni^{4+} and Co^{3+} to Co^{4+}. During the oxygen loss plateau, the layered component is activated to remove Li_2O from the M layer leaving MO_2 in the electrode structure, MO_2 then serve as a host structure for reversible lithium intercalation/deintercalation so that the electrode can deliver capacity above 200 mAh g^{-1} between 2.0 V and 4.7 V [336]. However, the extensive removal of lithium and oxygen evolution results in the instability of electrode structure leading to breakdown of lattices and phase transformation from layered to spinel during the subsequent cycles. The unusually large charge capacity in the first cycle may be rationalized thus: when charging across the plateau at 4.5 V, parts of the metal ion are reduced accompanied with the removal of Li and O. The Mn ions are activated due to reduction and will participate in the following electrochemical reactions. The removal of Li and O from the lattice leads to the structural rearrangement, and the metal ions may migrate to the Li layer[337]. Part of removed oxygen from oxygen molecules, may be reduced in the discharge stage and provide extra capacity. Although some oxygen vacancies remain on the surface after the discharge process, the majority of oxygen vacancies are eliminated as well as certain amount of cation site,

resulting in large irreversible capacity during the first and second cycles [338]. The discharge profiles however indicate the re-insertion of lithium-ions and the accompanying reduction of the transition metal ions from +4 oxidation state [336]. While majority of the initial voltage-capacity profile fits the layered oxide narrative, nevertheless there are a few exceptions. For example, in the initial discharge curves, the plateau regions at ~2.7 V and ~2.1 V are associated with the intercalation/deintercalation of lithium ions from/to the empty octahedral site of the cubic spinel structure, which is followed by a cubic to tetragonal phase transition involving Jahn−Teller distortion [98]. Furthermore, the typical cycling performance of $LiNi_{0.2}Mn_{0.6}Co_{0.2}O_2$/Li cells is measured at $10mAg^{-1}$ during 50 cycles (Figure 8-6(b)). The specific capacity of the charge and discharge decreases steadily in the initial cycling stages until the 3rd round, where it is stabilized above a specific capacity of 210 $mAhg^{-1}$. In the first ten cycles, the Coulombic efficiency is raised from about 67% to almost 95% at the 10th cycle and remains at least 90 % until the 50th cycle. Specifically, the discharge capacity (with an initial capacity of 258 $mAhg^{-1}$) retains about 83% of its initial capacity, whereas the charge capacity; initially at 450 $mAhg^{-1}$ was only able to retain 58% of its capacity over the cycle period. It was reported that $LiNi_{0.3}Mn_{0.6}Co_{0.1}O_2$ with a similar chemistry and prepared by co-precipitation method delivers an initial discharge capacity of about 75 mAh g^{-1} (2.5 – 4.6 V) at a charging rate of 0.5 $mAcm^{-2}$ [327]. Furthermore, Table 8.1 shows comparison of method and performance of this work with published reports. To investigate the rate capability of the fabricated electrodes, the cells were charged and discharged at various current rates. Galvanostatic charge-discharge curves of $LiNi_{0.2}Mn_{0.6}Co_{0.2}O_2$ at current rates of 20, 100, 200, 400 and 1000 mA g^{-1} in the voltage range of 2.0 and 4.7 V are shown in Figure 8-6(c). The specific discharge capacity

upon increasing current rate to 20, 100, 200, 400 and 1000 mAg^{-1} are 180, 141, 116, 94, and 84, mAh g^{-1} respectively. On reducing the current rate to the initial value 20 mA g^{-1} after the rate performance testing, the $LiNi_{0.2}Mn_{0.6}Co_{0.2}O_2$ electrode still retains more than 97 % of its specific capacity with a value 175 mAh g^{-1}, indicating a good reversibility and high rate capability.

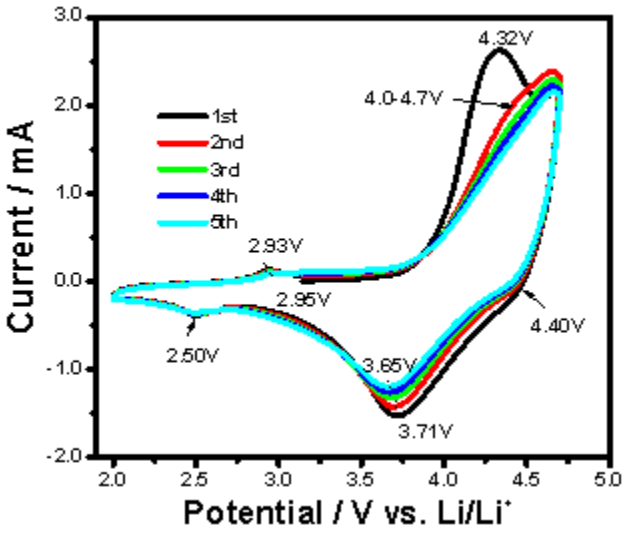

Figure 8-7| Cyclic voltammetry of Li $Ni_{0.2}Mn_{0.6}Co_{0.2}O_2$ cathode electrode at scan speed of 1.0 mV/s.

The cyclic voltammetry (CV) was conducted for $LiNi_{0.2}Mn_{0.6}Co_{0.2}O_2$ to evaluate the redox potential of the transition metal ions during cycling. Figure 8-7represents the first five cycles of the CV traces of the material between 2.0 and 4.7 V at 1 mV s^{-1} in which metallic lithium acts as the counter and reference electrodes. The shape of the CV provides some insight into the phase transitions that occur during lithium insertion and extraction. The anodic peak at 4.0–4.7 V is associated predominantly with the oxidation of Ni^{2+} to Ni^{3+}/Ni^{4+}, whereas the reverse sweep cathodic peak at 3.71 V is decreased to 3.65 V when the cycle progresses. The high redox potential 4.45 V/4.40V in the sample is due to the partial redox contribution from $Co^{3+} \leftrightarrow Co^{4+}$ that corresponds to the second electron transfer [339]. The small anodic peak at first charge seen around 2.93 V is as expected, and is attributable to $Mn^{3+} \rightarrow Mn^{4+} + e^-$ oxidation reaction, where the potential moves to a higher value (2.95 V at the 5th cycle) as the cycle advances. Moreover, the reduction peak below 3.0 V is allocated to the reduction of Mn^{4+} to Mn^{3+} [340]. This result is agreement with our earlier result that the Mn^{3+} oxidation state (from the spinel phase) is present at first charge.

Table 8.1 Comparison of this work with the performance of published flame/electric furnace spray pyrolyzed Li NMC oxides. Also, performance comparison is made between Li NMC oxide from co-precipitation and plasma-based method (this work) with similar chemistry.

	Synthesis		Chemistry	Voltage	Current rate	Initial Discharge (mAh/g)	Discharge after cycling(mAh/g)
Ref.	Method	Temp. /°C					
[341]	Electric furnace	900 (6h)	$0.2Li_2MnO_3 0.8LiNi_{0.33}Mn_{0.33}Co_{0.33}O_2$	2-4.8 V	25 mA/g	242	208(50 cycles)
[341]	Electric furnace	900 (6h)	$0.4Li_2MnO_3 0.6LiNi_{0.33}Mn_{0.33}Co_{0.33}O_2$	2-4.8 V	25 mA/g	283	229(50 cycles)
[341]	Electric furnace	900 (6h)	$0.5Li_2MnO_3 0.5LiNi_{0.33}Mn_{0.33}Co_{0.33}O_2$	2-4.8 V	25 mA/g	291	266(50 cycles)
[341]	Electric furnace	900 (6h)	$0.8Li_2MnO_3 0.2LiNi_{0.33}Mn_{0.33}Co_{0.33}O_2$	2-4.8 V	25 mA/g	234	204(50 cycles)
[342]	Electric furnace	700 (6h)	$0.3Li_2MnO_3 0.7LiNi_{0.5}Mn_{0.5}O_2$	2-4.8 V	30 mA/g	177	<<177

[342]	Electric furnace	750 (6h)	$0.3Li_2MnO_3 0.7LiNi_{0.5}Mn_{0.5}O_2$	2-4.8 V	30 mA/g	202	<<202
[342]	Electric furnace	800 (6h)	$0.3Li_2MnO_3 0.7LiNi_{0.5}Mn_{0.5}O_2$	2-4.8 V	30 mA/g	215	205(40 cycles)
[342]	Electric furnace	850 (6h)	$0.3Li_2MnO_3 0.7LiNi_{0.5}Mn_{0.5}O_2$	2-4.8 V	30mA/g	212	<<212
[343]	Electric furnace	900 (6h)	$LiNi_{0.33}Mn_{0.33}Co_{0.33}O_2$	2.75-4.5V	0.1C	195	<<195
[343]	Electric furnace	900 (6h)	$LiNi_{0.8}Mn_{0.05}Co_{0.15}O_2$		0.1C	218	<<218
[344]	Flame	800 (3h)	$LiNi_{0.33}Mn_{0.33}Co_{0.33}O_2$	2.8-4.4V		168	120(30 cycles)
[345]	Co-precipitation	450 (12h) 900 (12h)	$LiNi_{0.3}Mn_{0.6}Co_{0.1}O_2$	2.5-4.6V	0.5mA/cm^2	80	<<80
This work	Plasma	-	$LiNi_{0.20}Mn_{0.60}Co_{0.20}O_2$	2-4.7V	10mA/g	258	210(50 cycles)

8.4 Chapter Summary

Nickel manganese cobalt (NMC) oxides have been pursued for stable and high energy density cathodes in lithium ion batteries for years. The current synthesis techniques based on co-precipitation and hydrothermal techniques require reaction timescales on the order of several hours making them difficult for scale-up. Here, we present a scalable manufacturing technique based on atmospheric plasma-based spray pyrolysis for producing NMC (and Li-NMC) with reaction timescales of the order of minutes. Results show that the chemistry of resulting materials (Ni/Mn/Co ratio) can be controlled from precursor composition. Specifically, the compound $LiNi_{0.2}Mn_{0.6}Co_{0.2}O_2$, is prepared by the atmospheric plasma-assisted synthesis method. The resulting $LiNi_{0.2}Mn_{0.6}Co_{0.2}O_2$ cathode material demonstrates a durable performance with an initial discharge specific capacity of 258 mAh g^{-1} while maintaining above 210 mAh g^{-1} after 50 cycles.

CHAPTER 9

CONCLUSIONS AND RECOMMENDATIONS

9.1 Conclusions

A synthesis technique based on plasma oxidation of liquid droplets for producing mixed metal oxide solid solutions with controllable composition over a wide-ranging composition, has been successfully demonstrated. Specific experiments were presented with binary and ternary metal oxides involving nickel, manganese and iron as elements. The selective formation of rocksalt and spinel solid solution is a direct consequence of the precise compositional control shown in this method and will be very useful in altering catalytic properties in many process applications. As an example, we have demonstrated rapid screening of several mixed metal oxide solid solution systems by testing a series of manganese substituted nickel ferrite materials for their activity with OER reaction in alkaline media. The results showed that the presence of a small amount of manganese ($z=0.20$) caused a significant drop in the overpotential with excellent Tafel kinetics.

Additionally, we have shown through series of time-controlled experiments that the processes leading up to the formation of metastable solid-solution, specifically the non-stoichiometric complex oxides involve the nucleation of monometallic oxide phases from an amorphous oxide nutrient followed by their solid-state reaction into an intermediate mixed oxide phase until the non-stoichiometric mixed phase is formed. Evidence also suggests the spontaneity of the plasma process is heavily reliant upon the large exothermic

heat released from the recombinative reactions among plasma species present in the plasma media.

By synergistically combining Ir with W, a mixed-metal oxide phase with noble metal content as low as 1% had anodic stability in acid with promising OER catalysis. The critical electrocatalytic properties were enabled by oxidation in a non-equilibrium plasma environment, with traditional thermal oxidation instead resulting in significantly inferior OER activity. Although much work remains to be done to fundamentally explain the shift in catalysis, the materials characterization indicated the plasma method led to better catalysis by promoting larger crystals of the homogenous iridium polytungstate phase. The new material has promise for advancing the scalability of acidic water electrolysis. Additionally, the results demonstrate that the wide composition space of thermally processed oxides which have failed to show noteworthy catalysis may yield different outcomes and new active compositions of metastable phases when processed instead via non-equilibrium plasma oxidation.

A series of $La_{1-x}Ca_xNi_{0.5}Co_{0.5}O_{3-\delta}$ double perovskite electrocatalysts in basic media OER has been prepared *via* the plasma route. Activity trend has been validated with DFT calculations, leading to a new activity descriptor for charge-transfer type oxides. The catalyst with calcium content of $x = 0.1$ shows overpotential comparable with the best OER perovskite based electrocatalysts reported, with overpotential as low as 330 mV at current density of 10 $mAcm^{-2}$ in alkaline media and controlled current chronoamperometry displayed a 2h stable potential-time profile for all electrocatalysts under study. The high activity and stability of the low-calcium content perovskite is ascribed to the small charge transfer gap resulting into stronger transition metal 3*d*–O 2*p* hybridization, the O 2*p* band

occupying the valence band in the band structure. As a result, a strategy for enhancing hybridization and hence OER activity in charge transfer oxides would be to design catalysts with O 2*p* band several energy levels away from the Fermi level.

Also, it is demonstrated in this dissertation, for the first time, the synthesis of a mixed spinel-layered oxide and lithium-excess layered cathode materials by atmospheric plasma spray pyrolysis method. The obtained $LiNi_{0.2}Mn_{0.6}Co_{0.2}O_2$ cathodes exhibited an initial discharge capacity of about 258 mAh g^{-1} at a current of 10 mA g^{-1} rate with high electrochemical cycling stability. The cycle life shows satisfactory cathode stability as the discharge capacity remains above 210 mAh g^{-1}after 50 cycles. Plasma spray pyrolysis was also proven to be a futuristic single-step synthesis of lithiated NMC compounds, and as such is potentially useful for obtaining NMC cathode materials with rather controlled composition, crystallinity, and morphology at high production rates.

To conclude, the plasma-based oxidation of liquid precursors has been demonstrated to be a scalable and viable route for synthesizing efficient materials for energy conversion and storage processes, specifically, in electrocatalytic water splitting and rechargeable battery applications. The study has also demonstrated that many of the complex oxide-based energy materials in current literature may be underperforming as a result of non-homogeneity of phase. We have compared performances of the oxide prepared *via* plasma and materials prepared through thermal oxidation in electrochemical conversion processes, and the performance of the plasma-synthesized oxides ranges from norm to exceedingly better in many of these examples. This superior performance is attributed to the firm control of composition enabled by the non-equilibrium conditions in the plasma media highlighting the significance of designing materials far from equilibrium

in solving the grand challenges in energy science. Overall, the study of the rudimentary nucleation and growth pathways regarding the formation of non-equilibrium complex oxides has intellectual merit, and thus will add to our current understanding of the design and synthesis of non-equilibrium materials.

9.2 Recommendations and Future Experiments

The precise structural distinctions which led to the outstanding activity of the plasma-prepared $W_{1-x}Ir_xO_{3-\delta}$ samples as compared with the thermally oxidized samples is still rather inconclusive, although Raman and X-ray photoelectron spectroscopy offer little insight. Extended X-ray Absorption Fine Structure or EXAFS is another test based on synchrotron X-rays, which would provide additional insights or perhaps even conclusive evidence about the superior performance of plasma-synthesized samples by probing the local structure of Ir atoms in WO_3 lattice to retrieve information such as coordination number, distance of neighboring atoms, and disorder of neighboring atoms. Additionally, there has been a growing interest in the correlation of OER activity with oxygen vacancies *via* lattice oxygen mediation[45, 55], and so, measurement of the oxygen vacancies (δ) in the plasma-synthesized samples and comparing that with the thermally prepared oxides can help gain more understanding about this dichotomy.

It was established that the recombinative heating plays a crucial role in the formation mechanism of complex oxides derivable from the plasma method. Perhaps a synergy of this exothermic heat and the plasma species are responsible for this outcome. So, a method for isolating some of these species could be instructive to understanding the mechanism of formation of oxides going forward. To investigate the impact of the charged and neutral particles in the oxidation of metal precursors, it is essential to decouple the

effects of the charged particles from neutral species because it is unclear the role both species play. Electromagnetic or dielectric filters can help screen out charged particles in the plasma, allowing only the neutrals. Another recommended method for plasma species screening is to introduce chemical scavengers into the liquid precursors to screen out the solvated electrons. The chemical scavengers proposed are chemical agents which leaves no cationic footprint in the final product. For example, $NaNO_3$ is an important scavenger for H and $e^-_{(aq)}$ but would leave Na^+ in the complex metal oxide. Hence, the proposed scavengers would be hydrogen peroxide (H_2O_2) − a good scavenger for OH, H and $e^-_{(aq)}$ and 2-propanol – an excellent scavenger for OH and H only but a weak scavenger for $e^-_{(aq)}$, acetone is another recommended chemical scavenger for solvated electrons. Oxygen atom neutral is an important species which may be contributing a lot to the oxidation mechanism, therefore; experiments to attenuate its contribution will be to key establishing the oxide formation mechanism. Fortunately, there are catalysts that facilitate the surface recombination reaction of O neutrals into O_2 molecules, which can be adopted in future experiments.

The plasma oxidation rate is rapid due to the fast kinetics resulting from rapid heating and cooling rates of the plasma. One speculation is that the synergy from heat and plasma in hot plasmas are necessary for the formation of complex metal oxides. This speculation will be debunked if successful, an experiment to decouple the effect of reactive heating temperature in the plasma oxidation process. This can be realized by performing an experiment to oxidize liquid precursors in atmospheric cold plasma. Cold plasmas are partially ionized plasmas with low concentration of radicals, the recombination of these radicals are key components of the plasma energetics. However, in the event that this

experiment is not successful, an experiment that combines rapid externally heating source and cold plasma should be investigated. Tungsten heating lamps or xenon lamps can have ramp rate between 50 - 300°C per sec, mimicking the fast heating rate in thermal plasmas. This is the heat source currently in use by the semiconductor industries in a process known as rapid thermal processing (RTP). Also, stand-alone RTP should be carried out on liquid precursors regardless of the outcome of the last recommended experiment.

REFERENCES

1. Jain, A.; Ong, S. P.; Hautier, G.; Chen, W.; Richards, W. D.; Dacek, S.; Cholia, S.; Gunter, D.; Skinner, D.; Ceder, G., Commentary: The Materials Project: A materials genome approach to accelerating materials innovation. *Apl Materials* **2013,** *1* (1), 011002.
2. Tabor, D. P.; Roch, L. M.; Saikin, S. K.; Kreisbeck, C.; Sheberla, D.; Montoya, J. H.; Dwaraknath, S.; Aykol, M.; Ortiz, C.; Tribukait, H., Accelerating the discovery of materials for clean energy in the era of smart automation. *Nat. Rev. Mater.* **2018,** *3*, 5-20.
3. Boix, P. P.; Nonomura, K.; Mathews, N.; Mhaisalkar, S. G., Current progress and future perspectives for organic/inorganic perovskite solar cells. *Materials today* **2014,** *17* (1), 16-23.
4. THE COST COMPONENTS OF A LITHIUM ION BATTERY. 2016.
5. Lewis, N. S.; Nocera, D. G. J. P. o. t. N. A. o. S., Powering the planet: Chemical challenges in solar energy utilization. **2006,** *103* (43), 15729-15735.
6. Bruggeman, P.; Iza, F.; Lauwers, D.; Gonzalvo, Y. A., Mass spectrometry study of positive and negative ions in a capacitively coupled atmospheric pressure RF excited glow discharge in He–water mixtures. *Journal of Physics D: Applied Physics* **2009,** *43* (1), 012003.
7. Moreno-Hernandez, I. A.; MacFarland, C. A.; Read, C. G.; Papadantonakis, K. M.; Brunschwig, B. S.; Lewis, N. S. J. E.; Science, E., Crystalline nickel manganese antimonate as a stable water-oxidation catalyst in aqueous 1.0 MH 2 SO 4. **2017,** *10* (10), 2103-2108.
8. Abdi, F. F.; Berglund, S. P., Recent developments in complex metal oxide photoelectrodes. *Journal of Physics D: Applied Physics* **2017,** *50* (19), 193002.
9. BESAC, B. E. S. A. C., Grand Challenges. United States Department of Energy, O. o. S., Ed. United States Department of Energy: 2007.
10. G.R. Flemming, M. A. R., Directing Matter and Energy: Five Challenges for Science and the Imagination. 2007.
11. Li, F.; Li, J.-F.; Zhao, L.-D.; Xiang, K.; Liu, Y.; Zhang, B.-P.; Lin, Y.-H.; Nan, C.-W.; Zhu, H.-M. J. E.; Science, E., Polycrystalline BiCuSeO oxide as a potential thermoelectric material. **2012,** *5* (5), 7188-7195.
12. Goodenough, J. B., Design considerations. *Solid State Ionics* **1994,** *69* (3), 184-198.
13. Bockris, J. O. M.; Otagawa, T., The Electrocatalysis of Oxygen Evolution on Perovskites. *Journal of The Electrochemical Society* **1984,** *131* (2), 290-302.
14. Katz, J. E.; Gingrich, T. R.; Santori, E. A.; Lewis, N. S., Combinatorial synthesis and high-throughput photopotential and photocurrent screening of mixed-metal oxides for photoelectrochemical water splitting. *Energy & Environmental Science* **2009,** *2* (1), 103-112.
15. Subedi, A.; Zhang, L.; Singh, D. J.; Du, M. H., Density functional study of FeS, FeSe, and FeTe: Electronic structure, magnetism, phonons, and superconductivity. *Physical Review B* **2008,** *78* (13), 134514.

16. Armijo, J. J. O. o. m., The kinetics and mechanism of solid-state spinel formation—A review and critique. **1969,** *1* (2), 171-198.
17. Stein, A.; Keller, S. W.; Mallouk, T. E. J. S., Turning down the heat: Design and mechanism in solid-state synthesis. **1993,** *259* (5101), 1558-1564.
18. Banger, K.; Yamashita, Y.; Mori, K.; Peterson, R.; Leedham, T.; Rickard, J.; Sirringhaus, H. J. N. m., Low-temperature, high-performance solution-processed metal oxide thin-film transistors formed by a 'sol–gel on chip'process. **2011,** *10* (1), 45.
19. Rojas, R. M.; Vila, E.; García, O.; de Vidales, J. L. M. J. J. o. M. C., Thermal behaviour and reactivity of manganese cobaltites Mn x Co 3–x O 4 (0.0⩽ x⩽ 1.0) obtained at low temperature. **1994,** *4* (10), 1635-1639.
20. Matsushita, Y.; Ueda, H.; Ueda, Y. J. N. M., Flux crystal growth and thermal stabilities of LiV 2 O 4. **2005,** *4* (11), 845.
21. Pechini, M. P., Method of preparing lead and alkaline earth titanates and niobates and coating method using the same to form a capacitor. Google Patents: 1967.
22. Lengyel, M.; Zhang, X.; Atlas, G.; Bretscher, H. L.; Belharouak, I.; Axelbaum, R. L., Composition optimization of layered lithium nickel manganese cobalt oxide materials synthesized via ultrasonic spray pyrolysis. *Journal of The Electrochemical Society* **2014,** *161* (9), A1338-A1349.
23. Seley, D.; Ayers, K.; Parkinson, B. A., Combinatorial Search for Improved Metal Oxide Oxygen Evolution Electrocatalysts in Acidic Electrolytes. *ACS Combinatorial Science* **2013,** *15* (2), 82-89.
24. Kumar, V.; Kim, J. H.; Pendyala, C.; Chernomordik, B.; Sunkara, M. K., Gas-phase, bulk production of metal oxide nanowires and nanoparticles using a microwave plasma jet reactor. *The Journal of Physical Chemistry C* **2008,** *112* (46), 17750-17754.
25. Hasegawa, M.; Kato, Y.; Kagawa, M.; Syono, Y., Effect of additive oxides on ultrafine CeO 2 particles synthesized by the spray-ICP technique. *Journal of materials science letters* **1996,** *15* (18), 1608-1611.
26. Suzuki, M.; Kagawa, M.; Syono, Y.; Hirai, T., Synthesis of ultrafine single-component oxide particles by the spray-ICP technique. *Journal of Materials science* **1992,** *27* (3), 679-684.
27. Schaefer, M.; Kumar, A.; Sankaran, R. M.; Schlaf, R., Synthesis and in vacuo deposition of iron oxide nanoparticles by microplasma-assisted decomposition of ferrocene. *Journal of Applied Physics* **2014,** *116* (13), 133703.
28. Wegner, K.; Pratsinis, S. E. J. C. E. S., Scale-up of nanoparticle synthesis in diffusion flame reactors. **2003,** *58* (20), 4581-4589.
29. Marr, M.; Kuhn, J.; Metcalfe, C.; Harris, J.; Kesler, O., Electrochemical performance of solid oxide fuel cells having electrolytes made by suspension and solution precursor plasma spraying. *Journal of Power Sources* **2014,** *245*, 398-405.
30. Chang, S.-M.; Rodríguez Tolava, E. F.; Yang, Y.-J.; Li, H.-C.; Lee, R.-C.; Wu, N.-L.; Hsu, C.-C., One-Step Fast Synthesis of Li4Ti5O12 Particles Using an Atmospheric Pressure Plasma Jet. *Journal of the American Ceramic Society* **2014,** *97* (3), 708-712.
31. Smith, B., and Weng, W. E. Go, *China - A History in Art*. Gemini Smith Inc.: New York, 1972.
32. Ring, T. A., *Fundamentals of ceramic powder processing and synthesis*. Elsevier: 1996.

33. Gopalakrishnan, J. J. C. o. M., Chimie douce approaches to the synthesis of metastable oxide materials. **1995,** *7* (7), 1265-1275.
34. Sakka, S. J. J. o. s.-g. s.; technology, Sol-gel technology as reflected in journal of sol-gel science and technology. **2003,** *26* (1-3), 29-33.
35. Berger, W. G. a. E., *Dtsch. Reichspatent* **1939,** *736* (411).
36. Dislich, H.; Hinz, P. J. J. o. N.-C. S., History and principles of the sol-gel process, and some new multicomponent oxide coatings. **1982,** *48* (1), 11-16.
37. Ormerod, R. M. J. C. S. R., Solid oxide fuel cells. **2003,** *32* (1), 17-28.
38. Shaju, K.; Rao, G. S.; Chowdari, B. J. E. A., Performance of layered Li (Ni1/3Co1/3Mn1/3) O2 as cathode for Li-ion batteries. **2002,** *48* (2), 145-151.
39. Suntivich, J.; May, K. J.; Gasteiger, H. A.; Goodenough, J. B.; Shao-Horn, Y. J. S., A perovskite oxide optimized for oxygen evolution catalysis from molecular orbital principles. **2011,** *334* (6061), 1383-1385.
40. Liang, Y.; Wang, H.; Zhou, J.; Li, Y.; Wang, J.; Regier, T.; Dai, H. J. J. o. t. A. C. S., Covalent hybrid of spinel manganese–cobalt oxide and graphene as advanced oxygen reduction electrocatalysts. **2012,** *134* (7), 3517-3523.
41. Gaultois, M. W.; Barton, P. T.; Birkel, C. S.; Misch, L. M.; Rodriguez, E. E.; Stucky, G. D.; Seshadri, R. J. J. o. P. C. M., Structural disorder, magnetism, and electrical and thermoelectric properties of pyrochlore Nd2Ru2O7. **2013,** *25* (18), 186004.
42. Qiao, B.; Wang, A.; Yang, X.; Allard, L. F.; Jiang, Z.; Cui, Y.; Liu, J.; Li, J.; Zhang, T. J. N. c., Single-atom catalysis of CO oxidation using Pt 1/FeO x. **2011,** *3* (8), 634.
43. He, J.; Liu, Y.; Funahashi, R. J. J. o. M. R., Oxide thermoelectrics: The challenges, progress, and outlook. **2011,** *26* (15), 1762-1772.
44. Trotochaud, L.; Ranney, J. K.; Williams, K. N.; Boettcher, S. W. J. J. o. t. A. C. S., Solution-cast metal oxide thin film electrocatalysts for oxygen evolution. **2012,** *134* (41), 17253-17261.
45. Mefford, J. T.; Rong, X.; Abakumov, A. M.; Hardin, W. G.; Dai, S.; Kolpak, A. M.; Johnston, K. P.; Stevenson, K. J. J. N. c., Water electrolysis on La 1− x Sr x CoO 3− δ perovskite electrocatalysts. **2016,** *7*, 11053.
46. Cheng, F.; Shen, J.; Peng, B.; Pan, Y.; Tao, Z.; Chen, J. J. N. c., Rapid room-temperature synthesis of nanocrystalline spinels as oxygen reduction and evolution electrocatalysts. **2011,** *3* (1), 79.
47. Iizuka, K.; Wato, T.; Miseki, Y.; Saito, K.; Kudo, A. J. J. o. t. A. C. S., Photocatalytic reduction of carbon dioxide over Ag cocatalyst-loaded ALa4Ti4O15 (A= Ca, Sr, and Ba) using water as a reducing reagent. **2011,** *133* (51), 20863-20868.
48. Wang, S.; Hou, Y.; Wang, X., Development of a Stable MnCo2O4 Cocatalyst for Photocatalytic CO2 Reduction with Visible Light. *ACS Applied Materials & Interfaces* **2015,** *7* (7), 4327-4335.
49. Yoshino, A. S., K.; Nakajima, T. 1985.
50. Ohzuku, T.; Makimura, Y. J. C. L., Layered lithium insertion material of LiCo1/3Ni1/3Mn1/3O2 for lithium-ion batteries. **2001,** *30* (7), 642-643.
51. Liu, W.; Farrington, G.; Chaput, F.; Dunn, B. J. J. o. T. E. S., Synthesis and electrochemical studies of spinel phase LiMn2 O 4 cathode materials prepared by the Pechini process. **1996,** *143* (3), 879-884.

52. Tang, Y.; Yang, L.; Fang, S.; Qiu, Z. J. E. A., Li4Ti5O12 hollow microspheres assembled by nanosheets as an anode material for high-rate lithium ion batteries. **2009,** *54* (26), 6244-6249.
53. Peng, H.; Wu, Q.; Xiao, L. J. J. o. s.-g. s.; technology, Low temperature synthesis of Li 5 La 3 Nb 2 O 12 with cubic garnet-type structure by sol–gel process. **2013,** *66* (1), 175-179.
54. Bachman, J. C.; Muy, S.; Grimaud, A.; Chang, H.-H.; Pour, N.; Lux, S. F.; Paschos, O.; Maglia, F.; Lupart, S.; Lamp, P. J. C. r., Inorganic solid-state electrolytes for lithium batteries: mechanisms and properties governing ion conduction. **2015,** *116* (1), 140-162.
55. Kim, T. W.; Choi, K.-S. J. S., Nanoporous BiVO4 photoanodes with dual-layer oxygen evolution catalysts for solar water splitting. **2014,** *343* (6174), 990-994.
56. Prévot, M. S.; Guijarro, N.; Sivula, K. J. C., Enhancing the Performance of a Robust Sol–Gel-Processed p-Type Delafossite CuFeO2 Photocathode for Solar Water Reduction. **2015,** *8* (8), 1359-1367.
57. Xiong, D.; Xu, Z.; Zeng, X.; Zhang, W.; Chen, W.; Xu, X.; Wang, M.; Cheng, Y.-B. J. J. o. M. C., Hydrothermal synthesis of ultrasmall CuCrO 2 nanocrystal alternatives to NiO nanoparticles in efficient p-type dye-sensitized solar cells. **2012,** *22* (47), 24760-24768.
58. Gaur, S.; Haynes, D. J.; Spivey, J. J. J. A. C. A. G., Rh, Ni, and Ca substituted pyrochlore catalysts for dry reforming of methane. **2011,** *403* (1-2), 142-151.
59. Lima, S.; Assaf, J.; Pena, M.; Fierro, J. J. A. C. A. G., Structural features of La1− xCexNiO3 mixed oxides and performance for the dry reforming of methane. **2006,** *311*, 94-104.
60. Estephane, J.; Aouad, S.; Hany, S.; El Khoury, B.; Gennequin, C.; El Zakhem, H.; El Nakat, J.; Aboukaïs, A.; Aad, E. A. J. i. j. o. h. e., CO2 reforming of methane over Ni–Co/ZSM5 catalysts. Aging and carbon deposition study. **2015,** *40* (30), 9201-9208.
61. Ohta, H.; Sugiura, K.; Koumoto, K. J. I. c., Recent progress in oxide thermoelectric materials: p-type Ca3Co4O9 and n-type SrTiO3−. **2008,** *47* (19), 8429-8436.
62. Ohtaki, M.; Araki, K.; Yamamoto, K. J. J. o. E. M., High thermoelectric performance of dually doped ZnO ceramics. **2009,** *38* (7), 1234-1238.
63. Terasaki, I.; Sasago, Y.; Uchinokura, K. J. P. R. B., Large thermoelectric power in NaCo 2 O 4 single crystals. **1997,** *56* (20), R12685.
64. Li, S.; Funahashi, R.; Matsubara, I.; Ueno, K.; Yamada, H. J. J. o. M. C., High temperature thermoelectric properties of oxide Ca9Co12O28. **1999,** *9* (8), 1659-1660.
65. Shen, J.; Liu, X.; Zhu, T.; Zhao, X. J. J. o. m. s., Improved thermoelectric properties of La-doped Bi 2 Sr 2 Co 2 O 9-layered misfit oxides. **2009,** *44* (7), 1889-1893.
66. Androulakis, J.; Migiakis, P.; Giapintzakis, J. J. A. P. L., La 0.95 Sr 0.05 CoO 3: an efficient room-temperature thermoelectric oxide. **2004,** *84* (7), 1099-1101.
67. Kobayashi, W.; Hébert, S.; Pelloquin, D.; Pérez, O.; Maignan, A. J. P. R. B., Enhanced thermoelectric properties in a layered rhodium oxide with a trigonal symmetry. **2007,** *76* (24), 245102.
68. Meesala, Y.; Jena, A.; Chang, H.; Liu, R.-S. J. A. E. L., Recent advancements in Li-ion conductors for all-solid-state Li-ion batteries. **2017,** *2* (12), 2734-2751.
69. Kamaya, N.; Homma, K.; Yamakawa, Y.; Hirayama, M.; Kanno, R.; Yonemura, M.; Kamiyama, T.; Kato, Y.; Hama, S.; Kawamoto, K. J. N. m., A lithium superionic conductor. **2011,** *10* (9), 682.

70. Thangadurai, V.; Weppner, W. J. A. F. M., Li6ALa2Ta2O12 (A= Sr, Ba): novel garnet-like oxides for fast lithium ion conduction. **2005,** *15* (1), 107-112.
71. Fanah, S. J.; Yu, M.; Huq, A.; Ramezanipour, F. J. J. o. M. C. A., Insight into lithium-ion mobility in Li 2 La (TaTi) O 7. **2018,** *6* (44), 22152-22160.
72. Bruce, P. G.; West, A. J. J. o. T. E. S., The A-C Conductivity of Polycrystalline LISICON, Li2+ 2x Zn1− x GeO4, and a Model for Intergranular Constriction Resistances. **1983,** *130* (3), 662-669.
73. Billaud, J.; Eames, C.; Tapia-Ruiz, N.; Roberts, M. R.; Naylor, A. J.; Armstrong, A. R.; Islam, M. S.; Bruce, P. G. J. A. E. M., Evidence of Enhanced Ion Transport in Li-Rich Silicate Intercalation Materials. **2017,** *7* (11), 1601043.
74. SBIR, U. N. https://www.navysbir.com/n16_2/N162-107.htm.
75. Jiao, Y.; Zheng, Y.; Jaroniec, M.; Qiao, S. Z. J. C. S. R., Design of electrocatalysts for oxygen-and hydrogen-involving energy conversion reactions. **2015,** *44* (8), 2060-2086.
76. McCrory, C. C. L.; Jung, S.; Ferrer, I. M.; Chatman, S. M.; Peters, J. C.; Jaramillo, T. F., Benchmarking Hydrogen Evolving Reaction and Oxygen Evolving Reaction Electrocatalysts for Solar Water Splitting Devices. *Journal of the American Chemical Society* **2015,** *137* (13), 4347-4357.
77. Kadakia, K.; Datta, M. K.; Velikokhatnyi, O. I.; Jampani, P.; Park, S. K.; Saha, P.; Poston, J. A.; Manivannan, A.; Kumta, P. N. J. i. j. o. h. e., Novel (Ir, Sn, Nb) O2 anode electrocatalysts with reduced noble metal content for PEM based water electrolysis. **2012,** *37* (4), 3001-3013.
78. Sun, W.; Cao, L.-m.; Yang, J. J. J. o. M. C. A., Conversion of inert cryptomelane-type manganese oxide into a highly efficient oxygen evolution catalyst via limited Ir doping. **2016,** *4* (32), 12561-12570.
79. Grimaud, A.; May, K. J.; Carlton, C. E.; Lee, Y.-L.; Risch, M.; Hong, W. T.; Zhou, J.; Shao-Horn, Y. J. N. c., Double perovskites as a family of highly active catalysts for oxygen evolution in alkaline solution. **2013,** *4*, 2439.
80. Nørskov, J. K.; Abild-Pedersen, F.; Studt, F.; Bligaard, T. J. P. o. t. N. A. o. S., Density functional theory in surface chemistry and catalysis. **2011,** *108* (3), 937-943.
81. Hong, W. T.; Risch, M.; Stoerzinger, K. A.; Grimaud, A.; Suntivich, J.; Shao-Horn, Y. J. E.; Science, E., Toward the rational design of non-precious transition metal oxides for oxygen electrocatalysis. **2015,** *8* (5), 1404-1427.
82. Sabatier, P., Hydrogénations et déshydrogénations par catalyse. *Berichte der deutschen chemischen Gesellschaft* **1911,** *44* (3), 1984-2001.
83. Morozan, A.; Jousselme, B.; Palacin, S. J. E.; Science, E., Low-platinum and platinum-free catalysts for the oxygen reduction reaction at fuel cell cathodes. **2011,** *4* (4), 1238-1254.
84. Zhang, J.; Yang, H.; Fang, J.; Zou, S. J. N. l., Synthesis and oxygen reduction activity of shape-controlled Pt3Ni nanopolyhedra. **2010,** *10* (2), 638-644.
85. Paffett, M.; Daube, K.; Gottesfeld, S.; Campbell, C. J. J. o. e. c.; electrochemistry, i., Electrochemical and surface science investigations of PtCr alloy electrodes. **1987,** *220* (2), 269-285.
86. Feng, Y.-Y.; Zhang, G.-R.; Ma, J.-H.; Liu, G.; Xu, B.-Q. J. P. C. C. P., Carbon-supported Pt_{χ} Ag nanostructures as cathode catalysts for oxygen reduction reaction. **2011,** *13* (9), 3863-3872.

87. Domínguez, C.; Pérez-Alonso, F.; Salam, M. A.; De La Fuente, J. G.; Al-Thabaiti, S.; Basahel, S.; Peña, M.; Fierro, J.; Rojas, S. J. i. j. o. h. e., Effect of transition metal (M: Fe, Co or Mn) for the oxygen reduction reaction with non-precious metal catalysts in acid medium. **2014,** *39* (10), 5309-5318.
88. Zhu, Y.; Zhou, W.; Yu, J.; Chen, Y.; Liu, M.; Shao, Z. J. C. o. M., Enhancing electrocatalytic activity of perovskite oxides by tuning cation deficiency for oxygen reduction and evolution reactions. **2016,** *28* (6), 1691-1697.
89. Manthiram, A. J. A. c. s., An outlook on lithium ion battery technology. **2017,** *3* (10), 1063-1069.
90. Armand, M.; Tarascon, J. M., Building better batteries. *Nature* **2008,** *451*, 652.
91. (Office of Technology Transitions), D. o. E., **July 2016**.
92. Xia, H.; Luo, Z.; Xie, J., Nanostructured LiMn2O4 and their composites as high-performance cathodes for lithium-ion batteries. *Progress in Natural Science: Materials International* **2012,** *22* (6), 572-584.
93. Thackeray, M. M.; David, W. I. F.; Bruce, P. G.; Goodenough, J. B., Lithium insertion into manganese spinels. *Materials Research Bulletin* **1983,** *18* (4), 461-472.
94. Shin, Y.; Manthiram, A., Factors Influencing the Capacity Fade of Spinel Lithium Manganese Oxides. *Journal of The Electrochemical Society* **2004,** *151* (2), A204-A208.
95. Gummow, R. J.; de Kock, A.; Thackeray, M. M., Improved capacity retention in rechargeable 4 V lithium/lithium-manganese oxide (spinel) cells. *Solid State Ionics* **1994,** *69* (1), 59-67.
96. Xia, Y.; Yoshio, M., An Investigation of Lithium Ion Insertion into Spinel Structure Li-Mn-O Compounds. *Journal of The Electrochemical Society* **1996,** *143* (3), 825-833.
97. Xiao, B.; Sun, X. J. A. E. M., Surface and Subsurface Reactions of Lithium Transition Metal Oxide Cathode Materials: An Overview of the Fundamental Origins and Remedying Approaches. **2018,** *8* (29), 1802057.
98. Park, S.-H.; Oh, S.-W.; Yoon, C.-S.; Myung, S.-T.; Sun, Y.-K., LiNi0.5Mn1.5 O 4 Showing Reversible Phase Transition on 3 V Region. *Electrochemical and Solid-State Letters* **2005,** *8* (3), A163-A167.
99. Myung, S.-T.; Noh, H.-J.; Yoon, S.-J.; Lee, E.-J.; Sun, Y.-K., Progress in High-Capacity Core–Shell Cathode Materials for Rechargeable Lithium Batteries. *The journal of physical chemistry letters* **2014,** *5* (4), 671-679.
100. Sun, Y. K.; Kim, D. H.; Yoon, C. S.; Myung, S. T.; Prakash, J.; Amine, K., A Novel Cathode Material with a Concentration-Gradient for High-Energy and Safe Lithium-Ion Batteries. *Advanced Functional Materials* **2010,** *20* (3), 485-491.
101. Pakhare, D.; Shaw, C.; Haynes, D.; Shekhawat, D.; Spivey, J. J. J. o. C. U., Effect of reaction temperature on activity of Pt-and Ru-substituted lanthanum zirconate pyrochlores (La2Zr2O7) for dry (CO2) reforming of methane (DRM). **2013,** *1*, 37-42.
102. Pakhare, D.; Spivey, J. J. C. S. R., A review of dry (CO 2) reforming of methane over noble metal catalysts. **2014,** *43* (22), 7813-7837.
103. Kubicek, M.; Bork, A. H.; Rupp, J. L. J. J. o. M. C. A., Perovskite oxides–a review on a versatile material class for solar-to-fuel conversion processes. **2017,** *5* (24), 11983-12000.
104. Goldschmidt, V. J. M. N. K., Skrifter Norske Videnskaps-Akad. **1926,** (2).
105. Hagenmuller, P., *Preparative methods in solid state chemistry*. Elsevier: 2012.

106. Takashi, S., EFFECT OF ELECTRONIC STRUCTURE AND TOLERANCE FACTOR ON CO OXIDATION ACTIVITY OF PEROVSKITE OXIDES. *Chemistry Letters* **1980,** *9* (1).
107. Suntivich, J.; Hong, W. T.; Lee, Y.-L.; Rondinelli, J. M.; Yang, W.; Goodenough, J. B.; Dabrowski, B.; Freeland, J. W.; Shao-Horn, Y., Estimating Hybridization of Transition Metal and Oxygen States in Perovskites from O K-edge X-ray Absorption Spectroscopy. *The Journal of Physical Chemistry C* **2014,** *118* (4), 1856-1863.
108. Kool, T. W., *Properties of perovskites and other oxides*. World Scientific: 2010.
109. Narayanan, S.; Ramezanipour, F.; Thangadurai, V. J. I. c., Dopant Concentration–Porosity–Li-Ion Conductivity Relationship in Garnet-Type Li5+ 2 x La3Ta2–x Y x O12 (0.05≤ x≤ 0.75) and Their Stability in Water and 1 M LiCl. **2015,** *54* (14), 6968-6977.
110. Scrosati, B.; Garche, J. J. J. o. p. s., Lithium batteries: Status, prospects and future. **2010,** *195* (9), 2419-2430.
111. Galven, C.; Fourquet, J.-L.; Suard, E.; Crosnier-Lopez, M.-P.; Le Berre, F. J. D. T., Mechanism of a reversible CO 2 capture monitored by the layered perovskite Li 2 SrTa 2 O 7. **2010,** *39* (17), 4191-4197.
112. Domen, K.; Yoshimura, J.; Sekine, T.; Tanaka, A.; Onishi, T. J. C. l., A novel series of photocatalysts with an ion-exchangeable layered structure of niobate. **1990,** *4* (4-6), 339-343.
113. Gopalakrishnan, J.; Bhat, V. J. I. c., A2Ln2Ti3O10 (A= potassium or rubidium; Ln= lanthanum or rare earth): a new series of layered perovskites exhibiting ion exchange. **1987,** *26* (26), 4299-4301.
114. Marquardt, M. A.; Ashmore, N. A.; Cann, D. P. J. T. S. F., Crystal chemistry and electrical properties of the delafossite structure. **2006,** *496* (1), 146-156.
115. Nie, X.; Wei, S.-H.; Zhang, S. J. P. r. l., Bipolar doping and band-gap anomalies in delafossite transparent conductive oxides. **2002,** *88* (6), 066405.
116. Lin, F.; Markus, I. M.; Nordlund, D.; Weng, T.-C.; Asta, M. D.; Xin, H. L.; Doeff, M. M. J. N. c., Surface reconstruction and chemical evolution of stoichiometric layered cathode materials for lithium-ion batteries. **2014,** *5*, 3529.
117. Takata, T.; Tanaka, A.; Hara, M.; Kondo, J. N.; Domen, K. J. C. T., Recent progress of photocatalysts for overall water splitting. **1998,** *44* (1-4), 17-26.
118. Hill, R. J.; Craig, J. R.; Gibbs, G. J. P.; minerals, c. o., Systematics of the spinel structure type. **1979,** *4* (4), 317-339.
119. Kathiraser, Y.; Thitsartarn, W.; Sutthiumporn, K.; Kawi, S., Inverse NiAl2O4 on LaAlO3–Al2O3: Unique Catalytic Structure for Stable CO2 Reforming of Methane. *The Journal of Physical Chemistry C* **2013,** *117* (16), 8120-8130.
120. Chen, J. Y.; Miller, J. T.; Gerken, J. B.; Stahl, S. S. J. E.; Science, E., Inverse spinel NiFeAlO 4 as a highly active oxygen evolution electrocatalyst: promotion of activity by a redox-inert metal ion. **2014,** *7* (4), 1382-1386.
121. Wu, G.; Wang, J.; Ding, W.; Nie, Y.; Li, L.; Qi, X.; Chen, S.; Wei, Z., A Strategy to Promote the Electrocatalytic Activity of Spinels for Oxygen Reduction by Structure Reversal. **2016,** *55* (4), 1340-1344.
122. Aleshin, E.; Roy, R. J. J. o. t. A. C. S., Crystal chemistry of pyrochlore. **1962,** *45* (1), 18-25.
123. Roy, R. J. S. S. I., Synthesizing new materials to specification. **1989,** *32*, 3-22.

124. Nagabhushana, G.; Shivaramaiah, R.; Navrotsky, A. J. P. o. t. N. A. o. S., Direct calorimetric verification of thermodynamic instability of lead halide hybrid perovskites. **2016,** *113* (28), 7717-7721.
125. Sclafani, A.; Herrmann, J. J. T. J. o. P. C., Comparison of the photoelectronic and photocatalytic activities of various anatase and rutile forms of titania in pure liquid organic phases and in aqueous solutions. **1996,** *100* (32), 13655-13661.
126. Sanna, S.; Esposito, V.; Andreasen, J. W.; Hjelm, J.; Zhang, W.; Kasama, T.; Simonsen, S. B.; Christensen, M.; Linderoth, S.; Pryds, N. J. N. m., Enhancement of the chemical stability in confined δ-Bi 2 O 3. **2015,** *14* (5), 500.
127. Sun, W.; Dacek, S. T.; Ong, S. P.; Hautier, G.; Jain, A.; Richards, W. D.; Gamst, A. C.; Persson, K. A.; Ceder, G. J. S. a., The thermodynamic scale of inorganic crystalline metastability. **2016,** *2* (11), e1600225.
128. Van Santen, R. A., The Ostwald step rule. *The Journal of Physical Chemistry* **1984,** *88* (24), 5768-5769.
129. ten Wolde, P. R.; Frenkel, D. J. P. C. C. P., Homogeneous nucleation and the Ostwald step rule. **1999,** *1* (9), 2191-2196.
130. Ostwald, W. Z., *Phys. Chem.* **1879,** *22*, 289.
131. Turnbull, D., *Metallurgical Transactions A* **1981,** *124*, 695.
132. Hillert, M., *Phase equilibria, phase diagrams and phase transformations: their thermodynamic basis*. Cambridge University Press: 2007.
133. Miracle, D. B.; Senkov, O. N. J. A. M., A critical review of high entropy alloys and related concepts. **2017,** *122*, 448-511.
134. Stone, F. S., The significance for oxide catalysis of electronic properties and structure. *Journal of Solid State Chemistry* **1975,** *12* (3), 271-281.
135. Liang, X.; Wang, X.; Zhuang, Y.; Xu, B.; Kuang, S.; Li, Y. J. J. o. t. A. C. S., Formation of CeO2− ZrO2 solid solution nanocages with controllable structures via Kirkendall effect. **2008,** *130* (9), 2736-2737.
136. Liu, M.; Wang, L.; Lu, G. M.; Yao, X.; Guo, L. J. E.; Science, E., Twins in Cd 1− x Zn x S solid solution: highly efficient photocatalyst for hydrogen generation from water. **2011,** *4* (4), 1372-1378.
137. Cordischi, D.; Faticanti, M.; Minelli, G.; Occhiuzzi, M.; Porta, P., LaAl1−xMnxO3 perovskite-type oxide solid solutions: structural, magnetic and electronic properties. *Physical Chemistry Chemical Physics* **2003,** *5* (7), 1467-1473.
138. Skoug, E. J.; Cain, J. D.; Morelli, D. T. J. A. P. L., High thermoelectric figure of merit in the Cu3SbSe4-Cu3SbS4 solid solution. **2011,** *98* (26), 261911.
139. Zha, S.; Xia, C.; Meng, G. J. J. o. P. S., Effect of Gd (Sm) doping on properties of ceria electrolyte for solid oxide fuel cells. **2003,** *115* (1), 44-48.
140. Hubert-Pfalzgraf, L. G. J. P., Heterometallic alkoxides and oxoalkoxides as intermediates in chemical routes to mixed metal oxides. **1994,** *13* (8), 1181-1195.
141. Dikmen, S.; Shuk, P.; Greenblatt, M.; Gocmez, H. J. S. S. S., Hydrothermal synthesis and properties of Ce1− xGdxO2− δ solid solutions. **2002,** *4* (5), 585-590.
142. Tang, X.; Li, Y.; Huang, X.; Xu, Y.; Zhu, H.; Wang, J.; Shen, W. J. A. C. B. E., MnOx–CeO2 mixed oxide catalysts for complete oxidation of formaldehyde: effect of preparation method and calcination temperature. **2006,** *62* (3-4), 265-273.
143. Kamal, C. S.; Rao, T. V.; Reddy, P.; Sujatha, K.; Ajayi, B. P.; Jasinski, J. B.; Rao, K. R. J. R. A., Unravelling the energy transfer mechanism in bismuth co-activation of

LaInO 3: Sm 3+/Ho 3+ nanophosphor for color-tunable luminescence. **2017,** *7* (16), 9724-9731.
144. Samuel, T.; Kamal, C. S.; Ravipati, S.; Ajayi, B. P.; Veeraiah, V.; Sudarsan, V.; Rao, K. R. J. O. M., High purity green photoluminescence emission from Tb3+, Bi3+ co-doped LaGaO3 nanophosphors. **2017,** *69*, 230-237.
145. Zuo, C.; Zha, S.; Liu, M.; Hatano, M.; Uchiyama, M. J. A. M., Ba (Zr0. 1Ce0. 7Y0. 2) O3–δ as an electrolyte for low-temperature solid-oxide fuel cells. **2006,** *18* (24), 3318-3320.
146. Narendar, Y.; Messing, G. L. J. C. T., Mechanisms of phase separation in gel-based synthesis of multicomponent metal oxides. **1997,** *35* (3), 247-268.
147. Choy, J.-H.; Yoo, J.-S.; Kang, S.-G.; Hong, S.-T.; Kim, D.-G. J. M. r. b., Ultra-fine Pb (Mg13Nb23) O3 (PMN) powder synthesized from metal-citrate gel by thermal shock method. **1990,** *25* (3), 283-291.
148. Selvaraj, U.; Komarneni, S.; Roy, R. J. J. o. t. A. C. S., Synthesis of Glass-like Cordierite from Metal Alkoxides and Characterization by 27Al and 29Si MASNMR. **1990,** *73* (12), 3663-3669.
149. Delattre, L.; Roy, M.; Babonneau, F. J. J. o. S.-G. S.; Technology, Design of homogeneous hybrid materials through a careful control of the synthetic procedure. **1997,** *8* (1-3), 567-570.
150. Cousin, P.; Ross, R. J. M. S.; A, E., Preparation of mixed oxides: a review. **1990,** *130* (1), 119-125.
151. Kong, L. B.; Ma, J.; Huang, H., Preparation of the solid solution Sn0.5Ti0.5O2 from an oxide mixture via a mechanochemical process. *Journal of Alloys and Compounds* **2002,** *336* (1), 315-319.
152. Hsu, C.-Y.; Yeh, J.-W.; Chen, S.-K.; Shun, T.-T. J. M.; A, M. T., Wear resistance and high-temperature compression strength of Fcc CuCoNiCrAl 0.5 Fe alloy with boron addition. **2004,** *35* (5), 1465-1469.
153. Yeh, J. W.; Chen, S. K.; Lin, S. J.; Gan, J. Y.; Chin, T. S.; Shun, T. T.; Tsau, C. H.; Chang, S. Y. J. A. E. M., Nanostructured high-entropy alloys with multiple principal elements: novel alloy design concepts and outcomes. **2004,** *6* (5), 299-303.
154. Cantor, B.; Chang, I.; Knight, P.; Vincent, A. J. M. S.; A, E., Microstructural development in equiatomic multicomponent alloys. **2004,** *375*, 213-218.
155. Kuznetsov, A. V.; Shaysultanov, D. G.; Stepanov, N.; Salishchev, G. A.; Senkov, O. N. J. M. S.; A, E., Tensile properties of an AlCrCuNiFeCo high-entropy alloy in as-cast and wrought conditions. **2012,** *533*, 107-118.
156. Chou, H.-P.; Chang, Y.-S.; Chen, S.-K.; Yeh, J.-W. J. M. S.; B, E., Microstructure, thermophysical and electrical properties in AlxCoCrFeNi ($0 \leq x \leq 2$) high-entropy alloys. **2009,** *163* (3), 184-189.
157. Çinar, E.; Koçyiğit, S.; Aytimur, A.; Uslu, İ.; Akdemir, A. J. M.; A, M. T., Synthesis, Characterization, and Thermoelectric Properties of Electrospun Boron-Doped Barium-Stabilized Bismuth-Cobalt Oxide Nanoceramics. **2014,** *45* (9), 3929-3937.
158. Tsai, C.-F.; Wu, P.-W.; Lin, P.; Chao, C.-G.; Yeh, K.-Y. J. J. J. o. A. P., Sputter deposition of multi-element nanoparticles as electrocatalysts for methanol oxidation. **2008,** *47* (7R), 5755.
159. Yao, Y.; Huang, Z.; Xie, P.; Lacey, S. D.; Jacob, R. J.; Xie, H.; Chen, F.; Nie, A.; Pu, T.; Rehwoldt, M.; Yu, D.; Zachariah, M. R.; Wang, C.; Shahbazian-Yassar, R.; Li, J.;

Hu, L., Carbothermal shock synthesis of high-entropy-alloy nanoparticles. **2018,** *359* (6383), 1489-1494.
160. Pettit, F.; Randklev, E.; Felten, E. J. J. o. t. A. C. S., Formation of NiAl2O4 by solid state reaction. **1966,** *49* (4), 199-203.
161. Rao, B. G.; Mukherjee, D.; Reddy, B. M., Novel approaches for preparation of nanoparticles. In *Nanostructures for Novel Therapy*, Elsevier: 2017; pp 1-36.
162. Danks, A.; Hall, S.; Schnepp, Z. J. M. H., The evolution of 'sol–gel'chemistry as a technique for materials synthesis. **2016,** *3* (2), 91-112.
163. Walton, R. I. J. C. S. R., Subcritical solvothermal synthesis of condensed inorganic materials. **2002,** *31* (4), 230-238.
164. Schafhautl, The latest geological hypotheses and their relation to science in genera. *Royal Bavarian Academy of Sciences* **1845,** *20*, 557-596.
165. Ajayi, B. P.; Jermy, B. R.; Ogunronbi, K. E.; Abussaud, B. A.; Al-Khattaf, S., n-Butane dehydrogenation over mono and bimetallic MCM-41 catalysts under oxygen free atmosphere. *Catalysis Today* **2013,** *204*, 189-196.
166. Ajayi, B.; Jermy, B. R.; Abussaud, B.; Al-Khattaf, S. J. J. o. P. M., Oxidative dehydrogenation of n-butane over bimetallic mesoporous and microporous zeolites with CO 2 as mild oxidant. **2013,** *20* (5), 1257-1270.
167. Modeshia, D. R.; Walton, R. I. J. C. S. R., Solvothermal synthesis of perovskites and pyrochlores: crystallisation of functional oxides under mild conditions. **2010,** *39* (11), 4303-4325.
168. Inoue, M.; Otsu, H.; Kominami, H.; Inui, T. J. J. o. t. A. C. S., Synthesis of yttrium aluminum garnet by the glycothermal method. **1991,** *74* (6), 1452-1454.
169. Huang, Y.; Wu, J.; Wei, Y.; Lin, J.; Huang, M. J. J. o. A.; Compounds, Hydrothermal synthesis of K2La2Ti3O10 and photocatalytic splitting of water. **2008,** *456* (1-2), 364-367.
170. Baukal, W.; BECK, H.-P.; Kuhn, W.; Sieglen, R. In *Preparation of a beta-alumina ceramic for the sodium-sulphur battery using a chemical powder preparation method*, International Power Sources Symposium Committee, International Power Sources Symposium, 10 th, Brighton, England, 1976.
171. Ham, W. K.; Holland, G. F.; Stacy, A. M. J. J. o. t. A. C. S., Low-temperature synthesis of superconducting La2-xMxCuO4: direct precipitation from NaOH/KOH melts. **1988,** *110* (15), 5214-5215.
172. Pratsinis, S. E.; Vemury, S. J. P. t., Particle formation in gases: a review. **1996,** *88* (3), 267-273.
173. Ulrich, G.; Subramanian, N. J. C. S.; Technology, III. Coalescence as a rate-controlling process. **1977,** *17* (3-4), 119-126.
174. Punginsang, M.; Wisitsoraat, A.; Tuantranont, A.; Phanichphant, S.; Liewhiran, C., Ultrafine Bi2WO6 nanoparticles prepared by flame spray pyrolysis for selective acetone gas-sensing. *Materials Science in Semiconductor Processing* **2019,** *90*, 263-275.
175. Kammler, H. K.; Pratsinis, S. E.; Morrison Jr, P. W.; Hemmerling, B. J. C.; flame, Flame temperature measurements during electrically assisted aerosol synthesis of nanoparticles. **2002,** *128* (4), 369-381.
176. Abram, C.; Mezhericher, M.; Beyrau, F.; Stone, H. A.; Ju, Y., Flame synthesis of nanophosphors using sub-micron aerosols. *Proceedings of the Combustion Institute* **2019,** *37* (1), 1231-1239.

177. Laine, R.; Marchal, J.; Kim, S.; Azurdia, J.; Kim, M. J. C. N.; III, N., Liquid-Feed Flame Spray Pyrolysis of Single and Mixed Phase Mixed-Metal Oxide Nanopowders. **2006,** *159*, 1-10.
178. Teoh, W. Y.; Amal, R.; Mädler, L. J. N., Flame spray pyrolysis: An enabling technology for nanoparticles design and fabrication. **2010,** *2* (8), 1324-1347.
179. Coburn, J. W.; Winters, H. F. J. J. o. v. S.; Technology, Plasma etching—A discussion of mechanisms. **1979,** *16* (2), 391-403.
180. Pai, P.; Chao, S. S.; Takagi, Y.; Lucovsky, G. J. J. o. V. S.; Technology A: Vacuum, S.; Films, Infrared spectroscopic study of SiO x films produced by plasma enhanced chemical vapor deposition. **1986,** *4* (3), 689-694.
181. Xu, W.; Ye, Z.; Zeng, Y.; Zhu, L.; Zhao, B.; Jiang, L.; Lu, J.; He, H.; Zhang, S. J. A. P. L., ZnO light-emitting diode grown by plasma-assisted metal organic chemical vapor deposition. **2006,** *88* (17), 173506.
182. Cheung, N. W. J. N. I.; Materials, M. i. P. R. S. B. B. I. w.; Atoms, Plasma immersion ion implantation for ULSI processing. **1991,** *55* (1-4), 811-820.
183. Macák, K.; Kouznetsov, V.; Schneider, J.; Helmersson, U.; Petrov, I. J. J. o. V. S.; Technology A: Vacuum, S.; Films, Ionized sputter deposition using an extremely high plasma density pulsed magnetron discharge. **2000,** *18* (4), 1533-1537.
184. Ritchie, R. H. J. P. R., Plasma losses by fast electrons in thin films. **1957,** *106* (5), 874.
185. Tendero, C.; Tixier, C.; Tristant, P.; Desmaison, J.; Leprince, P. J. S. A. P. B. A. S., Atmospheric pressure plasmas: A review. **2006,** *61* (1), 2-30.
186. Bianchi, L. Projection par plasma d'arc et plasma inductif de dépots céramiques: nécanismes de formation de la première couche et relation avec les propriétés mécaniques des dépots. Limoges, 1995.
187. Park, J.; Henins, I.; Herrmann, H.; Selwyn, G.; Jeong, J.; Hicks, R.; Shim, D.; Chang, C. J. A. P. L., An atmospheric pressure plasma source. **2000,** *76* (3), 288-290.
188. Hubert, J.; Moisan, M.; Ricard, A. J. S. A. P. B. A. S., A new microwave plasma at atmospheric pressure. **1979,** *34* (1), 1-10.
189. Jordan, E. H.; Xie, L.; Gell, M.; Padture, N.; Cetegen, B.; Ozturk, A.; Ma, X.; Roth, J.; Xiao, T.; Bryant, P. J. J. o. T. S. T., Superior thermal barrier coatings using solution precursor plasma spray. **2004,** *13* (1), 57-65.
190. Gell, M.; Jordan, E. H.; Teicholz, M.; Cetegen, B. M.; Padture, N. P.; Xie, L.; Chen, D.; Ma, X.; Roth, J. J. J. o. T. S. T., Thermal barrier coatings made by the solution precursor plasma spray process. **2008,** *17* (1), 124-135.
191. Padture, N.; Schlichting, K.; Bhatia, T.; Ozturk, A.; Cetegen, B.; Jordan, E.; Gell, M.; Jiang, S.; Xiao, T.; Strutt, P. J. A. m., Towards durable thermal barrier coatings with novel microstructures deposited by solution-precursor plasma spray. **2001,** *49* (12), 2251-2257.
192. Xie, L.; Jordan, E. H.; Padture, N. P.; Gell, M. J. M. S.; A, E., Phase and microstructural stability of solution precursor plasma sprayed thermal barrier coatings. **2004,** *381* (1-2), 189-195.
193. Warren, B. J. T. i. n. c. r. f. t. r., X-Ray Diffraction; Courier Corporation: 1969. **2017**.

194. Edwards, A., HP Klug and LE Alexander, x-ray diffraction procedures for polycrystalline and amorphous materials: Wiley-Interscience, New York, 2nd edn., 1974, xxv+ 966 pp. price£ 18.55. Elsevier: 1975.
195. Rietveld, H. J. J. o. a. C., A profile refinement method for nuclear and magnetic structures. **1969,** *2* (2), 65-71.
196. Toby, B. H. J. P. d., R factors in Rietveld analysis: How good is good enough? **2006,** *21* (1), 67-70.
197. Toby, B. H. J. J. o. a. c., EXPGUI, a graphical user interface for GSAS. **2001,** *34* (2), 210-213.
198. Rodríguez-Carvajal, J. J. P. B. C. M., Recent advances in magnetic structure determination by neutron powder diffraction. **1993,** *192* (1-2), 55-69.
199. Dollase, W. J. J. o. A. C., Correction of intensities for preferred orientation in powder diffractometry: application of the March model. **1986,** *19* (4), 267-272.
200. Momma, K.; Izumi, F. J. J. o. a. c., VESTA 3 for three-dimensional visualization of crystal, volumetric and morphology data. **2011,** *44* (6), 1272-1276.
201. Humphrey, W.; Dalke, A.; Schulten, K. J. J. o. m. g., VMD: visual molecular dynamics. **1996,** *14* (1), 33-38.
202. Goldstein, J. I.; Newbury, D. E.; Michael, J. R.; Ritchie, N. W.; Scott, J. H. J.; Joy, D. C., *Scanning electron microscopy and X-ray microanalysis*. Springer: 2017.
203. Goldstein, J., *Practical scanning electron microscopy: electron and ion microprobe analysis*. Springer Science & Business Media: 2012.
204. Bard, A. J.; Faulkner, L. R. J. E. M., Fundamentals and applications. **2001,** *2*, 482.
205. Jung, S.; McCrory, C. C.; Ferrer, I. M.; Peters, J. C.; Jaramillo, T. F. J. J. o. M. C. A., Benchmarking nanoparticulate metal oxide electrocatalysts for the alkaline water oxidation reaction. **2016,** *4* (8), 3068-3076.
206. Spurgeon, J. M.; Velazquez, J. M.; McDowell, M. T. J. P. C. C. P., Improving O 2 production of WO 3 photoanodes with IrO 2 in acidic aqueous electrolyte. **2014,** *16* (8), 3623-3631.
207. Pourbaix, M. J. N., Atlas of electrochemical equilibria in aqueous solution. **1974,** *307*.
208. Perdew, J. P.; Burke, K.; Ernzerhof, M., Generalized Gradient Approximation Made Simple. *Physical Review Letters* **1996,** *77* (18), 3865-3868.
209. Andriotis, A. N.; Mpourmpakis, G.; Lisenkov, S.; Sheetz, R. M.; Menon, M., U-calculation of the LSDA + U functional using the hybrid B3LYP and HSE functionals. *physica status solidi (b)* **2013,** *250* (2), 356-363.
210. Dudarev, S. L.; Botton, G. A.; Savrasov, S. Y.; Humphreys, C. J.; Sutton, A. P., Electron-energy-loss spectra and the structural stability of nickel oxide: An LSDA+U study. *Physical Review B* **1998,** *57* (3), 1505-1509.
211. Kresse, G.; Joubert, D., From ultrasoft pseudopotentials to the projector augmented-wave method. *Physical Review B* **1999,** *59* (3), 1758-1775.
212. Jain, A.; Ong, S. P. J. A. M., A. Jain, SP Ong, G. Hautier, W. Chen, WD Richards, S. Dacek, S. Cholia, D. Gunter, D. Skinner, G. Ceder, and KA Persson, APL Mater. 1, 011002 (2013). **2013,** *1*, 011002.
213. Yandulov, D. V.; Schrock, R. R. J. S., Catalytic reduction of dinitrogen to ammonia at a single molybdenum center. **2003,** *301* (5629), 76-78.

214. Pratsinis, S. E., Flame aerosol synthesis of ceramic powders. *Progress in Energy and Combustion Science* **1998,** *24* (3), 197-219.
215. Messing, G. L.; Zhang, S. C.; Jayanthi, G. V., Ceramic powder synthesis by spray pyrolysis. *Journal of the American Ceramic Society* **1993,** *76* (11), 2707-2726.
216. Lewis, D. J., Technique for Producing Mullite and Other Mixed-Oxide Systems. *Journal of the American Ceramic Society* **1991,** *74* (10), 2410-2413.
217. Marshall, B.; Telford, I.; Wood, R., A field method for the determination of zinc oxide fume in air. *Analyst* **1971,** *96* (1145), 569-578.
218. Mueller, R.; Jossen, R.; Pratsinis, S. E.; Watson, M.; Akhtar, M. K., Zirconia nanoparticles made in spray flames at high production rates. *Journal of the American Ceramic Society* **2004,** *87* (2), 197-202.
219. Deng, H.; Belharouak, I.; Cook, R. E.; Wu, H.; Sun, Y.-K.; Amine, K., Nanostructured lithium nickel manganese oxides for lithium-ion batteries. *Journal of The Electrochemical Society* **2010,** *157* (4), A447-A452.
220. Gerken, J. B.; Chen, J. Y. C.; Massé, R. C.; Powell, A. B.; Stahl, S. S., Development of an O2-Sensitive Fluorescence-Quenching Assay for the Combinatorial Discovery of Electrocatalysts for Water Oxidation. *Angewandte Chemie International Edition* **2012,** *51* (27), 6676-6680.
221. Xiang, C.; Suram, S. K.; Haber, J. A.; Guevarra, D. W.; Soedarmadji, E.; Jin, J.; Gregoire, J. M., High-Throughput Bubble Screening Method for Combinatorial Discovery of Electrocatalysts for Water Splitting. *ACS Combinatorial Science* **2014,** *16* (2), 47-52.
222. Burns, R. G., The uptake of cobalt into ferromanganese nodules, soils, and synthetic manganese (IV) oxides. *Geochimica et Cosmochimica Acta* **1976,** *40* (1), 95-102.
223. Ko, S. W.; Li, J.; Podraza, N. J.; Dickey, E. C.; Trolier-McKinstry, S., Spin Spray-Deposited Nickel Manganite Thermistor Films For Microbolometer Applications. *Journal of the American Ceramic Society* **2011,** *94* (2), 516-523.
224. Noh, H.-J.; Yeo, S.; Kang, J.-S.; Zhang, C. L.; Cheong, S.-W.; Oh, S.-J.; Johnson, P. D., Jahn-Teller effect in spinel manganites probed by soft x-ray absorption spectroscopy. *Applied Physics Letters* **2006,** *88* (8), 081911.
225. MIYAHARA, S., Jahn-Teller Distortion in Magnetic Spinels. *J. Phys. Soc. Japan* **1962,** *17,* 181-184.
226. de Györgyfalva, G. D. C. C.; Reaney, I. M., Decomposition of NiMn2O4 spinels. *Journal of Materials Research* **2003,** *18* (6), 1301-1308.
227. Díez, A.; Schmidt, R.; Sagua, A. E.; Frechero, M. A.; Matesanz, E.; Leon, C.; Morán, E., Structure and physical properties of nickel manganite NiMn2O4 obtained from nickel permanganate precursor. *Journal of the European Ceramic Society* **2010,** *30* (12), 2617-2624.
228. Kiselev, E. A.; Proskurnina, N. V.; Voronin, V. I.; Cherepanov, V. A., Phase equilibria and crystal structures of phases in the La-Fe-Ni-O system at 1370 K in air. *Inorganic Materials* **2007,** *43* (2), 167-175.
229. Xiao-Xia, T.; Manthiram, A.; Goodenough, J. B., NiMn2O4 revisited. *Journal of the Less Common Metals* **1989,** *156* (1), 357-368.
230. Weil, L.; Bertaut, F.; Bochirol, L., Propriétés magnétiques et structure de la phase quadratique du ferrite de cuivre. *J. Phys. Radium* **1950,** *11* (5), 208-212.

231. Birajdar, A. A.; Shirsath, S. E.; Kadam, R. H.; Patange, S. M.; Mane, D. R.; Shitre, A. R., Rietveld Structure Refinement and Cation Distribution of Cr. *ISRN Ceramics* **2012,** *2012*, 5.
232. Chekin, F.; Tahermansouri, H.; Besharat, M. R., Nickel oxide nanoparticles prepared by gelatin and their application toward the oxygen evolution reaction. *Journal of Solid State Electrochemistry* **2014,** *18* (3), 747-753.
233. Yeager, M. P.; Su, D.; Marinković, N. S.; Teng, X., Pseudocapacitive NiO Fine Nanoparticles for Supercapacitor Reactions. *Journal of The Electrochemical Society* **2012,** *159* (10), A1598-A1603.
234. Bao, J.; Zhang, X.; Fan, B.; Zhang, J.; Zhou, M.; Yang, W.; Hu, X.; Wang, H.; Pan, B.; Xie, Y., Ultrathin Spinel-Structured Nanosheets Rich in Oxygen Deficiencies for Enhanced Electrocatalytic Water Oxidation. *Angewandte Chemie International Edition* **2015,** *54* (25), 7399-7404.
235. Singh, R. N.; Singh, J. P.; Lal, B.; Thomas, M. J. K.; Bera, S., New NiFe2−xCrxO4 spinel films for O2 evolution in alkaline solutions. *Electrochimica Acta* **2006,** *51* (25), 5515-5523.
236. Strasser, P.; Koh, S.; Anniyev, T.; Greeley, J.; More, K.; Yu, C.; Liu, Z.; Kaya, S.; Nordlund, D.; Ogasawara, H.; Toney, M. F.; Nilsson, A., Lattice-strain control of the activity in dealloyed core–shell fuel cell catalysts. *Nature Chemistry* **2010,** *2*, 454.
237. Jakšić, M. M., Electrocatalysis of hydrogen evolution in the light of the brewer—engel theory for bonding in metals and intermetallic phases. *Electrochimica Acta* **1984,** *29* (11), 1539-1550.
238. Brinley, E.; Babu, K. S.; Seal, S., The solution precursor plasma spray processing of nanomaterials. *JOM* **2007,** *59* (7), 54-59.
239. Choi, Y.; Lin, M. e. C.; Liu, M. J. A. C. I. E., Computational study on the catalytic mechanism of oxygen reduction on La0. 5Sr0. 5MnO3 in solid oxide fuel cells. **2007,** *46* (38), 7214-7219.
240. Van Roosmalen, J.; Huijsmans, J.; Plomp, L. J. S. S. I., Electrical conductivity in La1− xSrxMnO3+ δ. **1993,** *66* (3-4), 279-284.
241. Dinamarca, R.; Garcia, X.; Jimenez, R.; Fierro, J.; Pecchi, G. J. M. R. B., Effect of A-site deficiency in LaMn0. 9Co0. 1O3 perovskites on their catalytic performance for soot combustion. **2016,** *81*, 134-141.
242. Ahuja, P.; Ujjain, S. K.; Sharma, R. K.; Singh, G. J. R. A., Enhanced supercapacitor performance by incorporating nickel in manganese oxide. **2014,** *4* (100), 57192-57199.
243. Elsiddig, Z. A.; Xu, H.; Wang, D.; Zhang, W.; Guo, X.; Zhang, Y.; Sun, Z.; Chen, J. J. E. A., Modulating Mn4+ ions and oxygen vacancies in nonstoichiometric LaMnO3 perovskite by a facile sol-gel method as high-performance supercapacitor electrodes. **2017,** *253*, 422-429.
244. Mahendiran, R.; Tiwary, S.; Raychaudhuri, A.; Ramakrishnan, T.; Mahesh, R.; Rangavittal, N.; Rao, C. J. P. R. B., Structure, electron-transport properties, and giant magnetoresistance of hole-doped LaMnO 3 systems. **1996,** *53* (6), 3348.
245. Suryanarayanan, R.; Berthon, J.; Zelenay, I.; Martinez, B.; Obradors, X.; Uma, S.; Gmelin, E. J. J. o. a. p., Thermoelectric power, specific heat, and giant magnetoresistance of La 0.85 MnO 3. **1998,** *83* (10), 5264-5269.

246. Yokokawa, H.; Sakai, N.; Kawada, T.; Dokiya, M. J. S. S. I., Thermodynamic stabilities of perovskite oxides for electrodes and other electrochemical materials. **1992,** *52* (1-3), 43-56.
247. De Bruijn, T. J. W.; De Jong, W. A.; Van Den Berg, P. J., Thermal decomposition of aqueous manganese nitrate solutions and anhydrous manganese nitrate. Part 1. Mechanism. *Thermochimica Acta* **1981,** *45* (3), 265-278.
248. Gallagher, P. K.; Schrey, F.; Prescott, B., The thermal decomposition of aqueous manganese (II) nitrate solution. *Thermochimica Acta* **1971,** *2* (5), 405-412.
249. Malavasi, L.; Galinetto, P.; Mozzati, M. C.; Azzoni, C. B.; Flor, G., Raman spectroscopy of AMn 2 O 4 (A= Mn, Mg and Zn) spinels. *Physical Chemistry Chemical Physics* **2002,** *4* (15), 3876-3880.
250. Wickham, D., Solid-phase equilibria in the system NiO · Mn2O3 · O2. *Journal of Inorganic and Nuclear Chemistry* **1964,** *26* (8), 1369-1377.
251. Stull, D. R., Vapor pressure of pure substances. Organic and inorganic compounds. *Industrial & Engineering Chemistry* **1947,** *39* (4), 517-540.
252. Yang, B. L.; Chan, S. F.; Chang, W. S.; Chen, Y. Z., Surface enrichment in mixed oxides of Cu, Co, and Mn, and its effect on CO oxidation. *Journal of Catalysis* **1991,** *130* (1), 52-61.
253. Kingery, W. D., The chemistry of ceramic grain boundaries. In *Pure and Applied Chemistry*, 1984; Vol. 56, p 1703.
254. Gillot, B.; Buguet, S.; Kester, E.; Baubet, C.; Tailhades, P., Cation valencies and distribution in the spinels CoxCuyMnzFeuO4+δ (δ≥0) thin films studied by X-ray photoelectron spectroscopy. *Thin Solid Films* **1999,** *357* (2), 223-231.
255. Drouet, C.; Laberty, C.; Fierro, J. L. G.; Alphonse, P.; Rousset, A., X-ray photoelectron spectroscopic study of non-stoichiometric nickel and nickel–copper spinel manganites. *International Journal of Inorganic Materials* **2000,** *2* (5), 419-426.
256. Aduru, S.; Contarini, S.; Rabalais, J. W., Electron-, x-ray-, and ion-stimulated decomposition of nitrate salts. *The Journal of Physical Chemistry* **1986,** *90* (8), 1683-1688.
257. Vasquez, R. P., X-ray photoelectron spectroscopy study of Sr and Ba compounds. *Journal of Electron Spectroscopy and Related Phenomena* **1991,** *56* (3), 217-240.
258. Hueso, J.; Espinós, J.; Caballero, A.; Cotrino, J.; González-Elipe, A., XPS investigation of the reaction of carbon with NO, O2, N2 and H2O plasmas. *Carbon* **2007,** *45* (1), 89-96.
259. Yuvaraj, S.; Fan-Yuan, L.; Tsong-Huei, C.; Chuin-Tih, Y., Thermal decomposition of metal nitrates in air and hydrogen environments. *The Journal of Physical Chemistry B* **2003,** *107* (4), 1044-1047.
260. Ranz, W.; Marshall, W., Evaporation from drops. *Chem. Eng. Prog* **1952,** *48* (3), 141-146.
261. Gobichon, A.-E.; Auffrédic, J.-P.; Louër, D. J. S. S. I., Thermal decomposition of neutral and basic lanthanum nitrates studied with temperature-dependent powder diffraction and thermogravimetric analysis. **1996,** *93* (1-2), 51-64.
262. Bretos, I.; Jiménez, R.; Ricote, J.; Calzada, M. L. J. C. S. R., Low-temperature crystallization of solution-derived metal oxide thin films assisted by chemical processes. **2018,** *47* (2), 291-308.

263. Conte, M.; Iacobazzi, A.; Ronchetti, M.; Vellone, R., Hydrogen economy for a sustainable development: state-of-the-art and technological perspectives. *Journal of Power Sources* **2001,** *100* (1), 171-187.
264. Rosen, M. A.; Scott, D. S., Comparative efficiency assessments for a range of hydrogen production processes. *International Journal of Hydrogen Energy* **1998,** *23* (8), 653-659.
265. Turner, J. A., Sustainable Hydrogen Production. *Science* **2004,** *305* (5686), 972-974.
266. Cao, R.; Lai, W.; Du, P., Catalytic water oxidation at single metal sites. *Energy & Environmental Science* **2012,** *5* (8), 8134-8157.
267. Park, S.; Shao, Y.; Liu, J.; Wang, Y., Oxygen electrocatalysts for water electrolyzers and reversible fuel cells: status and perspective. *Energy & Environmental Science* **2012,** *5* (11), 9331-9344.
268. Mayousse, E.; Maillard, F.; Fouda-Onana, F.; Sicardy, O.; Guillet, N., Synthesis and characterization of electrocatalysts for the oxygen evolution in PEM water electrolysis. *International Journal of Hydrogen Energy* **2011,** *36* (17), 10474-10481.
269. Siracusano, S.; Di Blasi, A.; Baglio, V.; Brunaccini, G.; Briguglio, N.; Stassi, A.; Ornelas, R.; Trifoni, E.; Antonucci, V.; Aricò, A. S., Optimization of components and assembling in a PEM electrolyzer stack. *International Journal of Hydrogen Energy* **2011,** *36* (5), 3333-3339.
270. Wu, X.; Tayal, J.; Basu, S.; Scott, K., Nano-crystalline RuxSn1−xO2 powder catalysts for oxygen evolution reaction in proton exchange membrane water electrolysers. *International Journal of Hydrogen Energy* **2011,** *36* (22), 14796-14804.
271. Spurgeon, J. M.; Lewis, N. S., Proton exchange membrane electrolysis sustained by water vapor. *Energy & Environmental Science* **2011,** *4* (8), 2993-2998.
272. Haxel, G. B.; Hedrick, J. B.; Orris, G. J.; Stauffer, P. H.; Hendley Ii, J. W. *Rare earth elements: critical resources for high technology*; 087-02; 2002.
273. Fabbri, E.; Habereder, A.; Waltar, K.; Kötz, R.; Schmidt, T. J., Developments and perspectives of oxide-based catalysts for the oxygen evolution reaction. *Catalysis Science & Technology* **2014,** *4* (11), 3800-3821.
274. Trasatti, S., Electrocatalysis in the anodic evolution of oxygen and chlorine. *Electrochimica Acta* **1984,** *29* (11), 1503-1512.
275. Minguzzi, A.; Fan, F.-R. F.; Vertova, A.; Rondinini, S.; Bard, A. J., Dynamic potential–pH diagrams application to electrocatalysts for water oxidation. *Chemical Science* **2012,** *3* (1), 217-229.
276. Abaci, S.; Pekmez, K.; Yildiz, A., The influence of nonstoichiometry on the electrocatalytic activity of PbO2 for oxygen evolution in acidic media. *Electrochemistry Communications* **2005,** *7* (4), 328-332.
277. Amadelli, R.; Armelao, L.; Velichenko, A. B.; Nikolenko, N. V.; Girenko, D. V.; Kovalyov, S. V.; Danilov, F. I., Oxygen and ozone evolution at fluoride modified lead dioxide electrodes. *Electrochimica Acta* **1999,** *45* (4), 713-720.
278. Bertoncello, R.; Cattarin, S.; Frateur, I.; Musiani, M., Preparation of anodes for oxygen evolution by electrodeposition of composite oxides of Pb and Ru on Ti. *Journal of Electroanalytical Chemistry* **2000,** *492* (2), 145-149.

279. Cao, J.; Zhao, H.; Cao, F.; Zhang, J., The influence of F− doping on the activity of PbO2 film electrodes in oxygen evolution reaction. *Electrochimica Acta* **2007,** *52* (28), 7870-7876.
280. Cattarin, S.; Guerriero, P.; Musiani, M., Preparation of anodes for oxygen evolution by electrodeposition of composite Pb and Co oxides. *Electrochimica Acta* **2001,** *46* (26), 4229-4234.
281. Patel, P. P.; Datta, M. K.; Velikokhatnyi, O. I.; Kuruba, R.; Damodaran, K.; Jampani, P.; Gattu, B.; Shanthi, P. M.; Damle, S. S.; Kumta, P. N., Noble metal-free bifunctional oxygen evolution and oxygen reduction acidic media electro-catalysts. *Scientific Reports* **2016,** *6*, 28367.
282. Shinde, A.; Jones, R. J.; Guevarra, D.; Mitrovic, S.; Becerra-Stasiewicz, N.; Haber, J. A.; Jin, J.; Gregoire, J. M. J. E., High-Throughput Screening for Acid-Stable Oxygen Evolution Electrocatalysts in the (Mn–Co–Ta–Sb) O x Composition Space. **2015,** *6* (2), 229-236.
283. Pérez-Viramontes, N. J.; Escalante-García, I. L.; Guzmán-Martínez, C.; Galván-Valencia, M.; Durón-Torres, S. M., Electrochemical study of Ir–Sn–Sb–O materials as catalyst-supports for the oxygen evolution reaction. *Journal of Applied Electrochemistry* **2015,** *45* (11), 1165-1173.
284. Sun, W.; Cao, L.-m.; Yang, J., Conversion of inert cryptomelane-type manganese oxide into a highly efficient oxygen evolution catalyst via limited Ir doping. *Journal of Materials Chemistry A* **2016,** *4* (32), 12561-12570.
285. Oakton, E.; Lebedev, D.; Fedorov, A.; Krumeich, F.; Tillier, J.; Sereda, O.; Schmidt, T. J.; Copéret, C., A simple one-pot Adams method route to conductive high surface area IrO2–TiO2 materials. *New Journal of Chemistry* **2016,** *40* (2), 1834-1838.
286. Oakton, E.; Lebedev, D.; Povia, M.; Abbott, D. F.; Fabbri, E.; Fedorov, A.; Nachtegaal, M.; Copéret, C.; Schmidt, T. J., IrO2-TiO2: A High-Surface-Area, Active, and Stable Electrocatalyst for the Oxygen Evolution Reaction. *ACS Catalysis* **2017,** *7* (4), 2346-2352.
287. Trotochaud, L.; Ranney, J. K.; Williams, K. N.; Boettcher, S. W., Solution-Cast Metal Oxide Thin Film Electrocatalysts for Oxygen Evolution. *Journal of the American Chemical Society* **2012,** *134* (41), 17253-17261.
288. Fominykh, K.; Chernev, P.; Zaharieva, I.; Sicklinger, J.; Stefanic, G.; Döblinger, M.; Müller, A.; Pokharel, A.; Böcklein, S.; Scheu, C.; Bein, T.; Fattakhova-Rohlfing, D., Iron-Doped Nickel Oxide Nanocrystals as Highly Efficient Electrocatalysts for Alkaline Water Splitting. *ACS Nano* **2015,** *9* (5), 5180-5188.
289. De Koninck, M.; Poirier, S.-C.; Marsan, B., Cu x Co3 − x O4 Used as Bifunctional Electrocatalyst: Physicochemical properties and electrochemical characterization for the oxygen evolution reaction. *Journal of The Electrochemical Society* **2006,** *153* (11), A2103-A2110.
290. Ajayi, B. P.; Kumari, S.; Jaramillo-Cabanzo, D.; Spurgeon, J.; Jasinski, J.; Sunkara, M., A rapid and scalable method for making mixed metal oxide alloys for enabling accelerated materials discovery. *Journal of Materials Research* **2016,** *31* (11), 1596-1607.
291. Pourbaix, M., *Atlas of Electrochemical Equilibria in Aqueous Solutions*. Pergamon Press: Oxford, 1966.
292. Wang, A.; Li, J.; Zhang, T., Heterogeneous single-atom catalysis. *Nature Reviews Chemistry* **2018,** *2* (6), 65-81.

293. Kubo, T.; Nishikitani, Y., Deposition Temperature Dependence of Optical Gap and Coloration Efficiency Spectrum in Electrochromic Tungsten Oxide Films. *Journal of The Electrochemical Society* **1998,** *145* (5), 1729-1734.
294. Ross-Medgaarden, E. I.; Wachs, I. E., Structural Determination of Bulk and Surface Tungsten Oxides with UV−vis Diffuse Reflectance Spectroscopy and Raman Spectroscopy. *The Journal of Physical Chemistry C* **2007,** *111* (41), 15089-15099.
295. Xiao, Z.; Zhang, L.; Tian, X.; Fang, X., Fabrication and structural characterization of porous tungsten oxide nanowires. *Nanotechnology* **2005,** *16* (11), 2647-2650.
296. Ng, K. T.; Hercules, D. M., Studies of nickel-tungsten-alumina catalysts by x-ray photoelectron spectroscopy. *The Journal of Physical Chemistry* **1976,** *80* (19), 2094-2102.
297. Kerkhof, F. P. J. M.; Moulijn, J. A.; Heeres, A., The XPS spectra of the metathesis catalyst tungsten oxide on silica gel. *Journal of Electron Spectroscopy and Related Phenomena* **1978,** *14* (6), 453-466.
298. Woodhouse, M.; Parkinson, B. A., Combinatorial approaches for the identification and optimization of oxide semiconductors for efficient solar photoelectrolysis. *Chemical Society Reviews* **2009,** *38* (1), 197-210.
299. Gregoire, J. M.; Xiang, C.; Liu, X.; Marcin, M.; Jin, J., Scanning droplet cell for high throughput electrochemical and photoelectrochemical measurements. *Review of Scientific Instruments* **2013,** *84* (2), 024102.
300. Kyômen, T.; Yamazaki, R.; Itoh, M., Valence and spin state of Co and Ni ions and their relation to metallicity and ferromagnetism in ${\mathrm{LaCo}}_{0.5}{\mathrm{Ni}}_{0.5}{\mathrm{O}}_{3}$. *Physical Review B* **2003,** *68* (10), 104416.
301. Dowden, D. A., Crystal and Ligand Field Models of Solid Catalysts. *Catalysis Reviews* **1972,** *5* (1), 1-32.
302. Calle-Vallejo, F.; Inoglu, N. G.; Su, H.-Y.; Martínez, J. I.; Man, I. C.; Koper, M. T. M.; Kitchin, J. R.; Rossmeisl, J., Number of outer electrons as descriptor for adsorption processes on transition metals and their oxides. *Chemical Science* **2013,** *4* (3), 1245-1249.
303. Gebhard, F., *The mott metal-insulator transition: models and methods*. Springer: Berlin, 1997.
304. Lufaso, M. W.; Woodward, P. M., Prediction of the crystal structures of perovskites using the software program SPuDS. *Acta Crystallographica Section B* **2001,** *57* (6), 725-738.
305. Glazer, A., Simple ways of determining perovskite structures. *Acta Crystallographica Section A* **1975,** *31* (6), 756-762.
306. Shannon, R., Revised effective ionic radii and systematic studies of interatomic distances in halides and chalcogenides. *Acta Crystallographica Section A* **1976,** *32* (5), 751-767.
307. Egerton, R. F., Applications of Energy-Loss Spectroscopy. In *Electron Energy-Loss Spectroscopy in the Electron Microscope*, Springer US: Boston, MA, 1996; pp 301-402.
308. Kumar, V.; Kumar, R.; Shukla, D. K.; Gautam, S.; Chae, K. H.; Kumar, R., Electronic structure and electrical transport properties of LaCo1−xNixO3 ($0 \leq x \leq 0.5$). *Journal of Applied Physics* **2013,** *114* (7), 073704.
309. Abbate, M.; de Groot, F. M. F.; Fuggle, J. C.; Fujimori, A.; Tokura, Y.; Fujishima, Y.; Strebel, O.; Domke, M.; Kaindl, G.; van Elp, J.; Thole, B. T.; Sawatzky, G. A.; Sacchi,

M.; Tsuda, N., Soft-x-ray-absorption studies of the location of extra charges induced by substitution in controlled-valence materials. *Physical Review B* **1991,** *44* (11), 5419-5422.
310. S.J. Pennycook, P. D. N., *Scanning transmission electron microscopy: imaging and analysis*. Springer Science & Business Media: 2011.
311. Zaanen, J.; Sawatzky, G. A.; Allen, J. W., Band gaps and electronic structure of transition-metal compounds. *Physical Review Letters* **1985,** *55* (4), 418-421.
312. Chen, D.; Chen, C.; Baiyee, Z. M.; Shao, Z.; Ciucci, F., Nonstoichiometric Oxides as Low-Cost and Highly-Efficient Oxygen Reduction/Evolution Catalysts for Low-Temperature Electrochemical Devices. *Chemical Reviews* **2015,** *115* (18), 9869-9921.
313. Armstrong, A.; Robertson, A.; Bruce, P., Overcharging manganese oxides: Extracting lithium beyond Mn4+. *Journal of power sources* **2005,** *146* (1-2), 275-280.
314. Stoyanova, R.; Zhecheva, E.; Alcántara, R.; Tirado, J. L.; Bromiley, G.; Bromiley, F.; Boffa Ballaran, T., Lithium/nickel mixing in the transition metal layers of lithium nickelate: high-pressure synthesis of layered Li[LixNi1−x]O2 oxides as cathode materials for lithium-ion batteries. *Solid State Ionics* **2003,** *161* (3), 197-204.
315. Kang, S. H.; Kim, J.; Stoll, M. E.; Abraham, D.; Sun, Y. K.; Amine, K., Layered Li(Ni0.5−xMn0.5−xM2x′)O2 (M′=Co, Al, Ti; x=0, 0.025) cathode materials for Li-ion rechargeable batteries. *Journal of Power Sources* **2002,** *112* (1), 41-48.
316. Hwang, B. J.; Tsai, Y. W.; Chen, C. H.; Santhanam, R., Influence of Mn content on the morphology and electrochemical performance of LiNi1−−CoMnO2 cathode materials. *Journal of Materials Chemistry* **2003,** *13* (8), 1962-1968.
317. Denis, Y.; Yanagida, K.; Kato, Y.; Nakamura, H., Electrochemical activities in Li2MnO3. *Journal of The Electrochemical Society* **2009,** *156* (6), A417-A424.
318. Jouanneau, S.; Eberman, K.; Krause, L.; Dahn, J., Synthesis, Characterization, and Electrochemical Behavior of Improved Li [Ni x Co1− 2x Mn x] O 2 (0.1⩽ x⩽ 0.5). *Journal of The Electrochemical Society* **2003,** *150* (12), A1637-A1642.
319. Kang, S.-H.; Kempgens, P.; Greenbaum, S.; Kropf, A.; Amine, K.; Thackeray, M., Interpreting the structural and electrochemical complexity of 0.5 Li 2 MnO 3· 0.5 LiMO 2 electrodes for lithium batteries (M= Mn 0.5− x Ni 0.5− x Co 2x, 0≤ x≤ 0.5). *Journal of Materials Chemistry* **2007,** *17* (20), 2069-2077.
320. Gummow, R.; Thackeray, M., Lithium-cobalt-nickel-oxide cathode materials prepared at 400 C for rechargeable lithium batteries. *Solid State Ionics* **1992,** *53*, 681-687.
321. Bau, J. A.; Li, P.; Marenco, A. J.; Trudel, S.; Olsen, B. C.; Luber, E. J.; Buriak, J. M., Nickel/iron oxide nanocrystals with a nonequilibrium phase: Controlling size, shape, and composition. *Chemistry of Materials* **2014,** *26* (16), 4796-4804.
322. Guo, Y. G.; Hu, J. S.; Wan, L. J., Nanostructured materials for electrochemical energy conversion and storage devices. *Advanced Materials* **2008,** *20* (15), 2878-2887.
323. Taniguchi, I.; Song, D.; Wakihara, M., Electrochemical properties of LiM1/6Mn11/6O4 (M= Mn, Co, Al and Ni) as cathode materials for Li-ion batteries prepared by ultrasonic spray pyrolysis method. *Journal of power Sources* **2002,** *109* (2), 333-339.
324. Patey, T. J.; Ng, S. H.; Büchel, R.; Tran, N.; Krumeich, F.; Wang, J.; Liu, H.-K.; Novák, P., Electrochemistry of LiV3O8 nanoparticles made by flame spray pyrolysis. *Electrochemical and solid-state letters* **2008,** *11* (4), A46-A50.

325. Ernst, F. O.; Kammler, H. K.; Roessler, A.; Pratsinis, S. E.; Stark, W. J.; Ufheil, J.; Novák, P., Electrochemically active flame-made nanosized spinels: LiMn2O4, Li4Ti5O12 and LiFe5O8. *Materials chemistry and physics* **2007,** *101* (2-3), 372-378.
326. Spin-State Transition in LaCoO3: Direct Neutron Spectroscopic Evidence of Excited Magnetic States. *Phys. Rev. Lett.* **2006,** *97* (24), 247208.
327. Xiao, J.; Chernova, N. A.; Whittingham, M. S., Influence of Manganese Content on the Performance of LiNi0.9−yMnyCo0.1O2 ($0.45 \leq y \leq 0.60$) as a Cathode Material for Li-Ion Batteries. *Chemistry of Materials* **2010,** *22* (3), 1180-1185.
328. Saavedra-Arias, J. J.; Karan, N. K.; Pradhan, D. K.; Kumar, A.; Nieto, S.; Thomas, R.; Katiyar, R. S., Synthesis and electrochemical properties of Li (Ni0. 8Co0. 1Mn0. 1) O2 cathode material: Ex situ structural analysis by Raman scattering and X-ray diffraction at various stages of charge–discharge process. *Journal of Power Sources* **2008,** *183* (2), 761-765.
329. Julien, C.; Massot, M., Spectroscopic studies of the local structure in positive electrodes for lithium batteries. *Physical Chemistry Chemical Physics* **2002,** *4* (17), 4226-4235.
330. Ramana, C.; Massot, M.; Julien, C., XPS and Raman spectroscopic characterization of LiMn2O4 spinels. *Surface and Interface Analysis: An International Journal devoted to the development and application of techniques for the analysis of surfaces, interfaces and thin films* **2005,** *37* (4), 412-416.
331. Julien, C.; Massot, M., Raman spectroscopic studies of lithium manganates with spinel structure. *Journal of Physics: Condensed Matter* **2003,** *15* (19), 3151.
332. Shaju, K. M.; Subba Rao, G. V.; Chowdari, B. V. R., X-ray photoelectron spectroscopy and electrochemical behaviour of 4 V cathode, Li(Ni1/2Mn1/2)O2. *Electrochimica Acta* **2003,** *48* (11), 1505-1514.
333. Li, D.; Kato, Y.; Kobayakawa, K.; Noguchi, H.; Sato, Y., Preparation and electrochemical characteristics of LiNi1/3Mn1/3Co1/3O2 coated with metal oxides coating. *Journal of Power Sources* **2006,** *160* (2), 1342-1348.
334. Bréger, J.; Meng, Y. S.; Hinuma, Y.; Kumar, S.; Kang, K.; Shao-Horn, Y.; Ceder, G.; Grey, C. P., Effect of High Voltage on the Structure and Electrochemistry of LiNi0.5Mn0.5O2: A Joint Experimental and Theoretical Study. *Chemistry of Materials* **2006,** *18* (20), 4768-4781.
335. Kalyani, P.; Chitra, S.; Mohan, T.; Gopukumar, S., Lithium metal rechargeable cells using Li2MnO3 as the positive electrode. *Journal of power sources* **1999,** *80* (1-2), 103-106.
336. Johnson, C. S.; Kim, J. S.; Lefief, C.; Li, N.; Vaughey, J. T.; Thackeray, M. M., The significance of the Li2MnO3 component in 'composite' xLi2MnO3·(1−x)LiMn0.5Ni0.5O2 electrodes. *Electrochemistry Communications* **2004,** *6* (10), 1085-1091.
337. Yabuuchi, N.; Yoshii, K.; Myung, S.-T.; Nakai, I.; Komaba, S., Detailed Studies of a High-Capacity Electrode Material for Rechargeable Batteries, Li2MnO3−LiCo1/3Ni1/3Mn1/3O2. *Journal of the American Chemical Society* **2011,** *133* (12), 4404-4419.
338. Hu, M.; Pang, X.; Zhou, Z., Recent progress in high-voltage lithium ion batteries. *Journal of Power Sources* **2013,** *237*, 229-242.

339. Martha, S. K.; Nanda, J.; Veith, G. M.; Dudney, N. J., Electrochemical and rate performance study of high-voltage lithium-rich composition: Li1.2Mn0.525Ni0.175Co0.1O2. *Journal of Power Sources* **2012,** *199*, 220-226.
340. Lu, Z.; MacNeil, D. D.; Dahn, J. R., Layered Cathode Materials Li [Ni x Li (1 / 3 − 2x / 3) Mn (2 / 3 − x / 3)] O 2 for Lithium-Ion Batteries. *Electrochemical and Solid-State Letters* **2001,** *4* (11), A191-A194.
341. Son, M. Y.; Hong, Y. J.; Choi, S. H.; Kang, Y. C., Effects of ratios of Li 2 MnO 3 and Li (Ni 1/3 Mn 1/3 Co 1/3) O 2 phases on the properties of composite cathode powders in spray pyrolysis. *Electrochimica Acta* **2013,** *103*, 110-118.
342. Hong, Y. J.; Kim, J. H.; Kim, M. H.; Kang, Y. C., Electrochemical properties of 0.3 Li 2 MnO 3· 0.7 LiNi 0.5 Mn 0.5 O 2 composite cathode powders prepared by large-scale spray pyrolysis. *Materials Research Bulletin* **2012,** *47* (8), 2022-2026.
343. Ju, S. H.; Kang, Y. C., The characteristics of Ni–Co–Mn–O precursor and Li (Ni 1/3 Co 1/3 Mn 1/3) O 2 cathode powders prepared by spray pyrolysis. *Ceramics International* **2009,** *35* (3), 1205-1210.
344. Kim, J. H.; Yi, J. H.; Ko, Y. N.; Kang, Y. C., Electrochemical properties of nano-sized LiNi 1/3 Co 1/3 Mn 1/3 O 2 powders in the range from 56 to 101nm prepared by flame spray pyrolysis. *Materials Chemistry and Physics* **2012,** *134* (1), 254-259.
345. Xiao, J.; Chernova, N. A.; Whittingham, M. S., Influence of Manganese Content on the Performance of LiNi0. 9− y Mn y Co0. 1O2 (0.45≤ y≤ 0.60) as a Cathode Material for Li-Ion Batteries†. *Chemistry of Materials* **2009,** *22* (3), 1180-1185.

APPENDICES

Appendix 1: Williamson-Hill Plots

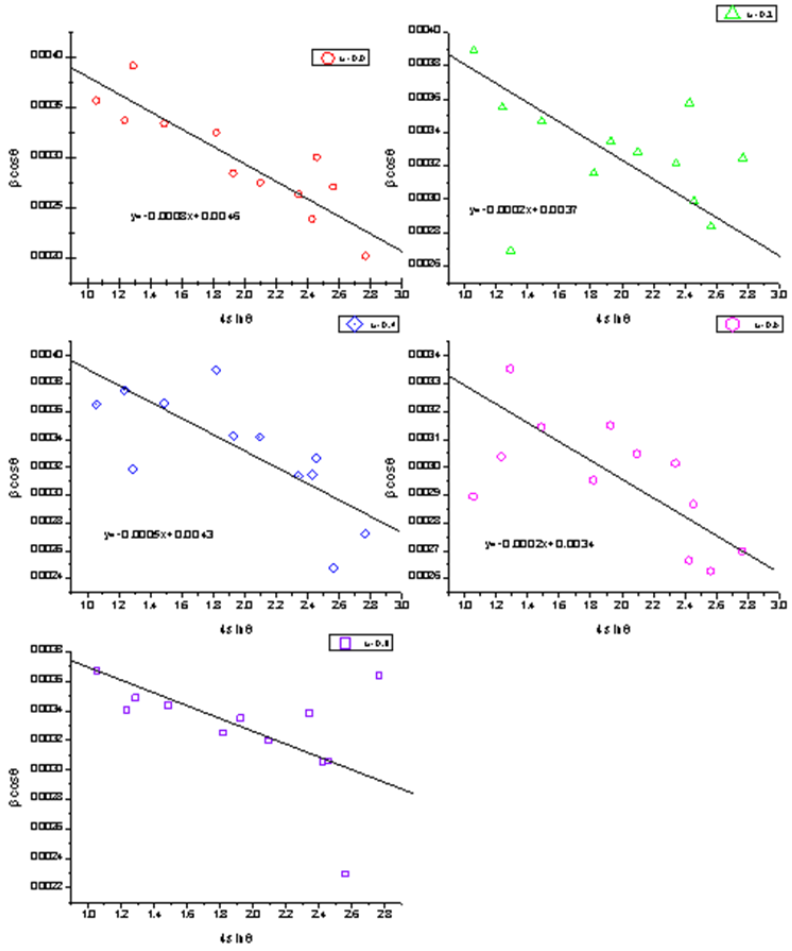

Figure A1 The linear fits of the Williamson-Hall plots for composition υ=0.0, 0.2, 0.4, 0.6 and 0.8

Appendix 2: Rietveld Refinement Table

Table A2 Values of atomic coordinates (x, y, z) and occupancy (g) determined from Rietveld refinement of XRD pattern of $NiMn_{0.2}Fe_{1.8}O_4$ (Cation distribution from Rietveld refinement)

Atom	x=y=z	Occ.(g)
Ni	0.1250	0.0998(2)
Mn	0.1250	0.1499(1)
Fe	0.1250	0.7501(1)
Ni	0.5000	0.9002(1)
Mn	0.5000	0.0501(1)
Fe	0.5000	1.0499(1)

The data were processed to analyze all of the samples using the computer Program FullProf.2k (Version 4.30—Apr, 2008-ILL JRC) in the Rietveld method for structure refinement. Program refinement of the first samples was started with the space group Fd3m, origin at −3 m, O in 32e−, A site in 8f, and B site in 16c. The global parameters, such as 2θ-zero and background, were refined. Cation distribution from XRD patterns based on Bertaut method.

Appendix 3: Determination of Turnover Frequency

Turnover frequency (TOF) was determined as the number of OER reaction conversions occurring per catalyst active site per time. With the uncertainty in the number of metal cation sites exposed to the electrolyte and contributing to the reaction, both a lower bound and an upper bound estimate to the TOF were calculated. Due to possible sub-nm porosity from combusted organic components during the rapid plasma oxidation as well as a possible semi-permeable hydrous layer at the catalyst surface under operation, some non-surface metal sites may contribute to the reaction. The lower bound turnover frequency (TOF_{LB}) was therefore estimated assuming all metal sites contribute to the reaction. The upper bound turnover frequency (TOF_{UB}), in contrast, was calculated assuming that only metal cations at the surface of the catalyst were capable of being active reaction sites.

The lower bound was calculated by:

$$TOF_{LB} = \frac{JM_{cat}}{nFl}$$

where J is the current density at the overpotential under evaluation, M_{cat} is the molecular weight of the catalyst, n is the number of moles of electrons per mole of reaction (n= 4 for OER),F is the Faraday's constant, and ℓ is the catalyst mass loading per electrode projected area. For the catalyst $W_{1-x}Ir_xO_{3-\delta}$, the molecular weight was approximated by assuming charge balance with only the predominant oxidation states W^{6+}, Ir^{4+}, and O^{2-}, which gives $W_{1-x}Ir_xO_{3-x}$. Thus, for the catalyst $W_{1-x}Ir_xO_{3-x}$:

$$M_{cat} = 231.84 - 7.62\ x\ \frac{g}{mol}$$

Determining the upper bound turnover frequency required an estimate of the catalyst surface area. An electrochemically active surface area can be estimated by measuring the electrode double layer capacitance and comparing it to an estimated flat sample capacitance. However, large experimental error and unknown capacitance values for theoretically flat catalyst materials made this an unreliable method. Instead, the upper bound was calculated using the Brunauer–Emmett–Teller (BET) gas adsorption method to measure catalyst surface area. BET analysis was performed with the Micromeritics Tristar 3000 porosimeter. Samples were carefully weighed and degassed before performing the measurements to remove any adsorbed contaminants from the surface and pores of the sample. Calculations for the BET surface area were done by using the TriStar 3000 analysis program. The number of metal cation sites per surface area was *approximated* by determining the molecular volumetric concentration of the catalyst, assuming a uniform molecule distribution (i.e., roughly cubic arrangement), and relating it the molecular surface concentration. Note that this is inherently an approximation for metal cation surface concentration, since the method neglects crystal structure and surface orientation, which are not precisely known for rough polycrystalline nanoparticulates with multiple possible phases. Two different mathematical approaches were used to relate $C_{cat,surf}$, the catalyst molecule concentration by surface area, to $C_{cat,vol}$, the catalyst molecule concentration by volume, both yielding identical results. In the first method, a spherical particle of radius, R, is assumed and the number of molecules at the surface, N_s, is determined by integrating across the volume of a shell with width equal to the distance between molecules:

$$N_s = \int_R^{R+a} 4\pi C_{cat,vol} R^2 dR = \frac{4}{3}\pi C_{cat,vol}(3R^2 a + 3Ra^2 + a^3)$$

And for the spherical particle:

$$C_{cat,surf} = \frac{N_s}{4\pi R^2} \approx aC_{cat,vol}\ for\ R \gg a$$

Assuming uniformly distributed molecules in roughly cubic arrangement, the intermolecular distance is:

$$a \sim C_{cat,vol}^{-1/3}$$

$$C_{cat,surf} \sim C_{cat,vol}^{2/3}$$

Alternatively, in the second approach, a cubic particle with *N* molecules per side of length *L* is assumed:

$$C_{cat,vol} = \frac{N^3}{L^3}$$

$$N_s = N_{total} - N_{interior} = N^3 - (N-2)^3$$

$$N_s = 6\left(N^2 - 2N + \frac{4}{3}\right) \approx 6N^2\ for\ large\ N$$

$$C_{cat,surf} = \frac{N_S}{6L^2} \approx \frac{N^2}{L^2}$$

with both methods providing the same molecular surface concentration estimate of:

$$C_{cat,surf} \approx \left(C_{cat,vol}\right)^{2/3} \approx \left(\frac{\rho_{cat} N_A}{M_{cat}}\right)^{2/3}$$

where N_A is Avagadro's number, and ρ_{cat} is the mass density of the catalyst. ρ_{cat} was estimated assuming a linearly weighted average between the density of WO_3 and IrO_2. For the catalyst $W_{1-x}Ir_xO_{3-x}$:

$$\rho_{cat} = (1-x)\rho_{WO3} + x\rho_{IrO2} = 7.16 + 4.5x\,\frac{g}{cm^3}$$

The upper bound was then calculated by:

$$TOF_{UB} = \frac{JAN_A}{nFC_{cat,surf}A_{BET}} = \frac{JN_A}{nF\left(\frac{\rho_{cat}N_A}{M_{cat}}\right)^{2/3} lS_{BET}}$$

where N is the electrode projected area, A_{BET} is the catalyst surface area as measured by BET, and S_{BET} is the BET-measured specific surface area per mass of catalyst.

WO_3 by itself is a very kinetically sluggish surface for OER, with a measured overpotential of 1.58 V at 10 mA cm^{-2}. Thus, in the mixed metal $W_{1-x}Ir_xO_{3-\delta}$ catalyst, the Ir cation sites are presumed to support the large majority of oxygen evolution turnover. An Ir-specific turnover frequency was thus calculated to highlight the activity of the Ir sites accounting for their fraction of the total metal cations, assuming 100% reaction at Ir sites:

$$TOF_{LB,Ir} = \frac{TOF_{LB}}{x}$$

$$TOF_{UB,Ir} = \frac{TOF_{UB}}{x}$$

Appendix 4: Detailed Raman Spectra Characterization

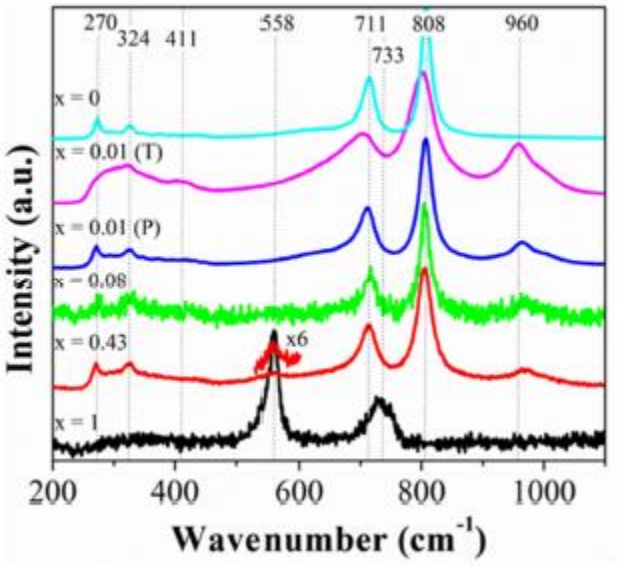

Figure A4 Raman spectra for each plasma-oxidized $W_{1-x}Ir_xO_{3-\delta}$ composition.

The Raman bands for all W-containing catalyst samples displayed the characteristic peaks attributed to crystalline WO_3. Pure WO_3 (x = 0) had four well-resolved Raman peaks thatcorrespond to the fundamental modes of WO_3 at 270, 324, 711, and 808 cm^{-1}.[290] The bands at 711 and 808 cm^{-1} have been assigned to the W-O-W stretching frequencies, with the band at 270 cm^{-1} corresponding to the W-O-W bending mode. The peak at 324 cm^{-1} has been assigned to the O-W-O bending vibration. For all mixed $W_{1-x}Ir_xO_{3-\delta}$ samples there was an additional Raman band peaking at ~960 cm^{-1} not present in either WO_3 or IrO_2, which the literature generally attributes to the *v*s (W=O terminal) symmetric stretching mode.[288-289]Similar Raman features have been reported for numerous metal heteropolyoxo tungstate species. [289] This Raman band at ~960 cm^{-1} thus reflects distortion among the tungsten oxide framework and further supports the presence of an iridium

polytungstate phase. Also, the noticeable broadening of the Raman bands of the thermal sample relative to the plasma sample have been correlated to greater nanocrystallinity.[290]

Appendix 5: Detailed XPS Characterization

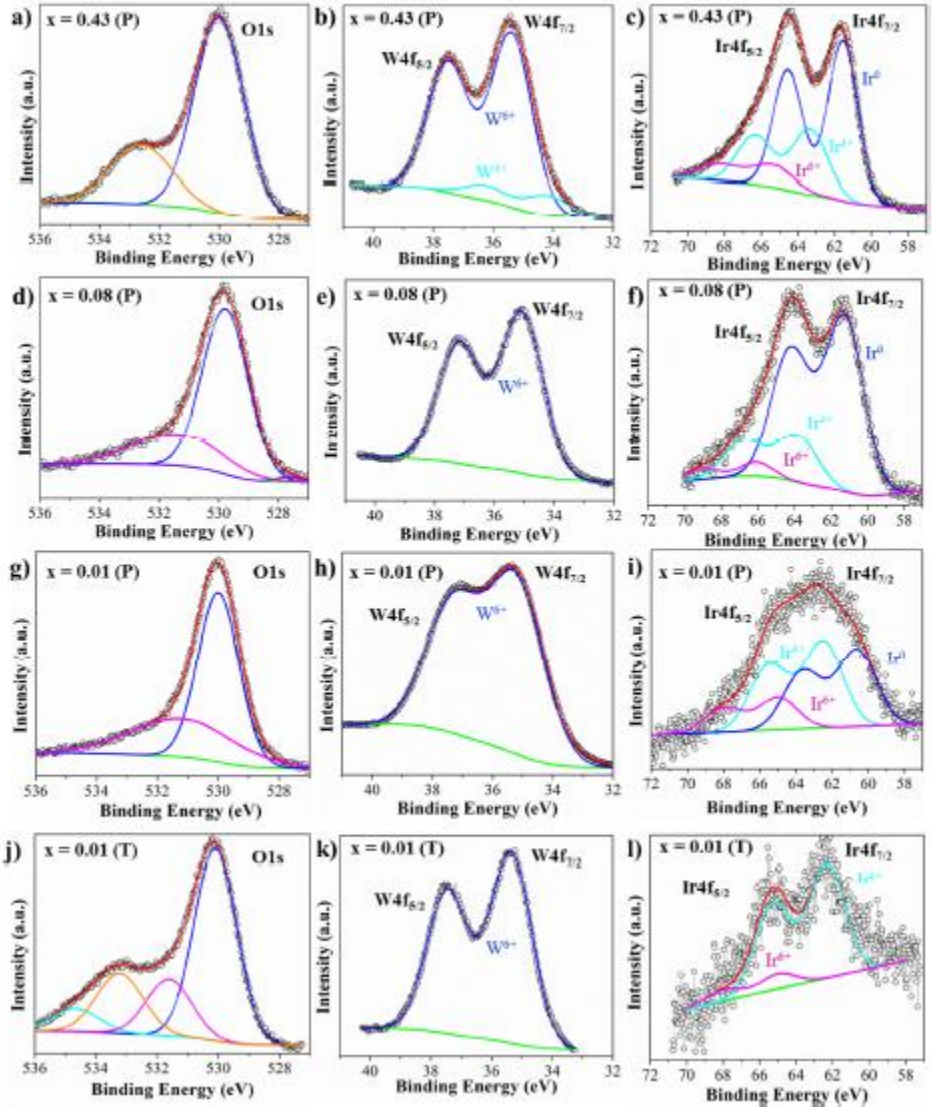

Figure A4 XPS spectra for the O1s, W4f, and Ir4f peaks for plasma-oxidized (a-c) $W_{0.57}Ir_{0.43}O_{3-\delta}$, (d-f) $W_{0.92}Ir_{0.08}O_{3-\delta}$, and (g-i) $W_{0.99}Ir_{0.01}O_{3-\delta}$, and (j-l) thermally oxidized $W_{0.99}Ir_{0.01}O_{3-\delta}$.

Appendix 6: Structure Parameters and R-factors of Rietveld Refined Samples.

Table A6 Structure parameters and R-factors of Rietveld refined samples.

	x = 0.0(P)	*x* = 0.01(T)	*x* = 0.01(P)	*x* = 0.08(P)		*x* = 0.43(P)		
Phase	[1]WO_3	WO_3	WO_3	WO_3	[2]Ir	WO_3	Ir	[3]IrO_2
wt. fraction	1.0000	1.0000	1.0000	0.97104	0.02896	0.63986	0.22686	0.13328
Density(g/cm^3)	7.260	7.180	7.259	7.258	22.537	7.262	22.512	11.661
R_{wp}	0.092	0.0621	0.073	0.0688		0.0734		
R_p	0.0674	0.0497	0.0568	0.0506		0.0524		
R_{Bragg}	0.0496	0.0637	0.0597	0.0402		0.1542		
a(Å)	7.315(1)	7.390(1)	7.329(1)	7.329(1)	3.841(1)	7.321(0)	3.842(0)	4.502(1)
b(Å)	7.531(1)	7.537(1)	7.518(1)	7.523(1)	3.841(1)	7.529(1)	3.842086	4.502(1)
c(Å)	7.701(1)	7.703(1)	7.698(1)	7.697(1)	3.841(1)	7.695(1)	3.842086	3.151(1)
α(°)	90.21(1)	89.38(2)	89.65(1)	89.74(1)	90	89.68(1)	90	90
β(°)	89.33(1)	89.35(1)	89.37(1)	89.35(1)	90	89.29(1)	90	90
γ(°)	90.04(2)	89.61(2)	89.91(1)	89.96(2)	90	89.95(1)	90	90
Volume(Å^3)	424.24(9)	428.97(15)	424.13(9)	424.36(9)	56.65(2)	424.11(7)	56.72	63.86(2)
GU	0	36.49	782.2(44)	570.6	0.00	36.49	36.49	36.49
GV	-43.2	-43.20	-43.2(6)	-41.04	-43.20	-43.20	-43.20	-43.2
GW	14.26	14.26	36.21(6)	14.26	14.26	14.26	14.26	14.26
GP	0	0.00	0.00	0	0.00	0.00	0.00	0
LX	23.47	38.94	18.38	19.01(3)	27.11(2)	13.14(2)	8.58(2)	0
LY	3.346	3.35	3.35	3.346	3.35	3.35	3.35	91.36(10)
S/L	0.02555	0.03	0.03	0.02555	0.03	0.03	0.03	0.02555
H/L	0.04787	0.05	0.05	0.04787	0.05	0.05	0.05	0.05
stec	0	8.39	0.00	0.00	0.00	0.00	0.00	0.00
L_{23}	0	0.00	-0.27	0.00	0.00	0.00	0.00	0.00

[1]Triclinic phase (Space Group: $\bar{P}_1$), [2]Cubic phase (Space Group: Fd$\bar{3}$m), [3]Tetragonal phase (Space Group: P 42/m n m).

Note: a, b, and c are the lattice constants. α, β, and γ are the unit cell angles. GU, GV and GW are the Gaussian terms for U, V and W in the Cagliotti function, GP is the Gaussian crystallite size broadening, LX is the Lorentzian isotropic crystallite size broadening while LY is the isotropic strain broadening. S/L is the axial divergence S term, H/L isthe axial divergence H term, stec represents Lorentzian anisotropic strain broadening, and L_{23} is represents the anisotropic Lorentzian microstrain.

Appendix 7: Detailed XPS Characterization

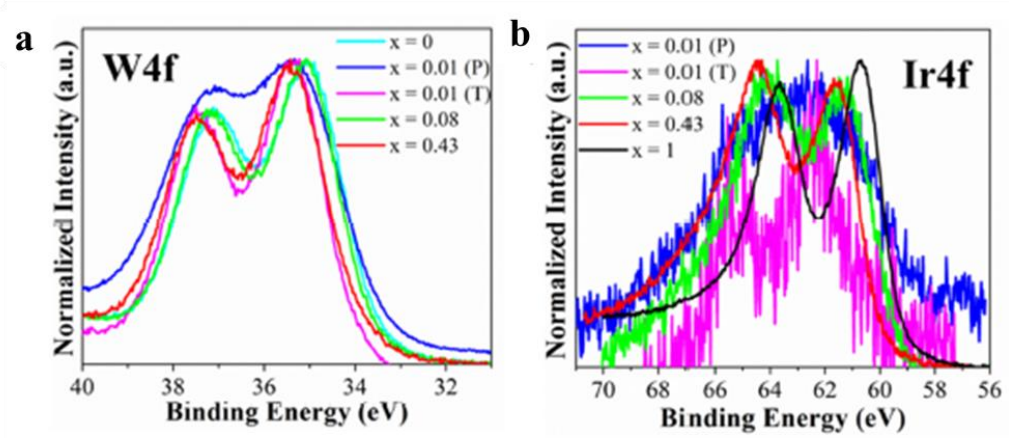

Figure A7 Combined XPS spectra with normalized intensity for the (a) W4f and (b) Ir4f peaks.

Appendix 8: Detailed XPS Characterization

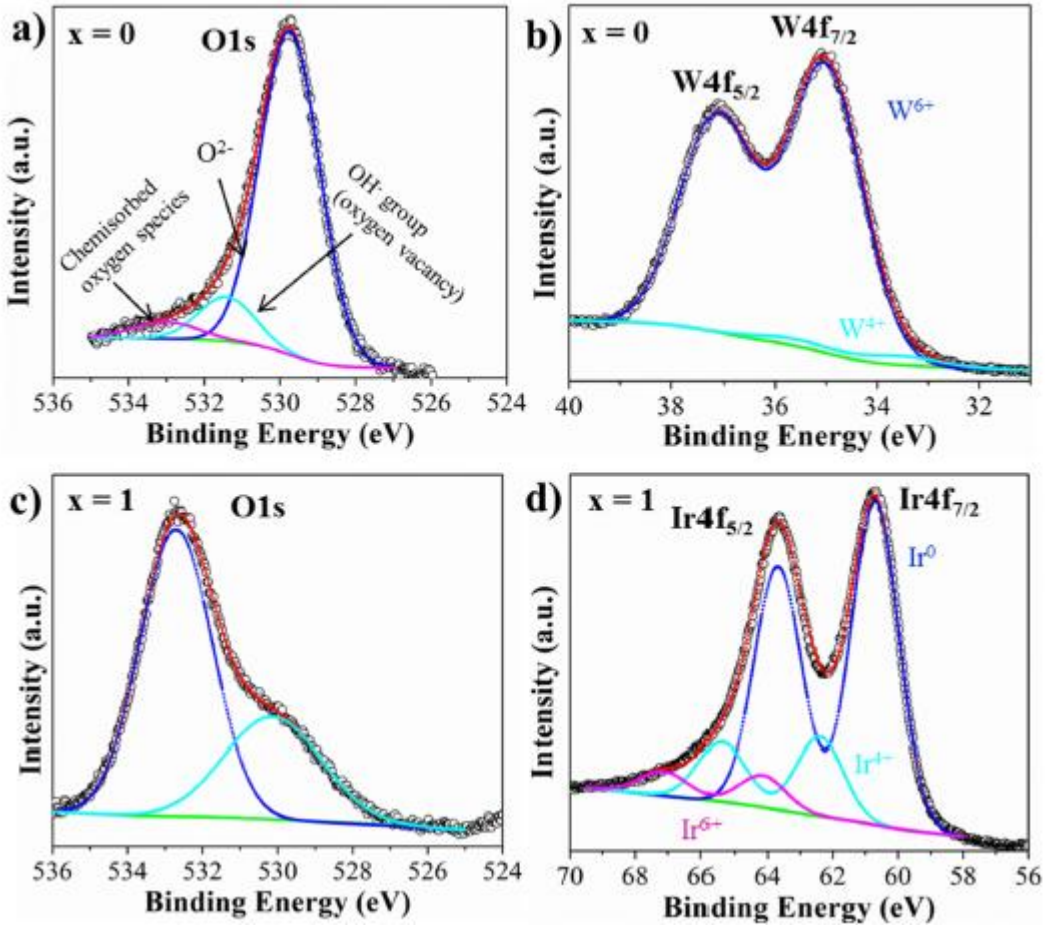

Figure A8 XPS spectra for plasma-oxidized (a-b) WO_3 (x = 0) showing the (a) O1s and (b) W4f peaks, and for (c-d) IrO_2 (x = 1) showing the (c) O1s and (d) Ir4f peaks.

Appendix 9: Elemental Analysis

Table A9 (a) Summary of elemental analysis of Ni, Mn and Co in $LiNi_{0.20}Mn_{0.60}Co_{0.20}O_2$

Method	Ni (at. %)	Mn (at. %)	Co (at. %)
ICP-MS	19.96	58.93	21.11
TEM-EDS	19.91	59.04	21.04
XPS	19.41	52.12	28.46

Table A9 (b) ICP-MS raw data for elemental composition of Li, Ni, Mn and Co in $LiNi_{0.20}Mn_{0.60}Co_{0.20}O_2$[a]

Run	Mn (ppb)	Co (ppb)	Ni (ppb)	Li (ppb)
1	29810	10080	10670	50978
2	29670	10100	10690	50410
3	29930	10100	10660	52597
mean	29800	10090	10670	51328
S.D.	132.7	14.13	15.26	1135
% RSD	0.445	0.14	0.143	2.21
atom %	29.25	10.47	9.91	50.37

[a] SD is the standard deviation of triplicate samples, where % RSD is the relative standard deviation defined as the percentage of the SD to the sample mean.

Table A9 (c) TEM-EDS raw data (in atom %[b]) for elemental analysis of four grains of $LiNi_{0.20}Mn_{0.60}Co_{0.20}O_2$ [a]

Grain	Mn (at. %)	Ni (at. %)	Co (at. %)
1	18.99	6.73	5.75
2	21.74	7.67	7.72
3	19.19	6.92	7.66
4	23.08	6.68	8.45
mean	20.75	7	7.395
SD	1.99501	0.458476	1.153964
% RSD	9.614508	6.549653	15.60465
atom %	59.04112	19.91748	21.0414

[a] SD is the standard deviation from elemental analysis of four grains shown in STEM image of Figure S1, where % RSD is the relative standard deviation defined as the percentage of the SD to the sample mean. **[b]**The balance is oxygen, which was ignored in calculation, and lithium composition is not captured because it is below the detection limit of the instrument.

Appendix 10: Elemental Analysis

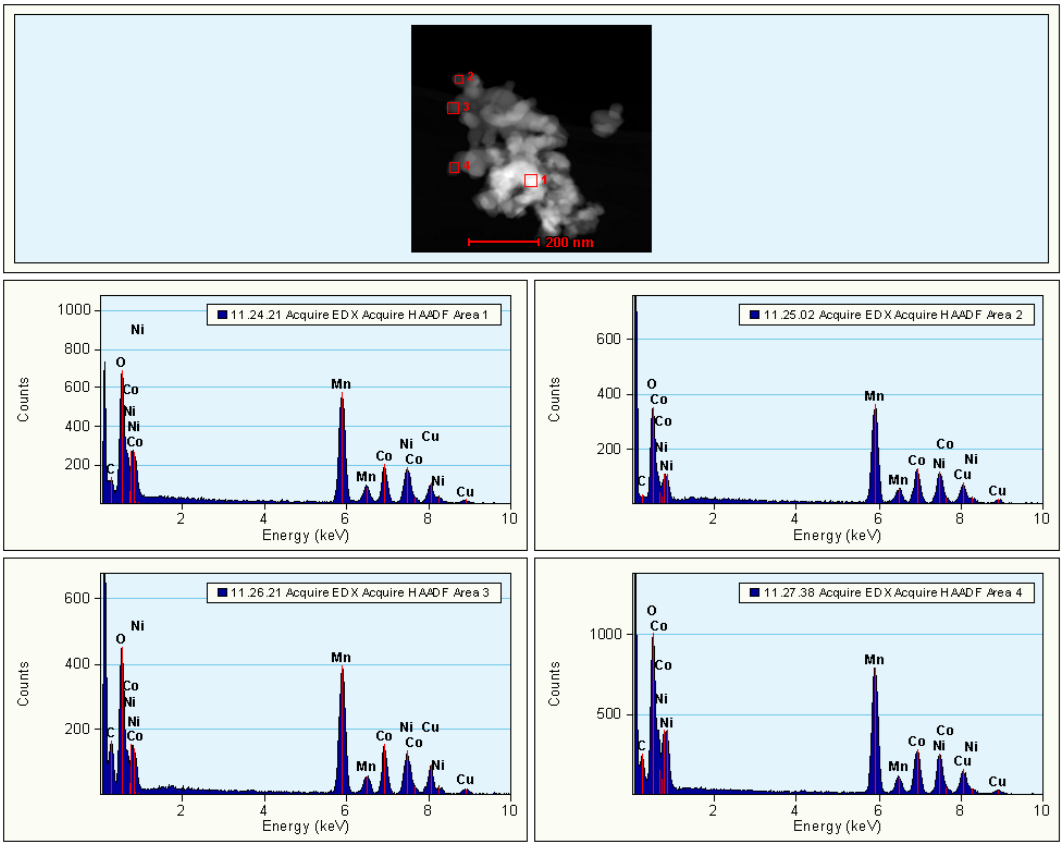

Figure A10 (a) Top: Four different grains of the LiNi0.2Mn0.6Co0.2O2 probed for Energy-dispersive X-ray (EDS) analysis. Below: TEM-EDS spectra of the four selected probe areas whose area is indicative of the composition of nickel, manganese and cobalt. The Cu spectra is as result of the Cu grid used for sample preparation. Note: Lithium spectra is not captured because it is below the detection limit of the instrument. ICP-MS analysis was carried out to confirm lithium amount

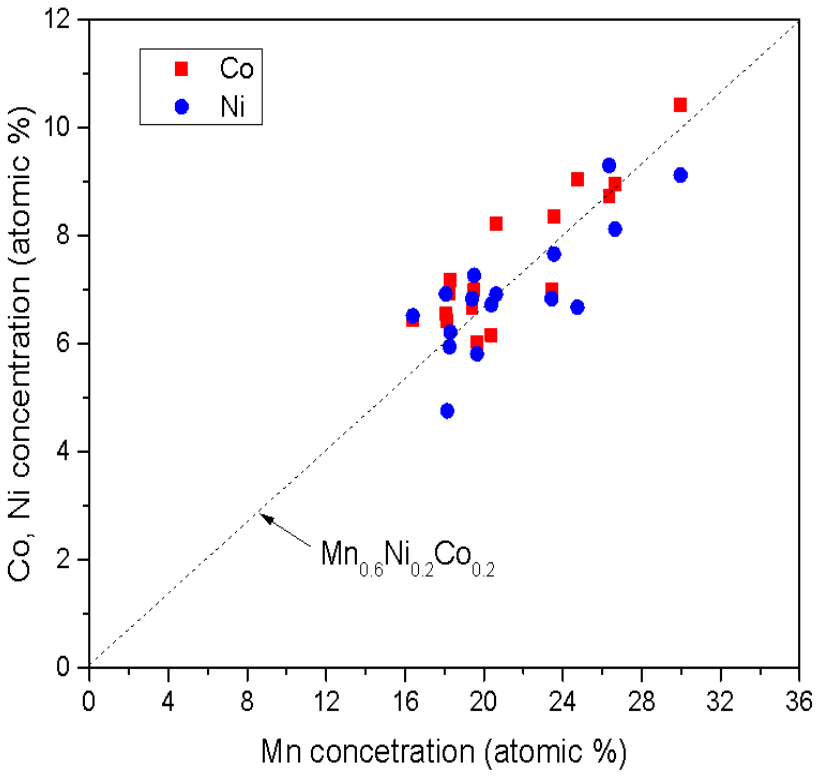

Figure A10 (b) Scatter plot of Mn-Ni-Co with the reference 45˚line in the proportion 3:1:1 respectively. Mn composition is on the horizontal axis while Ni and Co composition are on the vertical axis. All compositions were derived from the integration of the TEM-EDS spectra using a software

Appendix 11: Analysis of the Thermal Decomposition of Precursors

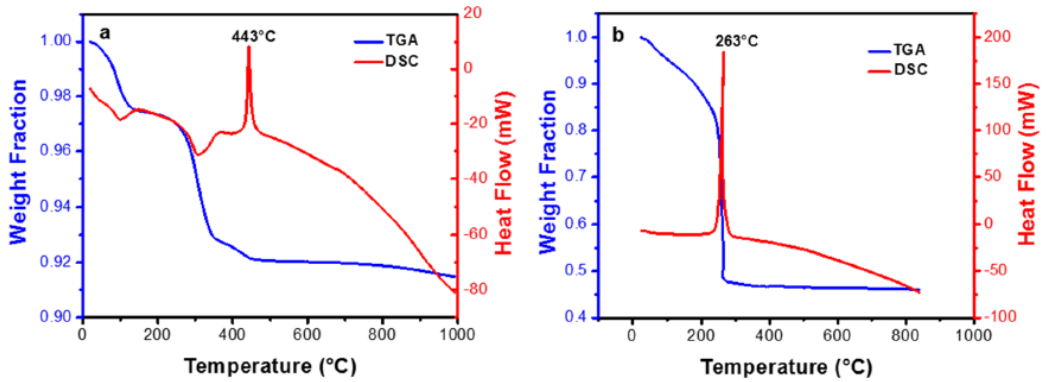

Figure A11. TGA (blue lines) and DSC (red lines) profiles of the (a) tungsten (ammonium paratungstate hydrate, $(NH_4)_6[W_{12}O_{39}]\cdot_{4.8}H_2O$, molecular weight: 3024.48 g/mol) and (b) iridium (iridium acetate, $(CH_3COO)_4Ir$, molecular weight: 428.42 g/mol) precursors used in this work.

Figure A11 shows the results of thermogravimetric analysis (TGA) and differential scanning calorimeter (DSC) measurements under a flowing air atmosphere of the tungsten and iridium precursors used to produce $W_{1-x}Ir_xO_{3-\delta}$. This experiment was carried out in order to elucidate the thermal events of the solid-gas interfacial reactions through thermal decomposition of catalyst sample precursors and to determine the synthesis temperature at which the speciation of the crystalline phase will occur. For the W precursor (ammonium paratungstate hydrate) the thermal decomposition profile is shown in Figure A11(a). The results indicate that the decomposition happens in three notable steps. The first weight loss step in the TGA curve occurred from 21 - 140 ºC, which is attributed to the release of water

as the hydrated precursor becomes anhydrous as well as the release of some trace amounts of ammonia. The weight loss due to the $\cdot 4.8H_2O$ hydrate should theoretically be 2.86 wt. %, which agreed well with the measured 2.80 wt. % loss at 140 ºC according to the TGA profile. DSC indicated that this drying step into anhydrous ammonium paratungstate is endothermic in nature with a negative heat flow. The second weight loss step, from 140 - 364 ºC, in the TGA curve could be due to ammonia and water vapor liberation according to the equation:

$$(NH_4)_6[W_{12}O_{39}] \rightarrow 6NH_3 + 3H_2O + 12WO_3$$

The observed weight loss from the TGA in this temperature region was ~5.0 wt. %, which corresponded well with a theoretical value from the above loss of ammonia and water vapor of 5.15 wt. %. This step was again endothermic according to the DSC curve. The third and final weight loss step occurred from 413 - 470 ºC and had a sharp exothermic peak at 443 ºC as shown in the DSC profile that can be ascribed to the crystallization of the amorphous WO_3 phase to a crystalline WO_3 phase. The thermally synthesized $W_{1-x}Ir_xO_{3-\delta}$ samples in this work were fabricated at well above 443 ºC (processed at 500 ºC), so it is expected that the crystalline phase of WO_3 will result under the thermal processing conditions used in this work. The theoretical ceramic yield of $(NH_4)_6[W_{12}O_{39}]\cdot 4.8H_2O$ to the remaining metal oxide as per the formula:

$$Y_{WO3}\% = \frac{12 \times MWt(WO_3)}{MWt(W\ precursor)} \times 100\%$$

has a value of 92.3 wt. %, which was in strong agreement with the observed yield from the TGA of 92.0 wt. %.

The decomposition profile of the iridium acetate precursor showed only one main step, which occurred from 230 - 294 ºC, with a sharp exothermic peak at ~263 ºC as seen on the DSC curve (Figure A11(b)). This peak is related to complex solid-gas-solid reactions probably involving the production of metallic iridium (Ir^0), iridium oxide (Ir^{4+}) and volatile hydrocarbon products. The TGA weight fraction retained at 263 ºC was 46.80 wt. %, while the theoretical yield for IrO_2 (Ir^{4+}) and Ir (Ir^0) are 52.34 wt. % and 44.90 wt. %, respectively. Therefore, the TGA yield is consistent with a mixed phase of Ir and IrO_2. Thus, a thermally synthesized oxide catalyst at the furnace temperature of 500 ºC in this work may decompose the acetate precursor into both metallic iridium and iridium oxide phases.

Appendix 12: Publisher's Permission Guidelines/Approvals

A12.1 Elsevier

4/22/2019 Rightslink® by Copyright Clearance Center

Copyright Clearance Center RightsLink®

Home | Create Account | Help

Title: Atmospheric plasma spray pyrolysis of lithiated nickel-manganese-cobalt oxides for cathodes in lithium ion batteries

Author: Babajide Patrick Ajayi,Arjun Kumar Thapa,Uroš Cvelbar,Jacek B. Jasinski,Mahendra K. Sunkara

Publication: Chemical Engineering Science

Publisher: Elsevier

Date: 31 December 2017

© 2017 Elsevier Ltd. All rights reserved.

LOGIN

If you're a copyright.com user, you can login to RightsLink using your copyright.com credentials. Already a RightsLink user or want to learn more?

Please note that, as the author of this Elsevier article, you retain the right to include it in a thesis or dissertation, provided it is not published commercially. Permission is not required, but please ensure that you reference the journal as the original source. For more information on this and on your other retained rights, please visit: https://www.elsevier.com/about/our-business/policies/copyright#Author-rights

BACK | CLOSE WINDOW

Copyright © 2019 Copyright Clearance Center, Inc. All Rights Reserved. Privacy statement. Terms and Conditions.
Comments? We would like to hear from you. E-mail us at customercare@copyright.com

A12.2 Royal Society of Chemistry

RE: Permission request

CONTRACTS-COPYRIGHT (shared) <Contracts-Copyright@rsc.org>
Tue 4/23/2019 2:18 AM
To: Ajayi,Babajide Patrick <babajide.ajayi@louisville.edu>

Dear Babajide

I do not know if you have already had a reply to this.

The Royal Society of Chemistry (RSC) hereby grants permission for the use of your paper(s) specified below in the printed and microfilm version of your thesis. You may also make available the PDF version of your paper(s) that the RSC sent to the corresponding author(s) of your paper(s) upon publication of the paper(s) in the following ways: in your thesis via any website that your university may have for the deposition of theses, via your university's Intranet or via your own personal website. We are however unable to grant you permission to include the PDF version of the paper(s) on its own in your institutional repository. The Royal Society of Chemistry is a signatory to the STM Guidelines on Permissions (available on request).

Please note that if the material specified below or any part of it appears with credit or acknowledgement to a third party then you must also secure permission from that third party before reproducing that material.

Please ensure that the thesis states the following:

Reproduced by permission of The Royal Society of Chemistry

and include a link to the paper on the Royal Society of Chemistry's website.

Please ensure that your co-authors are aware that you are including the paper in your thesis.

Regards

Gill Cockhead
Publishing Contracts & Copyright Executive

Gill Cockhead
Publishing Contracts & Copyright Executive
Royal Society of Chemistry,
Thomas Graham House,
Science Park, Milton Road,
Cambridge, CB4 0WF, UK

A12.3 Cambridge University Press

Thank you for your order with RightsLink / Cambridge University Press

no-reply@copyright.com
Mon 4/22/2019 1:49 PM
To: Ajayi,Babajide Patrick <babajide.ajayi@louisville.edu>

CAMBRIDGE JOURNALS

Thank you for your order!

Dear Dr. Babajide Ajayi,

Thank you for placing your order through Copyright Clearance Center's RightsLink® service.

Order Summary

Licensee:	UofL, Chem Eng
Order Date:	Apr 22, 2019
Order Number:	4574321378762
Publication:	Journal of Materials Research
Title:	A rapid and scalable method for making mixed metal oxide alloys for enabling accelerated materials discovery
Type of Use:	Dissertation/Thesis
Order Total:	0.00 USD

View or print complete details of your order and the publisher's terms and conditions.

Sincerely,

Copyright Clearance Center

CURRICULUM VITA

Babajide Patrick Ajayi

Education & Qualifications

-University of Louisville (UofL), Louisville - Kentucky, United States (2013 – 2019)

- *Degree:* Ph.D. Chemical Engineering
- *Advisor*: Mahendra K. Sunkara, PhD
- *Dissertation Title*: Plasma oxidation of liquid precursors for complex metal oxides

-King Fahd Univ. of Petrol. & Minerals (KFUPM), Dhahran, Saudi Arabia (2011 – 2013)

- *Degree*: M.S. Chemical Engineering
- *Advisor*: Basim Abussaud, PhD
- *Thesis Title*: Oxidative dehydrogenation of n-butane over chromium and vanadium supported catalysts with CO_2 as mild oxidant: synthesis, characterization and kinetics

-Obafemi Awolowo University, Ile-Ife, Nigeria (2001 – 2007)

- *Degree:* B.Sc. Chemical Engineering
- *Advisor:* Ambrose Anozie, PhD
- *Project Title:* Simulation and exergy analysis of Nigeria Liquified Natural Gas (NLNG) process

Research Experience

August 2013 – Present| Conn Center for Renewable Energy Research, UofL, Louisville, KY

Position: Graduate Research Assistant

Outline: Designed microwave plasma spray pyrolysis process to produce complex metal oxides deployed in energy storage & conversion technologies

Key responsibilities:

- Development of a plasma spray method to produce mixed metal oxides with firm compositional control
- Fabrication of inexpensive and efficient water electrolyzer electrocatalysts and Li-ion cathode materials
- Synthesis and testing of alkaline-based ceramic for CO_2 capture applications

- Testing of mixed metal oxide catalysts in flow reactor for dry reforming of methane (*Active project*)
- Determination of structure-property relationships through characterization techniques such as XRD, Raman, FE-SEM, EDAX, etc.
- Advanced crystallographic analysis with *GSAS* using the Rietveld method
- Maintain laboratory instruments and enforce OSHA safety practices and high-quality lab documentation

Key achievement:

- Developed a plasma spray process for the accelerated discovery of next-generation complex oxides.
- Produced the lowest platinum group metal (PGM) content (1 %) ever published, with a competitive activity in a mixed PGM/non-PGM electrocatalysts for oxygen evolution reaction.

Sept. 2011 - May 2013| Center for Refining & Petrochemicals, KFUPM, Dhahran, Saudi Arabia

Position: Graduate Research Assistant

Outline: Developed catalysts for conversion of natural gas into platform molecules such as olefins, a precursor for high-value chemicals

Key responsibilities:

- Synthesis and modification of catalysts of micro and mesoporous structures for heterogeneous catalysis applications through hydrothermal technique.
- Catalyst evaluation and comparative studies using both flow and batch reactors.
- Application of various characterization techniques for investigating textural and surface properties of catalysts, e.g: TPx, BET, Pyridine FTIR, Raman.
- Determination of kinetic parameters for model fitting with *MATLAB* and *Mathematica*

Key achievement:

- The first to report a synergetic role of bimetallic catalysts based on vanadium and chromium oxides for improved conversion and selectivity to 1-butene in the dehydrogenation of butane

Industrial Experience

Sept. 2009 - Sept. 2011| Société Générale de Surveillance (SGS), Lagos, Nigeria

Position: Product Analyst & Engineer

Outline: Performed technical and analytical processing of reports based on business rules and processes on product classification, valuation, import eligibility and risk management

Key responsibilities:

- Check completeness and validity of information on document and ensures correct report issuance based on technical knowledge and expertise.
- Work with team to ensure target realization vis-à-vis productivity, quality and timeliness.
- Adhere to quality management system work processes and procedures and company policies.

Key achievement:

- Exceeded expectations in the number of files processed per day by more than 100 %

Sept. 2006 – Feb. 2007| Total Exploration & Production, Port-Harcourt, Nigeria

Position: Junior Engineer

Outline: Generated material balance reports of oil and gas pumped to terminal stations

Key responsibilities:

- Employed Production Data & Management System (PDMS) in production reporting and material balancing.
- Process simulation, process debottlenecking, and project development/management

Patent

M. K. Sunkara, B.P. Ajayi, D. Jaramillo-Cabanzo, A. Nambo (2016) "Production of Mixed Metal Oxide Nanostructured Compounds" U.S. Patent Application No. 15,342,048

Publications

Total Publications = 11, h-index = 6, Total Citations = 93

1. B.P. Ajayi[§], D. Jaramillo-Cabanzo[§], M.K. Sunkara, "One dimensional nanomaterial for lithium ion batteries" J Phys D: Appl. Phy., *Invited Review* (*Submitted*) ([§]*Authors contribute equally to this work*)
2. M. Z. Akram, V. Atla, A. Nambo, B.P. Ajayi, J. Jasinski, J. He, J.R. Gong, M. Sunkara, "Low-temperature and fast kinetics for CO_2 sorption using Li_6WO_6 nanowires",(2018) Nano Lett., 18, 4891-4899 (# of cit.= 2)
3. S. Kumari[§], B. P Ajayi[§], B. Kumar, J. B. Jasinski, M. K. Sunkara, J. M. Spurgeon (2017)," A low-noble-metal $W_{1-x}Ir_xO_{3-\delta}$ water oxidation electrocatalyst for acidic media *via* rapid plasma synthesis" Energy & Env. Sci, 10, 2432-2440. ([§]*Authors contribute equally to this work*) (# of cit.= 14)
4. B. P Ajayi, A. K. Thapa; U. Cvelbar, J. B. Jasinski, M.K. Sunkara, (2017), "Atmospheric plasma spray pyrolysis of lithiated nickel-manganese-cobalt oxides for cathodes in lithium ion batteries", Chem Eng Sci, 174, 302-310. (# of cit.= 2)
5. Ch. Satya Kamal, T.K. Visweswara Rao, P.V.S.S.S.N. Reddy, K. Sujatha, B. P. Ajayi, J. B. Jasinski, K. Ramachandra Rao (2017), "Unravelling the energy transfer mechanism in bismuth co-activation of $LaInO_3$: Sm^{3+}/Ho^{3+} nanophosphor for color-tunable luminescence" *RSC Adv*, 7, 9724-9731. (# of cit.= 9)

6. T. Samuel, Ch. Satya Kamal, S. Ravipati, B. P Ajayi, V. Veeraiah, V. Sudarsan, K. Ramachandra Rao (2017), "High purity green photoluminescence emission from Tb^{3+}, Bi^{3+} co-doped $LaGaO_3$ nanophosphors" Opt. Mater., 69, 230-237. (# of cit.= 5)

7. B. P Ajayi, S. Kumari, D. Jaramillo-Cabanzo, J. M. Spurgeon, J.B. Jasinski, M. K. Sunkara, (2016), "A rapid and scalable method for making mixed metal oxide alloys for enabling accelerated materials discovery" J Mater Res, 31, 1596-1607. (# of cit.= 8)

8. B.R. Jermy, B.P. Ajayi, B.A. Abussaud, S. Asaoka, S. Al-Khattaf (2015), "Oxidative dehydrogenation of n-butane to butadiene over Bi–Ni–O/γ-alumina catalyst" J Mol. Catal. A: Chem 400, 121-131. (# of cit.= 15)

9. B.P. Ajayi, B. Abussaud, B.R. Jermy, S.A. Khattaf (2014)," Kinetic modelling of n-butane dehydrogenation over CrO_x-VO_x/MCM-41 catalyst in a fixed bed reactor" Prog React Kinet Mech 39 (4), 341-353. (# of cit.= 1)

10. B.P. Ajayi, B.R. Jermy, K.E. Ogunronbi, B.A. Abussaud, S. Al-Khattaf (2013), "n-Butane dehydrogenation over mono and bimetallic MCM-41 catalysts under oxygen free atmosphere" Catal Today 204, 189-196(# of cit.= 25)

11. B.P. Ajayi, B.R. Jermy, B.A. Abussaud, S. Al-Khattaf (2013), "Oxidative dehydrogenation of n-butane over bimetallic mesoporous and microporous zeolites with CO_2 as mild oxidant" J Porous Mater, 20, 1257-1270. (# of cit.= 13)

Selected Presentations

1. B. Ajayi, M. K. Sunkara, D. Felipe Jaramillo-Cabanzo, "Plasma Oxidation of Liquid Precursors" 231st ECS Meeting, New Orleans, Louisiana, June 2017

2. B.P. Ajayi, S. Kumari, D. Jaramillo-Cabanzo, J. Spurgeon, J. Jasinski, M. K. Sunkara, "A Combinatorial Synthesis Technique for Mixed Metal Oxides for Accelerated Materials Discovery, Renewable Energy & Energy Efficiency (RE^3) Workshop, Louisville, Kentucky, May 2017

3. B. Ajayi, D. Felipe Jaramillo-Cabanzo, S. Kumari, J. M. Spurgeon, J. B. Jasinski, M.K. Sunkara, "Atmospheric Plasma Jet Oxidation of Solution Based Precursors for Enabling Material Discovery"230th ECS PRiME Meeting, Honolulu, Hawaii, September 2016

Professional Affiliations

- North American Catalysis Society (Tri-State), member since 2017
- Materials Research Society, member since 2016
- Electrochemical Society, member since 2015
- Nat'l Org. for the Professional Adv. of Black Chemists & Chemical Engrs.

Honors and Awards

- First Prize, Poster Session *RE^3 Workshop*, 2017
- NOBCChE Outstanding Service Award, 2016
- University of Louisville Ph.D. Fellowship Award, 2013-2015
- KFUPM Graduate Scholarship Award, 2011-2013